The GRAVITY interferometer and the Milky Way's Nuclear Star Cluster

Oliver Pfuhl

München 2012

The GRAVITY interferometer and the Milky Way's Nuclear Star Cluster

Oliver Pfuhl

Dissertation
an der Fakultät für Physik
der Ludwig–Maximilians–Universität
München

vorgelegt von
Oliver Pfuhl
aus München

München, den 23.04.2012

Erstgutachter: Prof. Dr. R. Genzel
Zweitgutachter: Prof. Dr. A. Burkert
Tag der mündlichen Prüfung: 17.7.2012

Contents

List of Figures

List of Tables

Zusammenfassung

Die vorliegende Arbeit ist thematisch zweigeteilt in einen instrumentellen Teil und einen astrophysikalischen Teil. Der instrumentelle Teil beschreibt die Entwicklung und Implementierung des Fiber Coupler und des Guiding Subsystemes, des zukünftigen VLTI Instrumentes GRAVITY. Der astrophysikalische Teil handelt von der Sternentstehungsgeschichte des Sternhaufens im Zentrum der Milchstraße, welche anhand von Bild- und Spektroskopiedaten, aufgenommen mit dem Very Large Telescope, abgeleitet wurde.
Das zukünftige VLTI Instrument GRAVITY wird mit Hilfe der interferometrischen Vereinigung von vier Teleskopen, Astrometrie mit einer Genauigkeit von Mikrobogensekunden erlauben. Das Instrument ist ein gemeinsames Projekt von mehreren europäischen Forschungsinstituten unter der Leitung des Max-Planck-Institutes für extraterrestrische Physik. Der Instrumentierungsteil dieser Arbeit beschreibt den Fiber Coupler und das Guiding Subsystem. Die Systeme dienen der optischen Strahlstabilisierung sowie der Lichtkopplung in GRAVITY. Um eine Messgenauigkeit von Mikrobogensekunden am Himmel zu erreichen, benötigt GRAVITY eine bisher unerreichte Stabilität des VLTI optischen Pfades. Aus diesem Grund wurde im Rahmen dieser Arbeit ein Guiding System entwickelt, welches die laterale und longitudinale Pupillenposition stabilisiert, sowie Bildverwacklungen innerhalb des VLTI Tunnels korrigiert. Die für die Stabilisierung nowendigen Aktuatoren sind in vier Fiber Coupler Einheiten enthalten. Je ein Fiber Coupler empfängt den Lichtstrahl von einem Teleskop und stabilisiert diesen. Desweiteren erlaubt jede Einheit, das optische Bild zu rotieren, die lineare Polarisation auszurichten, sowie optische Wegverzögerungen der Atmosphäre auszugleichen. Ein neuartiges Prismendesign ermöglicht den Wechsel zwischen einem On-axis sowie einem Off-axis Fringe-tracking Modus ohne optische Elemente auszutauschen oder zu bewegen. Mit Hilfe von parabolischen Spiegeln wird das Licht mit nur minimalen Verlusten in Single-mode Fasern gekoppelt. In dieser Arbeit werden Labormessungen des ersten Guiding Systems sowie des ersten Fiber Coupler Prototypen vorgestellt. Insbesondere die Regelungstechnik und deren Leistungsfähigkeit, sowie die optische Abbildungsqualität des Systems werden behandelt. Anhand der Messergebnisse wird die Leistung des Systems im späteren Einsatz prognostiziert und der Einfluß auf die Sensitivität von GRAVITY diskutiert.
Im astrophysikalische Teil dieser Arbeit werden Photometrie- und Spektroskopiedaten von 450 kalten Riesensternen innerhalb des zentralen Parsecs der Milchstraße ausgewertet. Mit Hilfe der starken CO Absorptionslinien im Infraroten, werden die effektiven Temperaturen der Riesen bestimmt. Darüber hinaus beinhaltet die Arbeit die tiefsten spektroskopis-

chen Beobachtungen, die je im Galaktischen Zentrum gemacht wurden. Anhand dieser tiefen Beobachtungen kann die Zahl der B9/A0 Hauptreihensterne in zwei Feldern bestimmt werden. Mit Hilfe der vorliegenden Daten ist es möglich ein Hertzsprung-Russell Diagramm der roten Riesen im Galaktischen Zentrum zu erstellen und aus dem Vergleich mit Modellsternpopulationen die Sternentstehungsgeschichte zu ermitteln. Es ergibt sich, dass (1) die Sternentstehungsrate von einem anfänglichen Maximum vor etwa 10 Milliarden Jahren auf ein Minimum vor ca. 1-2 Milliarden fiel. Während der letzten hundert Millionen Jahren jedoch stieg die Entstehungsrate wieder an; (2) etwa 80% der stellaren Masse bildete sich vor mehr als 5 Milliarden Jahren; (3) Abschätzungen der dynamischen Masse innerhalb des zentralen Parsecs favorisieren eine vorwiegende Sternenstehung mit einer Chabrier/Koupa Massenverteilung. Der Hauptteil der stellaren Masse scheint sich unter anderen Bedingungen und mit einer anderen Massenverteilung entwickelt zu haben, als die heute beobachtbare junge Sternscheibe. Diese enthält vorwiegend schwere Sterne. Dies kann darauf hindeuten, das die frühen Sterne sich zu einer Zeit bildeten, als das schwarze Loch Sgr A* noch deutlich leichter und dessen Einflusssphäre noch deutlich geringer war, als heute.

Abstract

This thesis is divided into two parts: an instrumentation part and an astrophysical part. The instrumentation part describes the development and implementation of the fiber coupler and guiding subsystems of the 2nd generation VLTI instrument GRAVITY. The astrophysical part describes the derivation of the star formation history of the Milky Way's nuclear star cluster based on imaging and spectroscopic data obtained at the Very Large Telescope.

The future VLTI instrument GRAVITY will deliver micro-arcsecond astrometry, using the interferometric combination of four telescopes. The instrument is a joint project of several European institutes lead by the Max Planck Institut für extraterrestrische Physik.

The instrumental part of this thesis describes the fiber coupler unit and the guiding system. They serve for beam stabilization and light injection in GRAVITY. In order to deliver micro-arcsecond astrometry, GRAVITY requires an unprecedented stability of the VLTI optical train. We therefore developed a dedicated guiding system, correcting the longitudinal and lateral pupil wanderas well as the image jitter in VLTI tunnel. The actuators for the correction are provided by four fiber coupler units located in the GRAVITY cryostat. Each fiber coupler picks the light of one telescope and stabilizes the beam. Furthermore each unit provides field de-rotation, polarization adjustment as well as atmospheric piston correction. A novel roof-prism design offers the possibility of on-axis as well as off-axis fringe tracking. Finally the stabilized beam is injected with minimized losses into single-mode fibers via parabolic mirrors. We present lab results of the first guiding- as well as the first fiber coupler prototype, in particular the closed loop performance and the optical quality. Based on the lab results we derive the on-sky performance of the systems and the implications concerning the sensitivity of GRAVITY.

The astrophysical part of this thesis presents imaging and integral field spectroscopy data for 450 cool giant stars within 1 pc from Sgr A*. We use the prominent CO bandheads to derive effective temperatures of individual giants. Additionally we present the deepest spectroscopic observation of the Galactic Center so far, probing the number of B9/A0 main sequence stars ($2.2 - 2.8\,M_{\odot}$) in two deep fields. From spectro-photometry we construct a Hertzsprung-Russell diagram of the red giant population and fit the observed diagram with model populations to derive the star formation history of the nuclear cluster. We find that (1) the average nuclear star-formation rate dropped from an initial maximum $\sim$10 Gyrs ago to a deep minimum 1-2 Gyrs ago and increased again during the last few hundred Myrs, and (2) that roughly 80% of the stellar mass formed more than 5 Gyrs

ago; (3) mass estimates within R $\sim$ 1 pc from Sgr A* favor a dominant star formation mode with a normal Chabrier/Kroupa initial mass function for the majority of the past star formation in the Galactic Center. The bulk stellar mass seems to have formed under conditions significantly different from the observed young stellar disks, perhaps because at the time of the formation of the nuclear cluster the massive black hole and its sphere of influence was much smaller than today.

Chapter 1

Introduction

The observation of celestial positions and motions (astrometry) has proven to be a powerful tool for studying the laws of nature since the early days of astronomy. The accurate measurement of planetary motions led to Newton's theory of gravity. Astrometric parallaxes provided distances to nearby stars and helped to understand the structure of our galaxy and the universe, while the observed deflection of a star due to the sun's gravitational field marked the breakthrough of Einstein's General Relativity. More recent astrometric measurements of stars proved the existence of the 4 million solar mass black hole SgrA* in the center of the Milky Way and in the near future, astrometry will be able to probe the space-time in the immediate vicinity of just the same black hole.

Interferometry has played an important role in the history of astronomy. Since the first size measurement of the star Betelgeuse by Michelson in the 1920's, the unrivaled resolution of astronomical interferometers has provided key parameters for the understanding of stars in all evolutionary stages. The advent of 8-10 m class telescopes and their interferometric combination allowed to resolve several Active Galactic Nuclei in the nearby universe, such as NGC 1068 and provided insights on accreting super massive black holes (SMBH) on spatial scales of ~ 1 pc.

The second generation instrument GRAVITY for the Very Large Telescope Interferometer (VLTI) will open a new era of high-resolution imaging and narrow-angle precision astrometry. It will be able to combine four telescopes, the 1.8 m Auxiliary Telescopes (AT) or the 8 m Unit Telescopes (UT) of the ESO observatory at Paranal. The large collecting area of the UTs and the capability of fringe-tracking will allow phase-referenced imaging of sources as faint as $m_K \approx 16$ at a ~ 3 milli-arcsecond resolution as well as micro-arcsecond precision astrometry. The improvement in angular resolution will be about a factor 15 compared to diffraction-limited imaging on current 10 m class telescopes.

In its dual-field mode, GRAVITY will provide relative position measurements between two objects with an accuracy of 10 μas, i.e. an angle equal to a Euro coin diameter seen at the distance of the moon. Measuring at that accuracy level means observing the universe in motion, since 10 μas/yr correspond to 5 m/s at a distance of 100 pc (close star-forming regions) and 50 km/s at a distance of 1 Mpc (Andromeda galaxy).

Chapter 2

Narrow-angle interferometric astrometry

Dual-feed interferometry is based on the simultaneous observation of two objects within the same telescope field of view (FoV). Yet, contrary to single-field interferometry, the object separation is larger than the interferometric FoV ($\sim$ PSF of a single telescope). For this reason both objects have to be combined in separate beam combiners. Since the maximum angular separation is typically only a few arcseconds, the beams of both objects are however affected by almost the same atmospheric turbulence (see Section 2.1). Thus, measuring the atmospheric turbulence on one object allows stabilizing the fringes of the second object. This method is called fringe-tracking. The bright object is observed with integration times shorter than the atmospheric coherence time (typically a few milliseconds). The fringe jitter, introduced by density fluctuations in the atmosphere, is then recorded and corrected. This allows long integration times on the second object without smearing of the fringe pattern. The difference of the fringe envelope position δOPD (optical path difference) of the two objects as seen by the beam combiners is directly related to the object separation $\Delta\vec{S}$ on sky and the telescope separation usually referred to as baseline $\vec{B}$. Figure 2.1 illustrates the relation. The fringe position difference δOPD is given by the following equation (e.g. Glindemann et al., 2003):

$$\delta\mathrm{OPD} = \Delta\vec{S} \cdot \vec{B} + \delta\mathrm{OPD}_{\mathrm{atm}} + \delta\mathrm{OPD}_{\mathrm{met}} \tag{2.1}$$

where $\delta\mathrm{OPD}_{\mathrm{atm}}$ is the random contribution of the atmospheric turbulence, $\delta\mathrm{OPD}_{\mathrm{met}}$ is the internal optical path difference and $\Delta\vec{S} \cdot \vec{B}$ is the angular separation of the two objects times the baseline. The internal delay $\delta\mathrm{OPD}_{\mathrm{met}}$ has to be monitored by a dedicated metrology as the optical train and the path of the objects therein are not known a-priori. The atmospheric turbulence $\delta\mathrm{OPD}_{\mathrm{atm}}$, is a statistical process, that averages to zero with time (see Section 2.1). Thus if the integration time is long enough, if the internal delay is monitored with sufficient accuracy and if the baseline geometry is well-known, then the object separation can be measured with very high precision given that $\delta\mathrm{OPD} = \Delta\vec{S} \cdot \vec{B}$. It is possible to achieve an angular precision of $\sim 10\,\mu$as on a 100 m baseline, provided that the fringe position and the internal delay can be measured with a 5 nm accuracy. For

the same baseline and an object separation of 1″ this angular precision also requires the baseline to be known on a 10^{-5} level, meaning 1 mm deviation over 100 m separation.

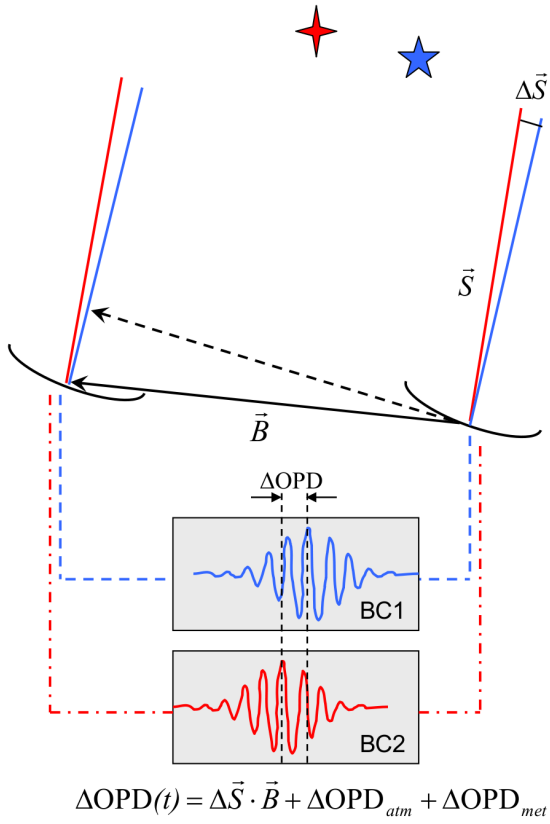

Figure 2.1 Principle of dual-feed astrometry (e.g. Glindemann et al., 2003). Two objects separated by $\Delta\vec{S}$ are observed with two telescopes separated by the baseline $\vec{B}$. The difference of the fringe envelope position δOPD of the two objects as seen by the beam combiners is a measure for the object separation on sky.

2.1 Atmosphere

As indicated previously, ground-based astrometry is fundamentally limited by Earth's atmosphere. This limitation manifests itself in scintillation, image blurring and image motion in case of single dish imaging. In case of multiple apertures, astrometry is limited by the fringe jitter introduced by the atmospheric turbulence. The jitter of two stars however can be correlated, depending on their separation and the aperture size (or baseline in case of an interferometer). This can be understood if one considers the path that the stellar beams travel through the atmosphere. Main contributor to the observed turbulence are atmosphere layers below 10 km. Assuming a height of 10 km, the beams of two stars 20″ apart,

are separated by 1 m. If observed with an 8 m telescope those beams mostly overlap and the resulting image jitter is correlated. This simple argument illustrates the definition of narrow-angle astrometry. Atmospheric perturbations are pictured as turbulence layers being transported across the telescope aperture. The turbulence layers are assumed to be frozen because the density cells change much slower than the time it takes to transport the cells across a typical aperture. Being a statistical process, statements on the resulting jitter can therefore only be made for integration times significantly longer than the time it takes to transport the turbulence layers across the aperture. Strictly speaking the narrow-angle regime is defined as (Shao & Colavita, 1992),

$$\theta << D/h \qquad\qquad t >> D/v \tag{2.2}$$

where θ is the source separation, D is the aperture diameter, h is the effective turbulence height, t is the integration time and v is the wind speed. The advantage of narrow-angle astrometry is that the differential motion of two sources is usually smaller and averages out much quicker than in the wide-angle case. Among the first to recognize the potential of narrow-angle astrometry was Lindegren (1980). However, the application in interferometry was only later proposed by Shao & Colavita (1992). They were the first to note the possibility of micro-arcsecond astrometry, using long baseline interferometry.
Assuming a Kolmogorov turbulent atmosphere, they derived a relation between the atmospheric turbulence and the differential astrometric error. The variance σ of the differential astrometry measurement can be written as (Shao & Colavita, 1992):

$$\sigma^2 \approx 5.25 B^{-4/3} \theta^2 t^{-1} \int C_n^2(h) h^2 v^{-1}(h) \mathrm{d}h \tag{2.3}$$

where B is the baseline, θ is the separation on sky, $C_n^2(h)$ is the turbulence strength as function of height h in meter above ground level and $v(h)$ is the wind profile. Measurements of the atmospheric parameters therefore allow calculating the residual astrometric error due to atmospheric fluctuations as function of baseline and source separation.
The relations between seeing ϵ_0, Fried parameter r_0, and the turbulence integral are given by Roddier (1981),

$$\epsilon_0 = 0.98 \lambda / r_0, \tag{2.4}$$

$$r_0^{-5/3} = 16.7 \lambda^{-2} (\cos\gamma)^{-1} \int_0^\infty C_n^2(h) \mathrm{d}h, \tag{2.5}$$

where λ is the observing wavelength and γ is the zenith angle. Figure 2.2 shows turbulence data from scintillation measurements (Dali Ali et al., 2010) and balloon experiments (von der Lühe, 1995) together with wind profiles of Aristidi et al. (2005) taken at the Paranal site. We find that the turbulence profile is well fit by a powerlaw with a steep exponential cutoff of the form $C_n^2(h) \propto h^\alpha \; e^{-10^{-13} h^3 \; [1/\mathrm{m}^3]}$ (dashed curves in Figure 2.2). For the exponent we find values of $\alpha = -0.87$ and $\alpha = -0.93$. By adding an exponential cutoff term, we can account for the steep decline of turbulence strength at heights greater than 15 km. A similar powerlaw dependence was noted earlier by Dali Ali et al. (2010),

Table 2.1 Typical atmosphere parameters

Data	seeing ϵ_0[a][″]	Fried r_0[a][m]	slope α	$h_{\rm eff}$[b][m]	$v_{\rm eff}$[c][ms^{-1}]
Dali Ali et al. (2010)	0.7	0.7	-0.93	3800	13.6
von der Lühe (1995)	0.4	1.2	-0.87	4200	14.7

[a] Assuming $\lambda = 2.2\mu m$ and zenith angle $\gamma = 0$.
[b] Effective turbulence height [m] above ground.
[c] Wind profile of Aristidi et al. (2005).

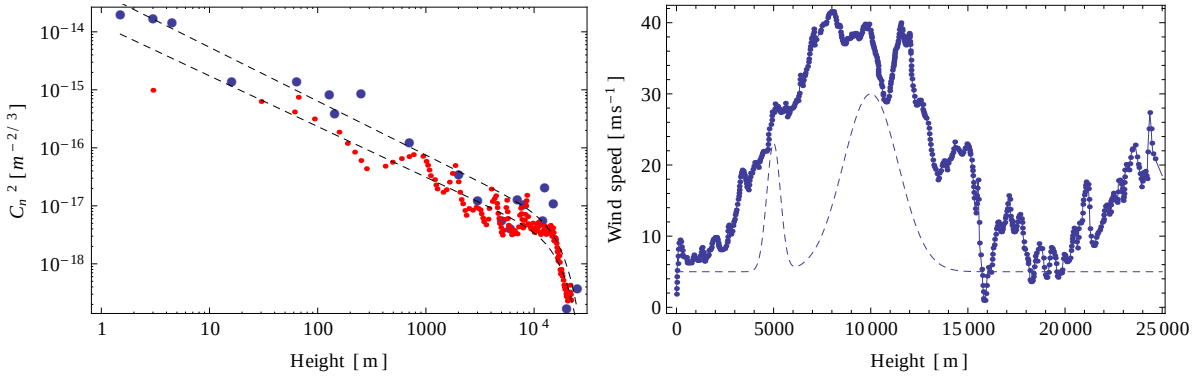

Figure 2.2 **Left:** Atmospheric turbulence strength $C_n^2(h)$ in Paranal as a function of height above ground measured with balloon experiments (red) (von der Lühe, 1995) and scintillation observations (blue) (Dali Ali et al., 2010). The dashed curves show the best-fitting power laws including an exponential cutoff. **Right:** Paranal wind profile taken from Aristidi et al. (2005). The dashed curve shows an ideal two layer wind model used for adaptive optics simulations (Bonaccini, 1996).

however adding an exponential term yields a better agreement with the data. Although the conclusions based on only two independent turbulence measurements have to be taken with caution, the slope of the turbulence spectrum seems to be independent of weather conditions. Worse conditions are mostly reflected in a scaled up turbulence spectrum. Useful parameters that characterize the atmospheric conditions are the effective turbulence height and the effective wind velocity. These quantities represent the weighted mean and are defined as (e.g. von der Lühe, 1995)

$$h_{\rm eff} = \left[\frac{\int C_n^2(h)\cdot h^{5/3}{\rm d}h}{\int C_n^2(h){\rm d}h}\right]^{3/5} \qquad v_{\rm eff} = \left[\frac{\int C_n^2(h)\cdot v^{5/3}{\rm d}h}{\int C_n^2(h){\rm d}h}\right]^{3/5} \tag{2.6}$$

Table 2.1 summarizes the inferred Paranal atmosphere parameters. Applying the measured turbulence and wind profiles together with Equation 2.3, we calculate an astrometric

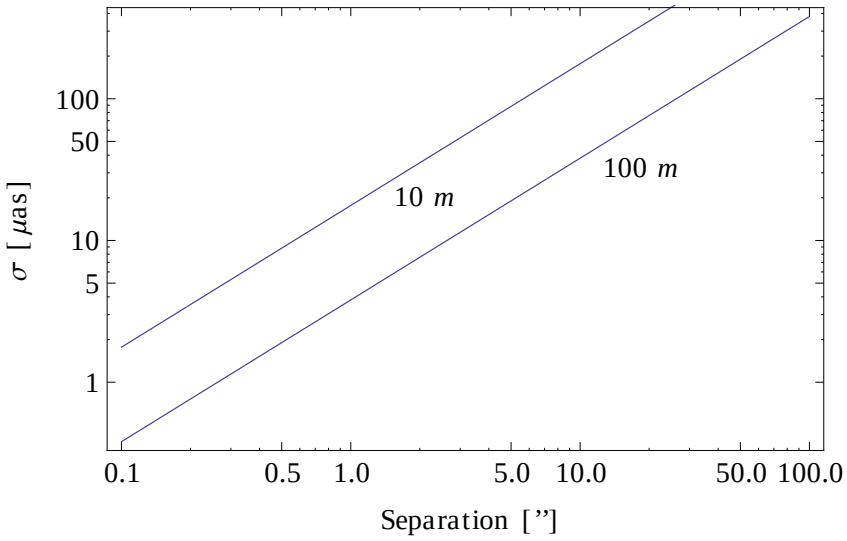

Figure 2.3 Astrometric error as a function of object separation for 10 and 100 m baselines, assuming a Kolmogorov turbulence, $0.4''$ seeing and an integration time of 300 s.

error of:

$$\sigma = \begin{pmatrix} 1420 \\ 2060 \end{pmatrix} B^{-2/3} \theta t^{-1/2} \ [\mu\text{as}], \quad \epsilon_0 \approx \begin{pmatrix} 0.4'' \\ 0.7'' \end{pmatrix}, \tag{2.7}$$

where θ is the object separation in arcseconds, B is the baseline length in meters and t is the integration time in seconds. The inferred effective turbulence height and wind velocity (Table 2.1) define the regime where Equation 2.7 is applicable, i.e. $\theta << B/4000$[m] and $t >> B/14\,[\text{ms}^{-1}]$ (Equation 2.2). The derived astrometric error is comparable to the one found by Shao & Colavita (1992) for good seeing conditions on Mauna Kea. Assuming that the turbulence slope stays roughly constant and only the scaling changes with seeing conditions, then the error scales with seeing as $\sigma \propto \epsilon_0^{5/6}$.
For very long baselines, the assumption of a strict Kolmogorov (infinite outer scale) turbulence overestimates the astrometric error. Dali Ali et al. (2010) found an outer scale length in Paranal of ~ 20 m. Depending on the assumed atmosphere model, this overestimates the error on the longest baselines by about a factor two (Shao & Colavita, 1992). In any case, Equation 2.7 represents conservative values; a finite outer scale slightly improves the results.

The astrometric error as a function of object separation is shown in Figure 2.3. Under good weather conditions and source separations of less than $2''$ it is possible to achieve astrometric errors $< 10\,\mu$as within an integration time of 5 minutes.

2.2 Baseline definition

Narrow-angle astrometry with two beam combiners requires measuring the differential optical path of the objects of interest (see Figure 2.1) at nm accuracy but it also requires precise knowledge of the telescope separation namely the baseline. Since telescopes are extended structures and not just simple points in the UV plane, the definition of the 3D baseline vector $\vec{B}$ requires some attention. Following Lacour & Bonnet (2011) the baseline definition depends on the actual observable. They define three baselines.
The most commonly used baseline definition is related to the absolute angular position of an object on sky. This definition is required for the delay line model, i.e. to calculate the necessary delay to be introduced by the delay lines to zero the optical path. The OPD follows from:

$$\mathrm{OPD} = \vec{B}_{\mathrm{W}} \cdot \vec{S} \tag{2.8}$$

where the *wide-angle baseline* $\vec{B}_{\mathrm{W}}$ is the vector connecting the pivot points of the telescopes and $\vec{S}$ is the vector pointing to the object on sky.
The *imaging baseline* relates the object structure on sky to the complex visibility measured by a single interferometer. In the simple case that the object consists of two point sources with unity visibility separated by the angle $\vec{\Delta S} = \vec{S}_1 - \vec{S}_2$ then the phase difference can be written as;

$$\delta\mathrm{OPD} = \vec{B}_{\mathrm{I}} \cdot \vec{S}_1 - \vec{B}_{\mathrm{I}} \cdot \vec{S}_2 = \vec{B}_{\mathrm{I}} \cdot \vec{\Delta S} \tag{2.9}$$

where $\vec{B}_{\mathrm{I}}$ is the vector connecting the weighted footprints of the object on the telescope primary mirrors. In case of GRAVITY, the footprint has to be weighted by the injection modes of the fibers.
The astrometric mode of GRAVITY uses two interferometers to measure distances on sky. Both beam combiners are optically tied by a dedicated metrology system. The system serves as a ruler for the separation on sky. In that respect it is convenient to define the *narrow-angle baseline* $\vec{B}_{\mathrm{NA}}$ as the vector connecting the points where the metrology receivers are located, i.e. where the baseline is physically realized. In case of GRAVITY, these are photodiodes mounted on the telescope spiders above the primary mirror. As in the imaging case, the OPD is related to the *narrow-angle baseline* as:

$$\delta\mathrm{OPD} = \vec{B}_{\mathrm{NA}} \cdot \vec{\Delta S} \tag{2.10}$$

Assuming that fringes of the two objects are centered at zero OPD, the metrology measures directly the δOPD.
Ideally all three baselines are exactly the same. However, the telescope design and the technical feasibility make them different. Typically the telescope primary mirror and the pivot point do not coincide (except for a siderostat). Furthermore, the actual pivot point is often not accessible and can not be equipped with metrology references. Therefore the different definitions of baselines, depending on the observable, are needed. Each baseline has to be calibrated independently since the separation of the respective points is only poorly known a priori. Figure 2.4 sketches the individual baselines in case of GRAVITY.

The calibration of the wide-angle baseline is rather simple. It requires finding the fringe position for a single object as function of baseline and source position. In case of the VLTI this baseline is typically calibrated to a sub-mm accuracy, meaning that the fringe position can be predicted at that level. Yet, the wide-angle calibration does not directly give the narrow-angle baseline. This can be simply understood from Equations 2.8 & 2.10. While the wide-angle phase (OPD) depends on the baseline projection on the source vector $\vec{S}$, the narrow-angle phase (δOPD) depends on orthogonal separation vector $\vec{\Delta S}$. Therefore the two projected baselines are perpendicular and thus independent from each other. In the following, the term baseline always refers to the narrow-angle baseline if not stated otherwise.

The baseline can be seen as the ruler for the distance measurement on sky. Aiming for a

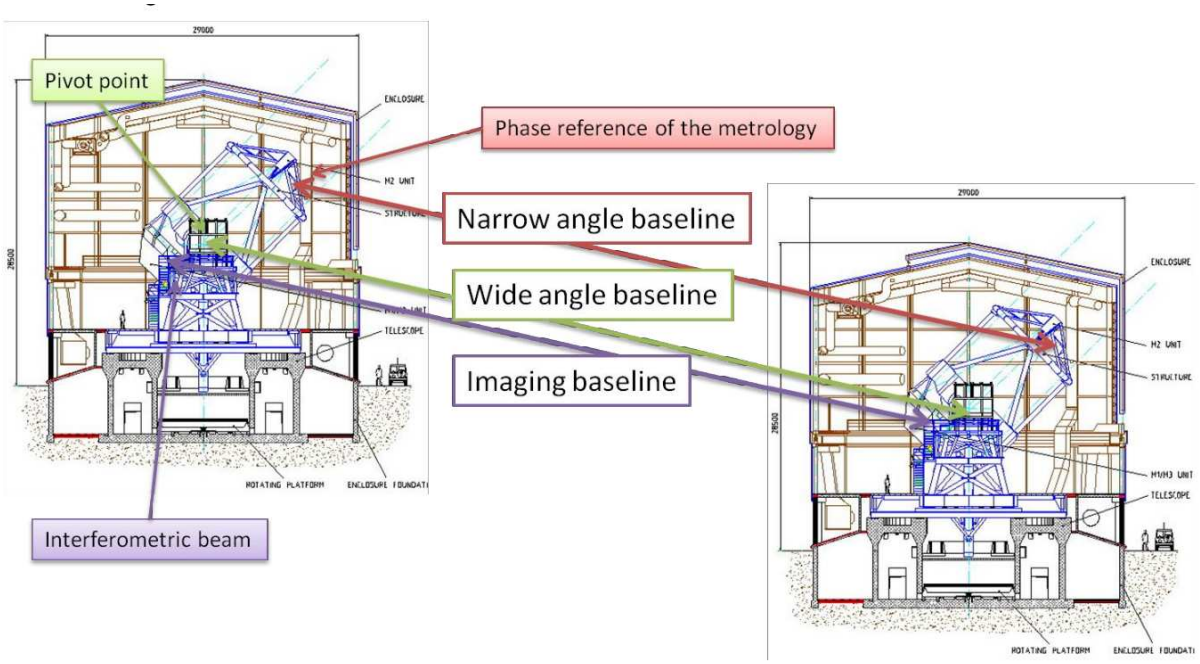

Figure 2.4 Sketch of the individual baselines. The wide-angle baseline is the vector connecting the pivot point of the two telescopes. The imaging baseline is represented by the vector connecting the center of illumination on the primary mirrors weighted by the fiber modes. The narrow-angle baseline connects the metrology references of the two telescopes. Figure courtesy of S. Lacour (from Lacour & Bonnet, 2011)

10 μas accuracy over the full 2″ FoV of the VLTI requires the baseline to be known at a 0.5×10^{-5} level, i.e. 0.5 mm deviation over 100 m baseline. Measuring separations at that level is already a non-trivial task. However, it gets more complicated, since the baseline changes with the target position on sky and that position changes constantly with the rotation of the earth. Since it is not clear if it is possible to measure the baseline at the required level, the approach is slightly different. Essentially none of the astrometric science

cases requires an absolute angular measurement at the level of few μas. The interesting quantity is a changing separation, meaning motion of celestial bodies. This is true for flares of the massive black holes SgrA* as well as for stellar motion due to planetary companions. It is therefore not necessary that the absolute baseline is known but it is required that the baseline is stable at the mm level. This requirement is easier to meet because it allows calibrating the baseline with objects on sky, where the separation is unknown but does not change. The issue of stability can be split into a mechanical stability and an optical stability.

2.3 Baseline stability

The mechanical baseline stability is related to the stiffness of the telescope structure, the alignment accuracy of the metrology receivers, wobble during rotation and other effects. Strictly speaking, only differential mechanical instabilities between the two telescopes affect the baseline. For example telescope flexure due to the weight of the telescope will only affect the baseline, if the telescopes flex in a different way. Since the VLT telescopes are built identical, the differential flexure is supposed to be small and only a second order effect.
However, we expect the (differential) telescope flexure and any misalignment (offset) of the metrology receivers to be the most important baseline errors. Since the narrow-angle baseline is only a 2D vector perpendicular to the pointing direction of the telescope, the calibration of the baseline errors can be simplified. The real baseline $\vec{B} = \vec{B}_m + \Delta\vec{B}_{\text{flex}} + \Delta\vec{B}_{\text{offset}}$ is the sum of the baseline returned by model of the VLTI $\vec{B}_m$ and the error terms $\Delta\vec{B}_{\text{flex}}$ and $\Delta\vec{B}_{\text{offset}}$. Both error terms can be disentangled because they depend on the altitude and azimuth of the target in a different way.
The metrology receivers are located at the telescope spiders above the primary mirror (and the pivot point). This means that the receivers will change their position with respect to the primary mirror if the telescope structure is subject to flexure. It is therefore reasonable to assume that the magnitude of the flexure term $\Delta\vec{B}_{\text{flex}}$ is related to the altitude of the target. The gravity vector projected on the narrow-angle baseline simply depends on the cosine of the altitude angle and lies in the plane of the zenith vector and the target pointing vector. Therefore to first order the flexure term will show a cosine dependence $|\Delta\vec{B}_{\text{flex}}| \propto \cos(a)$, where the flexure is zero at zenith pointings and maximum at horizon. Since the source separation vector changes orientation with the earth rotation, the direction of the flexure error term changes accordingly. In fact, the orientation changes with the image rotation seen by the Alt-Az telescope.
The offset term is related to a misalignment of the metrology receivers with respect to the primary mirror. To be more precise, with respect to the fiber-mode weighted illumination of the primary mirror. This offset $\Delta\vec{B}_{\text{offset}}$ is constant, but again the orientation of the source separation and thus, also the baseline error change due to image rotation. The resulting error terms are illustrated in Figure 2.5. Both error terms can be calibrated with visual binaries, where the separation does not change during the calibration. In principle,

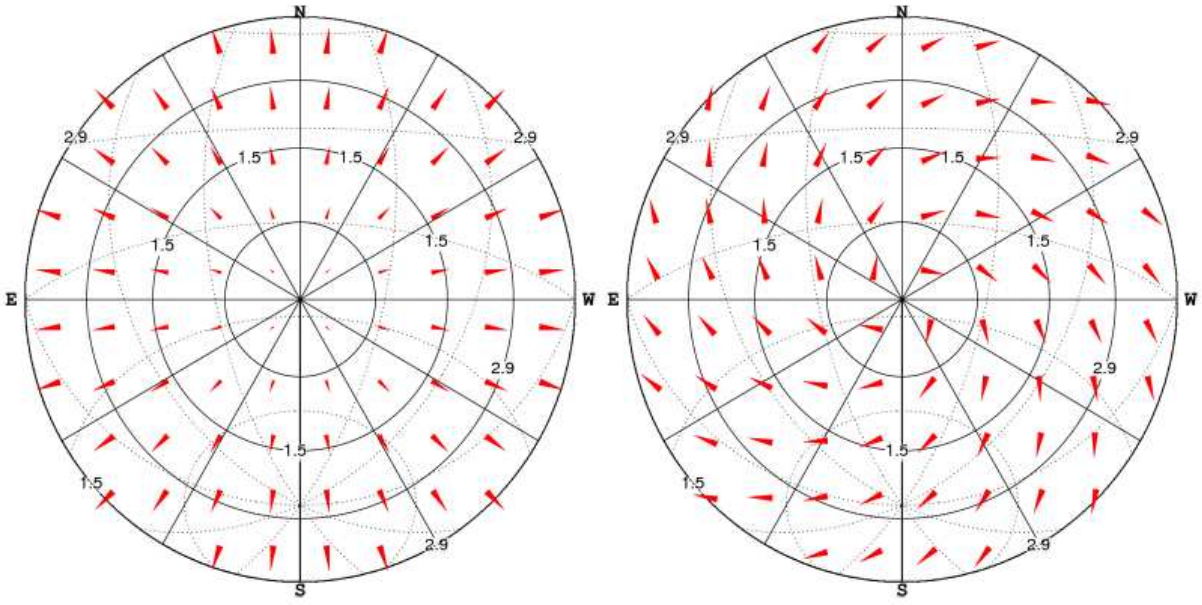

Figure 2.5 Narrow-angle baseline error as function of pointing direction. The number on each circle represents the airmass. Shown here is the baseline error due to telescope flexure (left) and due to a misalignment (right) of the metrology reference (from Lacour et al., 2011).

two binaries with different declination should be sufficient to calibrate both error terms. Monitoring one binary close to zenith avoids large flexure contributions and leaves only the offset term. Consequently the observation of a binary over a large altitude range allows to calibrate the flexure term. If higher order baseline errors, like telescope wobble, flexure hysteresis or other effects contribute in a non negligible way, then more binaries are necessary to calibrate the error terms. Simulations performed by Lacour et al. (2011) indicate that a number of six binaries is sufficient to calibrate the narrow-angle baseline at a 0.5 mm level.

2.4 Optical stability

While the mechanical stability is related to the endpoints of the narrow-angle baseline, the optical stability relates the optical path of the two objects and the metrology laser through the VLTI. The beam stability in the VLTI is important because of two reasons; injection efficiency and astrometric accuracy. Deriving the differential OPD of two objects requires several phase measurements; the phase of the fringe tracking channel, the science channel and the metrology phases from the two telescopes. Figure 2.6 shows the optical path of the two objects through the VLTI to the beam combiners. The beams are routed via the main delay lines (DL), one per interferometer arm into the VLTI lab. The beams

get separated, coupled into single-mode fibers, and eventually each object passes through a differential delay line (DDL). After the beam superposition, each interferometer (fringe tracking and science channel) returns a phase ($\phi_{\rm FT}$ and $\phi_{\rm SC}$). Internal optical path differences are monitored by the metrology. For that purpose a laser is split and injected into both beam combiners, traveling the same path as the stellar light in reverse direction (see Section 3.1.9). The relative phase of the two laser beams, recorded above the primary mirror, measures the internal OPD of the two objects in the respective interferometer arm ($\phi_{\rm M,1}$ and $\phi_{\rm M,2}$). Following Lacour & Bonnet (2011), the δOPD is then related to the individual phase measurements according to:

$$\delta\mathrm{OPD} = (\phi_{\rm FT} - \phi_{\rm SC})\frac{\lambda_s}{2\pi} + (\phi_{\rm M,1} - \phi_{\rm M,2})\frac{\lambda_m}{2\pi} \tag{2.11}$$

where λ_s is the science wavelength and λ_m is the metrology wavelength. The phase seen by the fringe tracker now depends on the projected baseline $\vec{B}\cdot\vec{\alpha}$ and the internal delays in the two interferometer arms. The fringe-tracker phase can then be derived from (Lacour & Bonnet, 2011):

$$\phi_{\rm FT} = [(\mathrm{DL}_{\rm FT,1} + \mathrm{DDL}_{\rm FT,1}) - (\mathrm{DL}_{\rm FT,2} + \mathrm{DDL}_{\rm FT,2} + \vec{B}\cdot\vec{\alpha})]\frac{2\pi}{\lambda_s} + I_{\rm FT,1} - I_{\rm FT,2} \tag{2.12}$$

Accordingly the phase of the science beam combiner follows from:

$$\phi_{\rm SC} = [(\mathrm{DL}_{\rm SC,1} + \mathrm{DDL}_{\rm SC,1}) - (\mathrm{DL}_{\rm SC,2} + \mathrm{DDL}_{\rm SC,2} + \vec{B}\cdot\vec{\beta})]\frac{2\pi}{\lambda_s} + I_{\rm SC,1} - I_{\rm SC,2} \tag{2.13}$$

where the main delay lines $\mathrm{DL}_{\rm FT,j}$ and $\mathrm{DL}_{\rm SC,j}$ compensate the optical path difference between the telescopes. The index j indicates the two interferometer arms. Although both objects pass through the same DLs, the distinction between science and fringe-tracking beam is necessary since optical imperfections and the fact that both beams only partially overlap can result in a slightly different optical path length. The differential delay lines $\mathrm{DDL}_{\rm SC,j}$ and $\mathrm{DDL}_{\rm FT,j}$ are introduced to compensate the small differential optical path between the two objects. Aberrations in the optical train can cause erroneous phase delays when injected into a single-mode fiber. These additional injection terms are denoted as $I_{\rm FT,j}$ and $I_{\rm SC,j}$. The metrology phases recorded at the telescopes can be derived from (Lacour & Bonnet, 2011; Gillessen, 2011):

$$\begin{aligned}
\phi_{\rm M,1} &= [(\mathrm{DL}_{\rm SC,1} + \mathrm{DDL}_{\rm SC,1}) - (\mathrm{DL}_{\rm FT,1} + \mathrm{DDL}_{\rm FT,1})]\frac{2\pi}{\lambda_m} + e_1 \\
\phi_{\rm M,2} &= [(\mathrm{DL}_{\rm SC,2} + \mathrm{DDL}_{\rm SC,2}) - (\mathrm{DL}_{\rm FT,2} + \mathrm{DDL}_{\rm FT,2})]\frac{2\pi}{\lambda_m} + e_2
\end{aligned} \tag{2.14}$$

where λ_m is the metrology wavelength. The additional error terms e_i take into account that the metrology phase is recorded at four discrete spots above the telescope primary mirror. Aberrations and misalignments can thus introduce a phase offset with respect to

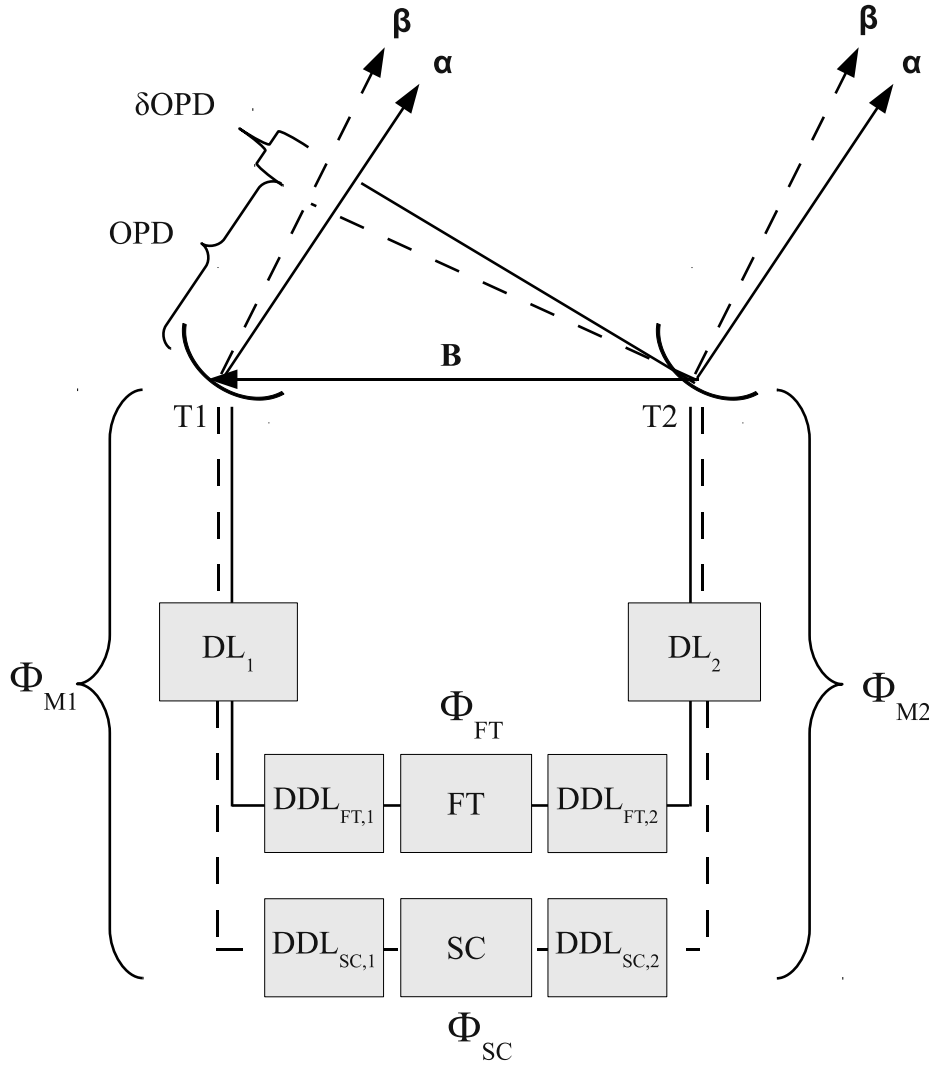

Figure 2.6 Optical concept of dual-field astrometry with GRAVITY. The light of two objects $\vec{\alpha}$ and $\vec{\beta}$ is collected by telescopes $T1$ and $T2$. The optical path difference between the telescopes is compensated with the main delay lines $\vec{B} \cdot \vec{\alpha} \approx \mathrm{DL}_1 - \mathrm{DL}_2$. The differential optical path between the two objects is compensated by the differential delay lines $\mathrm{DDL}_{i,j}$. The internal differential optical path between the two objects in each arm of the interferometer is monitored by the metrology ($\phi_{\mathrm{M},1}$ and $\phi_{\mathrm{M},2}$).

the average phase across the pupil.
Applying Equation 2.11 yields the measured differential optical path:

$$\delta\mathrm{OPD} = \vec{B}\cdot(\vec{\alpha}-\vec{\beta}) + (I_{\mathrm{FT,1}} - I_{\mathrm{FT,2}} + I_{\mathrm{SC,2}} - I_{\mathrm{SC,1}})\frac{\lambda_s}{2\pi} - (e_1 - e_2)\frac{\lambda_m}{2\pi} \tag{2.15}$$

In absence of injection and metrology errors, the sum of of the fringe tracker, science channel and the two metrology phases therefore returns the true differential optical path of the two objects. Inverting the equation, while knowing the baseline obviously gives the angular separation. However the error terms can lead to an erroneous OPD measurement and therefore need special attention.

2.5 Phase errors of science and fringe tracking channel

Using single-mode fibers in the beam combination allows a robust mathematical description of the error terms. The coupling into a single-mode fiber can be described as the overlap integral of the fiber mode $F(\vec{u})$ and the complex electrical field $E(\vec{u})$ coming from the star (Wagner & Tomlinson, 1982; Wallner et al., 2002). The coupling can be either calculated in the pupil or in the focal plane, where $\vec{u}$ is a vector in the respective plane. The normalized coupling integral can therefore be written as (e.g. Wagner & Tomlinson, 1982; Lacour & Bonnet, 2011):

$$\rho_{\mathrm{i,j}} = \frac{\int F_{\mathrm{i,j}}(\vec{u})\cdot E^*_{\mathrm{i,j}}(\vec{u})\ d\vec{u}}{\sqrt{\int |F_{\mathrm{i,j}}|^2\ d\vec{u}\cdot\int |E_{\mathrm{i,j}}|^2\ d\vec{u}}} \tag{2.16}$$

Since we are only interested in the average phase coupled into the fiber, the phase injection error is:

$$I_{\mathrm{i,j}} = \arg\left(\frac{\int F_{\mathrm{i,j}}(\vec{u})\cdot E^*_{\mathrm{i,j}}(\vec{u})\ d\vec{u}}{\sqrt{\int |F_{\mathrm{i,j}}|^2\ d\vec{u}\cdot\int |E_{\mathrm{i,j}}|^2\ d\vec{u}}}\right) \tag{2.17}$$

where index i represents either the fringe tracking or the science channel and index j denotes interferometer arm 1 and 2. In the following sections, the calculations are performed at the primary mirror of the telescope. Supposing the stellar wavefront is flat at the pupil (i.e. corrected by the AO), the electrical field can be simply described as (for simplicity the amplitude is set to unity):

$$\begin{aligned} E_{\mathrm{FT,j}} &= \exp\left(-i\frac{2\pi\vec{\alpha}\cdot\vec{u}}{\lambda_s}\right) \\ E_{\mathrm{SC,j}} &= \exp\left(-i\frac{2\pi\vec{\beta}\cdot\vec{u}}{\lambda_s}\right) \end{aligned} \tag{2.18}$$

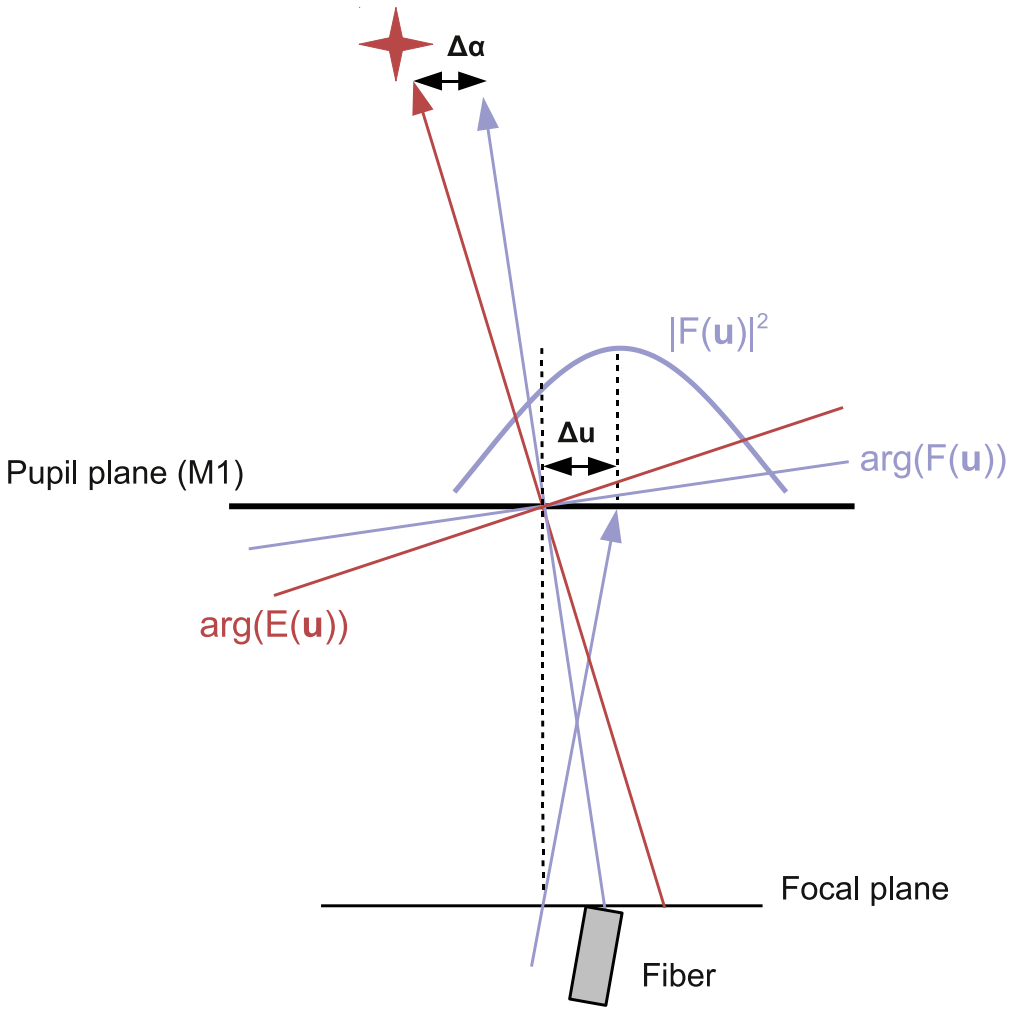

Figure 2.7 Injection into a single-mode fiber. The intensity $|F(\vec{u})|^2$ and phase $\arg(F(\vec{u}))$ of the fiber mode are shown in light blue. The incident wavefront and phase of the stellar light is shown in red. The fiber wavefront is perpendicular to the pointing of the fiber. In the presence of tip-tilt aberrations, the wavefront of the fiber is inclined by $\vec{\Delta\alpha}$ with respect to the star's incoming wavefront (in the pupil plane). In the focal plane, the inclined wavefront corresponds to a lateral displacement between the fiber and the image of the star. A tilted fiber in the focal plane however leads to a lateral pupil error $\vec{\Delta u}$ of the fiber amplitude with respect to the M1 center.

where $\vec{u}$ is now a 2D vector in the pupil plane. The injection into a single-mode fiber is illustrated in Figure 2.7. The fiber wavefront is perpendicular to the pointing of the fiber. Subject to tip-tilt jitter and lateral misalignment, the fiber pointing can deviate from the position of the star ($\vec{\Delta\alpha}_j$ and $\vec{\Delta\beta}_j$). This leads to an inclination between the fiber wavefront and the stellar wavefront. Pupil errors, such as a fiber, which is tilted with respect to the focal plane, causes an offset between the Gaussian amplitude and the center of the primary mirror M1 ($\vec{\Delta u}_{\mathrm{FT,j}}$ and $\vec{\Delta u}_{\mathrm{SC,j}}$). The fiber mode in the presence of misalignments can be described as (Wagner & Tomlinson, 1982; Lacour & Bonnet, 2011):

$$\begin{aligned} F_{\mathrm{FT,j}}(\vec{u}) &= \exp\left(-\frac{(\vec{u}-\vec{\Delta u}_{\mathrm{FT,j}})^2}{\sigma^2}\right)\cdot\exp\left(i\frac{2\pi(\vec{\alpha}-\vec{\Delta\alpha}_j)\cdot\vec{u}}{\lambda_s}\right) \\ F_{\mathrm{SC,j}}(\vec{u}) &= \exp\left(-\frac{(\vec{u}-\vec{\Delta u}_{\mathrm{SC,j}})^2}{\sigma^2}\right)\cdot\exp\left(i\frac{2\pi(\vec{\beta}-\vec{\Delta\beta}_j)\cdot\vec{u}}{\lambda_s}\right) \end{aligned} \tag{2.19}$$

Without loss of generality, we can define the phase at the pupil center, to be zero (see Figure 2.7):

$$\arg(F_{\mathrm{i,j}}(0)) = 0 \tag{2.20}$$

Optical aberrations in the VLTI train, that are able to affect the fiber phase, are therefore a baseline calibration issue.

2.5.1 Lateral pupil offset and no tip-tilt error

A displacement of the pupil will move the Gaussian mode of the fiber across the pupil. However, the wavefront is still perpendicular to the direction of the target if $\vec{\Delta\alpha} = 0$. Therefore the injection error is:

$$I = \arg\left(\int \exp\left(-\frac{(\vec{u}-\vec{\Delta u})^2}{\sigma^2}\right)\cdot\exp\left(i\frac{2\pi\vec{\alpha}\cdot\vec{u}}{\lambda_s}\right)\cdot\exp\left(-i\frac{2\pi\vec{\alpha}\cdot\vec{u}}{\lambda_s}\right)\, d\vec{u}\right) = 0 \tag{2.21}$$

Since the complex factor vanishes if the fiber wavefront is oriented parallel to the stellar wavefront, the argument of the integral is zero. Therefore the presence of a pupil error without additional tip/tilt error leaves the coupled phase unharmed.

2.5.2 Tip-tilt error and no pupil offset

Lateral misalignment between the fiber and the image of the star, causes a tilt of the fiber wavefront with respect to the star. However if the fiber is centered on the pupil

($\vec{\Delta u}_{\mathrm{FT,j}} = 0$), the integral reduces to:

$$\begin{aligned} I &= \arg\left(\int \exp\left(-\frac{(\vec{u})^2}{\sigma^2}\right) \cdot \exp\left(-i\frac{2\pi\vec{\Delta\alpha}\cdot\vec{u}}{\lambda_s}\right)\ d\vec{u}\right) \\ &= \arg\left(\sqrt{\pi}\ \sigma\ \exp\left(-\frac{\pi^2|\vec{\Delta\alpha}|^2\sigma^2}{\lambda_s^2}\right)\right) \\ &= 0 \end{aligned} \tag{2.22}$$

Again the argument of the integral vanishes. Therefore the phase coupled into the fiber is not affected by tip/tilt error alone. However, it is easy to see that the coupled flux $\rho^2 \propto \exp(-|\vec{\Delta\alpha}|^2)$ depends sensitively on the tip/tilt error. Although the phase is not affected, tip/tilt errors therefore lead to a significant loss of light.

2.5.3 Tip-tilt error in conjunction with pupil offsets

As described above, pupil and tip-tilt errors alone do not affect the phase coupled into the fiber. Yet, solving the integral in the presence of both error terms leads to:

$$\begin{aligned} I &= \arg\left(\int \exp\left(-\frac{(\vec{u}-\vec{\Delta u})^2}{\sigma^2}\right) \cdot \exp\left(-i\frac{2\pi\vec{\Delta\alpha}\cdot\vec{u}}{\lambda_s}\right)\ d\vec{u}\right) \\ &= \arg\left(\sqrt{\pi}\ \sigma\ \exp\left(-\frac{\pi^2|\vec{\Delta\alpha}|^2\sigma^2}{\lambda_s^2} - i\ \frac{2\pi\ \vec{\Delta\alpha}\cdot\vec{\Delta u}}{\lambda_s}\right)\right) \\ &= \frac{2\pi\vec{\Delta\alpha}\cdot\vec{\Delta u}}{\lambda_s} \end{aligned} \tag{2.23}$$

hence, as pointed out by Lacour & Bonnet (2011), the conjunction of pupil and tip/tilt error introduces a phase shift if coupled into a fiber.

2.6 Phase errors of the metrology

The metrology measures the optical path in reverse direction and stops above M1. The actual phase measurement is done at four discrete spots in the pupil plane (see Section 3.1.9). The weighted mean of the four measurements yields the metrology phase. Ideally the four spots are located symmetrically around the M1 center and the effective metrology pupil error $\vec{\Delta u}_{\mathrm{M,j}} = 0$. In case of a displacement, the metrology pupil error can be expressed as:

$$\vec{\Delta u}_{\mathrm{M,j}} = \int \vec{u} \sum \delta(\vec{u} - \vec{m}_k)\ d\vec{u} \tag{2.24}$$

where $\vec{m}_{\mathrm{k}}$ are the four metrology receivers and index j denotes one of the telescopes. Very similar to the phase error of the fringe tracking and science channel, the metrology phase

error can be calculated from (Lacour & Bonnet, 2011):

$$e_{\mathrm{j}} = \int \sum \delta(\vec{u} - \vec{m}_k)[\arg(F_{\mathrm{FT,j}}(\vec{u})) - \arg(F_{\mathrm{SC,j}}(\vec{u}))]\, d\vec{u} \tag{2.25}$$

The major difference is the missing stellar phase term and the additional weighting function taking into account the discrete metrology reference spots. Using Equation 2.19 and 2.24, the integral is easily found to be:

$$e_{\mathrm{j}} = \frac{2\pi\ (\vec{\alpha} - \vec{\Delta\alpha}_{\mathrm{j}}) \cdot \vec{\Delta u}_{\mathrm{M,j}}}{\lambda_m} - \frac{2\pi\ (\vec{\beta} - \vec{\Delta\beta}_{\mathrm{j}}) \cdot \vec{\Delta u}_{\mathrm{M,j}}}{\lambda_m} \tag{2.26}$$

2.7 Error budget

Introducing Equations 2.26 and 2.23 into the δOPD measurement (2.15) leads to the main equation of the GRAVITY *Astrometric Error Budget* (Lacour & Bonnet, 2011):

$$\begin{aligned} \delta\mathrm{OPD} &= (\vec{B} + \vec{\Delta u}_{\mathrm{M,2}} - \vec{\Delta u}_{\mathrm{M,1}}) \cdot (\vec{\alpha} - \vec{\beta}) \\ &+ \vec{\Delta\alpha}_1 \cdot (\vec{\Delta u}_{\mathrm{FT,1}} - \vec{\Delta u}_{\mathrm{M,1}}) \\ &- \vec{\Delta\alpha}_2 \cdot (\vec{\Delta u}_{\mathrm{FT,2}} - \vec{\Delta u}_{\mathrm{M,2}}) \\ &+ \vec{\Delta\beta}_2 \cdot (\vec{\Delta u}_{\mathrm{SC,2}} - \vec{\Delta u}_{\mathrm{M,2}}) \\ &- \vec{\Delta\beta}_1 \cdot (\vec{\Delta u}_{\mathrm{SC,1}} - \vec{\Delta u}_{\mathrm{M,1}}) \end{aligned} \tag{2.27}$$

As described in Section 2.2, the narrow-angle baseline is defined as the vector connecting the metrology reference points. Consequently, the first term of Equation 2.27 can be understood as the actual narrow angle baseline ($\vec{B}_{\mathrm{NA}} = \vec{B} + \vec{\Delta u}_{\mathrm{M,2}} - \vec{\Delta u}_{\mathrm{M,1}}$), where $\vec{B}$ connects the center of two primary mirrors. As previously described, a misplacement or bending of the metrology reference points directly translates into a baseline error (see Section 2.3) and can be seen as a zero-order error term, in the sense that the induced astrometric error scales with the object separation on sky. Achieving a 10μas accuracy for two objects separated by 2″ and a 100 m baseline requires $\vec{\Delta u}_{\mathrm{M,j}} < \frac{10\mu\mathrm{as}}{2''} 100\,\mathrm{m} = 0.5\,\mathrm{mm}$. The difference between the impact of the metrology and the fringe-tracking/science channel pupil error is, that the metrology changes the baseline. However, the metrology reference spots are fixed with respect to M1 and are only subject to a deformation of the telescope structure. Turning to the second order error terms in Equation 2.27, shows that a combination of tip/tilt and pupil errors are also able to introduce OPD. This particular error does not scale with the separation of the objects but depends on the ability to keep the fiber on each star and to center the fiber pupils on the metrology reference spots. Figure 2.8 shows the various pupils, which ideally coincide with the telescope pivot point. While the metrology pupil is mechanically fixed to M1, the two fiber modes can shift due to optical effects as delay line wobble, telescope motion etc. Typical pupil shifts in the VLTI are on the order 4% of the pupil, i.e. $\vec{\Delta u}_{\mathrm{FT,j}} \sim 32\,\mathrm{cm}$ at M1 (see Section 5.4.2). The atmospheric tip/tilt error is eventually corrected by the AO of the telescope, however the 200 m tunnel atmosphere

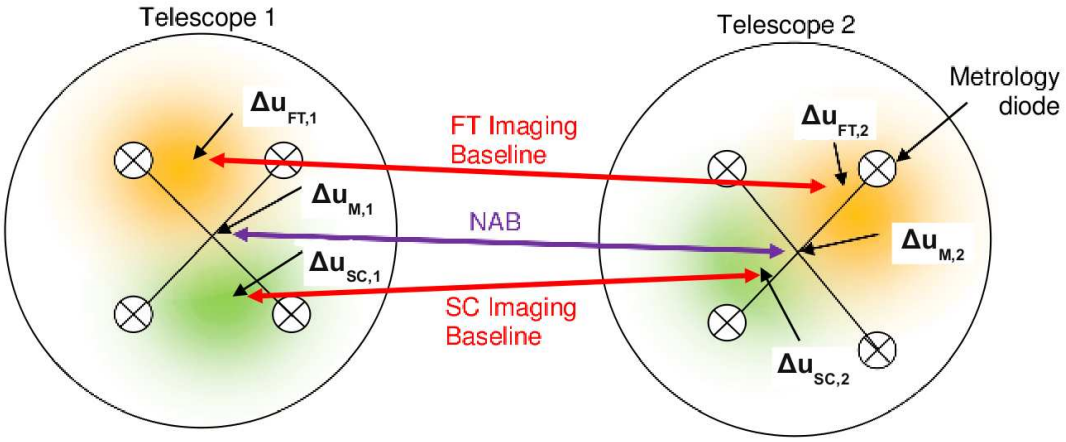

Figure 2.8 Different pupil positions as illustrated by Lacour & Bonnet (2011). The endpoints of the metrology define the narrow-angle baseline. Ideally the metrology pupil center coincides with the pivot point of the telescope. Deviations from the pivot point are denoted with $\vec{\Delta u}_{\mathrm{M,j}}$. Unlike the metrology pupil, the fringe tracking and science channel pupil are not fixed with respect to M1. Their position has to be actively controlled, ideally centering the fiber mode on the metrology pupil (from Lacour & Bonnet, 2011).

introduces ~ 50 mas RMS additional tilt error. Set aside the severe flux loss by an uncorrected tunnel tip/tilt, the additional OPD error due to the tilt and the pupil wander is of the order 78 nm (see Equation 2.27). Given that the δOPD has to be known at a ~ 5 nm precision to achieve the goal of 10 μas angular resolution, it is therefore necessary to actively stabilize the pupil wander and tilt jitter to meet the astrometric requirements.

Chapter 3

GRAVITY overview

GRAVITY has been proposed in 2005 as an adaptive optics assisted beam combiner for the second generation VLTI instrumentation (Eisenhauer et al., 2005b). The instrument will provide high precision narrow-angle astrometry and phase-referenced interferometric imaging at wavelengths between 1.95 μm and 2.45 μm.
The working principle of GRAVITY can be nicely illustrated, using the prime science goal as an example (e.g. Eisenhauer et al., 2008; Gillessen et al., 2010): Figure 3.1 illustrates the working principle. A bright wavefront reference star (IRS 7, $m_K = 6.5$, 5.57″ separation from SgrA*), outside the 2″ Field-of-View (FoV) of the VLTI, is picked with the PRIMA star separator and imaged onto the GRAVITY IR wavefront sensor located in the VLT Coudé laboratory. Alternatively stars, bright in the visible bands, can be used in combination with the optical wavefront sensor MACAO. The wavefront correction of either sensor is applied to the deformable mirror of the UT and provides a diffraction-limited image. The 2″ FoV of the VLTI contains both the science target (in this case Sgr A*) and the fringe-tracking star (IRS 16C, $m_K = 9.7$, 1.23″ separation). Both objects are re-imaged via the main delay lines in the GRAVITY beam combiner instrument.

Laser guiding beams are launched at the telescope spiders and at the star separators to track pupil and tip/tilt motion introduced in the VLTI tunnel. Sensors and actuators contained in the beam combiner instrument sense the motions and apply the corresponding corrections. Slow image drifts are meanwhile monitored by the acquisition camera. This camera also measures pupil motion lateral and longitudinal with respect to the optical axis.
The stabilized beam is then separated by the fiber coupler into the science- and the fringe-tracking object and coupled individually into single-mode fibers. The polarization and the differential optical path between the two objects is then adjusted by the fiber control unit using fibered differential delay lines (FDDL) and polarization rotators.
The actual beam superposition happens in an integrated optics (IO) chip, one for each object. Imprinted on the chip is a four phase-shift fringe sampling, that provides instantaneous phase and visibility information for all baselines.
The bright reference object feeds the fringe-tracking spectrometer. Here the phase and group delay is computed from five spectral channels at a rate of few hundred Hz. The

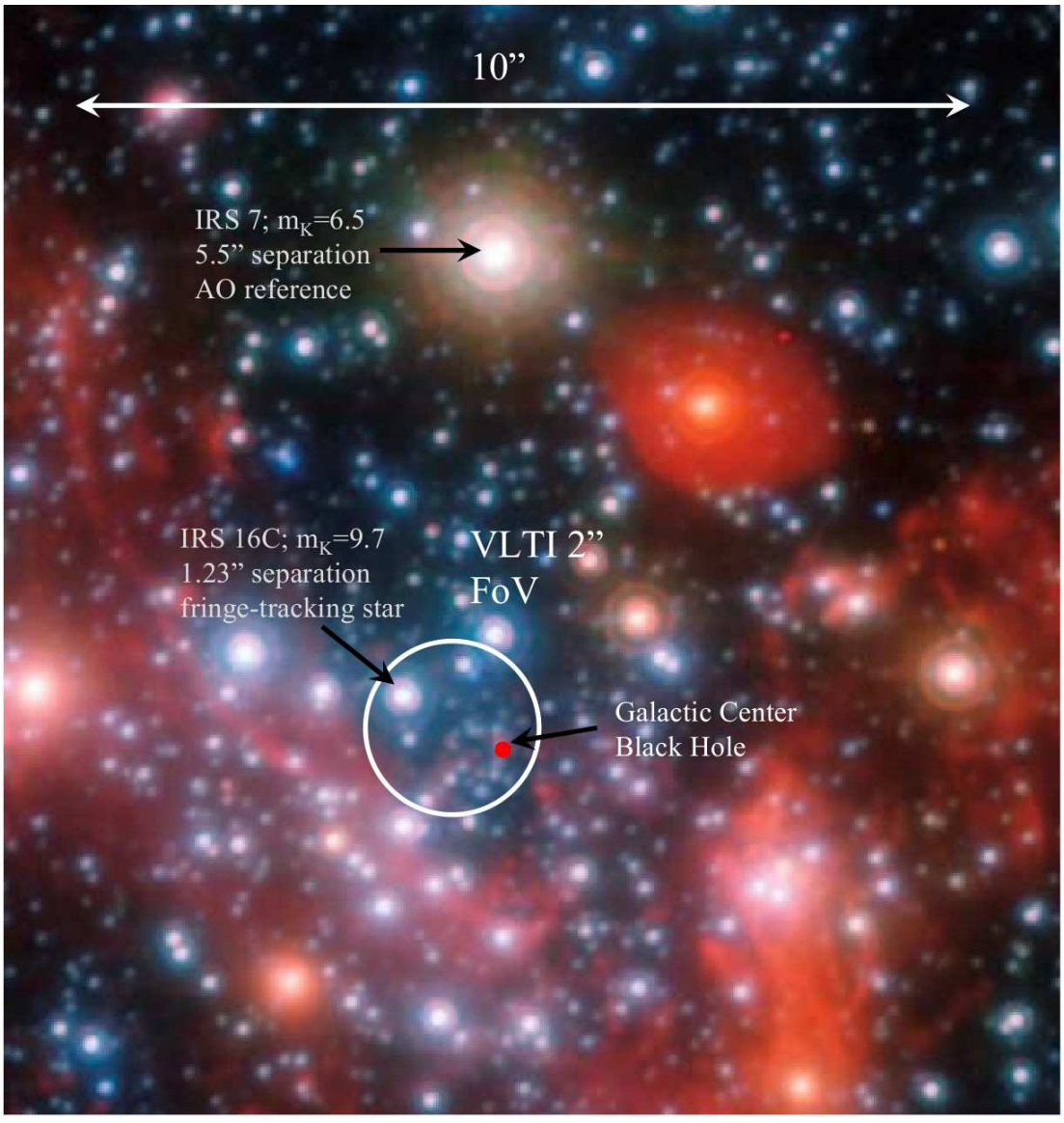

Figure 3.1 Working principle of GRAVITY illustrated for the Galactic Center. The infrared AO-loop is closed on the bright supergiant IRS 7. Using IRS 16C as fringe-tracking star allows to integrate long on the faint science object, i.e. in this case the super-massive black hole SgrA* .

corresponding OPD correction is applied to a piezo actuator contained in the fiber coupler. This allows stabilizing the fringes of the faint object and to use integration times significantly longer than the atmospheric coherence time. The science spectrometer, optimized for long, background-limited observations of the faint object offers a variety of observing modes. This includes low ($R \sim 22$) up to intermediate spectral resolution ($R \sim 4500$) modes. Additionally, both spectrometers offer the possibility to split and analyze linear polarization.
The internal differential OPD of the two objects is measured with a dedicated laser metrology. The laser is injected at the level of the IO chip and follows the optical path of the objects in reverse direction. The metrology interference pattern is then sampled after the primary mirror of the telescopes. The metrology signal is probed with a common phase-shifting technique in combination with photo diodes mounted to the telescope spiders.
GRAVITY provides simultaneously differential phase and visibility information for at least five spectral channels and two objects. This allows interferometric imaging and astrometry on six baselines, using the four Auxiliary- or the four Unit Telescopes.

3.1 GRAVITY subsystems

The following section describes the subsystems and components of GRAVITY. Figure 3.2 shows the location of the individual components at the telescopes and in the VLTI lab.

3.1.1 Wavefront sensor

Part of GRAVITY are four near-infrared wavefront sensors (WFS) to be installed in the Coudé lab of the 8 m Unit Telescopes (Hippler et al., 2008). Each WFS picks the AO reference star after the the star separator located at the Coudé focus (see small inset in Figure 3.2). The WFS operates at wavelengths between $1.4 - 2.4\,\mu$m. A mode selector allows to choose between on-axis and off-axis AO. The WFS uses a Shack-Hartmann design with 9×9 sub-apertures. The computed wavefront corrections are then sent to the deformable mirror M8.
Using either the infrared WFS or the already existing optical WFS, MACAO provides a diffraction-limited beam in the VLTI lab.

3.1.2 Cryostat

The complete beam combiner instrument is contained within a two ton cryostat made from steel and aluminum (Haug & Hofmann, 2011). Within the vacuum vessel, the subunits are installed on an optical bench and are stabilized to individual temperature levels between 80 K and 280 K. The bath-cryostat is cooled with liquid nitrogen. Depending on the detector requirements, the cryostat can be equipped with an additional closed-cycle cooler providing temperatures as low as 40 K. The vessel is especially designed to damp vibrations and to provide a stiff structure for the other subsystems. The cryo-temperature and

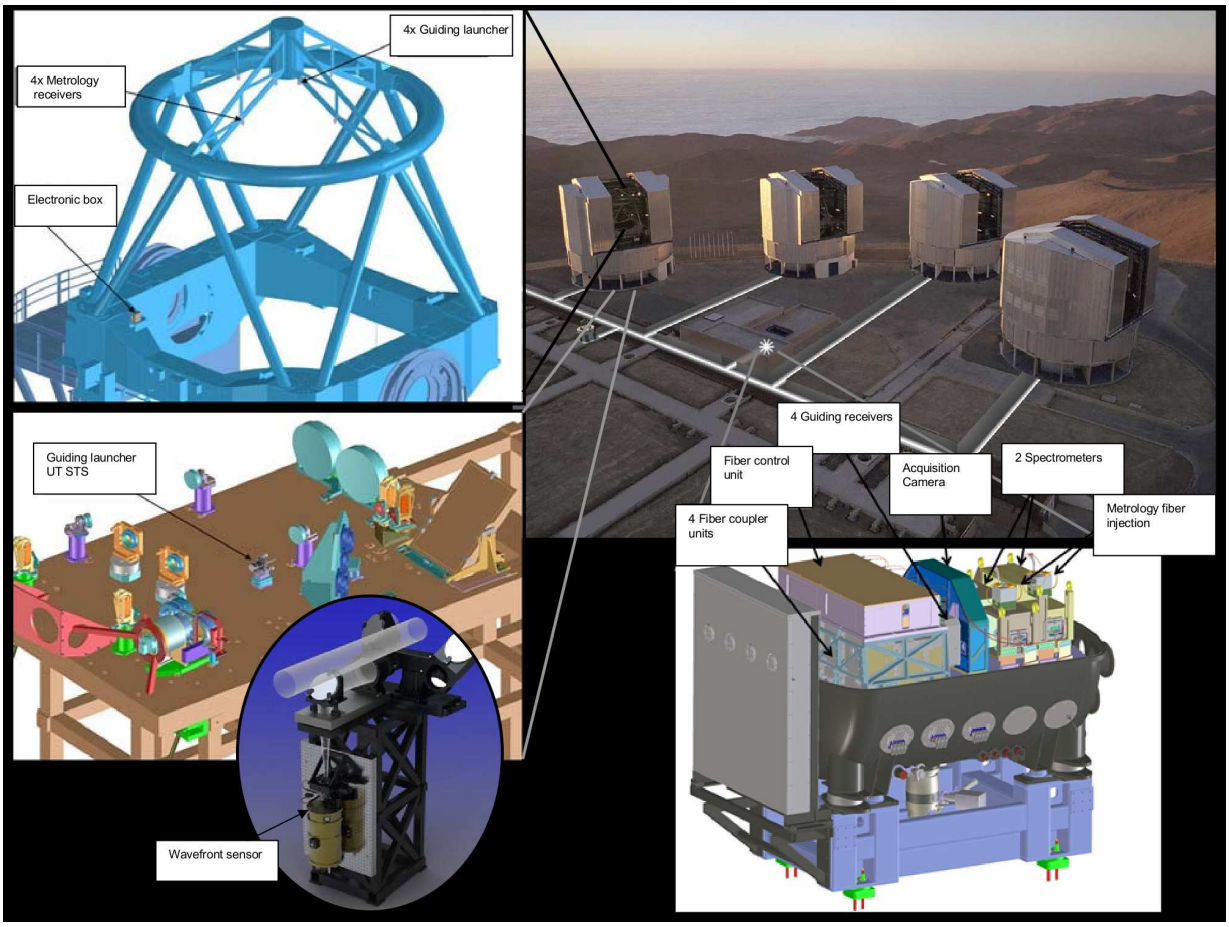

Figure 3.2 Overview over the individual subsystems of GRAVITY. Laser sources, installed at the telescope spiders, serve as reference beacons for the pupil guiding. The metrology receivers, also mounted to the spiders, monitor the internal optical path difference. A laser source installed on the star separator in the Coudé room serves as a beacon for the tip/tilt stabilization. The infrared wavefront sensor picks the designated AO beam after the star separator and provides a diffraction-limited image in the VLTI lab. Within the VLTI lab, the GRAVITY beam combiner instrument is located in a cryo- and vacuum vessel. For a description of the individual subsystems (fiber coupler, fiber control unit, acquisition camera, spectrometer and metrology) refer to the text.

vacuum ensures a negligible infrared background as well as stable internal optical paths. A 3D drawing of the cryostat is shown in the lower panel of Figure 3.2.

3.1.3 Fiber coupler

The beam combiner instrument contains four fiber coupler units. Each fiber coupler is fed by one telescope. The four units represent the entrance optics of the beam combiner instrument. Each fiber coupler provides the means to de-rotate the FoV and to stabilize tip/tilt and pupil jitter. A rotatable half-wave plate allows the adjustment and analysis of linear polarization. A cold stop is included for the background reduction. For internal calibration purposes, the fiber coupler is equipped with a retro-reflector that is able to map the GRAVITY fibers onto the acquisition camera. A reference metrology diode monitors the internal optical path between the integrated optics and the fiber coupler. A roof-prism in each unit allows separating two objects within the $2''$ FoV. In this dual-field mode, the two objects are coupled into separate single-mode fibers and after passing the differential delay lines and the polarization control unit, the light of each object is interfered in an integrated optics chip. One object, typically the brighter one, is used to measure and correct the fast atmospheric OPD variations. This allows integrating the fringes of the second (faint) object. In addition, the fiber coupler offers a single-field mode where fringe-tracking and science integration is done on the same object; a prerequisite for observations with high spectral resolution. The development of the fiber coupler unit is part of this thesis and a detailed description can be found in Chapter 4.

3.1.4 Fiber control unit

The main purpose of the fiber control unit is to control the polarization and to compensate the differential OPD between the two objects. The unit is described in detail in Perrin et al. (2011a).

The instrument concept uses single-mode fibers to inject light into the tiny waveguides of the beam combiner chips. Although difficult in terms of handling, the fibers of choice are made from fluoride glass to ensure maximum throughput in the K-band. The chosen fibers are standard, non-polarization maintaining fibers because this avoids to split polarization and as such to guarantee the best instrument sensitivity. However, this comes at the cost that in these fibers a linear polarized beam injected in the fiber remains linearly polarized but with a-priori unknown orientation at the output. It is therefore necessary to control the angle of polarization to ensure neutrality of the system with respect to polarizations and to maximize the fringe contrast. Since fiber optics are used, it is a natural choice to use fibered polarization rotators (FPR). This technique rotates twisted fiber loops in a particular way such that the output polarization can be changed. The technical details are proprietary and confidential information of the supplying company.

In addition to polarization rotation, the fiber control unit has to compensate for the differential optical path between the two objects. The maximum delay that has to be provided results from the largest possible object separation and the longest baseline, i.e.

$6'' \cdot 200\,\mathrm{m} \approx 6\,\mathrm{mm}$ of air-equivalent optical path. Such a delay can be achieved by fiber stretching. A fiber is wrapped around two half spools whose distance can be varied with a piezo linear stage. Depending on the number of loops, the achieved delay can be several millimeters of air equivalent optical path.

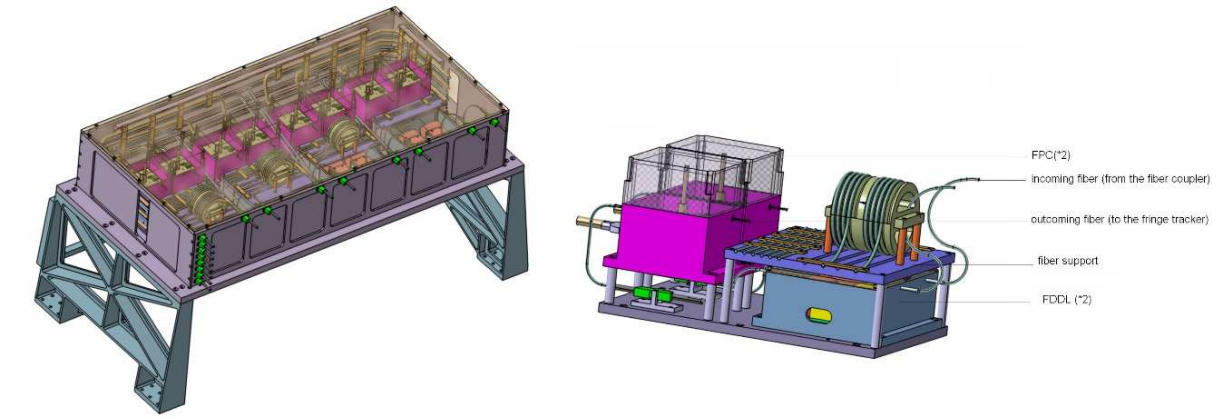

Figure 3.3 Left: view inside the fiber control unit. Right: one of the sub-units comprising two fibered polarization rotators, two fibered differential delay lines and a fiber spool (from Perrin et al., 2011a).

3.1.5 Integrated optics

GRAVITY has two interferometric beam combiners: the first one dedicated to the fringe-tracking object and the second one dedicated to the science object. The actual beam superposition of the telescopes is done in two integrated optics chips (IO) fed by the previously described single-mode fibers. Each chip consists of a silicon substrate carrying thin layers of silica. Various doping levels of the silica layers with varying refractive indices confine the waveguides vertically. The horizontal confinement is achieved through etching of a pre-defined mask (Jocou et al., 2010). The fringe coding chosen for GRAVITY is a pair-wise simultaneous ABCD sampling. This technique samples the fringe at four equidistant (90°) phase shifts. The output are four intensities ABCD, which contain the full information on the fringe visibility and phase. The pairwise combination of four telescopes results in a total of six baselines. Each baseline yields two observables, phase and visibility, retrieved by the ABCD sampling. The resulting circuit designed by IPAG and CEA/LETI (Perraut & Jocou, 2011) has four input and 24 output channels. Figure 3.4 shows the chip and its functionality. The obvious advantage of an IO chip is the compact design and stability of a complex optical system. A critical issue of the IO is the throughput. Taking into account bulk absorption in the chip, the glue transmission and Fresnel reflection at the surfaces, the effective throughput of the IO chip is $\approx 50\%$. The single-mode property of the IO chips ensures a spatial filtering of the wavefront. This means

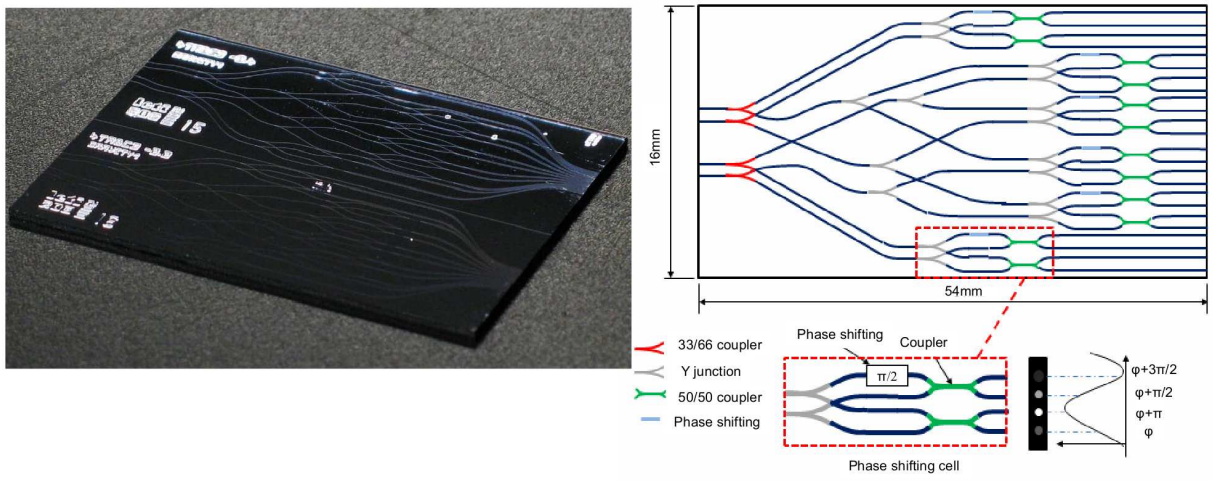

Figure 3.4 **Left:** Image of two beam combiner chips (from Perraut & Jocou, 2011). **Right:** Layout of the circuit. Four input channels corresponding to the four telescopes are seen on the left of the chip. Two successive couplers, with the coupling ratios of 66/33 and 50/50 respectively, split the light into three beams with equal intensity and feed the beam combination cell. This cell contains an achromatic $\pi/2$ phase shifter to create four outputs in phase quadrature. The combination chip has therefore 24 outputs (6 baselines $\times$ 4 (A,B,C,D) samples). The A,B,C,D channels probe each fringe at four equidistant 90° phase shifts.

that wavefront fluctuations are converted into photometric fluctuations without affecting the visibility. By design an IO chip is self-aligned and does not require maintenance or re-alignment.

3.1.6 Spectrometers

The 24 output channels of the two IO chips are imaged onto the fringe-tracking and the science spectrometer respectively (Straubmeier et al., 2010; Straubmeier & Fischer, 2011). Both spectrometers are thermally decoupled from the IO mount and the optical bench to keep them at 85 K avoiding any thermal background from the instrument.

Fringe-tracking spectrometer

The spectrometer of the fringe-tracking channel is optimized for high throughput and covers the K-band (1.95−2.45 μm) with five resolution elements ($R \sim 22$). The spectral dispersion is achieved with an air-spaced double prism. By introducing a Wollaston prism into the optical train it is possible to split linear polarization. Depending on the configuration 24 or 48 spectra are then imaged onto five pixels each. GRAVITY makes use of the most recent detector development; the ultra-low-noise ($\sim 3\,e^-$ read-noise, priv. comm. G.

Finger) 1 kHz frame rate SELEX detector. This new $24 \times 24\,\mu m^2$ pixel detector used in the fringe-tracking spectrometer provides the necessary leap in terms of sensitivity and speed to fringe-track on stars as faint as $m_K \approx 10$.

Science spectrometer

The science spectrometer offers three resolution modes as well as polarization splitting and unpolarized modes. The maximum ($R \sim 4500$) and intermediate resolution ($R \sim 500$) modes use grisms as dispersing elements while the low resolution ($R \sim 22$) uses a prism. The grisms and prism are mounted on a motorized filter wheel. Polarization splitting is done by a Wollaston prism mounted on a movable swing arm (see Figure 3.5). The individual spectra are imaged on a 2048×2048 pixel HAWAII 2RG array.
An integral function of the two spectrometers is the injection of the metrology laser backwards into the integrated optics beam combiner. The metrology laser emerging from two optical fibers is collimated, relayed and finally focused onto two of the 24 IO output channels by dedicated optics in the spectrometers. Back-scattering of the injected laser light is suppressed by custom-made notch filters at a level of optical density OD ≈ 16.

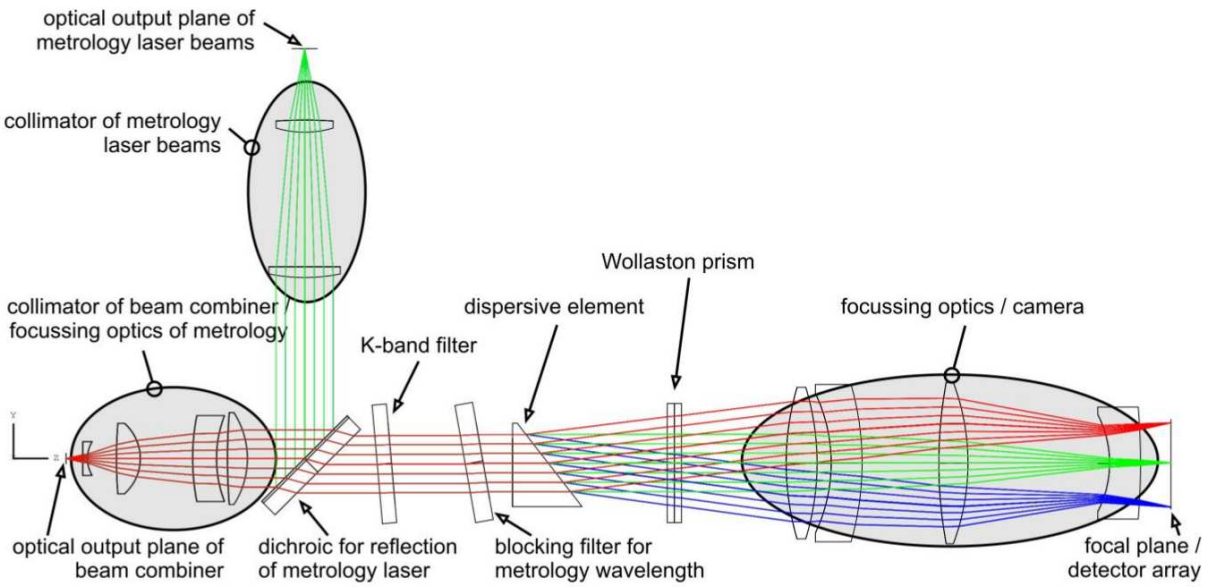

Figure 3.5 Science spectrometer layout. The output of the IO chip is dispersed by a grism, split by polarization and imaged on a HAWAII 2RG detector. Injection of the metrology laser happens via a 2-lens camera and a dichroic placed in the science beam. Laser stray-light is prevented from entering the spectrometer by a dedicated blocking filter (from Straubmeier & Fischer, 2011).

3.1.7 Acquisition camera

The acquisition camera, located behind the fiber coupler, monitors the telescope pointings as well as the pupil positions (see right panel, Figure 3.6). It ensures an optimum coupling of the two objects into the fibers and provides diagnostic tools for the optical train. The actual camera optics implementation comprises four modes (Amorim et al., 2010; Lima & Amorim, 2011):

- The *field imager* mode provides four H-band ($1.5 - 1.8\,\mu$m) sky images, that serve as a feedback for the current position of the science and the fringe-tracking object (for each telescope). This mode feeds the slow tip/tilt control-loop. In conjunction with the fiber coupler retro-reflector it also allows mapping the fiber positions in the field plane and therefore allows aligning the fibers with the objects on sky.

- The *pupil tracker* mode tracks laser beacons launched at the telescope spiders. Using a lenslet array this mode provides simultaneously the lateral (perpendicular to the optical axis) and the longitudinal pupil position. This information is used to stabilize the pupil in a closed-loop system. The sensing concept has been developed and tested in the course of this work (see Section 5.4). The concept is shown in Figure 3.6 (left panel).

- Quasi-static aberrations of the VLTI optical train are monitored by an *aberration sensor*. It analyzes the wavefront coming from each telescope by using a Shack-Hartmann design. The wavefront sensor is calibrated with the retro-reflector in the fiber coupler.

- The *pupil imager* shows the four telescope pupils in H-band. This function provides a sanity check for the pupil quality and the state of the system.

3.1.8 Guiding system

The guiding system consists of two independent systems working in conjunction with the acquisition camera and the actuators in the fiber coupler. One system stabilizes the field motion (tip/tilt) while the other system stabilizes the longitudinal and lateral pupil position. The development of the system has been a part of this thesis and is described in Chapter 5.
For the sake of completeness, a short overview is provided here. The AO uses a wavefront reference star to ensure a stabilized and corrected beam at the position of the Coudé focus. The *tip/tilt guiding* system takes over at the Coudé focus and corrects the tunnel atmosphere up to the VLTI lab. For this purpose, the system launches a laser beacon in a field plane of the star separator (STS), creating an artificial guide star. This beacon is picked up by a sensor in the cryostat that feeds a fast control-loop correcting the tunnel tip/tilt jitter.

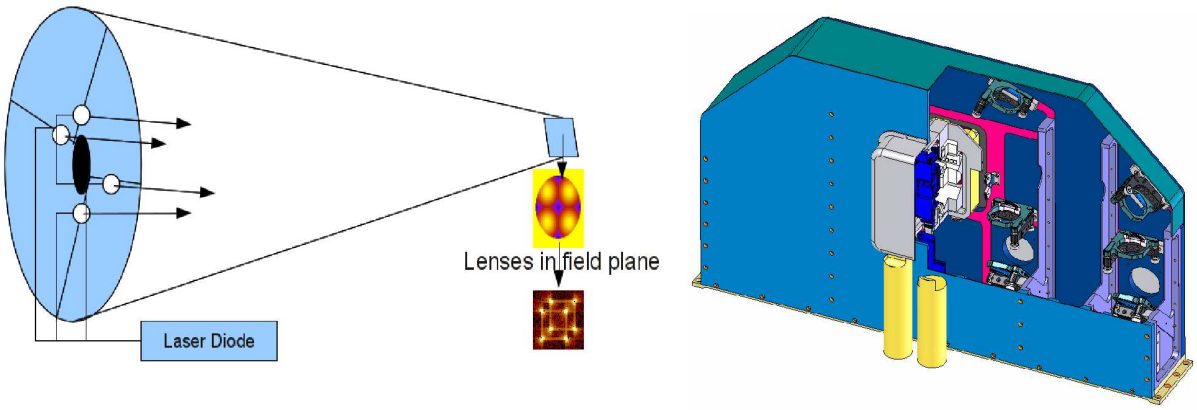

Figure 3.6 Concept of the pupil tracker (**left**). Four pupil laser beacons are re-imaged via a 2×2 lenslet array. The corresponding spot pattern is used to measure the lateral and longitudinal pupil position. The mechanical design of the camera (**right**) (from Amorim et al., 2010; Lima & Amorim, 2011).

The *pupil guiding* system uses the acquisition camera to track on laser beacons at the telescope spiders. As previously described, this allows correcting the lateral and longitudinal pupil motion between the telescope and the VLTI lab.
Both systems are an integral part of GRAVITY. They are required to minimize the astrometric error and to optimize the light injection, i.e. to increase the effective throughput of the beam combiner instrument.

3.1.9 Metrology

GRAVITY is able to measure the distance of two objects within the VLTI $2''$ FoV with unrivaled accuracy. Both objects are separated within the instrument and fed into separate beam combiners. The astrometric observable is the differential optical path difference (δOPD) introduced due to the angular separation of the two objects. To perform astrometric measurements with a micro-arcsecond accuracy, the internal differential path through the VLTI and the instrument has to be known (and tracked since Earth's rotation will permanently change it) at a few nm level. This internal δOPD is monitored by the *Metrology*. The concept is shown in Figure 3.7 (Bartko et al., 2010a; Gillessen, 2011). The system is designed to measure the δOPD of two objects separated by $\sim 1''$ on sky for a 100 m baseline with a residual error of less than 1 nm RMS.
The basic idea is to split a laser into two beams with a fixed phase relation and inject them backwards into the IO beam combiners. From both chips four beams will then travel exactly same optical path as the science light in reverse direction through the instrument and the VLTI. Close to every pupil plane the laser beams interfere and produce a fringe pattern. The differential OPD is then measured by phase-shifting the fringes and sampling

the corresponding intensity modulation with photo-diodes mounted on the spider arms holding M2.

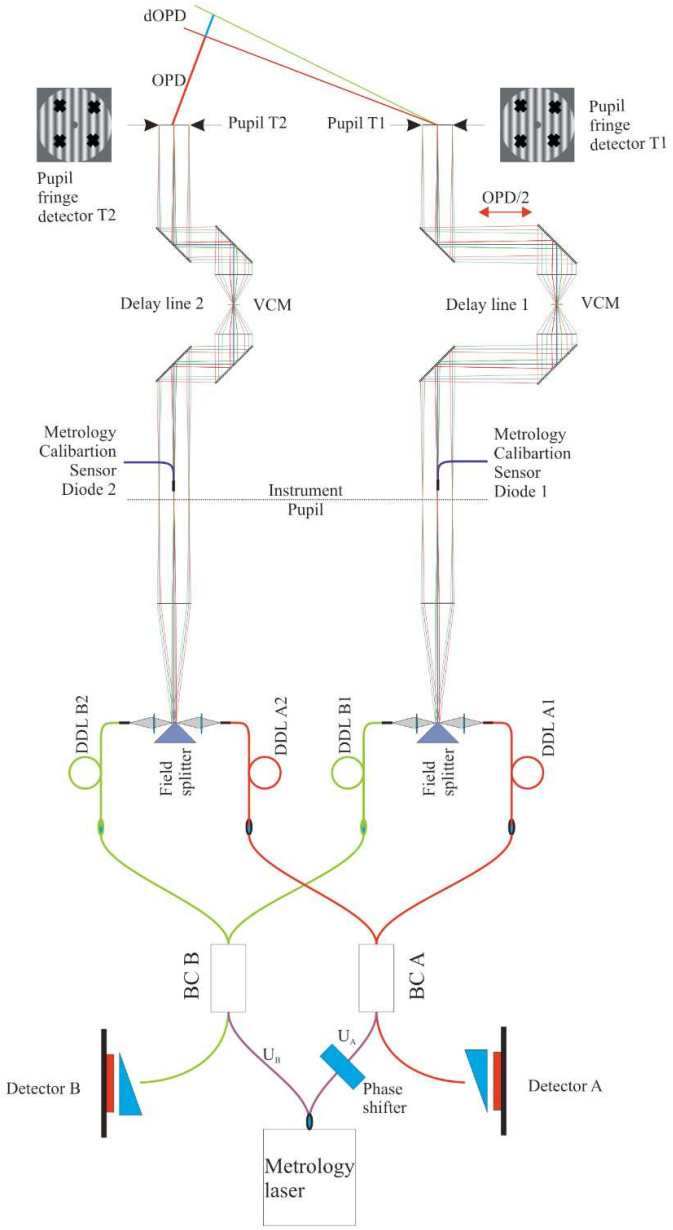

Figure 3.7 The metrology concept of GRAVITY shown for two telescopes. The laser is split and injected backwards in the integrated optics chips and travels the same optical paths as the stellar light through the VLTI in reverse direction. Detection of the resulting fringe pattern happens above the primary mirror M1, with four photo-diodes mounted on the telescope structure. Active phase shifting one of the laser arms at a kHz rate and recording the corresponding intensity modulation provides a reliable phase information of the internal optical path differences (from Gillessen, 2011).

Chapter 4

Fiber coupler

Part of this thesis was the development and testing of the GRAVITY fiber coupler. This includes the concept, the optical design, the definition of the optical- and mechanical tolerances, and the specification of filters and coatings. Furthermore it comprises the specification and characterization of the actuators and motors, the procurement of the individual optical components, and the validation of the optical functions and quality. The mechanical design was contributed by the MPE engineering department and parts of the manufacturing were done by the MPE workshop. The actuator electronics and the cabling were provided by the MPE electronics department.

The instrument GRAVITY will contain four fiber coupler units. The main purpose of the units is to pick up and stabilize the beams from the four telescopes, to split the FoV and to feed the light of two objects into single-mode fibers. Each fiber coupler contains the optics, motors and piezo actuators to de-rotate the field and to stabilize the beam tip/tilt and pupil wander. A rotatable half-wave plate allows adjusting and analyzing linear polarization. An internal cold stop reduces the thermal background. For calibration purposes, each unit is equipped with a retro-reflector that allows mapping the GRAVITY fibers onto the acquisition camera. The internal optical path between the integrated optics and the fiber coupler, is monitored by a metrology reference diode, providing the OPD feedback for the fibered delay lines. Each unit allows separating two objects (science and fringe tracking object) within the $2''$ FoV (UT). In this dual-field mode, the two objects are coupled into two single-mode fibers. After passing the differential delay lines and the polarization control unit, the light of each object coming from the four telescopes interferes in the integrated optics chip. The bright object is used to correct the atmospheric piston jitter and to stabilize the fringes of the second (faint) object. This allows integrating significantly longer than the atmospheric coherence time on the faint object. Instead of a few milli-seconds, the integration time can be as long as minutes, increasing the sensitivity by orders of magnitude. Additionally, the fiber coupler offers a single-field mode, where fringe-tracking and science integration is done on the same object. This particular mode can be chosen for bright objects, where high resolution spectroscopy is desired.
The mechanical structure of the fiber coupler is mounted on the optical bench in the

cryostat and kept at a constant temperature of 240 K. The temperature is a compromise between the thermal background and the operability of the stepper motors and piezo actuators. The latter are required for the fast OPD actuation (fringe-tracking) and to control tip/tilt and pupil wander of the incident beam. The tip/tilt stabilization, operated in closed loop, is driven by the acquisition camera and the guiding system. The guiding system tracks fast perturbations in the tunnel using laser beacons, while the acquisition camera guides slowly on a reference star. Another piezo actuator allows to control the pupil in the instrument. Driven by the acquisition camera, this actuator corrects pupil wander and alignment. The joint field and pupil stabilization is required to ensure an optimum coupling efficiency and to reduce the tip/tilt and pupil induced astrometric error (see Section 2.7).

4.1 Overview

The fiber coupler feeds the beam from one telescope into the single-mode fibers of the beam combiner instrument. The main optical parameters of the VLTI as stated in the *VLTI-Interface Control Document* (Gitton & Puech, 2009) are:

- Pupil diameter (UT): 8.0 m
- Pupil diameter (AT): 1.8 m
- Pupil diameter (VLTI lab): 18 ± 0.3 mm
- Field of View (UTs): diameter $> 2''$
- Field of View (ATs): diameter $> 4''$

Based on the VLTI parameters, the design specifications of the fiber coupler were set. The beam in the VLTI lab is compressed by a factor 444 in case of the UTs and by a factor 100 in case of the ATs. Therefore the nominal unvignetted $2''$ FoV on sky (UT) translates into $888''$ ($0.247\,^\circ$) in the lab. Given that the AT FoV angle in the lab is always smaller than the UT angle,in the following we always refer to the UT case, if not stated otherwise. Since the vignetted FoV of the VLTI is somewhat larger, we assumed for the design an oversized FoV of $8''$ on sky. Imaging the extended FoV on the acquisition camera eases the identification of objects in crowded fields and relaxes the requirements on the telescope pointing accuracy. Furthermore, the clear aperture of all surfaces is matched to a pupil, oversized by $\sim 20\%$ to be able to track and correct lateral pupil motion. The operating wavelengths spans from the visible to the IR. For the various control-loops, we use two lasers at 658 nm and 1200 nm, and for acquisition and science we use the astronomical H- and K-band. Consequently, the fiber coupler throughput is optimized at these wavelengths.

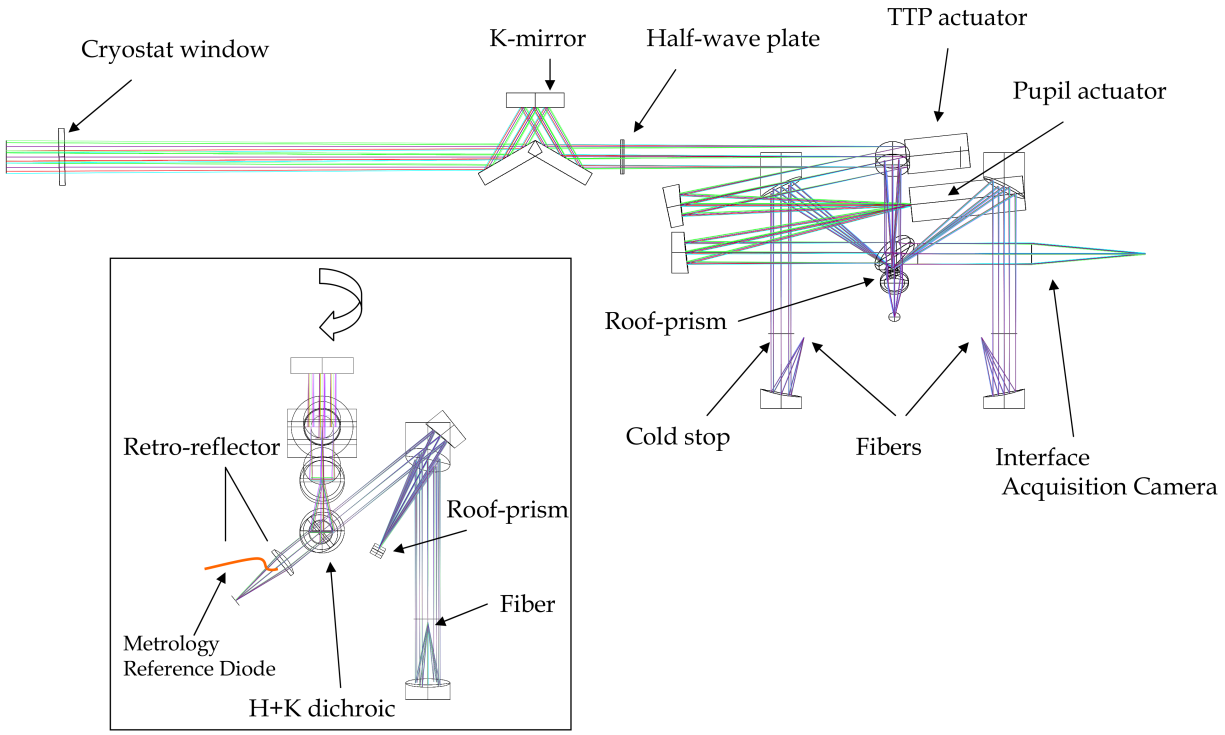

Figure 4.1 Optical design of the fiber coupler. The beam coming from one telescope enters the cryostat through a CaF_2 window. The rotatable K-mirror compensates the image rotation due to the telescope orientation. The half-wave plate controls the polarization orientation. The TTP and pupil actuators stabilize the incident beam. A dichroic in the collimated beam splits the acquisition (H-band) and guiding light from the science light (K-band). The science light is reflected to the roof-prism, where the field is split in science and fringe-tracking object. Each object is coupled via a parabolic relay into individual single-mode fibers. The acquisition and guiding (laser) light passes the dichroic and enters the acquisition camera. In order to align the objects with the fibers, the retro-reflector allows mapping the fiber position on the acquisition camera. The metrology reference diode monitors the optical path between the IO and the fiber coupler.

4.2 Optics

Each fiber coupler unit contains the following optical and mechanical elements:

- K-mirror mounted on a rotation stage, to de-rotate the FoV
- Half-wave plate, optimized for operation in K-band (1.95-2.45 μm) and at a temperature of $-33\,^{\circ}$C
- Piezo Z/tip/tilt platform, to correct piston and tip/tilt perturbations
- Piezo tip/tilt platform, to control lateral pupil motion
- Dichroic, splitting the guiding- and acquisition wavelength from the science wavelength (reflect $1.90 < \lambda < 2.45\,\mu$m; transmit $1.50 < \lambda < 1.80$ & 1.20 & $0.65\,\mu$m)
- Retro-reflector, to map the fiber position on the acquisition camera
- Metrology diode, to monitor the internal optical path between the fiber coupler and the IO
- Roof-prism to split the field (dual-field mode) or to act as a beam splitter (single-field mode)
- Off-axis parabolic mirrors, made from diamond-turned aluminum, to focus and collimate the beam

The bulk of the fiber coupler consists of aluminum. The complete structure, as well as the off-axis parabolic mirrors are made from aluminum. This avoids differential thermal contraction, keeping the optical properties constant and the system always in focus. The aluminum mirrors have an additional nickel coating that allows accurate diamond turning of the mirror surface. On top of the nickel, a layer of gold ensures high reflectivity in the infrared. Using off-axis parabolas avoids lenses and the corresponding chromatic errors in the design.
The layout of the fiber coupler is shown in the Figure 4.1. Although formally not part of the fiber coupler, the entrance window of the cryostat is included in the figure. After passing the CaF_2 window, the beam passes the K-mirror. The assembly of three flat mirrors is mounted on a rotation stage. It serves as a derotator, that compensates the field rotation induced by the telescope motion. After the K-mirror, a half-wave plate (HWP) is introduced in the optical path. Also mounted on a rotation stage, the HWP allows rotating the linear polarization of the incoming light. In combination with a wollaston prism in the spectrometer, this allows analyzing the object polarization. The entrance pupil of the instrument is placed on a flat mirror that is actively controlled by a piezo actuator. This actuator provides the fast tip/tilt and piston control (TTP) and it serves as a field selector. The second piezo actuator is located in an intermediate field plane. It allows to move the pupil within the instrument. Following a parabolic mirror, a dichroic

splits the collimated beam into the science band and the guiding and acquisition band. The H-band and optical light is transmitted to the acquisition camera and guiding system receiver. The science wavelength (K-band) is reflected to the fiber injection optics. The fiber injection optics consists of a camera that re-images the FoV onto the roof-prism. Here the field is split into two objects. Using another two parabolic mirrors each object is re-imaged and de-magnified at the position of the fibers. The fibers are mounted on XYZ translation stages that allow to focus and center the objects on the fibers. Behind the dichroic, a combination of an aspheric lens and a flat mirror acts as a retro-reflector for the metrology light. The dichroic is tuned such that $\sim 99\%$ of the light is reflected to the telescope but about 1% passes the dichroic, is retro-reflected and propagated to the acquisition camera. This allows re-imaging the metrology light from the fibers onto the camera. Knowing the fiber position on the camera allows a precise positioning of the object image on the fiber. Figure 4.2 shows a 3D view of the optical layout.

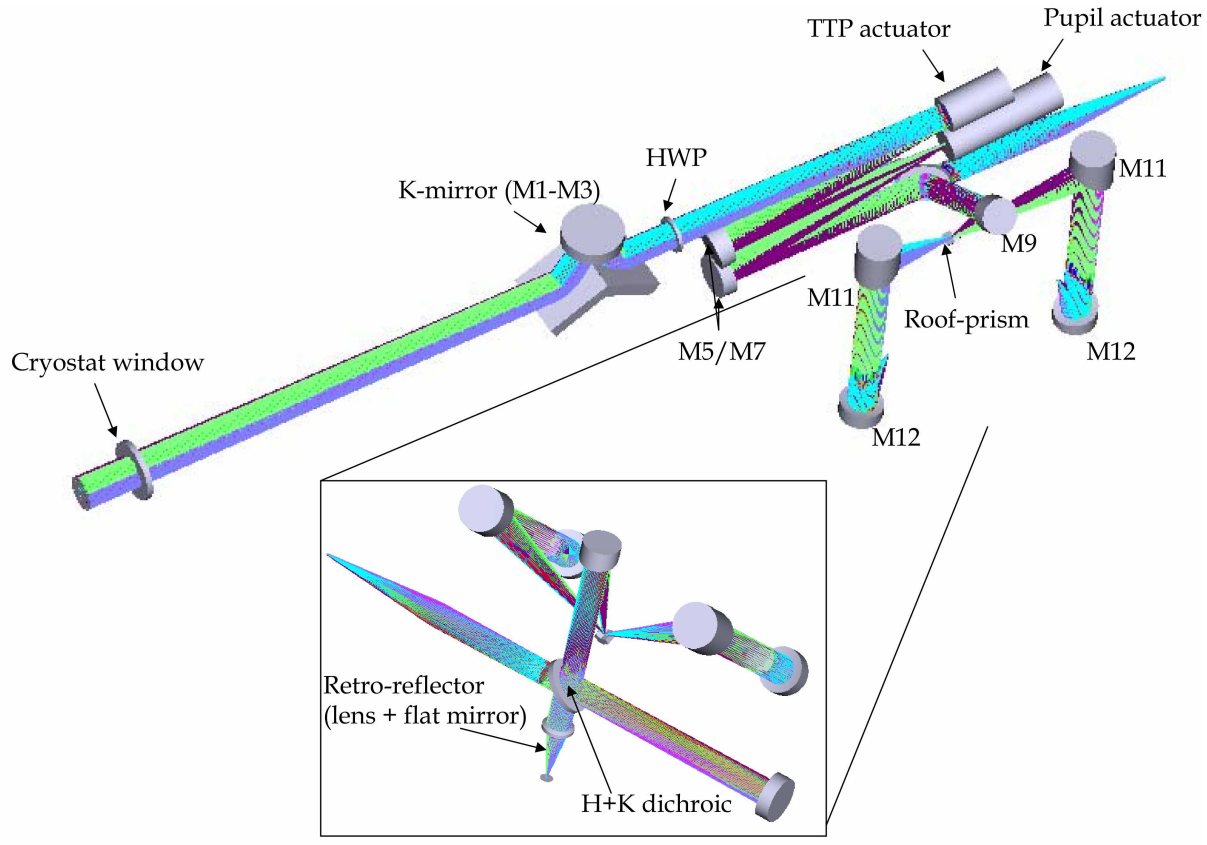

Figure 4.2 3D view of the fiber coupler optical design.

4.2.1 Notes on single-mode coupling

The classical way to couple light into a single-mode fiber is to place the fiber in the focus of a camera lens. The optimum f-number $F_\# = f/d$, i.e. the ratio of focal length to aperture diameter of the imaging system depends only on the fiber mode-field radius w_B. Following Wallner et al. (2002), the optimum f-number can be calculated according to the simple relation:

$$F_\# = f/d = 1.401 \cdot w_B/\lambda \tag{4.1}$$

Since the mode-field radius scales roughly linear with wavelength (Perrin et al., 2011a), the optimum f-number is actually independent of wavelength. The mode-field radius of the GRAVITY fibers is $w_B = 3.83\,\mu$m at $\lambda = 2.15\,\mu$m (Perrin et al., 2011a). This sets the f-number of the fiber coupler injection optics to:

$$F_\# = 2.5$$

The analytically derived $F_\#$ was confirmed by a *Zemax* physical optics simulation. In this simulation, we took the central obscuration of the telescope into account. As expected, the presence of the obscuration did not change significantly the optimum $F_\#$. The coupling efficiency can be calculated using Equation 2.16. The ideal coupling efficiency (without optical aberrations) of a uniform illuminated circular aperture into a single-mode fiber is 81%. Taking into account the central obscuration as in case of the VLT (VLT primary mirror diameter: 8.115 m, VLT secondary mirror diameter: 1.116 m), the ideal coupling is reduced to 77.8%.

4.2.2 Parabolic relay

In the fiber coupler we abandoned lenses in favor of off-axis parabolic mirrors. Using mirrors avoids typical lens aberrations such as chromaticity. Typical drawbacks of parabolas are off-axis aberrations. The prime condition for any parabola is that beams parallel to the axis of symmetry are focused to a common point, independent of beam diameter. However, beams not parallel to the axis suffer from coma. The aberration gets worse, the larger the off-axis angle is, which substantially limits the FoV with acceptable wavefront error. Yet, it is possible to compensate aberrations introduced by one parabolic mirror with a second one by tuning the focal lengths and off-axis distances of the relay. The first parabolic relay consisting of the mirrors $M5$ and $M7$ (see Fig. 4.2) is such an example. Both mirrors have the same focal length and off-axis distances, yet with opposite sign. This makes the relay symmetric with respect to a normal vector through the intermediate field center, i.e the symmetry axis of the pupil actuator. This symmetry cancels any aberrations apart from surface defects, providing a perfect collimated beam after $M7$. The combination of the three parabolas $M9$, $M11$ and $M12$ is more difficult and is governed by three conditions. The first two parabolas $M9$ and $M10$ demagnify the beam diameter from 18 mm to 9 mm to reduce the overall volume. The off-axis distance of $M9$ is determined by the minimum space required to fit the roof-prism next to the dichroic mount. The focal length of the

last parabola $M12$ is fixed to $f = 104.35\,\mathrm{mm}$ in order to match the optimum f-number $F_{\#} = 2.5$ (see Section 4.2.1). The off-axis distance of $M12$ is determined by the minimum space required to mount a fiber at the focus position. Given these preconditions, the only free parameter is the off-axis distance of $M11$. Since the off-axis directions of $M9$ and $M12$ are perpendicular to each other, the off-axis position of $M11$ also has two be adjusted in X and Y direction. Using the wavefront error as a minimization criteria, the *Zemax* optimization routine was used to find the optimum off-axis distance. The resulting optical performance is excellent for a large FoV (see Section 4.2.6).

4.2.3 Dual-field versus single-field mode

Among the main requirements for the fiber coupler is to provide a dual-field as well as a single-field mode. In order to avoid optic wheels or other movable parts, the goal was to design an optical element such that the two modes can be offered without additional actuators.
The field splitting (dual-field) is done by introducing a roof-prism, i.e. two angled flat mirrors with a sharp edge into a field plane. Starting from that basic concept, a special roof-prism was designed that offers both field- and beam-splitting capability. The prism substrate is fused silica, transparent in the IR. The roof surface of the prism consists of coated quadrants. Two gold coated quadrants constitute the typical roof-prism, i.e. two angled mirrors. The tilted mirrors split the field in two half's. The other two quadrants are coated with a beam-splitter- and anti-reflective (AR) coating. The bottom of the prism is again coated with gold. Thus in the single-field mode, the beam is split 50/50 at the first surface. The transmitted part is reflected at the bottom and exits the prism through the AR coated surface. The angles of the prism are tuned such that the exiting beam travels the same path as the dual-field mode. The beam traveling through the prism is slightly defocused due to the extended path. However, this can be partially compensated by re-focusing the fiber mounted on the translation stage. The roof-prism concept is illustrated in Figure 4.3. The f-number at the roof prism is $F_{\#} = 5.6$ corresponding to a diffraction limited point spread function (PSF) diameter of $\sim 15\,\mu\mathrm{m}$ in the K-band. The sharpness of the roof prism edge, determines the minimum object separation. It is limited by manufacturing processes and $< 10\,\mu\mathrm{m}$, therefore smaller than the diffraction limit.
Since the roof-prism is located in a field plane and the quadrants are only spaced by an equivalent of $1''$ on sky (0.16 mm), changing the mode only requires offsetting the internal tip/tilt actuator.

Alternative single-field mode

An alternative possibility to split the beam is to focus the light directly on the edge of a conventional roof-prism. This approach requires no additional complexity of the roof-prism design. Yet, a cut through the point-spread-function (PSF) at the site of the roof-prism implies diffraction seen in the pupil plane, which is limited by the cold stop. This causes a distorted PSF at the position of the fiber. To estimate the coupling efficiency of such a

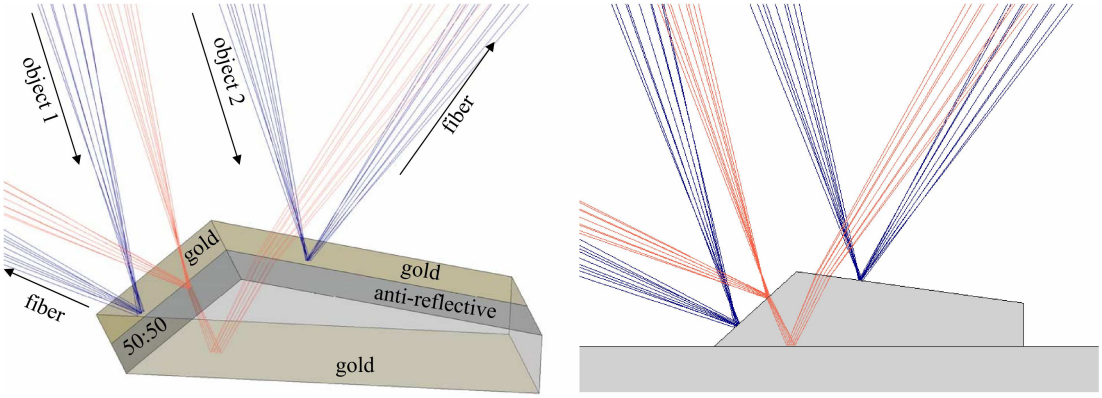

Figure 4.3 Left: 3D drawing of the roof-prism and the two operation modes (single/dual-field). In the dual-field mode two gold-coated quadrants split the field and reflect the light of two objects (blue rays) in opposite directions. The single-field mode splits the the light of one object (red rays) at the first surface. It reflects 50% of the light and transmits the other 50%. The transmitted light is reflected at the bottom of the roof-prism and exits the glass substrate at the opposite side of the prism. The following optical path is identical for both modes. Via a parabolic mirror relay, the two objects (or the split object) are coupled into two single-mode fibers. Right: roof-prism seen from the side.

distorted PSF, we performed a Zemax simulation. For the simulation we assumed a 50/50 split of the PSF and an infinitely sharp edge of the prism. Figure 4.5 shows the diffraction pattern at the position of the fiber. The edge of the roof-prism causes significant diffraction. Instead of ideally 50% being directed in the direction of one channel, only about 38% are propagated through the pupil stop. The rest is lost due to diffraction. The distorted PSF itself also causes a reduced coupling efficiency into the single-mode fiber. The coupling efficiency drops from nominally 77.8% to 62.7%. Taking into account diffraction losses at the pupil stop only 24% of the incoming light is coupled per beam (compared to and ideal value of 38.9%), meaning that the theoretical coupling losses are already significant. The real performance will be worse especially since the finite thickness of the edge was neglected in the simulation. According to the manufacturer, the edge chip is $> 5\,\mu$m. This corresponds to $\sim 1/3$ PSF, i.e. not negligible for the optical performance. Furthermore, this setup will be very sensitive to wavefront distortions. The alternative single-field mode is a backup solution that might be useful for calibration purposes. However it is not planned as a normal operation mode.

4.2.4 Half-wave plate

GRAVITY offers unpolarized as well as polarization-split operation. The latter operation allows analyzing the object linear polarization and provides a higher astrometric accuracy, at the cost of a lower Signal-to-Noise ratio (SNR). A Wollaston prism, mounted on a swing

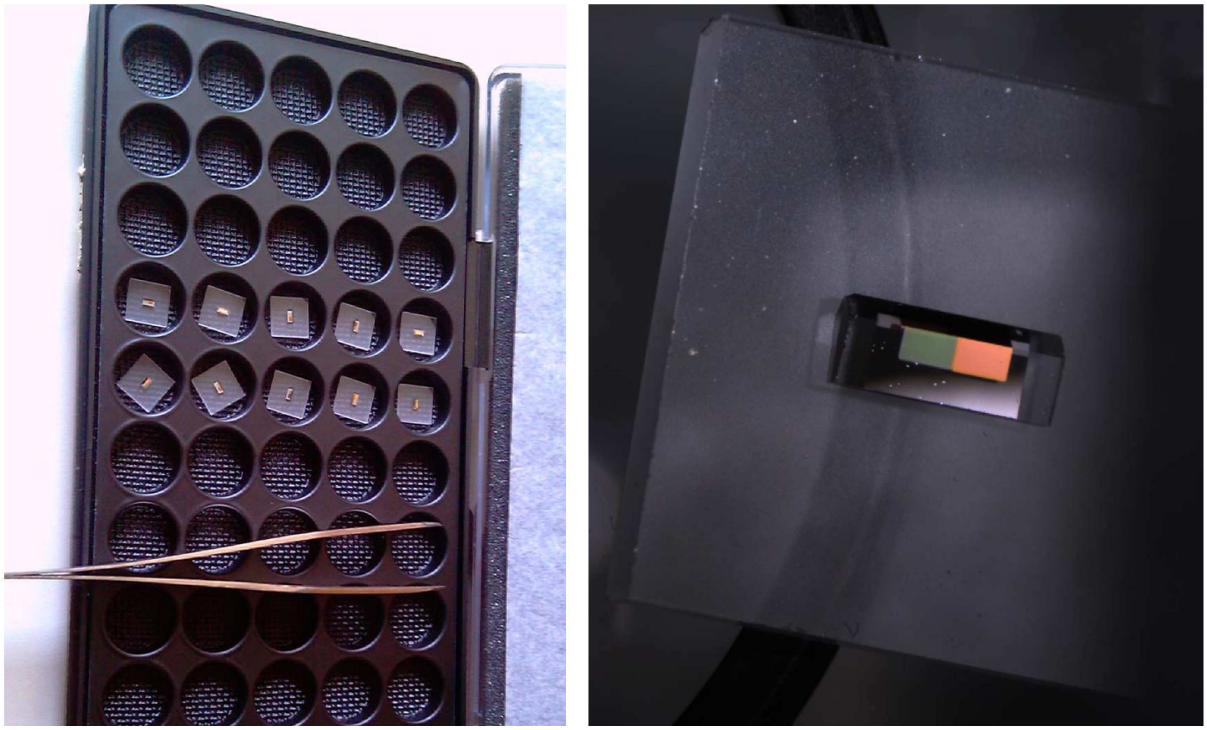

Figure 4.4 Left: Picture of the 10 roof-prisms delivered from *Zuend Precision Optics*. Each prism is glued on a $10 \times 10\,\mathrm{mm}^2$ N-BK7 glass plate for handling purposes. Right: One prism under the microscope. The prism base is $4 \times 1.5\,\mathrm{mm}^2$. The optical active area however is the central $0.3 \times 0.3\,\mathrm{mm}^2$.

arm is able to split the linear polarization states in the spectrometer. In combination with a half-wave plate in the fiber coupler, which allows rotating the linear polarization, the object polarization can be retrieved. This setup of both optical elements is a standard way of linear polarization analysis.
The basic principle of any wave plate uses a birefringent crystal, cut parallel to the optical axis of the crystal. Light polarized along this axis (extraordinary ray) travels through the crystal at a different speed than light with the perpendicular polarization, creating a phase difference between the two states. Typically the extraordinary axis has a higher refractive index and therefore is often referred to as the slow axis. Depending on the thickness of the crystal, light with polarization components along both axes will emerge in a different polarization state. In case of a half-wave plate, the shift between the extraordinary and the ordinary component is 180 °. This phase difference causes a rotation of linear polarized light traveling through the plate by twice the angle between incident polarization and crystal axis. Therefore by rotating the half-wave plate the orientation of the output polarization can be adjusted. If the phase shift however deviates from 180 °, the emerging beam becomes elliptically polarized. In other words, crosstalk between both polarization axes is introduced.

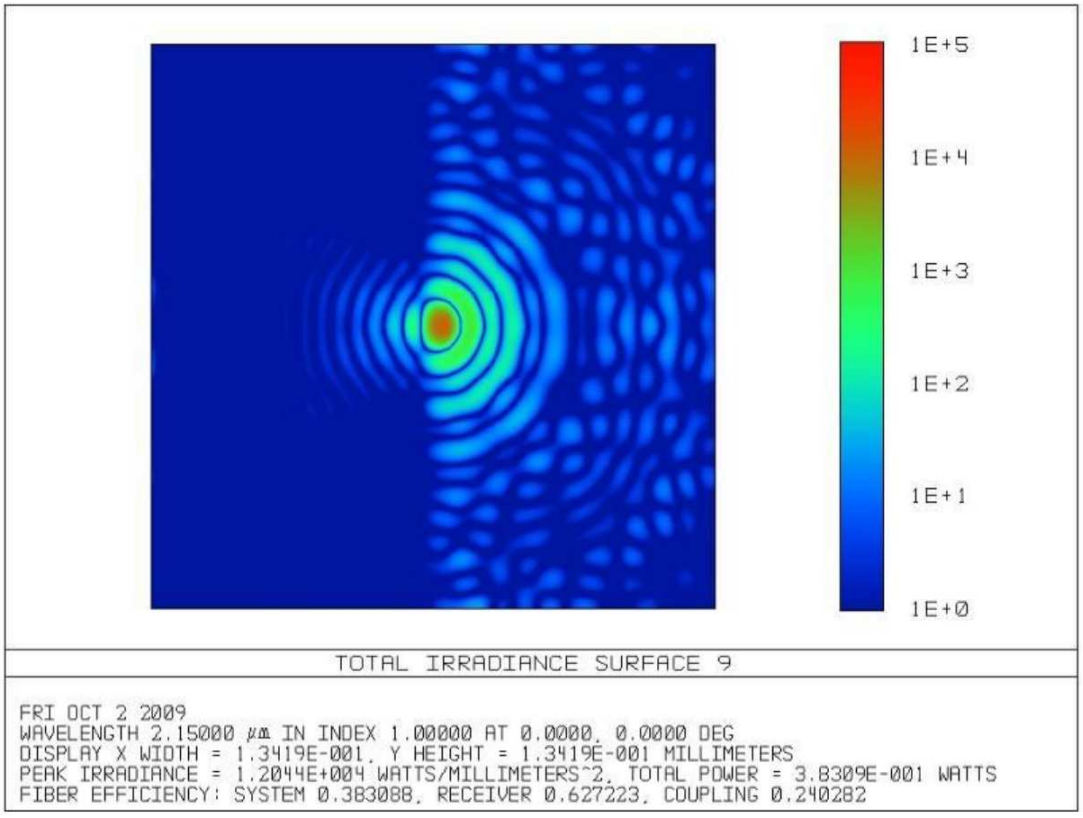

Figure 4.5 Simulated diffraction pattern at the position of the fiber in the case of a beam splitting at roof-prism edge. The PSF is essentially split in half, however diffraction after the roof-prism causes the irradiance seen in the left part of the image.

The phase difference introduced between the extraordinary and the ordinary ray traveling through a single birefringent crystal is:

$$\phi = \frac{2\pi}{\lambda_0} L(n_o - n_e)$$

where λ_0 is the vacuum wavelength, L the propagation length and n_i is the refractive index of the extraordinary and the ordinary ray (parallel and perpendicular to the optical axis of the crystal). It is obvious though, that a certain phase difference is only true for one particular wavelength. The typical refractive index difference is $n_0 - n_e \sim 0.01$. Therefore $L \approx 50\lambda_0$ to achieve a 180 ° phase shift. However, at $\lambda_0 = 2\,\mu$m the plate thickness is then only 0.1 mm. To obtain a mechanically stable plate, the thickness has to be m times this zero-order thickness. However this aggravates the wavelength dependent phase shift also by a factor m. To achromatize the wave plate a combination of birefringent materials of various thicknesses can be tuned such, that the phase difference is nearly constant over a certain wavelength range. In case of GRAVITY we use an achromatic wave plate consisting

of crystalline SiO_2 (quartz) and MgF_2. Both plates are oriented such that the optical axes are perpendicular to each other. In other words, a beam polarized along the optical axis of the first plate, travels along the slow (extraordinary) axis and then along the fast (ordinary) axis through the two plates. The half-wave plate is sketched in Figure 4.6. If the thickness of both plates is nearly similar, it is possible to obtain a zero-order 180 ° phase shift even at plate thicknesses of several millimeter. Furthermore, the different wavelength dependence

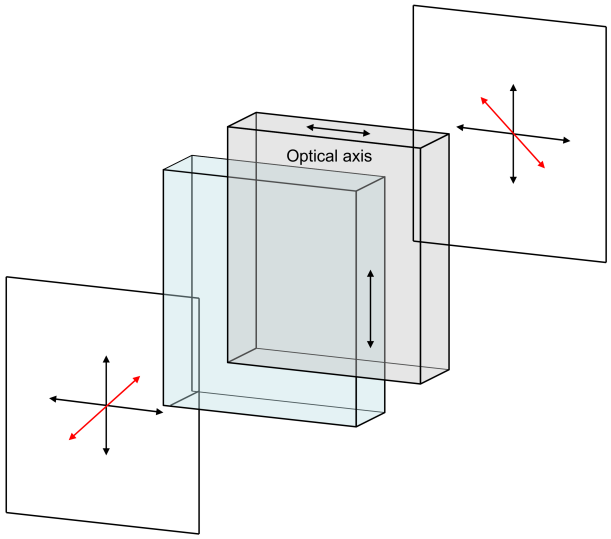

Figure 4.6 Principle of the half-wave plate used in the fiber coupler. The half-wave plate consists of two parallel thin MgF_2 and SiO_2 plates with perpendicular optical axis. A linear polarized beam (red arrow) passing through the plates changes its polarization orientation by twice the angle between incident polarization and one optical axis.

of the refractive indices allows tuning the phase shift in a certain wavelength range. Leaving the thicknesses of the two plates as a free parameter, we used a *Zemax* routine to optimize the phase difference in the K-band ($1.9 - 2.45\,\mu$m) according to the following equation:

$$\phi = \frac{2\pi}{\lambda}(L_{\mathrm{MgF_2}}(n_{\mathrm{MgF_2},o} - n_{\mathrm{MgF_2},e}) + L_{\mathrm{SiO_2}}(n_{\mathrm{SiO_2},o} - n_{\mathrm{SiO_2},e}))$$

We performed the optimization for room temperature and again for the operating temperature $-33\,^{\circ}$C. The temperature dependence of the refractive indices changes the phase difference significantly. Therefore we were not able to purchase off-the-shelf wave-plates, since those had been optimized for room temperature. Instead, we requested a custom-made wave plate for our particular operating temperature. Our best-fit plate thicknesses at $-33\,^{\circ}$ are:

$$L_{\mathrm{MgF_2}} = 1.337\,\mathrm{mm} \qquad L_{\mathrm{SiO_2}} = 1.693\,\mathrm{mm}$$

Figure 4.7 shows the phase difference as function of wavelength of a wave-plate optimized at $-33\,^{\circ}$C, reaching an accuracy across the broad wavelength range of $\pm 0.9\,^{\circ}$ P-V. At this accuracy another effect might actually limit the final performance: optical rotation of quartz. This effect leads to a wavelength dependence of the optical axis orientation. In other words, the amount of polarization rotation changes with wavelength. At the given thickness of the quartz plate, the optical rotation is of the order $\sim 2^{\circ}$ ($= 4^{\circ}$ polarization rotation) between 1.95 and 2.45 μm. The resulting crosstalk between polarization states is therefore $< 0.02\%$. For comparison we also show the characteristics of the same plate operated at room temperature.

The custom-made wave plate was manufactured by *Bernhard Halle Nachfl.GmbH*. The

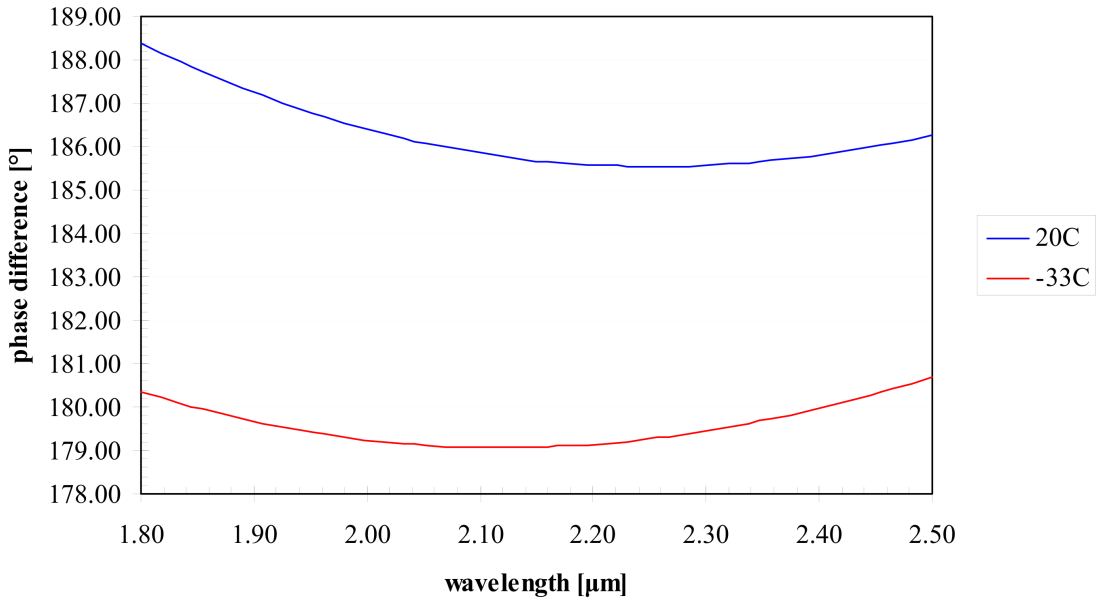

Figure 4.7 Calculated phase difference as function of wavelength for a half-wave plate optimized at $-33\,^{\circ}$C. For comparison the phase difference at room temperature is shown.

two crystals are optically contacted with one optical axis perpendicular to the second axis. One prototype, shown in Figure 4.8, has already been delivered and tested in a cryo-chamber to verify that the contact withstands the cooling.

The calculated properties of the half-wave plate in the range $1.90 - 2.45\,\mu$m can be summarized:

- Extra-/ordinary ray phase difference: $180^{\circ} \pm 0.9$
- Chromatic polarization rotation: $\sim 4^{\circ}$
- Polarization crosstalk: $< 0.02\%$

Figure 4.8 Half-wave plate (provided by *Bernhard Halle Nachfl*) in a test mount.

4.2.5 H/K dichroic

The dichroic within the fiber coupler plays an important role in the performance of the system. Placed in a collimated beam (see Figure 4.1 and 4.2), the dichroic splits the science- from the acquisition- and guiding wavelengths. While the K-band is reflected to the injection optics, the H-band, pupil guiding laser (1200 nm) and the tip/tilt laser (658 nm) pass through the dichroic, eventually being picked by the guiding receiver and the acquisition camera. We have contacted several potential suppliers, asking for a quotation. Among the specifications were the surface accuracy seen in reflection of $\lambda/20$ at 633 nm, a reflectivity greater than 99% in the K-Band and a transmission greater than 90% in the H-band as well as some transmission at the two laser wavelengths. Figure 4.9 shows one of the favored quotations. The promised average transmission between $1.5 - 1.8\,\mu$m is 98%, at $0.658\,\mu$m is 70% and at $1.2\,\mu$m is 97% while the average reflectivity at $1.908 - 2.45\,\mu$m is 99%, in agreement with the specifications. The favored dichroic substrate is fused-silica, given its low price and optical properties. Governed by the limited volume in the fiber coupler, we chose an elliptical substrate shape of 35×25 mm. The rather stringent dichroic requirements lead to a large number of coating layers. We therefore chose a thick substrate of 10 mm to compensate stress induced by the coating layers.

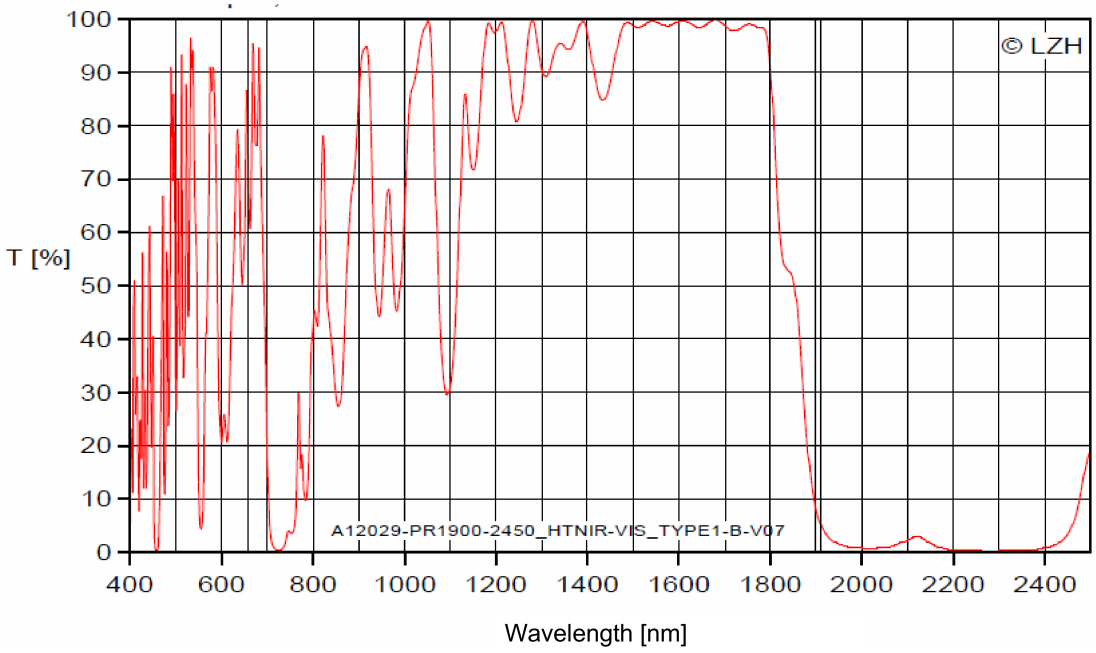

Figure 4.9 Simulated transmission of the dichroic. The dichroic is optimized for high reflectivity in K-band and for a good transmission in H-band as well as in a small window around 658 nm (Courtesy to S. Günster, Laser Zentrum Hannover).

4.2.6 Optical performance

Image quality

The optical quality of a camera is governed by the wavefront error introduced due to the optical components. A point source imaged by a perfect optical system with circular aperture creates a diffraction pattern, typically referred to as Airy pattern. Mathematically, the far field diffraction pattern is the squared modulus of the Fourier transform of the circular aperture. The resolution of such an ideal system is usually defined as the angle, where the first minimum of the intensity pattern occurs. This angle can be approximated by the well known "Rayleigh criterion":

$$\theta \approx 1.22 \frac{\lambda}{D}$$

where θ is the angle, λ is the effective wavelength and D is the diameter of the aperture. However, this is only true for aberration free systems. Real optical systems using lenses and mirrors inherit wavefront aberrations by design and by manufacturing limitations. Typically the optical quality is measured in terms of Strehl ratio. It is defined as the ratio of the peak intensity at the image plane compared to the theoretical maximum peak intensity of a perfect imaging system working at the diffraction limit. This ratio can be

easily calculated from the wavefront error according to the relation (Born & Wolf, 1980):

$$S \approx e^{-(2\pi\sigma)^2}$$

with σ being the root-mean-square deviation of the wavefront in waves. In single-mode coupling the Strehl ratio is a measure for the flux loss compared to the nominal coupling efficiency.
As described in Section 4.2.2 we used a design of various off-axis parabolas. By using symmetries and a combination of specific parabolas we achieved an almost aberration free design with excellent optical quality. Figure 4.10 shows the calculated wavefront error as function of field angle. The nominal dual-field wavefront error is close to zero at the field center and the maximum wavefront error for all wavelengths across the $\pm 2''$ UT FoV on sky $= \pm 0.247°$ lab is < 0.025 waves, corresponding to a Strehl ratio $> 98\%$. Across $1''$ the Strehl is even $> 99\%$. Because of the symmetry of the science and the fringe-tracking channel, the optical quality is equal for both fiber injection optics.
In case of the single-field mode the optical quality of the science and the fringe-tracking channel is different. While the reflected beam has the same optical quality as in the dual-field case, the beam propagating through the prism suffers from defocus and chromatic aberration. This can only be partially compensated by focusing the fiber. The resulting wavefront error for the propagated beam is shown in Figure 4.10. The nominal wavefront error is higher than the dual-field error. At $1''$ the Strehl already drops to 91%. Yet, in the single-field mode, only one object is needed in the FoV. Therefore the object can be placed on the roof-prism at the optimum position, meaning close to the field center. Close to the optical axis of the system the wavefront error is of the order 0.023 waves, corresponding to a Strehl ratio of again $> 98\%$. In that sense, the single-field mode performance is practically not degraded compared to the dual-field mode.

Tolerancing

The design intrinsic wavefront error does not account for manufacturing tolerances and surface defects of the individual optical components. Machining errors of the mechanical structure can lead to a displacement or tilt of the components, while deformations of the surfaces lead to a distorted wavefront. The sum of the individual error sources can lead to a significantly degraded optical quality of the system. However, over-specifying the required accuracies leads to an unnecessary cost increase of the instrument. Therefore we performed a detailed tolerancing of the individual optical components and the mechanical structure.
For the tolerancing we used the commercial software *Zemax* and applied a Monte-Carlo analysis of the optical quality. We defined for every component, mirrors and glass substrates, the surface accuracy as specified by the manufacturer. Furthermore, we defined the mechanical tolerances, namely de-centering and tilt, that can be achieved by MPE's workshop.

- surface irregularity (parabolas): $< \lambda/4$ RMS (at $\lambda = 633\,\mathrm{nm}$)

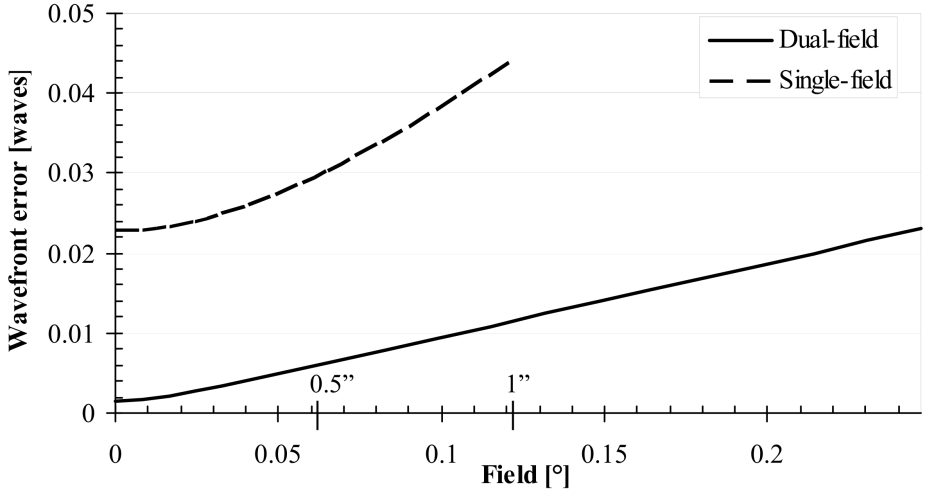

Figure 4.10 Nominal wavefront error of the dual-field mode as function of field angle in the 18 mm beam (solid line). Two tickmarks show the equivalent $0.5''$ and $1''$ field on sky (UT). The dashed line shows the wavefront error for the beam propagated through the roof-prism in the single-field mode. The reflected beam has the same error as in the dual-field case.

- surface irregularity (flat surfaces): $< \lambda/20$ RMS
- mechanical decenter: < 0.1 mm
- mechanical tilt: $< 0.05\,^{\circ}$

As a compensator, we allowed a changing focus and a tilt of the tip/tilt- and the pupil actuator. After defining the tolerances and compensators, we used the Monte-Carlo tool of *Zemax*. For N trial runs, the software adds to the nominal optical design random errors on the the individual surfaces and displaces the individual elements with an RMS as initially specified. For each trial, the compensators are then allowed to optimize the wavefront error. This value is stored for each trial. Given the complexity of the system and required computing time we only used 200 trials for the tolerance analysis. However, for the assumed tolerances the expected wavefront error is at a 90% confidence level better than 0.04 waves over the $2''$ FoV (Strehl$\sim$ 94%).

Transmission

Any stellar interferometer is a complex optical systems that requires delay lines and numerous other optical functions. Therefore optical throughput is always a major concern in these systems. For that reason, we designed the fiber coupler with regard to high throughput in the science band ($1.9 - 2.45\,\mu$m). The bulk absorption in MgF_2, fused silica,

and quartz is negligible in K-band (see e.g. product information of *Crystran Ltd.*; UK). Therefore only reflection losses have to be taken into account. Each fiber coupler unit comprises five glass surfaces, front- and back-surface of the cryostat window, the same for the half-wave plate and the tip of the single-mode fiber. For all glass surfaces inside vacuum, we assumed anti-reflective coatings with a typical loss of 0.5% per surface (according to various suppliers). Since the front surface of the cryostat window is exposed to ambient, we assumed in this case an increased loss due to dust of 1.5%. With the exception of the dichroic (with a loss of 1%; see Section 4.2.5), all other surfaces are gold-coated mirrors; in total ten reflections with a reflectivity of $> 99\%$ each in K-band. Multiplying the individual component losses yields a throughput of 85.9%. Taking into account the toleranced Strehl of 94%, the nominal coupling efficiency of 77.8% (Section 4.2.1) and some additional margin of 95%, the total throughput is ≈60%.

4.3 Mechanics

The mechanical layout of the fiber coupler was done together with the engineering department of MPE. All mechanical components required for the first unit have already been manufactured, partially by the MPE workshop and partially subcontracted. Special attention was paid to the manufacturing tolerances, since the optical quality depends significantly on the mechanical precision. The cabling of the numerous actuators contained in the unit was done with the help of the electronics department of MPE. The following subsections give an overview and highlight individual components.

4.3.1 Structure

Each of the four fiber coupler units is self-contained. The overall size of one unit is $230 \times 604 \times 372\,\mathrm{mm}^3$. Each box consists of more than 700 individual pieces and weighs 25 kg. The complete structure and several of the optical elements are manufactured from aluminum (AlMg4.5Mn0.7). The choice of the material matches the cryostat optical bench to ensure a temperature independent behavior, when cooled down to the operating temperature of 240 K. Figure 4.11 shows a CAD model of the final unit. The backside of the box provides the mechanical interface with the guiding system receiver. The whole structure will be screwed to the optical bench in the cryostat. Figure 4.12 shows the almost fully assembled fiber coupler.

4.3.2 Entrance shutter

The entrance aperture can be closed by a Melles Griot 04RDS001 shutter embedded in the front plate of the fiber coupler. It is a bi-stable shutter, with no power consumption and consequently no heat output during the closed and open state. Only closing or opening the shutter consumes some power with negligible heat output given the short time of operation.

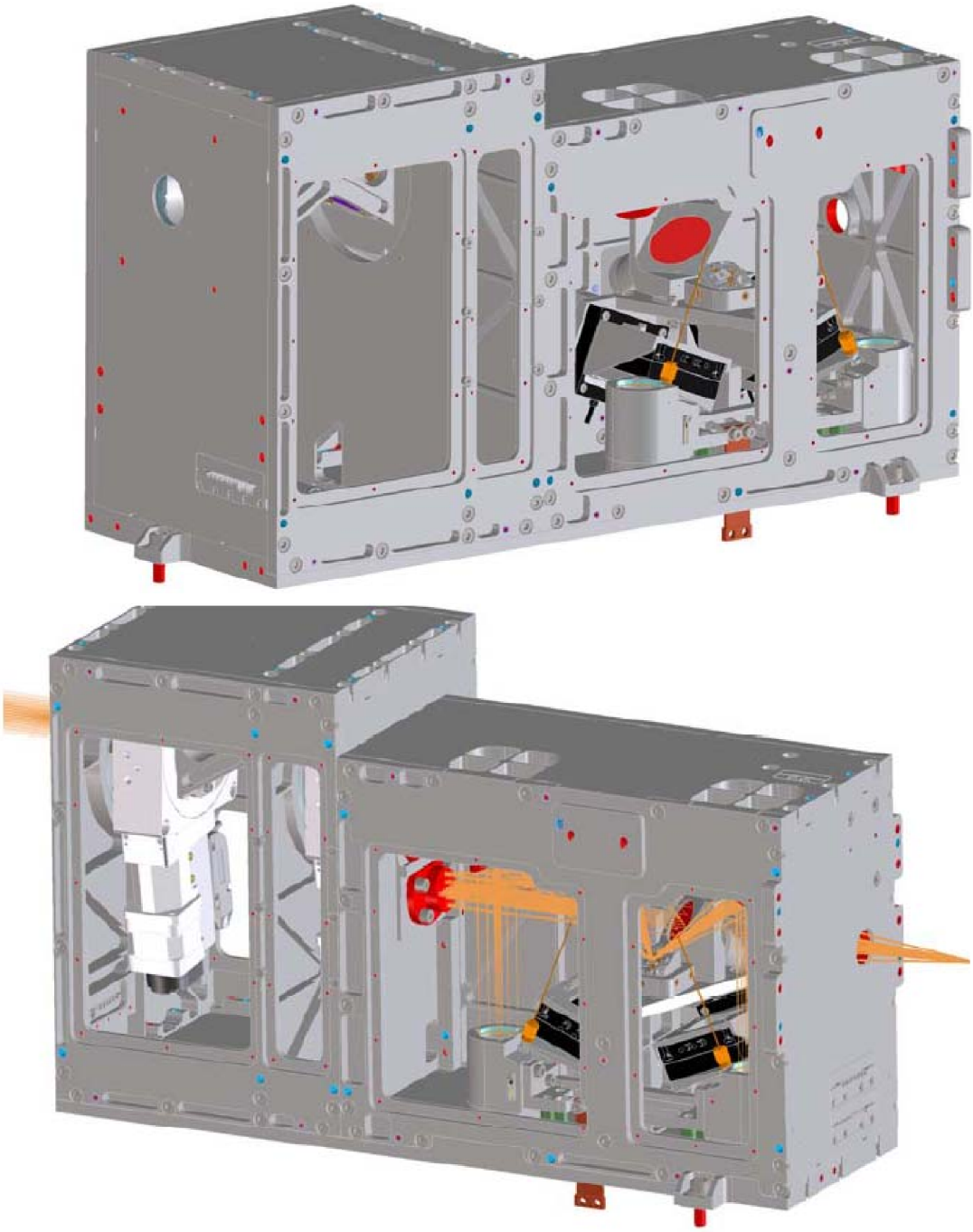

Figure 4.11 CAD model of the fiber coupler box with side plates removed. The entrance aperture, a 26.6 mm hole, that can be closed with a mechanical shutter, can be seen on the top. On the bottom the unit is shown with the optical beams included.

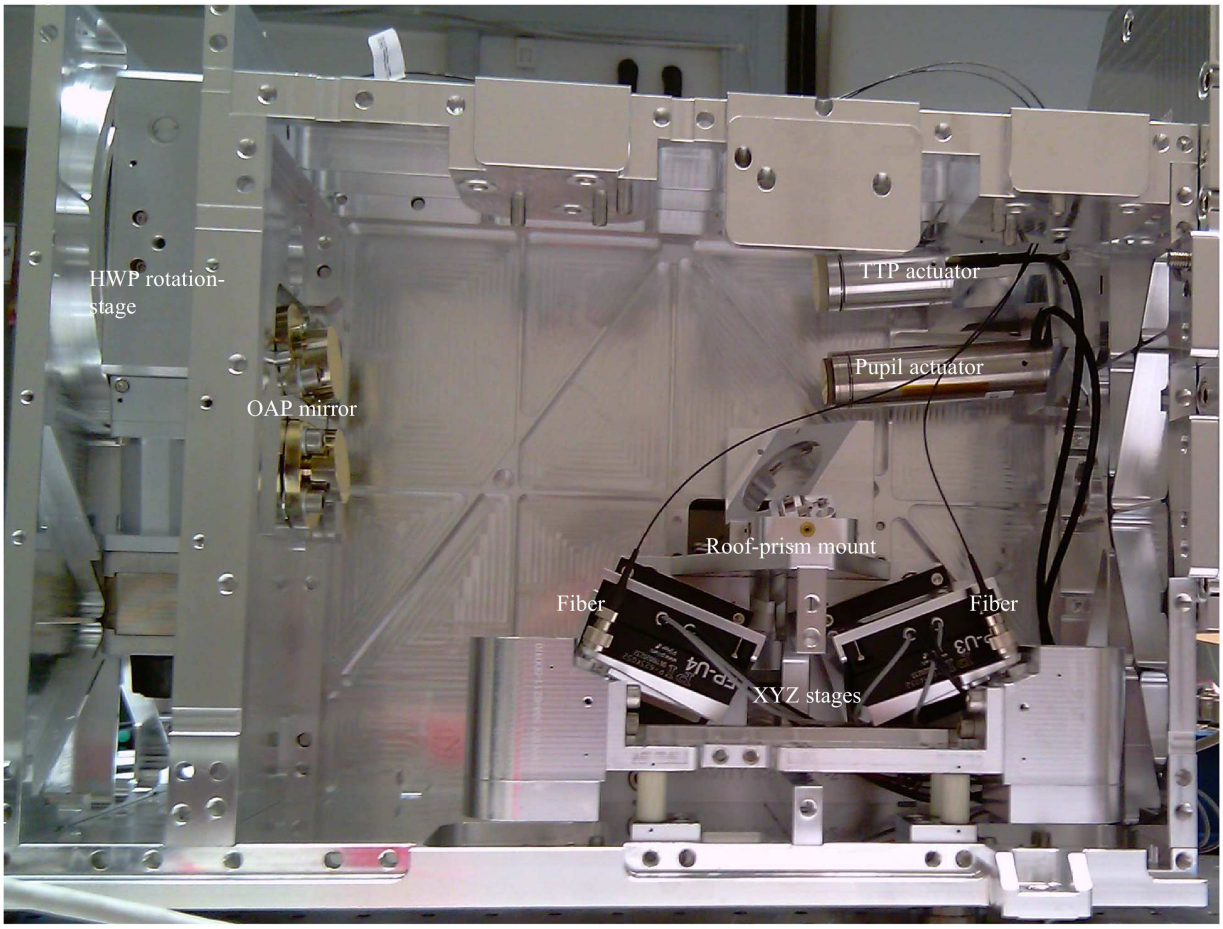

Figure 4.12 Picture of the partially assembled fiber coupler. Not included in the picture is the K-mirror. Still missing in the picture is the dichroic and the roof-prism.

The shutter was tested in a cryo-chamber, verifying that it works at 240 K according to specification.

4.3.3 K-mirror

The K-mirror consists of three gold-coated Zerodur mirrors mounted in an aluminum cage (see Fig. 4.13). The mirrors are front-supported to achieve minimum angular deviations. A copper-beryllium spring pushes the elements against the front mount. This prevents distortions due to differential thermal contraction of the mount and the optical surfaces. The clear aperture of the first and the last surface of the K-mirror is elliptical with a diameter of 55.2 × 28 mm and a thickness of 12 mm. The top mirror has a diameter of 50 mm and a thickness of 7 mm. The front mount serves as a baffle to reduce the background. The complete K-mirror mount is screwed on a modified commercial rotation stage (see Section 4.4.1). After delivery by *Bernhard Halle Nachfl.*, the surface accuracy of the mirrors has been measured with a FISBA interferometer. The individual surface accuracy better than $\lambda/20$ RMS at 633 nm and therefore compliant with the tolerancing specifications (e.g. Figure 4.13).

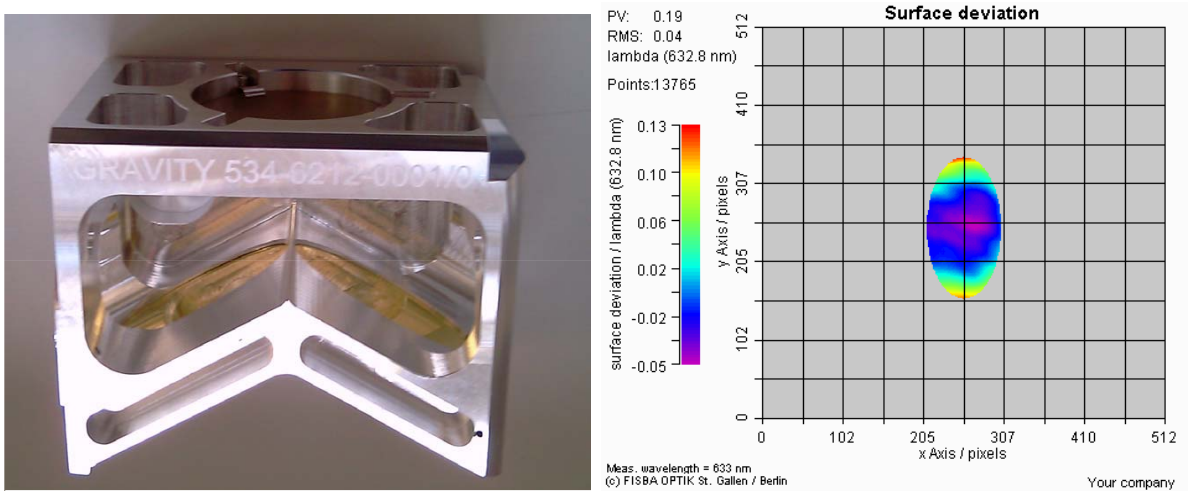

Figure 4.13 Left: K-mirror with mounted mirrors. Right: Surface accuracy of one elliptical mirror measured with a FISBA interferometer. The mirror shows some focus and spherical aberration, however the surface accuracy is $< \lambda/20$ RMS at λ =633 nm.

4.3.4 Retro-reflector

The fiber coupler contains a retro-reflector for calibration purposes. This device allows re-imaging the fiber's image and pupil plane on the acquisition camera. It is placed behind the H/K dichroic and uses the small fraction of metrology light ($\sim$ 1%) that is not reflected.

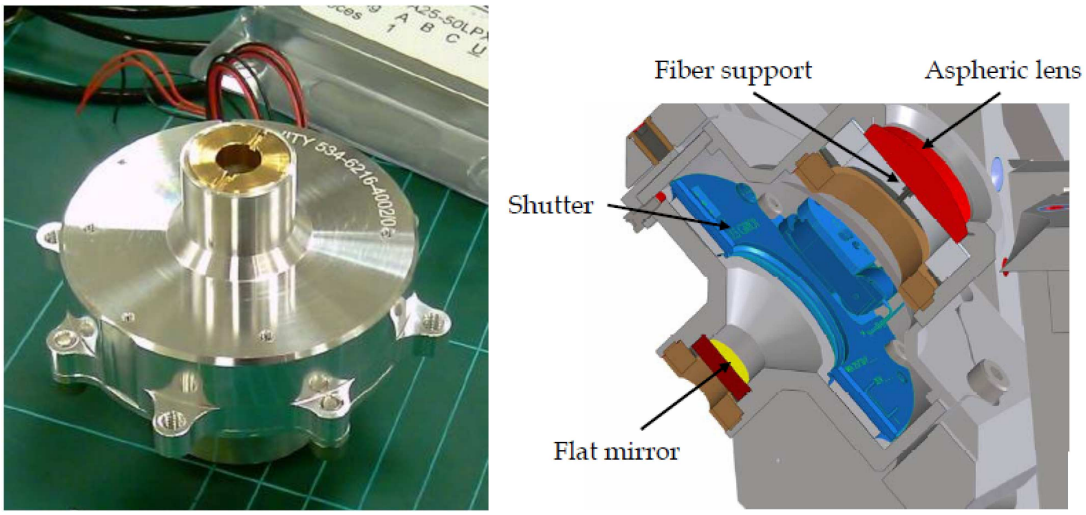

Figure 4.14 Left: Image of the retro-reflector assembly seen from the rear. The threaded copper plate, holding the flat mirror, can be adjusted along the optical axis to place the mirror at the focus of the lens. Right: Cut through the retro-reflector. The lens, the fiber support and the shutter position are illustrated.

To correctly re-image the pupil as well as the field, the retro-reflector is telecentric, with an aspheric lens placed one focal length (f=50 mm) behind the pupil plane. A flat mirror is placed in the focal plane. On the lens a tiny steel pin is glued that supports a multi-mode fiber. This fiber is routed to a photo diode that serves as an internal metrology reference (for further details, see Gillessen, 2011). Another shutter from Melles Griot is mounted between the lens and the mirror, that allows blinding the retro-reflector. The shutter is closed during normal operation of GRAVITY. It is only opened during alignment. The complete retro-reflector is mounted in a separate enclosure that can be detached from the fiber coupler for alignment purposes. Figure 4.14 shows the enclosure and a cut through the 3D model.

4.3.5 Diamond-turned mirrors

All off-axis parabolas are made from diamond-turned aluminum. Since aluminum is too soft to be post-polished, a nickel layer is deposited on the substrate. On top of the nickel, a layer of gold ensures high reflectivity in the infrared. In total, each fiber coupler contains seven off-axis parabolas. The mirrors $M5$ and $M7$ (see Figure 4.1) are identical off-axis parabolas with a radius of curvature of 400 mm and an off-axis distance of 42 mm. The mirror $M9$ with a curvature radius of 200 mm and an off-axis distance of 40 mm focuses the beam on the roof-prism. $M11$ is the most extreme off-axis parabola, with an off-axis distance of 105.5 mm and a curvature of 200 mm. The mirror $M12$ determines the magnification at the fiber tip, with a curvature radius of 104.35 mm and an off-axis distance

of 28 mm. The correct alignment of the mirror is ensured by pins together with flats at the mirror body, that fix the orientation.
The first set of purchased mirrors showed serious optical defects. The measured surface accuracy of $\lambda/7$ RMS at $\lambda = 633\,\text{nm}$ was according to specification, however the diamond machining left a visible groove pattern. These grooves caused strong light scattering and diffraction, imposing a severe limitation on the optical quality. For that reason, we changed the supplier and ordered a new set of mirrors. Those mirrors turned out to be very good in terms of surface accuracy and surface roughness. The previously seen groove pattern was also significantly smaller in this case. Figure 4.15 shows one of the parabolic mirrors before mounting and the measured surface accuracy. Given the surface accuracy of $\lambda/4$ P-V at 633 nm ($\lambda/20$ RMS) and a roughness of $R_q = 1.69\,\text{nm}$ over 0.3 mm test-length, the mirrors provides a suitable optical quality.

4.3.6 Roof-prism and mount

With a size of $1.5 \times 4\,\text{mm}^2$ the roof-prism is extremely small (see Section 4.2.3). To ease the handling, the prism is glued onto a 10 mm squared glass plate made from N-BK7. The glass plate is held by copper springs and the orientation is fixed by pins on a small aluminum mount. The complete structure can be laterally aligned with screws at the side. This allows centering the prism with respect to the focus of the corresponding parabolic mirror. Figure 4.16 shows the assembly.

4.4 Opto-mechanics

Various actuators in the fiber coupler are required to control the field and pupil position as well as to focus the fibers and to correct the atmospheric turbulence. All units are custom-made products, to work in vacuum and at a temperature of 240 K. The locations of the individual actuators are shown in Figure 4.12.

4.4.1 Rotation stages

The K-mirror and the half-wave plate are mounted on modified Newport URS100 B PP V6 rotation stages. Each stage is equipped with a 2-phase stepper motor and an optical encoder. The normal grease was changed to vacuum and low temperature qualified Braycote grease. The rotation stage has been tested successfully under vacuum and operating temperature conditions. As part of the tests, the wobble, in other words the irregular nutation of the rotation axis was measured to be smaller than 50 μrad during a full revolution. The motor resolution of the stepper motor is 0.35 mrad according to the manufacturer. Both numbers can be translated into an on-sky performance of the K-mirror.
The step resolution determines how smooth the field de-rotation works. Assuming the rotation axis coincides with the field center, the largest incremental motion occurs at the maximum field radius ($\sim 1''$). The increment step is then $\sim 2 \cdot 50 \cdot 10^{-6} \cdot 1'' = 0.1\,\text{mas}$.

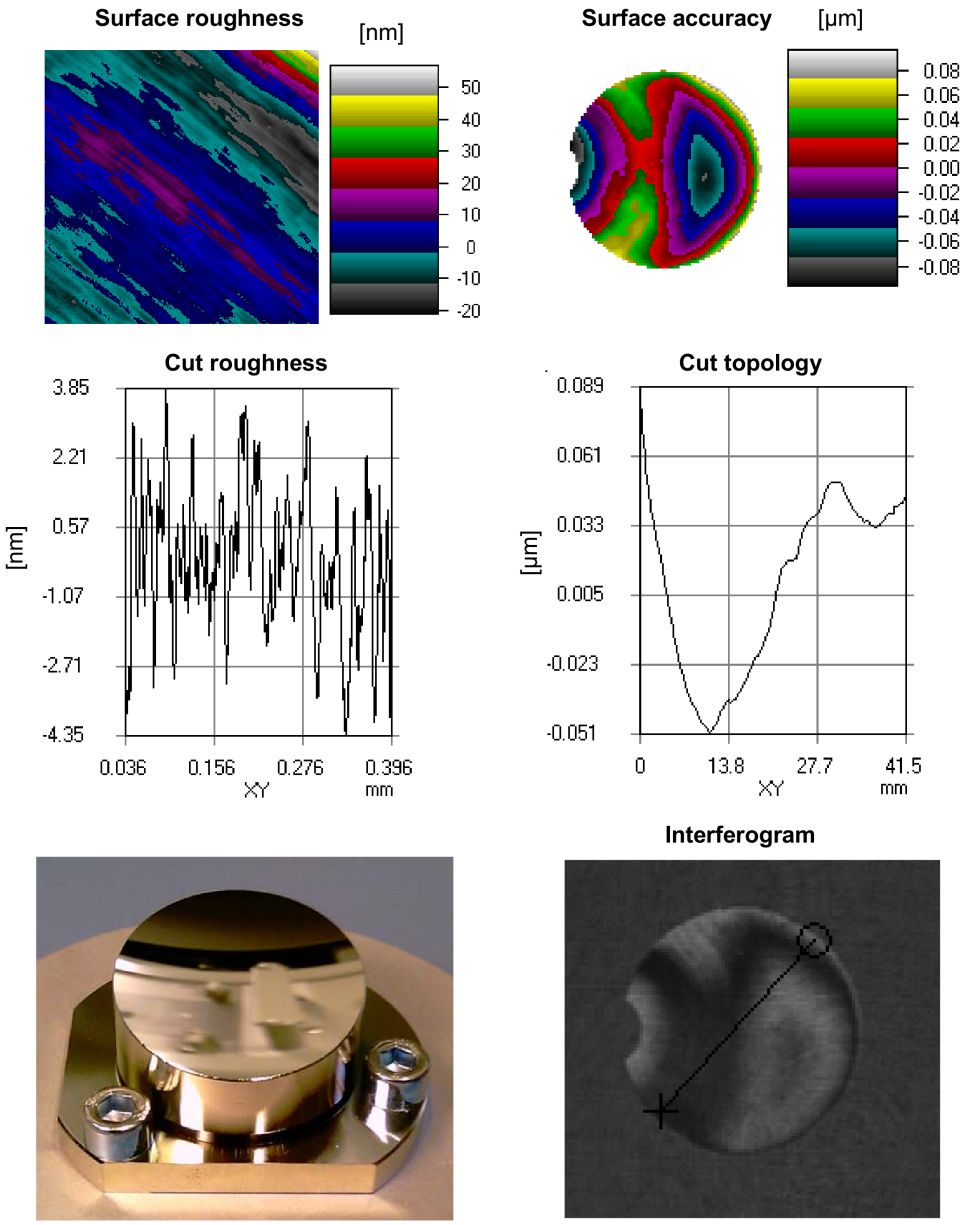

Figure 4.15 Picture of one diamond-turned parabolic mirror before mounting (lower left). The reflective coating is hard gold without an additional protective layer. The orientation of the mirror is fixed by the flat reference surfaces at the side and alignment pins in the fiber coupler. On the right, the measurement interferogram (lower right), the 2D surface accuracy (upper right) and a cut through the 2D surface accuracy (middle right) are shown. On the left, the surface roughness for a 0.4 mm^2 region (upper left), and a cut through the region (middle left) are shown. The surface accuracy across the full aperture is 36 nm RMS and the roughness is $R_q = 1.69$ nm (Courtesy to Kugler GmbH).

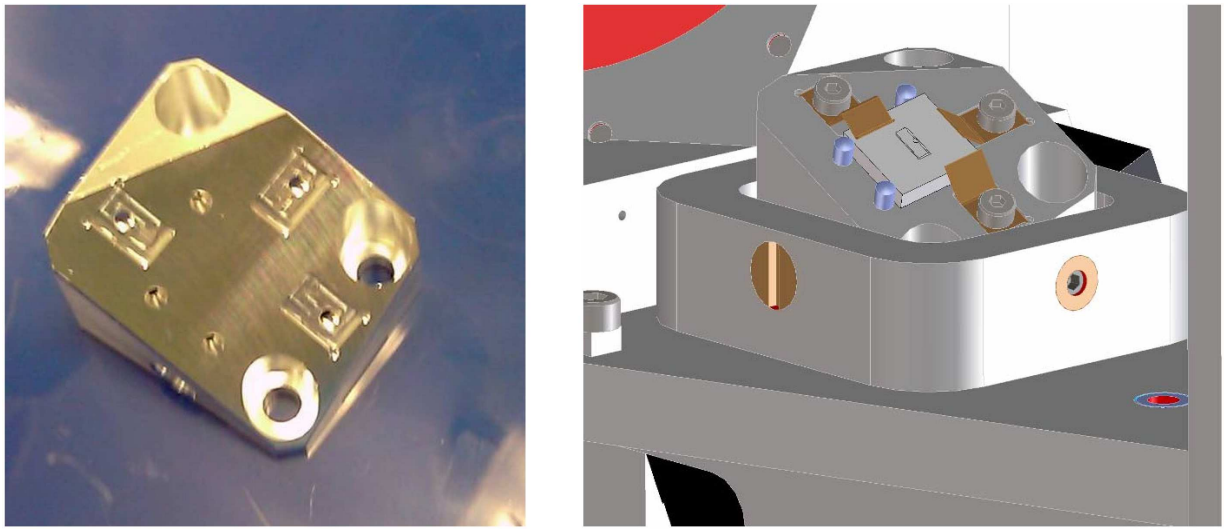

Figure 4.16 Left: Image of the roof-prism mount without clamps. Right: Drawing of the mount in the fiber coupler. The lateral position of the prism can be adjusted by alignment screws on the side of the mount.

The factor two has to be taken into account because the optical rotation is twice the actual mechanical rotation. The resolution corresponds to an incremental step of less than 1/500th of a PSF (60 mas).
The wobble of the rotation stage introduces a relative motion of the the field plane of $< 0.05\,^\circ/0.247\,^\circ = 0.2 \cdot \mathrm{FoV}$. Regarding the half-wave plate, the actuator precision allows to set the polarization with a $0.1\,^\circ$ accuracy, a factor ten better than the optical precision of the half-wave plate.

4.4.2 Tip/tilt/piston actuator

The tip/tilt/piston actuator is a Physik Instrumente S-325.3SL piezo actuator. Each unit is equipped with an internal feedback sensor. Given that the actuator operates at 240 K and in vacuum, the normal capacitative sensors were replaced by strain-gauge sensors. Several units of this type have already been tested and characterized at MPE. The full travel range of the actuator is 30 μm, or almost 60 μm of optical path at a ~ 1 nm resolution. In terms of tilt, the full stroke is 4 mrad or 8 mrad optical tilt at a 0.2 μrad resolution, corresponding to a stroke of $3.7''$ and 0.09 mas resolution on sky. Therefore the full FoV of the VLTI can be accessed, while leaving some margin for alignment corrections. The 60 μm OPD stroke is sufficient to compensate fast piston perturbations. Typically the OPD varies by a few micron on the timescale of a second (Gitton & Puech, 2009). Larger OPD variations have to be offloaded to the main delay lines.
Since the fringe-tracking and the tilt-correction loops require a fast actuator, the frequency response of the unit is an important design parameter. We have tuned the control parame-

ters to optimize the transfer function. Using the internal strain-gauge sensors, the transfer function of each unit was measured. Figure 4.17 shows a typical transfer function with a 3 dB cutoff around 300 Hz. The deviations among the individual units are negligible.

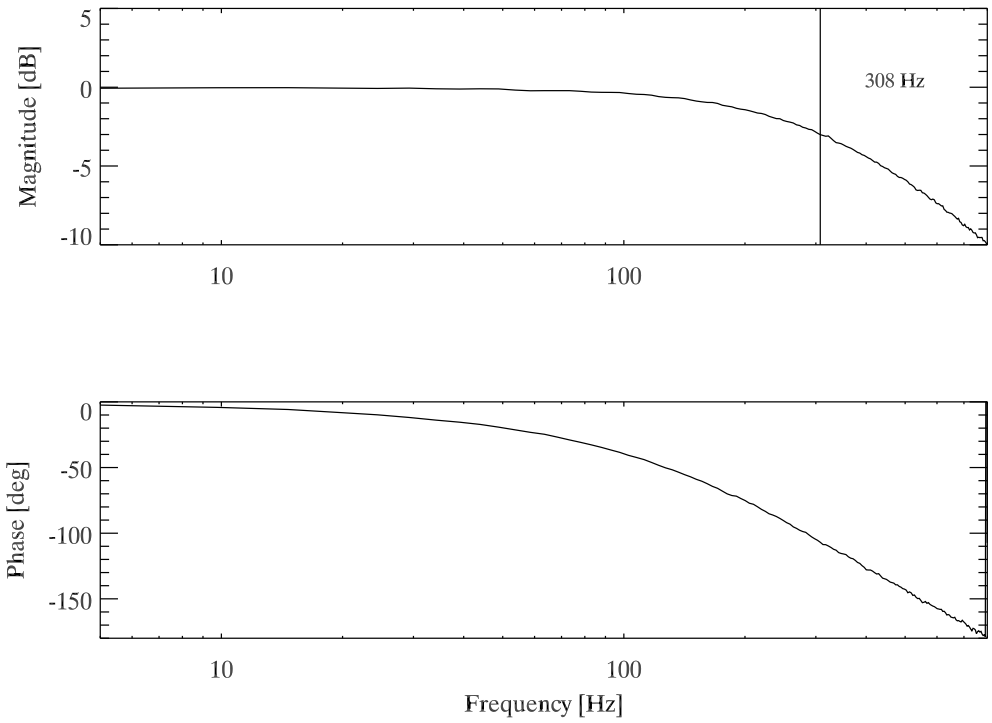

Figure 4.17 Transfer function of one tip/tilt/piston actuator, measured with the internal strain-gauge sensors of the unit. The 3 dB cutoff power, i.e. where the response is attenuated by a factor two, is located at 308 Hz.

4.4.3 Pupil actuator

The pupil actuator is a Physik Instrumente S-330.8SL piezo actuator with a 10 mrad tilt stroke (20 mrad optical tilt). Located at the focus of a parabola with 200 mm focal length, the actuator tilt can be converted into a pupil adjustment stroke of $20 \cdot 10^{-3} \cdot 200\,\text{mm} = 4\,\text{mm}$. Given that the pupil diameter in the VLTI lab is 18 mm, the relative stroke is 22%. The actuator is required to compensate the pupil wander that occurs between the telescope and the lab. The main causes of the pupil wander are the delay line wobble and the telescope run-out, which can move the pupil by $\sim 1\,\text{mm}$. However the pupil wander happens on timescales of minutes and therefore the actuator response is less critical.

4.4.4 Fiber positioner

The fiber positioner is a Physik Instrumente P-625.2CL translation stage, that is required to center and focus the fiber on the object. The full travel range along three axes is 0.5 mm at a few nm resolution. This leaves some alignment margin, given that the nominal field diameter at the fiber position is 0.2 mm (2″FoV UT). The fine resolution easily allows centering and focusing the fiber with its mode-field radius of 3.8 μm.

Chapter 5

Guiding system

Part of this thesis was the development and testing of the GRAVITY guiding system. This includes the overall concept, the optical design, the control-loop analysis and the hardware implementation. The mechanical design was contributed by the MPE engineering department and parts of the manufacturing were done by the MPE workshop. The amplifier- and control electronics were developed together with the MPE electronics department. The circuit design and manufacturing was done by the MPE electronic engineers, while the author focused on the filter bandwidths, the operational amplifier noise characteristics and the control-loop aspects of the electronics.

5.1 Overview

The GRAVITY guiding system comprises two independent control-loops. One system stabilizes the field motion (tip/tilt) and the other system stabilizes the longitudinal and lateral pupil wander.
The *tip/tilt guiding* system uses a laser-beacon launched at the star separator (STS) located in the Coudé room of the telescope. The beacon works as an artificial guide star for the VLTI tunnel. Since the tunnel is not evacuated and the wind on Paranal can be quite strong, the tunnel suffers from a substantial chimney effect. This causes turbulence within the tunnel and leads to internal seeing degradation. As measurements have shown, the tunnel seeing is dominated by tip/tilt jitter, i.e. fast image motion. Higher order aberrations contribute less than 10% of the variance. The telescope AO provides a diffraction-limited beam at the STS. From there, the tip/tilt guiding system takes over up to the VLTI lab, ensuring an optimum beam quality at the beam combiner instrument. The system uses a position sensitive diode in the beam combiner instrument, that tracks on the laser beacon and commands a tip/tilt mirror in the fiber coupler to stabilize the beam. Needless to say that the system exists four times, one tip/tilt guiding system per telescope.
The *pupil guiding* system uses laser beacons, mounted at the telescope spiders. Tracking on the beacons allows stabilizing the pupil wander between the telescope and the VLTI lab. The beacons are monitored by the acquisition camera. A special Shack-Hartmann optics

in the camera allows tracking the lateral as well as the axial pupil position, or in other words, the focus of the pupil. An actuator in the fiber coupler is used for the lateral pupil correction, while the axial position will be adjusted using the variable curvature mirror of the delay lines. Again the pupil guiding happens for all four telescopes independently.
Both systems are an integral part of GRAVITY. They are required to optimize the flux injection into the single-mode fibers, and therefore to increase the effective throughput of the instrument. Furthermore the combination of pupil- and tip/tilt correction is necessary (see Section 2.7) for micro-arcsecond astrometry. Figure 5.1 illustrates the guiding principle of GRAVITY.

5.2 Tip/tilt guiding system

5.2.1 Tunnel atmosphere and injection loss

The purpose of the tip/tilt control-loop is to correct image jitter introduced by the VLTI tunnel atmosphere. The perturbations of the tunnel atmosphere have been studied extensively. One of the major outcomes is that the perturbations are dominated by the lowest order optical disturbance, i.e. tip/tilt, that accounts for 90% of the tunnel atmosphere variance (Hippler & Hormuth, 2010). Naturally the perturbations introduced in the tunnel depend on the optical path a beam has to travel, ranging from a few ten up to a few hundred meters. Another factor are the ambient wind conditions, that fuel the turbulence in the tunnel. A median profile of the perturbations has been established by Gitton & Puech (2009). They describe the tip/tilt disturbance as a broken powerlaw with a break frequency around 1 Hz. Figure 5.2 shows their tunnel atmosphere model. The integration of the model yields a 1-axis tip/tilt RMS of 38 mas on sky (UT) during a 100 s exposure time. The corresponding 2-axis tip/tilt is about a factor $\sqrt{2}$ greater, i.e. 54 mas on sky (240 mas in case of the ATs). The injection loss in single-mode fibers as function of tilt can be calculated by solving Equation 2.5.2. The loss as function of tilt relative to the fiber mode-field radius has been published by Wallner et al. (2002). We used their loss curve and converted it to an equivalent angle on sky. For that it was necessary to convert the fiber offset in units of fiber mode-field radii ω_B into an angle on sky according to:

$$(\frac{\omega_B}{f}) = \frac{\lambda}{1.401D}$$

In case of the UTs ($D = 8\,\mathrm{m}$), the corresponding angle is $\frac{\omega_B}{f} = 41\,\mathrm{mas}$ at $\lambda = 2.15\,\mu\mathrm{m}$. For the ATs ($D = 1.8\,\mathrm{m}$), the equivalent angle is 181 mas. Using the mode-field equivalent angle on sky together with the loss curve of Wallner et al. (2002) the average loss as function of tilt error on sky can be retrieved. Since the atmospheric jitter introduces a tilt fluctuation rather than a static offset, only the loss as function of tilt RMS is of interest. For that we calculated the average loss for a tilt distribution of 10^4 random samples with a certain RMS. Figure 5.3 shows the coupling efficiency relative to the nominal coupling for various values of the tilt RMS. Given that the tunnel atmosphere model predicts a

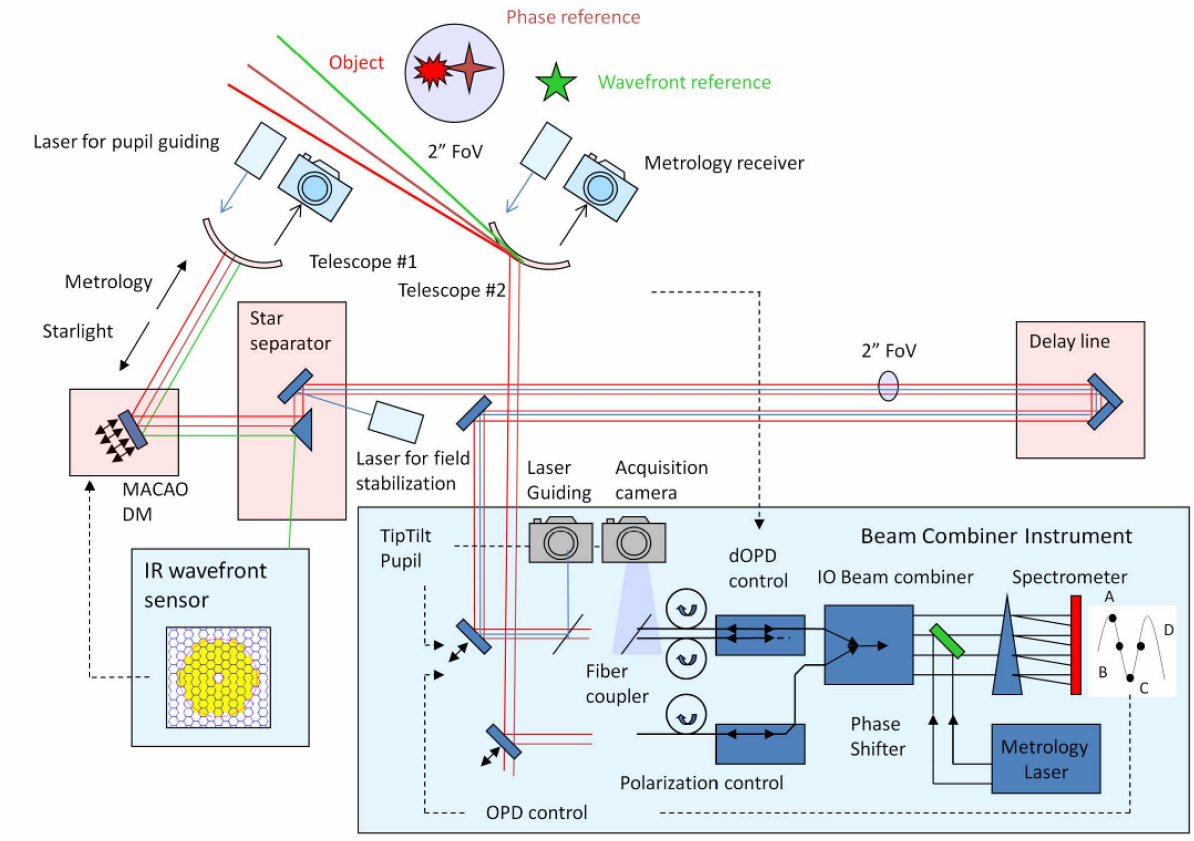

Figure 5.1 Working principle of the GRAVITY guiding system. Two independent control loops stabilize pupil wander and tip/tilt jitter of the optical train. The laser for the pupil guiding is launched at the telescope spiders. The beam propagates through the VLTI train and gets picked up by the acquisition camera in the beam combiner instrument. In combination with the pupil actuator within the fiber coupler, the pupil wander is sensed and stabilized. The tip/tilt guiding laser, launched at the star separator, is picked up by the guiding receiver and stabilizes the atmospheric jitter in the tunnel.

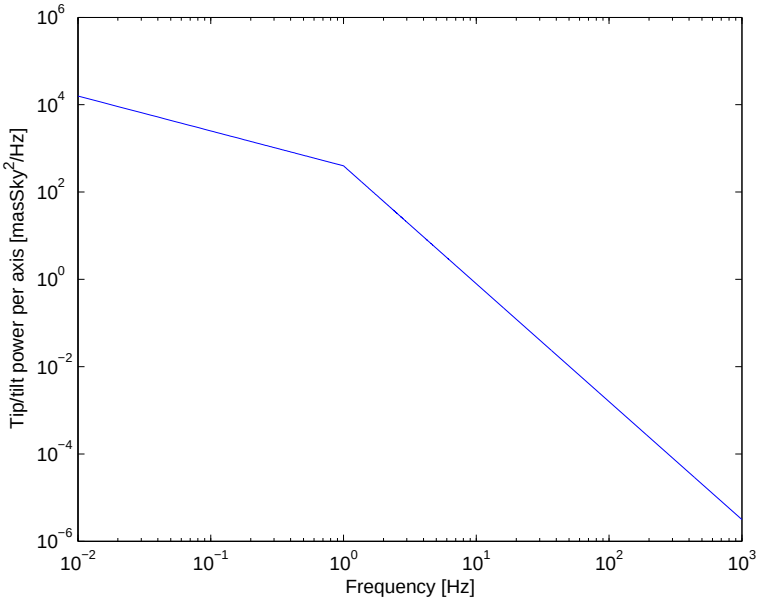

Figure 5.2 Median tip/tilt power spectrum of the VLTI tunnel atmosphere as described by Gitton & Puech (2009). The spectrum is described by a broken power law with a break frequency around 1 Hz. The integrated 1D disturbance corresponds to 38 mas RMS on sky (UT).

2-axis tilt RMS of 54 mas on sky (UT), the flux loss is tremendous. Only about 50% of the nominal flux is actually coupled into the fiber.
The impact of the large coupling fluctuation on the fringe-tracking control-loop is even more severe than only a loss of SNR, since large fluctuations cause flux dropouts and a corresponding loss of the fringe position. An initial study of Perrin et al. (2009) showed that a 1-axis RMS of 25 mas causes flux dropouts and leads the fringe-tracking loop to open during 2% of the time. The phase variation during the open-loop time smears the fringe of the faint science object and leads to an increase of the fringe position uncertainty, or in other words an increase of the astrometric phase error by 2-3 nm. Subsequent simulations by Perrin et al. (2011b) with a 1-axis tip/tilt < 15 mas RMS showed no performance degradation and a negligible open-loop time. Therefore, the tip/tilt guiding system was designed to suppress the tunnel jitter to < 15 mas RMS.

5.2.2 Tip/tilt laser beacon

One tip/tilt laser beacon is launched at the STS of each telescope. The beacon, supposed to track field motion, has to be injected in a field plane. Since injecting the laser should not vignette or add any optical elements to the VLTI optical train, the injection is done by focusing the laser onto a field mirror of the STS. This creates a bright scattering spot

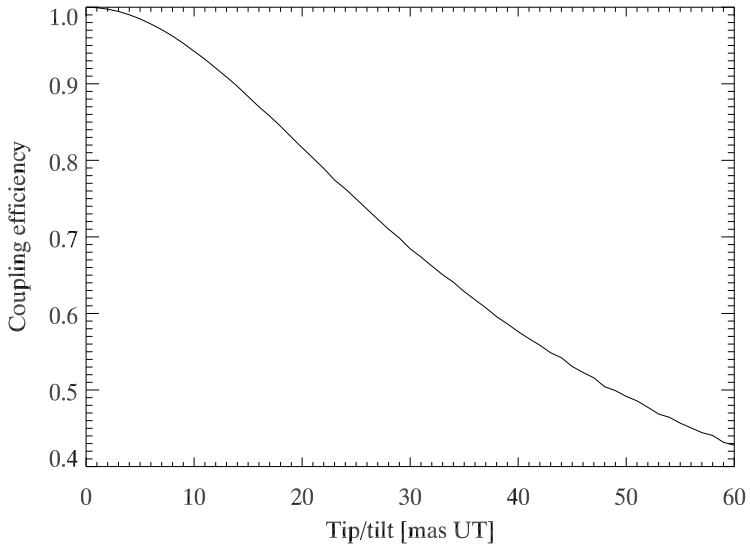

Figure 5.3 The loss of coupling efficiency relative to the nominal coupling (77.8%, see Sec 4.2.1) is shown as function of tilt jitter RMS (UT).

in the respective plane. In this way, an artificial guide star is introduced in the FoV. Tracking on this artificial star therefore allows stabilizing the image motion. The laser beam is launched at a shallow angle (5.8°) from below the optical axis. Figure 5.4 shows the injection principle. A shallow injection angle is favored because the scattering efficiency strongly depends on the angle between the specular reflection and the scattering direction. Nearly all the scattered power is radiated away in a small cone ($< 10°$) around the specular reflection. In our injection scheme, the specular reflection itself will be completely baffled within the star separator enclosure.

Launcher optics

The optical design of the tip/tilt laser beacon is such that it contains only off-the shelf optical components. The laser source is a commercial fiber-pigtailed laser diode with a wavelength of 658 nm and a nominal output power of 60 mW. A constant current laser driver housed in the STS LCU provides the power for the laser. The laser can be switched on and off, via a digital I/O. The laser fiber is connected via a FC connector to a beam collimator, creating an output beam of 7 mm diameter. The collimator is mounted in a lens tube system. Mounted in an adjustable extension of the lens tube, a $f = 600$ mm lens focuses the beam on the field mirror of the STS. The length of the extension can be adjusted by an internal thread to focus the beam. The whole lens tube system sits on a kinematic mount, that can be tilted along two axes. The mount allows an adjustment of the laser pointing by $\pm 4°$ at a resolution of $\sim 3'$. This allows to center the scattering spot

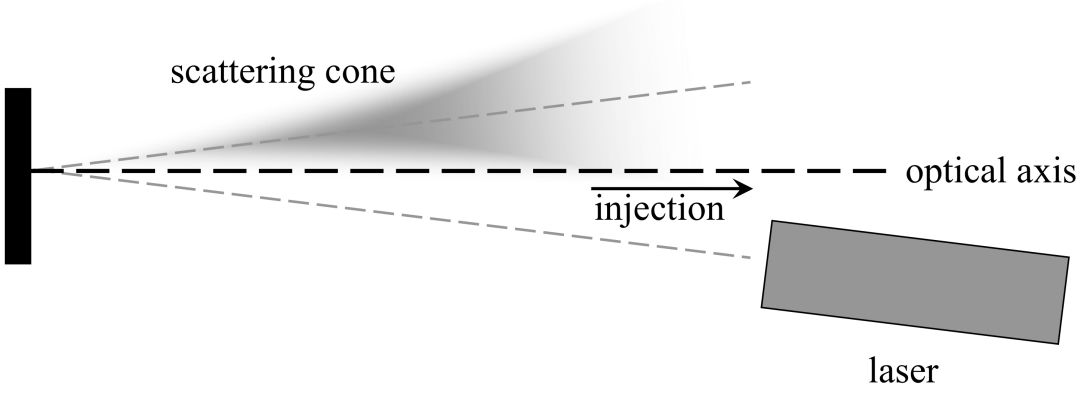

Figure 5.4 Sketch of the laser injection. The laser is launched below the optical axis and focused onto the field mirror. Only the light scattered in the direction of the optical axis is injected in the VLTI train. The specular reflection is baffled inside the STS housing.

on the mirror. If the beam is centered, the nominal launch angle is 5.8° with respect to the optical axis. The whole assembly is mounted on a magnetic plate that can be removed from the STS without loosing the initial alignment. Figure 5.5 shows one tip/tilt launcher installed on a UT STS. The laser points to the corresponding field mirror.

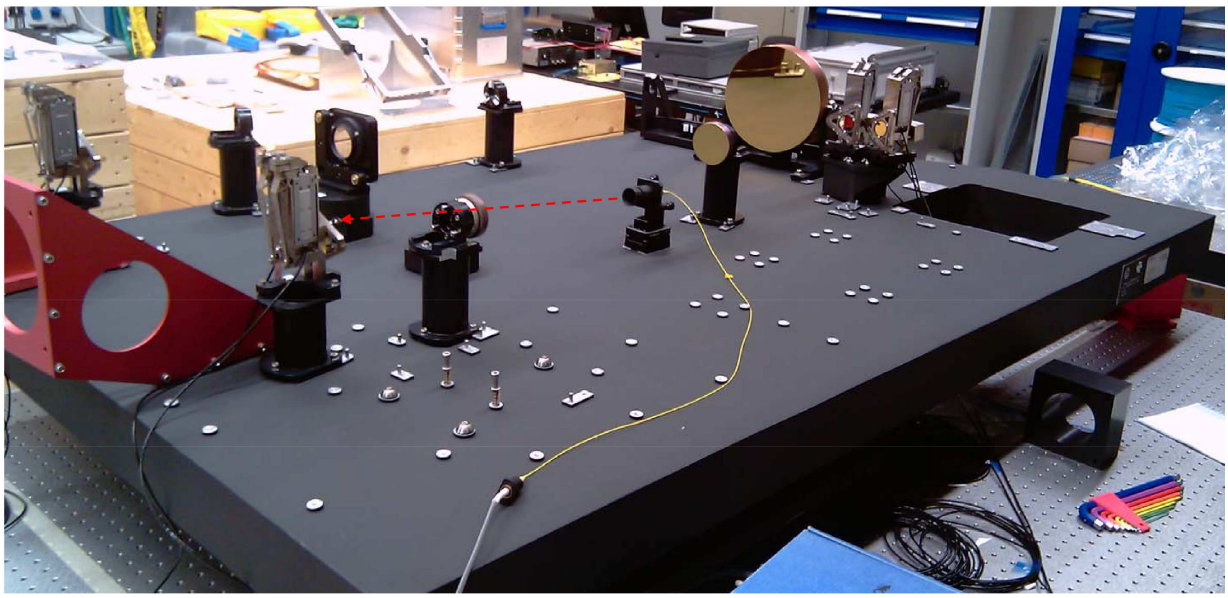

Figure 5.5 Picture of one tip/tilt laser launcher installed on a UT STS. The launch optics is fed by a fiber-pigtailed laser diode (yellow). The red arrow indicates the pointing direction of the beam, that is focused on the field mirror.

Scattering efficiency

Given that only the scattered light of the laser serves as a tip/tilt beacon, the scattering efficiency is an important parameter for the power budget of the receiver unit. We used an already installed tip/tilt launcher on the UT STS to measure the scattering efficiency of the laser. As previously described, the laser launcher is focused on the field mirror of the UT star separator. The field plane coincides with the focal point of the off-axis parabolic mirror seen in Figure 5.5 (large mirror in the center). This mirror is used to collimate the beam of the STS and to feed it into the VLTI delay lines. In the collimated beam of the STS, we placed a commercial telescope to focus the beam on a power-meter. The telescope aperture was stopped down to 80 mm, i.e. the nominal beam diameter within the VLTI optical train. The telescope transmission including a laser line filter was measured to be 65%. Taking this loss into account the scattering efficiency as function of scattering angle was simply calculated from the ratio of laser power exiting the launcher and the laser power measured at the focus of the telescope. Figure 5.6 shows the scattering behavior.
We found a scattering efficiency for the tip/tilt beacon angle (5.8°) of $2.1 \cdot 10^{-4}$, meaning that 12.6 μW of the initial 60 mW are scattered into the VLTI optical train.

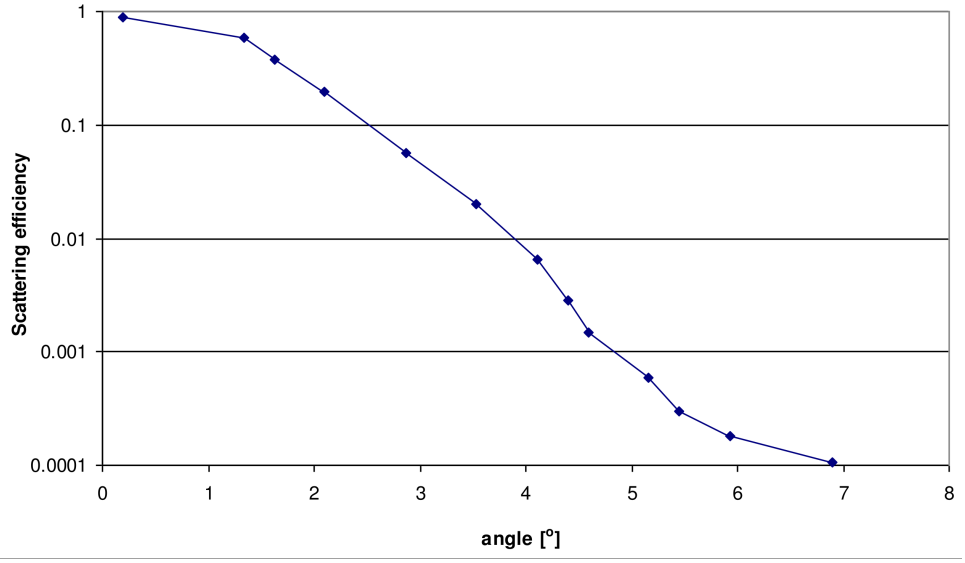

Figure 5.6 Scattering efficiency as function of angle between specular reflection and optical axis. The nominal scattering angle of the tip/tilt beacon is 5.8°, corresponding to a scattering efficiency of $2.1 \cdot 10^{-4}$.

5.2.3 Guiding receiver

Optical design

The tip/tilt guiding laser injected in the FoV travels the same optical path through the VLTI and the beam combiner instrument as the stellar light. As described in Chapter 4, the beam propagates through the fiber coupler up to the H/K dichroic. While the science wave band is reflected to the fiber injection optics, the laser wavelength passes the dichroic and exits the fiber coupler in a 18 mm collimated beam. The guiding receiver, which is mounted like a backpack on the fiber coupler, picks up the laser beam and images the beacon on a position sensitive diode (PSD). The beam pickup happens with another dichroic, which reflects the tip/tilt guiding laser and lets the pupil guiding laser and the stellar H-band light pass to the guiding receiver. We chose a silicon substrate dichroic since silicon is opaque at wavelengths shorter than 1100 nm. Together with a reflective coating it provides a high reflectivity (99%) of the 658 nm laser line and ensures that no stray-light is propagated to the acquisition camera. The pupil laser (1200 nm) and the stellar acquisition band ($1.5 - 1.8\,\mu$m) are able to pass the dichroic with negligible reflection losses (0.5%). Figure 5.7 shows the optical design of the receiver.
The reflected laser light is focused by a $f = 400$ mm lens onto the PSD. Given the focal length, the $4 \times 4\,\text{mm}^2$ active area of the diode corresponds to 0.573° or an equivalent FoV (UT) of $\pm 2.3''$ on sky (compare Sec. 4.1). Thus the FoV of the guiding receiver is a factor two larger than the nominal VLTI FoV. Therefore enough stroke margin is available to ensure that the artificial laser beacon is always visible on the guiding receiver.

Laser power budget

To derive the laser power available at the PSD, the VLTI, the fiber coupler and the guiding receiver throughput has to be taken into account. Based on the ICD (Gitton & Puech, 2009), the transmission between the STS and the VLTI lab at the laser wavelength 658 nm can be estimated to be $\sim$ 20%. This includes 12 protected gold-coated mirrors ($R \sim$ 93%) and five silver-coated mirrors ($R \sim 95\%$) as well as losses due to dust and coating degradation. The number of surfaces in the optical train between the AT star separators and the UT star separators is almost the same. In the subsequent calculations, the VLTI transmission in the UT and AT case is assumed to be equal. The fiber coupler throughput is about 44%, counting the seven gold-coated mirrors (95%), the dichroic transmission (70%) and the losses at the glass surfaces of the entrance window (93%) and the half-wave plate (96%). Finally the throughput of the guiding receiver is $\sim 85\%$, given that only two silver-coated mirrors (96%), one dichroic (99%) and a lens (93%) are affecting the beam. Therefore the total throughput is $\sim 7\%$. Taking into account the scattering efficiency of $2.1 \cdot 10^{-4}$ (Sec. 5.2.2), the 60 mW laser is reduced to $\sim 0.88\,\mu$W at the PSD.

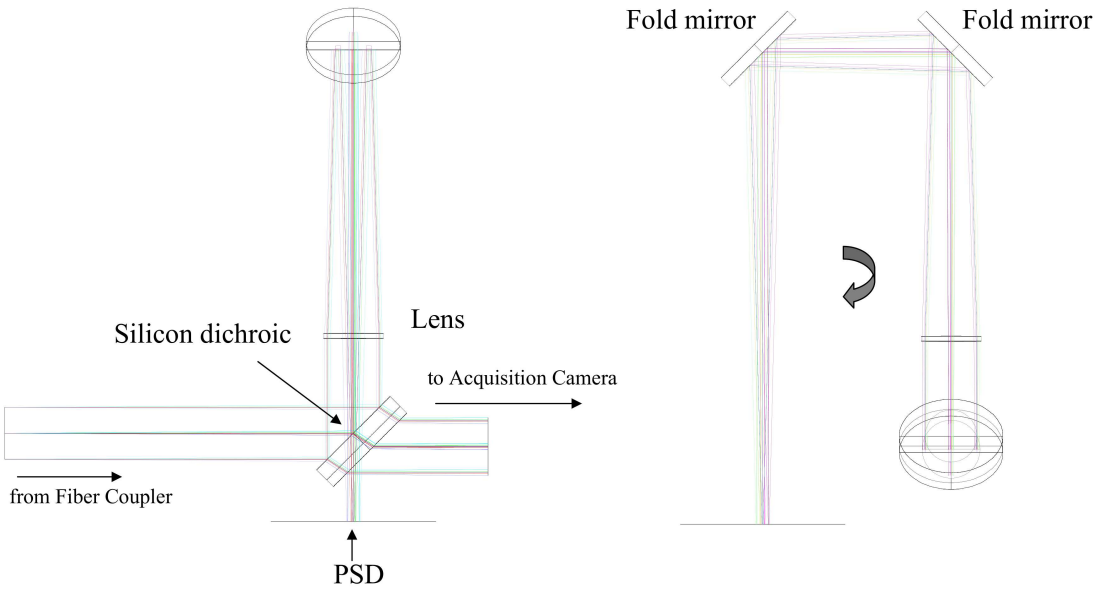

Figure 5.7 Optical design of the guiding receiver. The collimated beam exiting the fiber coupler (see Fig. 4.1) is split by a silicon dichroic in the guiding receiver. The 658 nm laser light is reflected, relayed via flat mirrors and focused with a commercial $f = 400$ mm lens on the position sensitive diode. The pupil guiding laser (1200 nm) and the stellar H-band light pass the dichroic to the acquisition camera. Since silicon is opaque at wavelengths shorter than 1100 nm, no laser stray-light is able to contaminate the propagated beam.

Mechanical design

The front of the guiding receiver structure is screwed to the fiber coupler unit. The structure is completely manufactured from aluminum, i.e. the same material as the fiber coupler. This avoids differential contraction of the material, when the unit is cooled down to the operating temperature of 240 K. Cylindrical pins ensure the correct alignment of the receiver and the fiber coupler. Figure 5.8 shows the assembly during testing. The open receiver can be seen in Figure 5.9. The large size of the box results from the long focal length of the lens, that provides a useful FoV on the diode. All optics, with the exception of the dichroic are off-the-shelf products. The fused silica lens is centered by three springs oriented at 120° with respect to each other. The springs are directly cut out of the mounting plate. The two fold mirrors provide the long focal distance. One of the fold mirrors sits on a tilt stage that allows aligning the beam with the diode. The sensor, a position sensitive diode, is mounted on a aluminum plate, that can be rotated by a few degrees. This allows aligning the diode coordinate system with the fiber coupler coordinate system, that is defined by the orientation of the tip/tilt actuator.

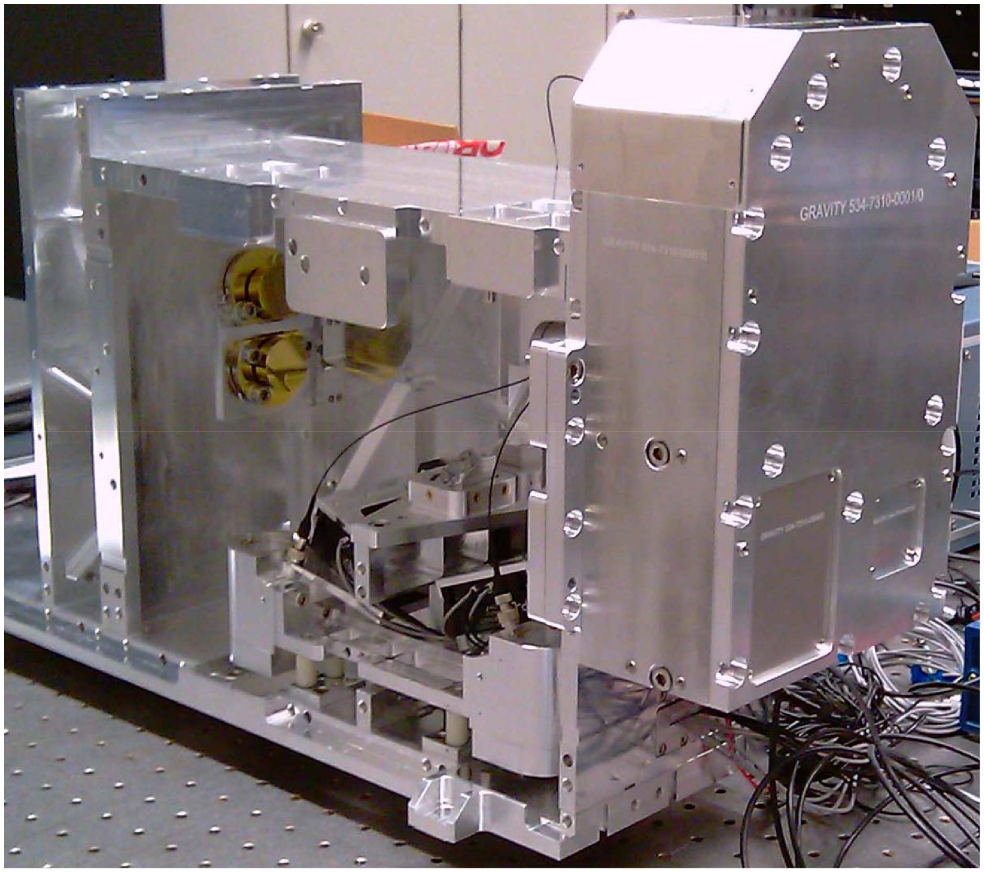

Figure 5.8 Guiding receiver mounted on the fiber coupler. In this picture, the beam exit of the guiding receiver is closed with a small aluminum plate. The connector cable for the diode enters the unit from the bottom.

5.2.4 Sensor

The tip/tilt guiding beacon is tracked with a position sensitive diode (PSD). A PSD consists of a uniform resistive layer formed at one or both surfaces of a high-resistivity semiconductor substrate, and a set of electrodes formed on the ends of the resistive layer for extracting position signals. The active area, which is also a resistive layer, has a PN junction that generates a photo-current if light hits the surface. When a light spot illuminates the PSD, an electric charge proportional to the light intensity is generated at the incident position. This electric charge is driven through the resistive layer and is collected by the output electrodes as photo-currents. The photo-current that is measured at a particular electrode is inverse proportional to the distance between the light spot and the electrode due to the increasing resistance. Since the electrons and the holes are transported in different layers, the 2D position can be retrieved by using two anodes and two cathodes oriented perpendicular to each other. By comparing the photo-currents at the output electrodes, the spot position can be derived. Figure 5.10 illustrates the position measurement. The

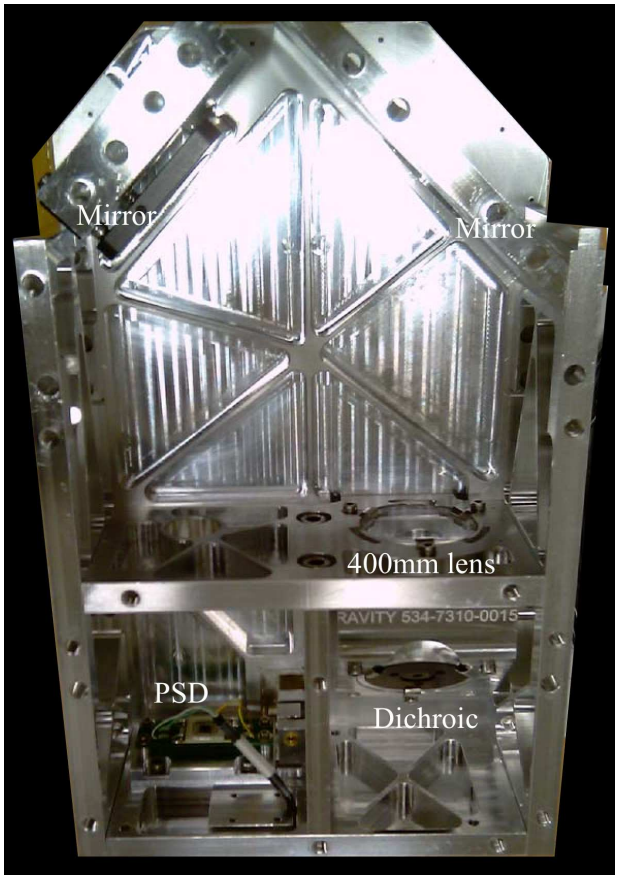

Figure 5.9 Interior of the guiding receiver. The positions of the lens, the dichroic and the folding mirrors are indicated. In this picture, a mirror replaces the dichroic. The left flat mirror is held by a kinematic mount that allows centering the beam on the position sensitive diode. The diode itself can be rotated by a few degrees to align the orientation of the diode with the piezo actuator in the fiber coupler.

photo-currents at the electrodes are amplified and measured as output voltages. Therefore, the position information of the light spot in case of a 2-dimensional PSD is contained in four output voltages. These output voltages can be directly used in an analogue control-loop.
The PSD used in the guiding receiver is a silicon duo-lateral PSD from Pacific Silicon Sensors. It has an active area of $4 \times 4\,\mathrm{mm}^2$ with a linear region of $2.8 \times 2.8\,\mathrm{mm}^2$. The four output voltages are amplified and converted into X-Y position voltages by an amplifier board developed by MPE. The amplifier is optimized for low-noise performance at very high amplification with a 3 dB bandwidth of 820 Hz. An on-board sample-and-hold chip allows storing and subtracting the dark current of the diode. This is necessary since the diode is operated at very low light levels. In this regime, leakage currents in the PSD are not negligible and have to be subtracted. The calibrated signals are then converted into

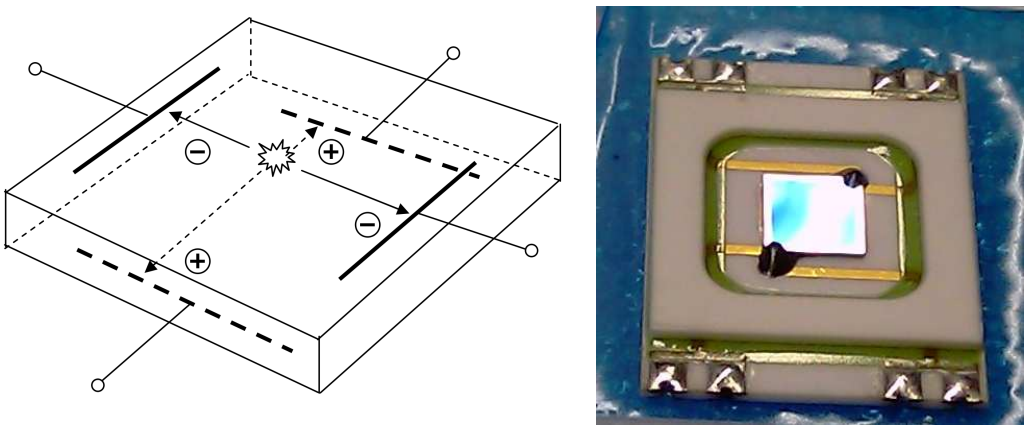

Figure 5.10 Left: Illustration of the working principle of a position sensitive diode (Hamamatsu, 2012). The incident light spot generates a photo-current. The resistance between the electrodes and the spot position is proportional to the distance. Therefore by comparing the currents of two electrodes derives the spot position along one axis. By measuring the electron and the hole currents in perpendicular directions, the 2D position can be retrieved. Right: Image of the silicon PSD used in the guiding receiver. The active area is $4 \times 4\,\mathrm{mm}^2$.

an X and Y voltage via the analogue circuitry.

Noise model

A detailed description of the noise characteristics of a PSD is given by Hamamatsu (2012). The performance of a PSD is driven by three main noise sources: the shot noise, the thermal noise and the noise generated by the operational amplifier. Apart from the shot noise, the noise sources depend on the interelectrode resistance, defined as the resistance between two opposite electrodes. An equivalent circuit for the PSD noise is shown in Figure 5.11. The position resolution of the PSD is determined by the signal-to-noise ratio (SNR). Since the spot position is directly related to the measured current, the position resolution follows from:

$$\frac{\Delta L}{L} = \frac{I_n}{I_p}$$

where I_n is the noise current and I_p is the photo-current. Contributing to the noise current is the shot noise I_s originating from the photon statistics and the discrete nature of electric charges. It follows from:

$$I_s = \sqrt{2q \cdot (I_p + I_d) \cdot B} \qquad [\mathrm{A}]$$

where q is the electron charge, B is the amplifier bandwidth in [Hz], I_p is the photo- and I_d the dark current. An additional noise source is the thermal noise current I_j, generated

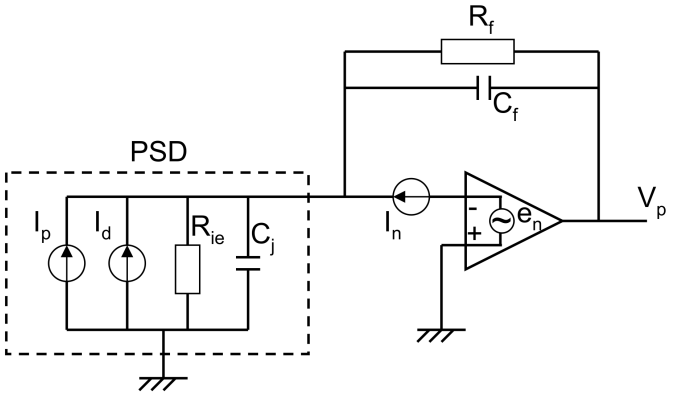

Figure 5.11 Equivalent noise circuit of the diode (Hamamatsu, 2012). The individual terms are the photo-current I_p, the dark-current I_d , the interelectrode resistance R_{ie}, the junction capacitance C_j, the feedback resistance R_f, the feedback capacitance C_f, the op-amp equivalent input noise voltage e_n, the op-amp equivalent input noise current i_n and the output voltage V_p.

from the finite interelectrode resistance. It follows from:

$$I_j = \sqrt{\frac{4kTB}{R_{ie}}} \qquad [\mathrm{A}]$$

where k is the Boltzmann constant and T is the temperature. The PSD is operated in a regime, where the feedback resistance is much greater than the interelectrode resistance ($R_f >> R_{ie}$). In other words, the PSD is operated with a large amplification. In this regime, the amplifier noise is determined by the equivalent input noise voltage of the op-amp, that induces current fluctuations across the PSD. It follows from:

$$I_{en} = \frac{e_n}{R_{ie}}\sqrt{B} \qquad [\mathrm{A}]$$

where e_n is the equivalent input noise voltage. The total noise current is therefore:

$$I_n = \sqrt{I_s^2 + I_j^2 + I_{en}^2} \qquad [\mathrm{A}]$$

The photo-current is related to the incident light power P multiplied by a responsivity factor G of the diode. Therefore the position resolution can be calculated from:

$$\frac{\Delta L}{L} = \frac{\sqrt{I_s^2 + I_j^2 + I_{en}^2}}{G \cdot P}$$

This allows deriving the position resolution as function of incident light power at the operating temperature (240 K) and the chosen amplifier bandwidth of 820 Hz. Using the

specifications stated in the op-amp and PSD data-sheets for $R_{ie} = 10\,\mathrm{k\Omega}$, $I_d = 30\,\mathrm{nA}$, $e_n = 3.3\,\mathrm{nV}/\sqrt{\mathrm{Hz}}$ and $G = 0.4\,\mathrm{A/W}$, yields a thermal noise of $I_j = 25.7\,\mathrm{pA}$ and an amplifier noise of $I_{en} = 7.4\,\mathrm{pA}$. At the light levels of interest, the shot noise is about a factor hundred smaller than the other noise sources. Therefore the position resolution follows from:

$$\frac{\Delta L}{L} = \frac{26.8\,[\mathrm{pA}]}{0.4\,[\mathrm{A/W}] \cdot P\,[\mathrm{W}]} = \frac{0.067}{P\,[\mathrm{nW}]} \tag{5.1}$$

Noise measurement

To verify the noise calculations, we set up a lab experiment to measure the position resolution of the PSD. A 658 nm laser was imaged on the PSD, attenuated by various neutral density filters. To block background light, a laser line filter was mounted in front of the PSD. The incident light power was measured with a power-meter. With a LabView routine the X-Y position voltage was recorded with a sampling rate of 1 kHz. During the measurement the laser power was attenuated by various filter combinations. The position error of the light spot was measured as the RMS of 1000 samples, corresponding to a record length of 1 s. Figure 5.12 shows the resulting one dimensional position RMS as a function of incident laser power. For comparison, the theoretical noise behavior derived in Equation 5.1 is shown. The measurements clearly reproduce the $1/P$ dependence of the position resolution. The measured values are only about a factor 1.5 above the theoretical limit. This means, that the developed amplifier works at or close to the theoretical optimum and that external noise sources are almost negligible. The performance is limited by the inherent properties of the PSD. Further improvements are only possible if the PSD device would be cooled to very low temperatures or if the bandwidth would be reduced. As described in Section 5.2.3, of the initial 60 mW laser about 0.88 μW incident power reach the PSD. Looking at Figure 5.12, the position resolution will be well below 0.1% of the diode half-length. Given that the assumptions on transmission and scattering are somewhat uncertain and that material inhomogeneities of the PSD fundamentally limit the resolution, we use a fiducial resolution of $dL/L = 0.1\%$. This can be converted into a position resolution on sky by multiplication with the equivalent FoV of 2.3″, resulting in a sensor noise of 2.3 mas RMS (UT).

5.3 Control-loop analysis

The response of linear time-invariant systems to an input signal can be described as a transfer function. It is convenient way to characterize a multitude of systems, be it a piezo reacting to an applied voltage or a plant reacting to heat input. Assuming an input signal as function of time $e(t)$ is converted by a system into the output $r(t)$ and assuming $E(s)$ and $R(s)$ are the Laplace transforms of $e(t)$ and $r(t)$, then the transfer function $G(s)$ of the system is related to the Laplace transforms according to (e.g. Franklin et al., 1998):

$$G(s) = \frac{R(s)}{E(s)} \tag{5.2}$$

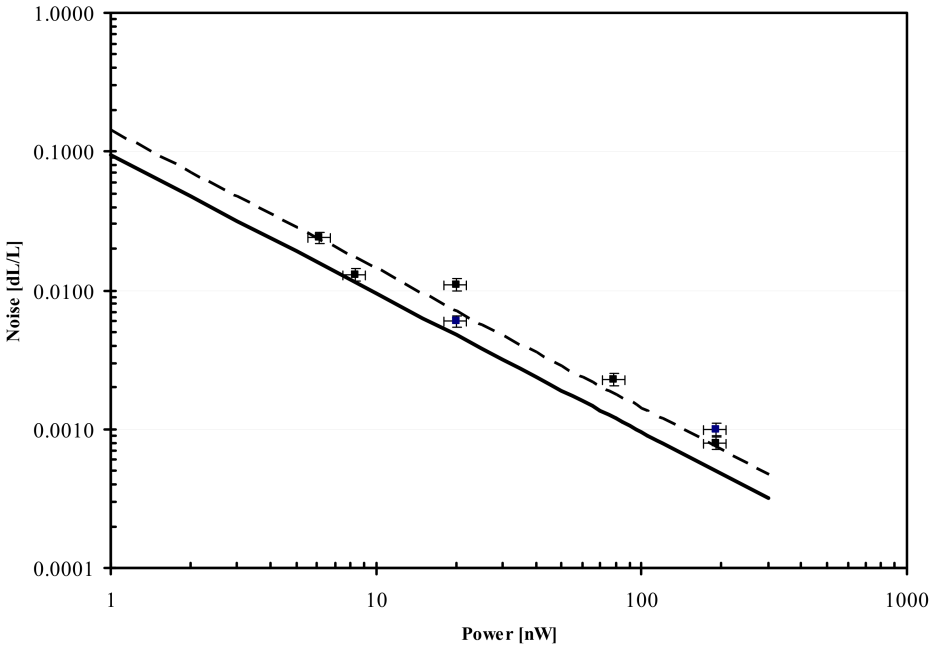

Figure 5.12 Position noise dL/L of the PSD as function of incident light power, where L corresponds to half of the PSD length. The one dimensional position error of the laser spot was recorded at 1 kHz. The position RMS during 1 s is shown for various laser powers on the PSD. The best-fitting $1/P$ dependence is shown as a dashed line. For comparison, the theoretical noise is plotted (solid line).

The transfer function provides a complete description of a system in the frequency domain. Given that atmospheric perturbations are usually described as frequency dependent powerlaws, it is therefore favorable to evaluate AO-like system performances using transfer functions.

5.3.1 Tip/tilt control-loop

The tip/tilt guiding system consists of two sensors, PSD and acquisition camera, commanding a common actuator. Its purpose is to correct the tip/tilt jitter induced by the tunnel atmosphere and to optimize the light injection into the single-mode fibers. The actuator is a piezo-driven mirror, installed in the fiber coupler (see Sec. 4.4.2). The acquisition camera images the FoV on sky and provides a reference for the fiber position at a frame rate of ~ 1 Hz. The low frame rate is set by readout of the detector and the object faintness. Thus the camera is only able to monitor slow tilt drifts. High frequency perturbations are therefore sensed by the PSD described in Section 5.2.4. The device locks on the artificial laser star injected at the star separator (Section 5.2.2). With the amplifier tuned

to a bandwidth of 820 Hz, it is able to measure and correct high frequency image jitter. However, the PSD sensor is intrinsically prone to drift on slow timescales. This can either happen due to electrical drifts of the amplifier and the op-amps therein or due to a drift of the laser spot on the star separator. For this reason, a high-pass filter is used to block frequencies below 0.05 Hz. In this scheme, the control-loop senses the high frequency jitter with the PSD but ignores the potential drifts of the device. The jitter stabilized image of the acquisition camera is then used to center the science and fringe-tracking object on the fiber.
The fast control-loop, namely the PSD amplifier, filter and PD controller are implemented in analogue electronics. The obvious advantage is that this saves software and hardware implementation of the fast PSD sensor in an ESO LCU based real-time system. The slow acquisition camera will be operated on the instrument control workstation since at the given frame rate it does not need real-time functionality. During operation each sensor can be independently switched on or off. It is also possible to use the actuator in blind mode with both sensors switched off. This makes the implementation and testing of the system easy and adds flexibility. The acquisition camera setpoint (i.e. the star position on sky) and the blind offsets can be set via the ICS. Figure 5.13 shows the control-loop scheme.
The feedback of the system shown in Figure 5.13 can be described as a transfer function $G_{sys,ol}(s)$ that relates the input signal $E(s)$ (in this case a disturbance) with the output signal $R(s)$. The system response itself can be described as a combination of individual transfer functions. The open-loop transfer function of the system can be described as:

$$G_{sys,ol}(s) = (G_{PSD} \cdot G_{fi} \cdot G_{PD} + G_{acq} \cdot G_{PI}) \cdot G_{act} \tag{5.3}$$

where G_{PSD}, G_{fi}, G_{acq} and G_{act} are the open-loop transfer functions of the PSD, the high-pass filter, the acquisition camera and the piezo actuator. The PD and PI controllers are represented by G_{PD} and G_{PI}. In this implementation of a feedback loop, the disturbance $E(s)$ is attenuated by the system response leading to a small residual $R(s)$, i.e. a corrected signal. In this case, the closed-loop transfer function is given by:

$$G_{sys,cl}(s) = \frac{R(s)}{E(s)} = \frac{1}{1 + G_{sys,ol}(s)} = \frac{1}{1 + (G_{PSD} \cdot G_{fi} \cdot G_{PD} + G_{acq} \cdot G_{PI}) \cdot G_{act}} \tag{5.4}$$

To predict the system response, it is necessary to model or measure the individual transfer functions. Since it is well suited for control-loop applications, *Matlab* was used for the modeling part, while the actuator transfer functions were measured in the lab.

5.3.2 Modeling the acquisition camera response

The field imager mode of the acquisition camera provides an H-band image of the VLTI FoV (see Section 3.1.7). Lima & Amorim (2011) simulated the field imager performance, by assuming a guide star of magnitude $m_H = 13$ and a sky background of an effective magnitude 13.4/arcsec^2 as reported for Paranal (Gitton & Puech, 2009). The pixel size on sky is 17.8 mas/pixel. The field imager PSF was derived by scaling the AO corrected PSF

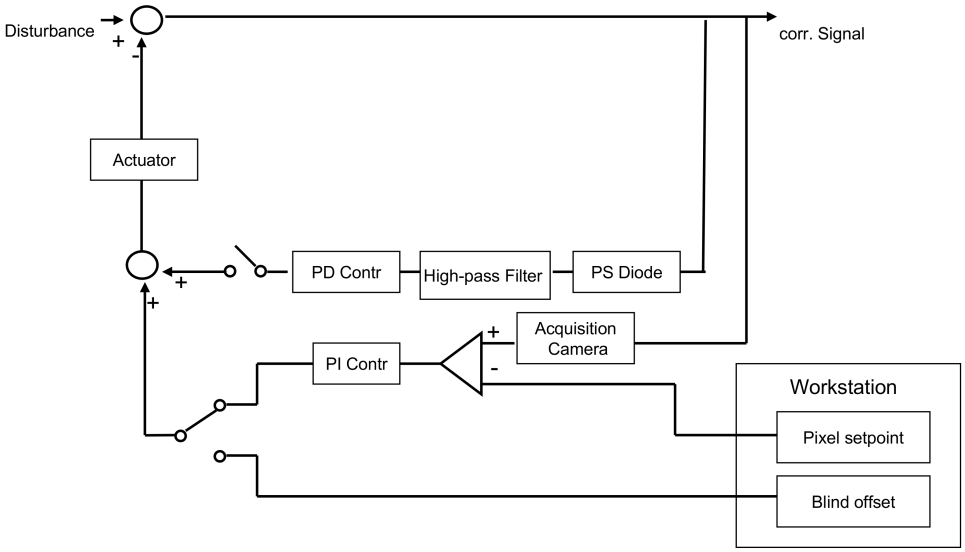

Figure 5.13 Control-loop scheme of the tip/tilt guiding system. Two sensors, the PSD and the acquisition camera covering high frequency and low frequency perturbations, command a common actuator in the fiber coupler. The PSD chain is implemented in analogue electronics, including the amplifier and the PD controller. An analogue high-pass filter effectively blinds the PSD for low frequency drifts, while the slow frame rate of the acquisition camera renders it insensitive to fast jitter. Both control-loop branches can be independently switched on or off. By sending a command via ICS it is possible to change the setpoint of the acquisition camera or to send a blind offset to the actuator.

obtained on a NACO observation of the Galactic Center. Taking into account the VLTI transmission (22%), the beam combiner instrument transmission (23%) and the detector quantum efficiency (80%), the field imager retrieves about 4% of the incident flux. By adding detector readout noise, photon noise and tip/tilt smearing of the image, a realistic observation was simulated. In the simulated image, the star position was retrieved and compared to the initial position. The resulting position error was retrieved for various integration times. Lima & Amorim (2011) find that the stellar position can be retrieved during 1 s integration with a residual RMS of 0.5 mas and 0.25 mas during 10 s integration. In terms of a control-loop, this position error enters as a sensor noise.
The camera response is of discrete nature. However it is possible to approximate the response in a continous representation using an average signal during the camera integration time, a sample-and-hold term and an additional short delay introduced due to computing overheads (see Hardy, 1998).
The average signal over an integration time T follows from:

$$e(t) = \frac{1}{T} \int_{t-T}^{t} r(u)\, du$$

The corresponding Laplace transform is:

$$G_T(s) = \frac{1 - e^{-Ts}}{Ts}$$

This term represents the integration time that is necessary to accumulate enough photons from the source. The sample-and-hold term represents the time it takes to read and digitize the full detector array. It can be approximated by a polynomial expansion. Using only the zero-order approximation, as typically done in adaptive optics simulations, leads to a transfer function of (Hardy, 1998; Franklin et al., 1998):

$$G_H(s) = \frac{1 - e^{-Ts}}{s}$$

Short delays τ due to computation overheads can be parameterized as:

$$G_\tau(s) = e^{-\tau s}$$

Thus the acquisition camera response is;

$$G_{acq}(s) = \frac{1 - e^{-Ts}}{Ts} \cdot \frac{1 - e^{-Ts}}{s} \cdot e^{-\tau s}$$

Together with the response of a conventional proportional-integral (PI) controller

$$G_{PI}(s) = K_P + \frac{K_I}{s}$$

and the sensor noise N the slow tip/tilt-rejection transfer function can be modeled. Figure 5.14 shows the corresponding block diagram.

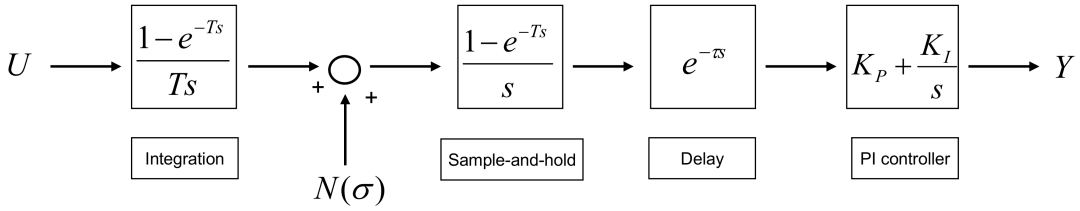

Figure 5.14 Representation of the acquisition camera open-loop response.

5.3.3 Modeling the PSD response

The PSD control-loop consists of the PSD, a high-pass filter to suppress slow signal drifts and a normal proportional-derivative (PD) controller. The diode noise N is taken from the

measurements in Section 5.2.4. The amplifier, the high-pass filter and the PD controller are built in an electronic circuit. The controller electronics board receives as an input the X-Y voltage of the PSD amplifier box. It filters the signal leaving only the high frequency component and provides the correction signal after the PD controller. The box also provides three additional voltage inputs. Two signals are for the X-Y acquisition camera tip/tilt offsets and one for the piston correction signal from the fringe-tracker. The various inputs are added and converted into three output voltages commanding the piezo actuator.
The PSD response can be modeled as a low-pass filter, where the amplifier bandwidth is realized by $f_b = 1/(2\pi\tau_{PSD})$. The high-pass filter with the lower frequency cutoff $f_c = 1/(2\pi\tau_{fi})$ and the PD controller response are standard textbook examples taken from e.g. Franklin et al. (1998). The high-pass filter response is given by:

$$G_{fi}(s) = \frac{\tau_{fi}s}{\tau_{fi}s + 1},$$

while the diode response can be modeled as:

$$G_{PSD}(s) = \frac{1}{(1 + \tau_{PSD})^2}$$

Together with the PD controller response $K_P + K_D s$ and the sensor noise N, the PSD part of the control-loop can be modeled. Figure 5.15 shows the corresponding block diagram.

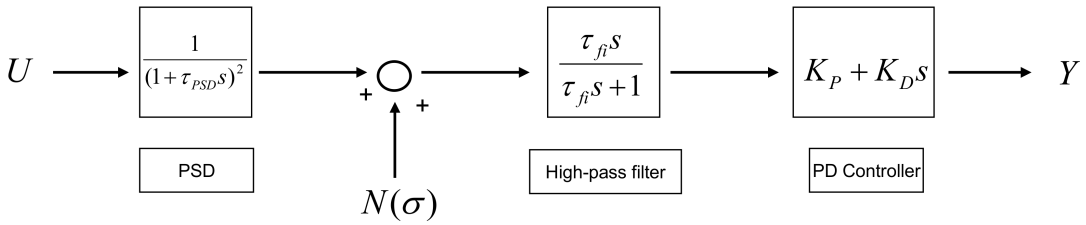

Figure 5.15 Representation of the PSD open-loop response.

Comparison between model and measured transfer function

Given that the acquisition camera was not available at the time of writing, only the PSD branch of the control-loop was verified experimentally. For the test, a collimated laser, injected in the fiber coupler, served as a reference beacon. The transfer function of the PSD, filter and actuator was measured by perturbing the laser beam with white noise and a subsequent recovery of the output power spectral density. In the test setup, the high-pass filter cutoff was tuned to $f_c = 1\,\text{Hz}$. For the modeling, the measured transfer function (Sect. 4.4.2) of the actuator was used as G_{act}. The model transfer function that had to be compared to the measured response was:

$$\frac{R(s)}{E(s)} = \frac{1}{1 + G_{model}}$$

with the open-loop transfer function

$$G_{model}(s) = G_{PSD}G_{fi}G_{PD}G_{act} = \frac{1}{(1+\tau_{PSD})^2} \cdot \frac{\tau_{fi}s}{\tau_{fi}s+1} \cdot G_{act} \cdot (K_p + K_D s)$$

where K_P and K_D are the proportional and derivative gains. In Figure 5.16, the model is compared to the measured closed-loop transfer function. Overall the agreement is very good. The system suppresses disturbance between $\sim$ 1 Hz and 150 Hz at a 10 dB level. Intentionally, low frequency perturbations are not corrected by the system. This will be done by the acquisition camera, as described in Section 5.3.2. The amplification of noise at 600 Hz is the so-called overshoot from the controller. However, it does not degrade the system performance and the closed-loop control remains stable because there is little power in $E(s)$ at a few 100 Hz.

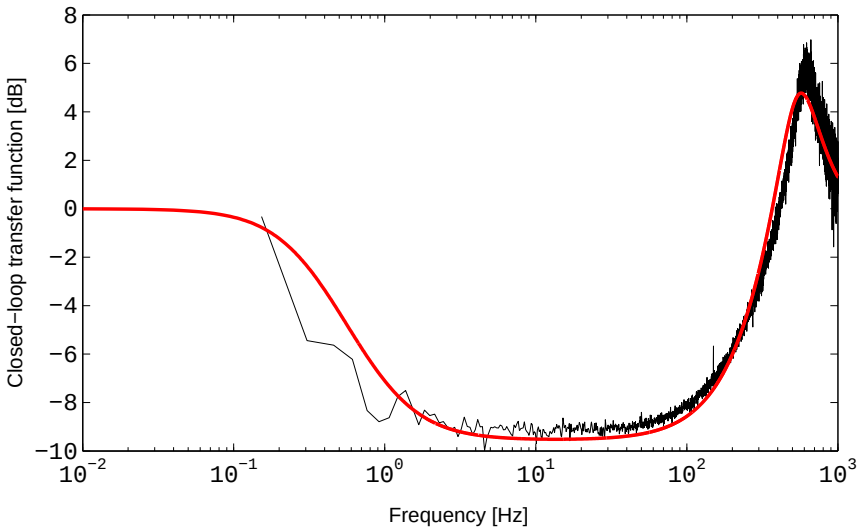

Figure 5.16 Measured transfer-function of the PSD control-loop. The solid red line shows the modeled response of the system. In this setup, the high-pass filter was tuned to a lower frequency cutoff of 1 Hz. The model and the measured response are in very good agreement. The measured curve stops at 0.1 Hz because the duration of the measurement was restricted to $\sim$ 10 s.

5.3.4 System response

While it was possible to measure the PSD part of the control-loop in the lab, the full system had to be modeled with *Matlab*. Using Equation 5.3 together with the model response of

the acquisition camera and the PSD (Section 5.3.2 & 5.3.3) as well as the measured transfer function of the actuator, leads to the system open-loop response:

$$G_{sys,ol}(s) = [\frac{1}{(1+\tau_{PSD})^2} \cdot \frac{\tau_{fi}s}{\tau_{fi}s+1} \cdot G_{PD}(s) + \frac{1-e^{-Ts}}{Ts} \cdot \frac{1-e^{-Ts}}{s} \cdot e^{-\tau s} \cdot G_{PI}(s)] \cdot G_{act} \quad (5.5)$$

and the corresponding closed-loop feedback:

$$\frac{R(s)}{E(s)} = \frac{1}{1+G_{sys,ol}(s)}$$

The following input parameters were used for the model:

- acquisition camera integration time $T = 1\,\mathrm{s}$
- computational delay $\tau = 0.5\,\mathrm{s}$
- bandwidth of PSD amplifier $f_b = 820\,\mathrm{Hz}$
- high-pass filter cutoff $f_c = 0.05\,\mathrm{Hz}$
- acquisition camera sensor noise (open loop) $N_{acq} = 0.5\,\mathrm{mas}$ RMS (Sec. 5.3.2)
- PSD sensor noise (open loop) $N_{PSD} = 2.3\,\mathrm{mas}$ RMS (Sec. 5.2.4)

The integration time was based on the fastest possible full frame read of a HAWAII detector, while the computational delay was estimated. Given the little computational effort consisting of reading a 4 Mpixel frame and determining the image shift by fitting a point source, the delay seems achievable. In fact, the simulation showed that a delay shorter than 0.5 s does not change the system performance significantly. However at delays of 1 s and more the performance degrades notably. Therefore in the future software implementation, the delay length has to be considered. During the fine-tuning of the model it became clear, that the high-pass filter cutoff had to be changed to 0.05 Hz compared to the 1 Hz as used in our lab experiment (Section 5.3.3). The optimum cutoff is directly related to the frame rate of the acquisition camera. In simple terms, the cutoff timescale (20 s) has to be significantly longer than the camera integration time (1 s). If the timescale is not at least a factor 10 greater than the frame rate, the system actually becomes instable for non-zero gains.
Using the input parameters in our model lead to the closed-loop performance shown in Figure 5.17. The modeled system attenuates disturbances between 0.1 Hz and 200 Hz by at least 15 dB. Only around 0.05 Hz, i.e. the filter cutoff, the attenuation is not as good. In this regime, the correction bands of the acquisition camera and the PSD overlap, which leads to a degraded performance.

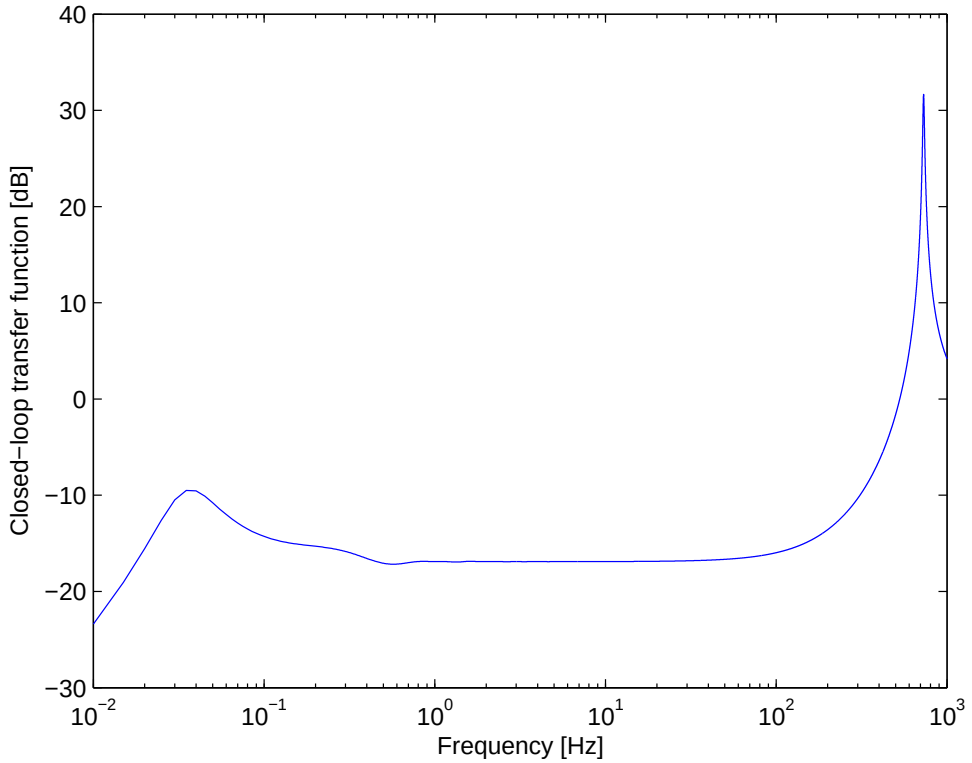

Figure 5.17 Modeled closed-loop transfer function of the tip/tilt guiding system.

5.3.5 Tip/tilt guiding system performance

Applying the system response to the tip/tilt power-spectrum (Sec. 5.2.1) yields the residual tip/tilt after closed-loop correction. The corresponding spectrum is shown in Figure 5.18. Integrating the corrected power-spectrum yields a residual tip/tilt of 7.0 mas RMS. Propagating the acquisition camera and PSD open-loop noise through the corresponding noise transfer functions returns a closed-loop noise of $N_{acq,CL} = 0.8$ mas RMS and $N_{PSD,CL} = 2.7$ mas RMS. The quadratic sum of the noise contributions yields the total closed-loop 1-axis residual tip/tilt of 7.5 mas RMS. Compared to the 38 mas RMS (2-axis: 54 mas) without correction, the guiding system is able to reduce the tip/tilt perturbation in the tunnel by a factor five.
According to the GRAVITY AO simulations performed by Clenet & Gendron (2010), about 10 mas RMS tip/tilt are not corrected by the AO. Thus the guiding system reduces the tunnel tip/tilt to a level, that the AO residuals are limiting the injection efficiency. The quadratic sum of the two contributions is about 12.5 mas RMS in total (2-axis: 17.7 mas RMS). As described in Section 5.2.1, the uncorrected tunnel tip/tilt leads to an injection efficiency of only 50% compared to the lossless injection. Comparing the 2-axis residual

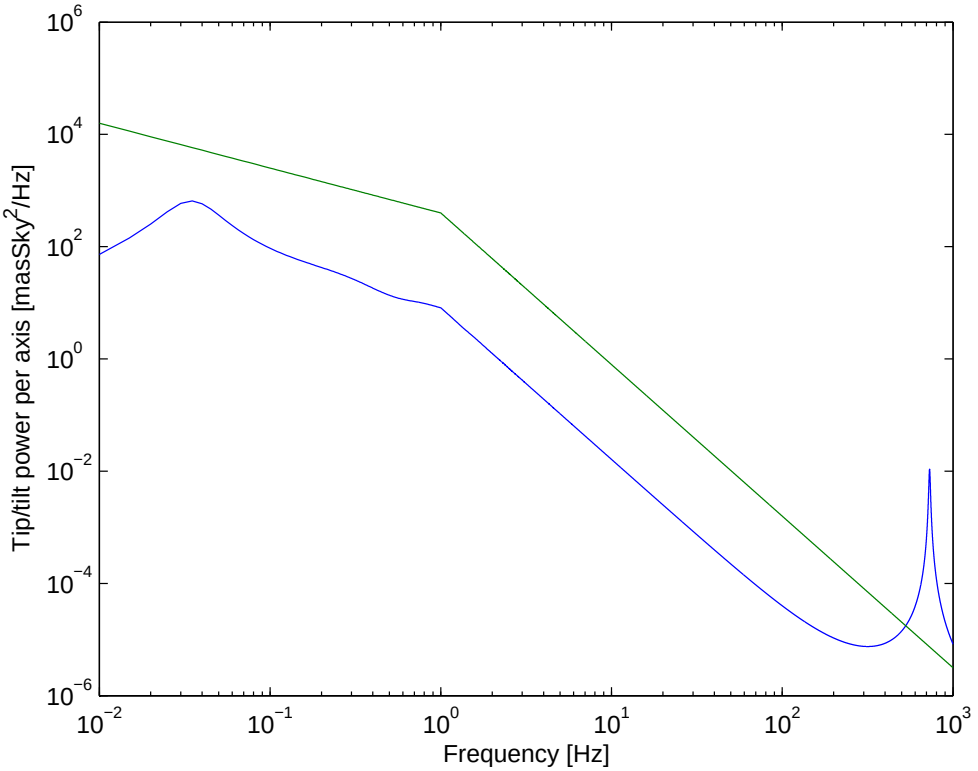

Figure 5.18 Power-spectrum of 1-axis tip/tilt perturbation of the VLTI tunnel without correction (green) and after correction by the guiding system (blue). The integrated disturbance of 38 mas RMS before correction is reduced to 7.0 mas RMS after correction.

tip/tilt with the loss curve in Section 5.2.1, implies that the injection efficiency can be increased to about 85% if the guiding system is used to correct the tunnel atmosphere. The remaining 15% loss originate mainly from the uncorrected AO tip/tilt.

5.4 Pupil guiding system

Given that one major astrometric error source originates from the combination of pupil shift and tilt error, also the pupil has to be actively stabilized. However, the nature of the pupil error is different than the tip/tilt error. While the field jitter is introduced due to the random fluctuations of the tunnel atmosphere, the pupil moves due to mechanical defects and temperature gradients. Changing telescope pointings and delay line positions, lead to pupil wander in the lab. The largest lateral pupil displacement can be attributed to the wobble of the delay line carriage. In fact, the displacement shows a periodicity connected to the circumference of the carriage wheels. Along the optical axis, the longitudinal pupil

position is set by the variable curvature mirror (VCM). Since the delay lines move during an observation, the VCM has to constantly adjust the pupil, to keep it at the nominal position in the VLTI lab. This adjustment is done by changing the curvature of a field mirror according to a blind pointing model. The pointing model limitations and the wobble lead to a pupil wander in the tunnel of up to 4% of the pupil diameter (3 mm shift of the 80 mm beam) in lateral and 1 m in the 80 mm beam in longitudinal direction (Gitton & Puech, 2009). Since the astrometric error formalism (Sec. 2.7) only deals with lateral pupil errors, it is convenient to treat the longitudinal pupil shift as a field dependent lateral pupil position. The fiducial 2″ FoV on sky of the 8 m UT translates into a field angle in the 80 mm beam of $2'' \cdot 8000/80 = 200''$. Therefore the effective lateral pupil error due to 1 m longitudinal pupil shift is $200'' \cdot 1\,\mathrm{m} \approx 1\,\mathrm{mm}$ or an equivalent of 1.3% of the pupil diameter. Thus the error is of the same order as the delay line wobble, and both terms have to be corrected.
Since the astrometric phase error is a product of the residual tip/tilt and pupil errors (Sec. 2.7), the required pupil stability depends on the achievable tip/tilt correction. Based on the estimated residual tip/tilt of 18 mas RMS (Sec. 5.3.5), the residual pupil shift has to be $< 0.5\%$ of the pupil, i.e. $< 40\,\mathrm{mm}$ at M1 to obtain an OPD residual $< 3.5\,\mathrm{nm}$.

5.4.1 Pupil tracking concept

In principle it is possible to track lateral pupil motion, using the telescope pupil, i.e. the image of M2. However initial simulations by Amorim & Eisenhauer (2010), showed that the pupil illuminated by the sky background is too faint to serve as a reference. Integration times of more than 100 s are required to achieve a decent SNR on the pupil image. Since the bandwidth of a control-loop is typically a factor 20 slower than the sensor bandwidth, the resulting loop can only act on timescales of several minutes. Although the pupil drifts in the tunnel are slow, the bandwidth of such a system is not sufficient. Therefore artificial beacons are required for the pupil guiding.
Launching a laser beacon in a pupil plane yields a spot in a pupil viewer. Tracking the spot allows to determine the pupil wander. However, not only the lateral pupil motion but also the axial position has to be monitored. Therefore, the developed pupil tracking concept uses a lenslet array, similar to a Shack-Hartmann wavefront sensor, where the longitudinal pupil error translates into a focus error. The lenslet, placed in the conjugate of the pupil plane (a field plane), provides multiple images of the beacon. In this way, lateral and longitudinal pupil motion can be detected simultaneously. While lateral pupil motion leads to a common shift of the images, longitudinal motion leads to a contraction or expansion of the spot pattern, depending on the direction. The concept is illustrated in Figure 5.19.

5.4.2 Measurement campaign in Paranal

During August 2010, a dedicated measurement campaign for GRAVITY took place at the VLTI in Paranal. Among the goals were:

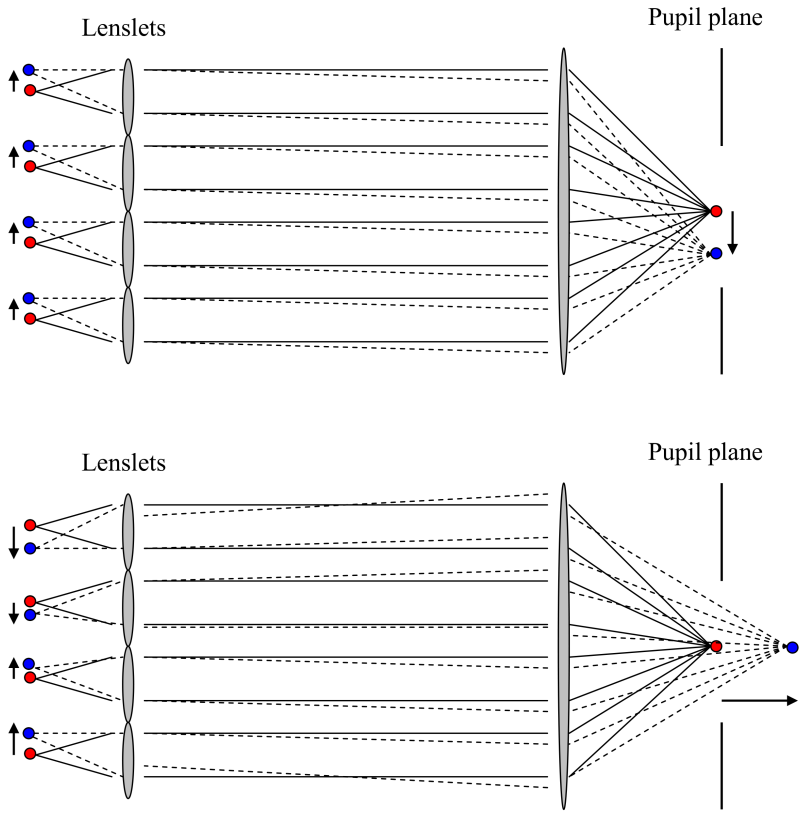

Figure 5.19 Concept of the pupil position detection. A laser beacon is launched above the telescope primary mirror. It is imaged by the VLTI as a spot in the pupil plane. The spot is collimated by the sensor pre-optics and re-imaged by a lenslet array positioned in the collimated beam. While a spot motion perpendicular to the optical axis leads to a common shift of the lenslet spots, a shift along the optical axis leads to a contraction or expansion of the spot pattern. This concept is identical to a Shack-Hartmann sensor, detecting wavefront tilt and defocus. But in this case, it is applied to a pupil image.

- to demonstrate the pupil tracking concept
- to verify that the equivalent of an longitudinal pupil exists at the level required for astrometry. In other words, that the optical quality of the pupil image is sufficient.
- to characterize the lateral and longitudinal pupil motion of the VLTI

For that purpose, a red laser diode was installed at a spider arm of UT4. In the VLTI lab, a commercial Shack-Hartmann Sensor (SHS) from *OPTOCRAFT*, equipped with a 500 mm focal length objective, was used to measure the pupil wander. The nominal FoV of the VLTI of 2″on sky is equivalent to 4.31 mrad in the VLTI lab. Therefore, the relevant field size of the objective was 2.16 mm, corresponding to 14 lenslets with a 0.15 mm pitch

on the SHS. The delivered software package of the SHS expressed the pupil shift in terms of tilt and defocus, that could be easily converted with the objective focal length into the corresponding lateral and longitudinal pupil motion.
The results of the campaign have been compiled in a technical report (Pfuhl, 2011). During the campaign, the pupil motion was measured under various conditions; with moving or static delay lines, at various delay line positions, and with or without telescope motion.
An important result was that it was possible to predict and measure the longitudinal pupil position with a residual error of < 0.04 m RMS and the lateral position with < 0.025 mm RMS (0.03% of the pupil). This showed that the pupil distortions induced by the optical train are small enough that the concept of a pupil holds at the level required for astrometry.
Furthermore, the pupil wander due to the delay line was characterized. Figure 5.20 shows a representative measurement where the delay line was moving at 10 mm/s over a range of 20 m optical path. The conditions represented a normal observation, where the VCM was actively adjusting the pupil position. The lateral position showed the previously reported (Gitton & Puech, 2009) wobble due to the delay line carriage. The peak frequency, visible in Figure 5.20, matches the wheel circumference of the carriage. The amplitude of the lateral variation of ~ 3 mm P-V is consistent with previous measurements.
While the lateral pupil measurement essentially confirmed the values reported by Gitton & Puech (2009), the longitudinal pupil wander had not been characterized before. The measurement revealed that the longitudinal pupil drifted by 0.7 m over 20 m optical path. The drift seems to originate from a mismatch between the VCM adjustment and the actual optical path change that accumulates with covered distance. This clearly shows the limitations of the VCM pointing model, which is supposed to keep the pupil at a constant position. The outliers visible in the measurement are ghosts and not real longitudinal position changes. They originate from contamination of the sensor with stray-light from the delay line metrology.

5.4.3 Pupil laser beacon

The pupil guiding system uses four light sources installed at the telescope spiders. The four light spots are re-imaged within the BC instrument by the acquisition camera pupil tracker (see Lima & Amorim, 2011).
Regarding the wavelength of the laser beacon, several constraints had to be met.

- GRAVITY infrared WFS: The entrance window blocks light at wavelength shorter than 1250 nm
- MACAO visible WFS: The the silicon based detector is sensitive to wavelength shorter than 1100 nm
- The M9 dichroic is designed to transmit light between 450-990 nm and to reflect between 1000-13000 nm.
- Acquisition camera: the pupil guiding wavelength has to be well outside of the acquisition band (1500-1800 nm)

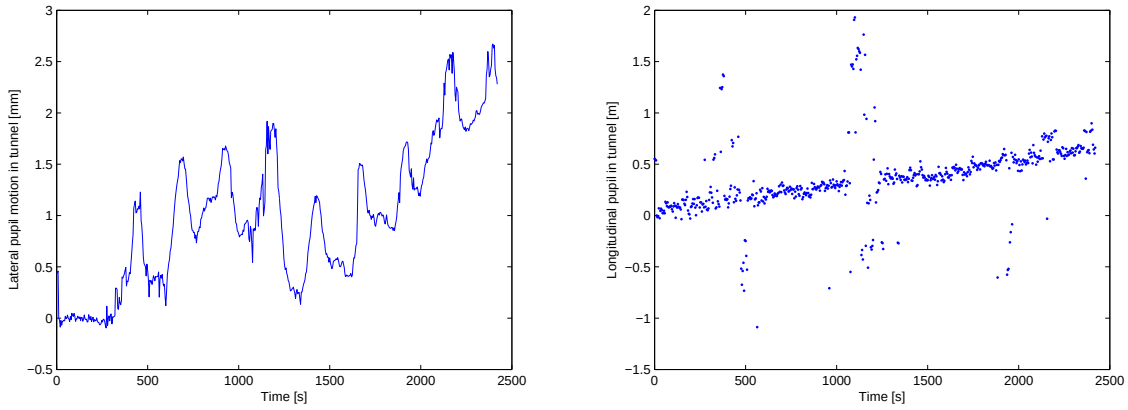

Figure 5.20 Left: measured lateral pupil motion along one axis, while the delay line was moving at 10 mm/s. Each peak reflects a full revolution of the carriage wheel. Right: longitudinal pupil drift over 20 m distance covered by the delay line (optical path). The drift originates from a mismatch between the VCM adjustment model and the actual covered distance.

Taking those constraints into account, the wavelength of choice is 1200 nm. This ensures, that both WFS (infrared and visible) are not affected by the laser and that the laser can be propagated and split in the acquisition camera. Concerning the laser power launched at the telescope, already 1 nW in case of the UTs and 0.05 nW in the case of the ATs is sufficient to provide sufficient SNR on the acquisition camera (Lima & Amorim, 2011). The pupil launcher opto-mechanical design is identical for the UT and the AT case. Only the mount that fixes the launcher box to the telescope spiders is different.
For the laser source, a 5 mW diode from *Frankfurt Laser Company* is coupled into a multi-mode fiber. Using three fiber splitters, the laser is distributed onto four output fibers. All splitters and fiber collimators in use are off-the shelf products with FC connectors. To reduce the laser power from mW to nW, the output fibers are equipped with fiber attenuators. The diode, the coupling optics and the fiber splitters are located in an electronic box to be mounted at the telescope. The box provides four FC connectors to feed the relay fibers that are routed along the telescope spiders up to the launch boxes.
The launch boxes are fixed with metal straps to the telescope spiders at a distance of 0.9 m (UT) and 0.2 m (AT) from the center of M2. Each individual box is made from aluminum with an outer dimension of $110 \times 73 \times 38\,\mathrm{mm}^3$. The box provides a FC connector for the laser relay fiber. Within the box a short fiber connects the FC connector with another fiber collimator. The pointing of the box can be adjusted with micro-meter screws. The position of the fiber collimator, i.e. the pupil point source can be fine tuned by moving the front plate holding the collimator along a modular grid. This allows positioning the collimator at a mm level with respect to M2. The design of the launch box and the location of the beacons are shown in Figure 5.21.

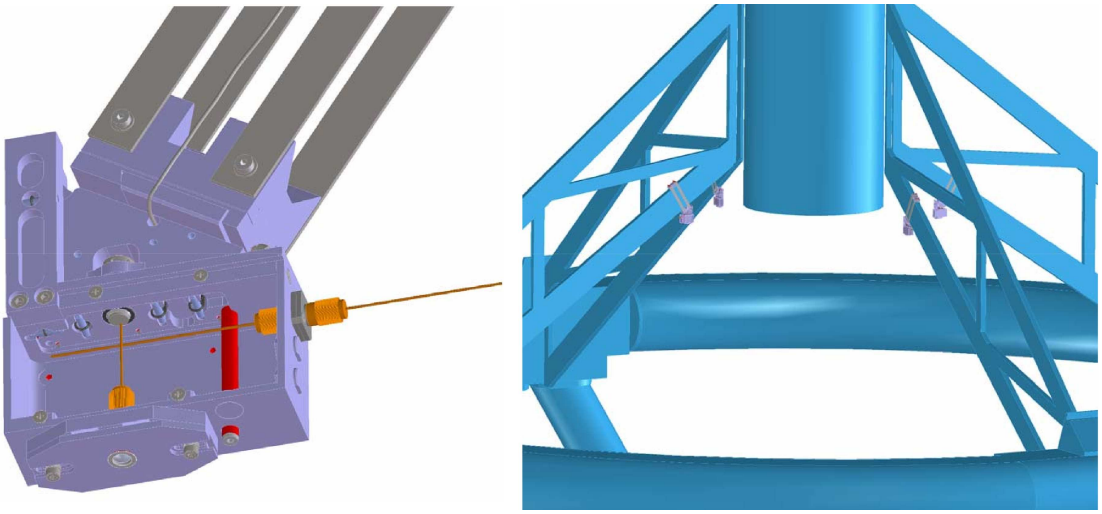

Figure 5.21 CAD drawing of one laser beacon launcher (left). Each telescope is equipped with four beacons, mounted on the spiders holding M2 (right). All four launchers are fed by a common laser diode via multi-mode fibers.

5.4.4 Pupil tracker

The pupil tracker of the acquisition camera provides the feedback for the pupil stabilization loop. The optical and mechanical development of the acquisition camera is the work-package of the University of Lisbon and not a part of this thesis. However, since the pupil tracker is the sensor for the pupil guiding system, its working principle and design is briefly described here. For a more detailed description of the unit, we refer to Lima & Amorim (2011).

Following the concept introduced in Section 5.4.1, the collimated laser is imaged on the detector by a 2×2 lenslet array, providing multiple pupil images. Given that the pupil rotates during an observation and that the center of the pupil can not be equipped with a beacon (occupied by M2), four beacons symmetric around M2 are used. By using the barycenter of the beacons, the pupil motion can be measured without being affected by pupil rotation. Therefore, instead of imaging only one beacon, four beacons are imaged per lenslet (see Figure 5.22). Similar to Section 5.4.1 a lateral pupil shift can be inferred from a common lateral shift of all four barycenters, while a longitudinal shift can be deduced from the barycenter distance across the pupil images.

Regarding the optical parameters, the FoV of each lenslet covers the inner 3.4 m of M1 (UT) with a pixel scale corresponding to 6 cm/pixel. Lima & Amorim (2011) simulated the performance of the pupil tracker in terms of position resolution. Using a diffraction model and taking into account detector characteristics such as measured detector noise, bad-pixel maps and flat fields, they found that the lateral pupil position can be retrieved with a residual error of 0.3 mm RMS at M1. The residual longitudinal pupil error corresponds to 12 mm RMS in the 80 mm tunnel.

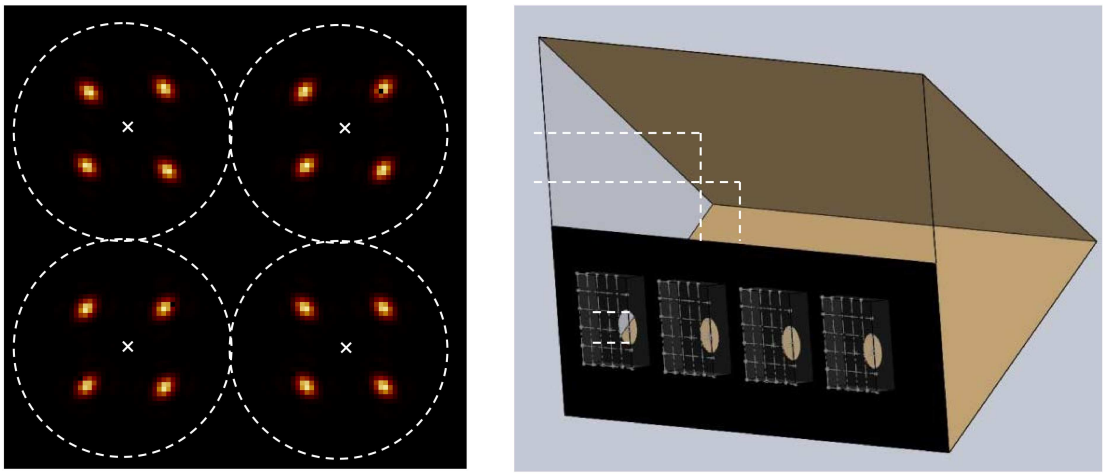

Figure 5.22 Left: Simulated detector image of the pupil tracker mode. Four lenslets (dashed circle) image the four laser beacons on the detector. The barycenter of the beacons (cross) is used to compute the lateral and longitudinal pupil shift. Right: CAD drawing of the lenslet array mounted in the acquisition camera. A prism with gold coated surfaces folds the beams coming from the four telescopes. The four output beams are imaged by lenslet arrays that are glued onto the prism (taken from Lima & Amorim, 2011).

5.4.5 Pupil control-loop

The lateral and longitudinal pupil control-loops are conceptually identical. Both use the pupil tracker of the acquisition camera as a sensor, implying that both loops use the same frame rate. The controller is in both cases a proportional-integral controller. However the actuators are different. The lateral pupil is corrected by a piezo in the fiber coupler, while the longitudinal pupil position is adjusted by the VCM of the delay line. The control-loop block diagram is shown in Figure 5.23 As described in Section 5.3.2, the acquisition camera response can be described as:

$$G_{acq}(s) = \frac{1 - e^{-Ts}}{Ts} \cdot \frac{1 - e^{-Ts}}{s} \cdot e^{-\tau s}$$

where T is the integration time and τ is the computational delay. The PI controller is described as:

$$G_{PI}(s) = K_P + \frac{K_I}{s}$$

with the integrator and proportional gain K_P and K_I. The corresponding closed-loop response of the system is then:

$$G_{sys,cl}(s) = \frac{1}{1 + G_{acq} \cdot G_{PI} \cdot G_{act}}$$

The response G_{act} of the piezo actuator was measured with its internal strain-gauge sensors. The response is similar to the transfer function shown in Figure 4.17, however with a

bandwidth of only 30 Hz. Since the response of the VCM has not been published, its response had to be estimated. Based on private communication, the VCM fully inflates on a timescale of a few seconds. Therefore we assumed a response similar to the piezo actuator, yet with a 3 dB bandwidth of only 1 s. To obtain the system response of the pupil control, only the input parameters had to be adjusted:

- acquisition camera integration time $T = 1\,\mathrm{s}$
- computational delay $\tau = 0.5\,\mathrm{s}$
- acquisition camera lateral position noise (open-loop) $N_{acq,lat} = 0.3\,\mathrm{mm}$ at M1 (Sec. 5.4.4)
- acquisition camera longitudinal position noise (open-loop) $N_{acq,long} = 12\,\mathrm{mm}$ in tunnel

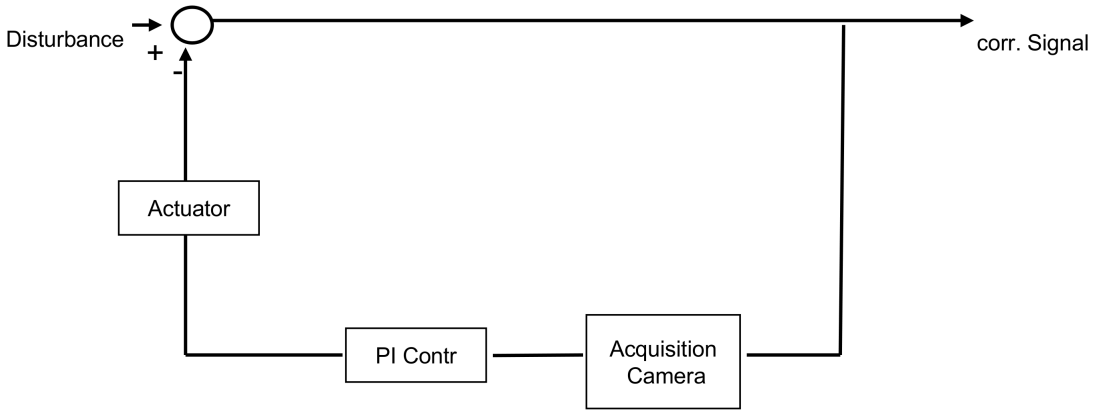

Figure 5.23 Block diagram of the pupil control-loop. The sensor is the pupil tracker of the acquisition camera, while the actuator is the piezo in the fiber coupler in case of lateral motion and the VCM in case of longitudinal motion.

The resulting transfer functions of the lateral and longitudinal pupil guiding are shown in Figure 5.24. Limited by the sensor and the VCM response, the pupil guiding can only act on timescales of a few seconds. However, the bandwidth is sufficient to cope with the slow pupil motions in the VLTI.

5.4.6 Pupil guiding performance

Given that we actually measured a pupil motion time-series of the VLTI (Section 5.4.2), we were able to apply the simulated transfer functions to the data. Since the data covers delay line motion over 20 m of optical path at a speed of 10 mm/s, this series represents the extreme case of a very long observation with quickly changing optical path. Therefore it is well suited to estimate the system performance. The simulated residual motion is shown in Figure 5.25. After closed-loop correction the residual lateral pupil jitter is $< 0.07\,\mathrm{mm}$ RMS

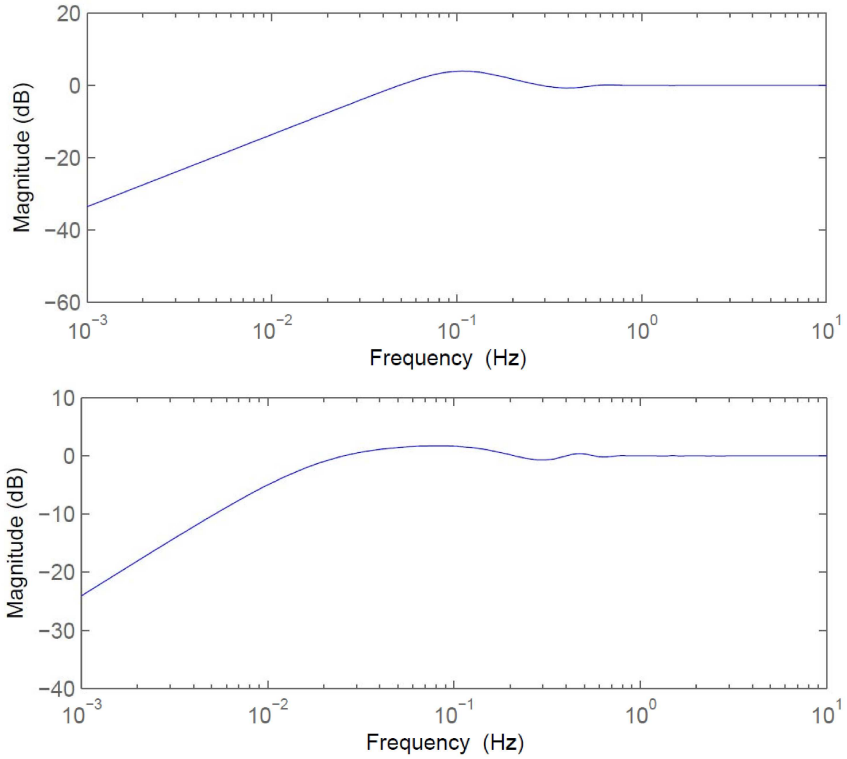

Figure 5.24 Pupil guiding system transfer functions. Top: lateral pupil guiding transfer function. Bottom: longitudinal pupil guiding transfer function.

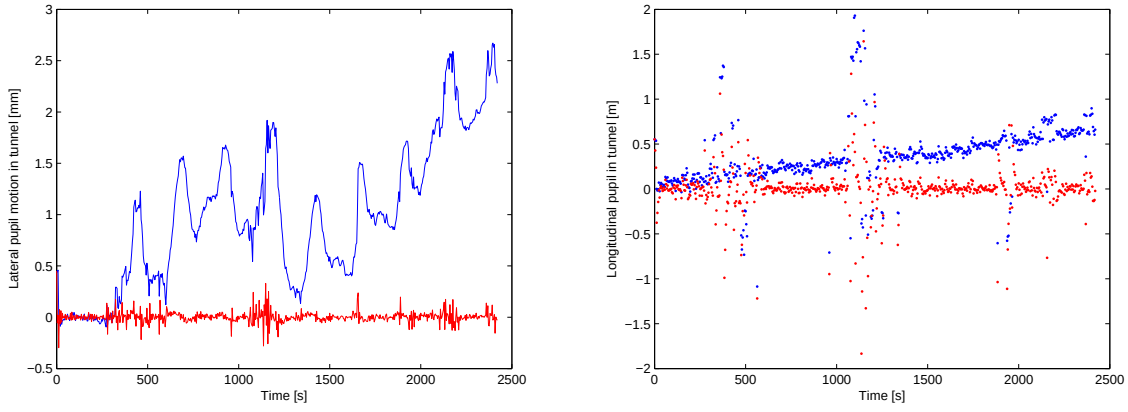

Figure 5.25 Left: Measured lateral pupil motion (blue) and the simulated residual motion after closed-loop correction (red). Right: Measured longitudinal pupil motion (blue) and simulated residual motion after correction (red).

(tunnel). This corresponds to $< 0.1\%$ pupil diameter. The longitudinal pupil correction leaves a residual jitter of $< 0.1\,\mathrm{m}$ RMS in the tunnel. This corresponds to a lateral pupil shift over $2''$ FoV of $< 0.13\%$ pupil diameter. In other words, the pupil guiding system reduces the lateral pupil motion by a factor 40 and the longitudinal motion by a factor 10. The resulting pupil error terms relevant for the astrometric error are of the same magnitude. Overall the system fulfills the goal of a residual lateral pupil motion $< 0.5\%$.

5.4.7 Importance of the guiding system for astrometry

The combination of uncorrected pupil- and tip/tilt error introduces a significant astrometric error. As described in Section 2.7, the $\approx 50\,\mathrm{mas}$ RMS (2-axis UT) tip/tilt jitter together with the typical lateral pupil wander of 4% (equal to 32 cm at the UT M1) lead to an OPD error of $\approx 78\,\mathrm{nm}$. This corresponds to an astrometric error of $160\,\mu\mathrm{as}$ on a 100 m baseline, which exceeds the astrometric goal of $10\,\mu\mathrm{as}$ by a factor 16.
The guiding system will reduce the tip/tilt jitter to $\approx 18\,\mathrm{mas}$ RMS (Sec. 5.3.5) and the pupil wander to $\sim 0.1\%$, i.e. 8 mm at M1 (Sec. 5.4.6). The resulting OPD error is reduced to $\approx 0.7\,\mathrm{nm}$ or an equivalent astrometric error of $\approx 1.4\,\mu\mathrm{as}$. In this regime, astrometry is limited by other error sources such as the atmosphere (Sec. 2.1).

Chapter 6

The star formation history of the Milky Way's Nuclear Star Cluster

This chapter is a reprint of the publication Pfuhl et al. 2011, ApJ, 741, 108.

6.1 Introduction

The Milky Way nuclear star cluster (NSC) is of special interest since it is the closest galactic nucleus. It offers the unique possibility to resolve the stellar population and to study the composition and dynamics close to a central black hole at an unrivaled level of detail. The ability to resolve individual stars together with continuous monitoring of the innermost stars has proven the existence of a $4.3 \times 10^6 M_\odot$ supermassive black hole (SMBH) (Eisenhauer et al., 2005a; Ghez et al., 2008; Gillessen et al., 2009) beyond any reasonable doubt. Surveys of galaxies have found scaling relations between the bulge mass and the mass of the central massive object of a galaxy (Ferrarese et al., 2006). This massive object can be either a NSC or a SMBH, depending on the bulge mass. SMBHs are typically found in massive bulges, while NSCs are common in low mass bulges. This indicates a mutual evolution of the bulge, the SMBH and the NSC. The Milky Way with its Bulge mass of $10^{10}\,M_\odot$ falls right in the transition region from galaxies, which are NSC dominated to galaxies, which are SMBH dominated (Graham & Spitler, 2009). For a critical discussion we refer to Seth et al. (2008, 2010). With a radius of 5 pc and a mass of $2 - 3 \times 10^7\,M_\odot$ (Launhardt et al., 2002), the Milky Way NSC is typical. This lucky coincidence makes the Milky Way's NSC an ideal test case for nuclear co-evolution of galaxies in general. The evolution of a galactic bulge and the central massive object (NSC or SMBH) as well as the physical reason for the scaling relation is however poorly understood. When does a NSC form? Does it evolve simultaneously with the bulge or from a preexisting bulge? How does the SMBH influence the star formation mode? In fact, the age of a NSCs is the largest uncertainty in the determination of its mass (Ferrarese et al., 2006). Deriving the star-formation history from integrated quantities as obtained from distant galaxies is highly model dependent and is especially uncertain for old ages. These limitations can be

overcome in the GC because the stellar populations can be resolved.
Numerous papers have studied the composition of the Milky Way's NSC. These studies have found that the stellar population can be divided into two classes. The cool and evolved giant stars and the hot and young main sequence/post-main sequence stars. The existence of massive young stars is evidence for very recent star formation (Forrest et al., 1987; Allen et al., 1990). The most massive stars (WR/O stars) reside in a fairly complex structure, which may be described as a combination of a prominent warped disk, a second disk-like structure highly inclined relative to the main disk, and a more isotropic component (Paumard et al., 2006; Lu et al., 2009; Bartko et al., 2009) at a projected distance of 0.8-12″ from the SMBH Sgr A* (1″ ≡ 0.04 pc, assuming a GC distance of 8.3 kpc). The GC disk features must have formed in a rapid star burst ∼ 6 Myrs ago (Paumard et al., 2006; Bartko et al., 2010b), with a highly unusual initial mass function (IMF) that favored the formation of massive stars ($dN/dm \sim m^{\alpha}$; $\alpha = -0.45$). This extreme IMF deviates significantly from the standard Chabrier/Kroupa IMF with a powerlaw slope of $\alpha = -2.3$ (Kroupa, 2001; Chabrier, 2003) and seems to exist only in the vicinity of the SMBH. A less massive population of ordinary B-stars can be found in the innermost 1″, the so called S-stars (Eisenhauer et al., 2005a; Ghez et al., 2008; Gillessen et al., 2009). The origin of the S-stars is a mystery, because the in-situ formation in the vicinity of the super massive black hole (SMBH) is very improbable. Yet, the K-band luminosity function (KLF) of the S-stars is consistent with a canonical Chabrier/Kroupa IMF. The largest population of the resolved stars however, are giants with masses between 1 and 2 $M_{\odot}$. Previous kinematic studies of this population have shown that the cluster dynamics are consistent with a relaxed system, slowly rotating in the plane of the galaxy (Trippe et al., 2008; Schödel et al., 2009). Detailed abundance determinations of luminous cool giants (Carr et al., 2000; Ramírez et al., 2000; Cunha et al., 2007) found a metallicity distribution peaking at [Fe/H] = 0.14 ± 0.16, close to the solar value.
The giant population is well suited for observations in the K-band. The giants have typical temperatures between 5100 and 2800 K. In this temperature range, the CO bandheads at $2.29 - 2.38\,\mu$m are the most prominent spectral lines in the K-band. The equivalent widths of these lines correlates with temperature (Kleinmann & Hall, 1986; Wallace & Hinkle, 1996; Förster Schreiber, 2000). This allows the determination of individual temperatures for the red giants (RG). Together with photometric data for the luminosities it is thus possible to construct a Hertzsprung-Russell (H-R) diagram of the GC population and thus to constrain the star formation history in the immediate vicinity of the SMBH. Detailed studies of the giant population of the Galactic Center have been performed previously by Blum et al. (2003) and Maness et al. (2007). Using a magnitude limited sample of 79 AGB and supergiant stars (50% complete at $m_K < 10$) within the central 5 pc, Blum et al. (2003) found a variable SFR. They claimed that roughly 75% of the stars are older than 5 Gyrs. An intermediate period of low star formation was followed by a recent (< 100 Myrs) period of increased star formation. Maness et al. (2007) used 329 giant stars ($m_K < 15.5$), more than 5 magnitudes deeper than Blum et al. (2003), albeit at the cost of covering only 12% of the total area in the central 1 pc. They found that the giant population is relatively warm, i.e young. Consequently they favored models with either a top-heavy IMF and a

constant star formation rate, or with a canonical IMF and an increasing star formation rate during the last few Gyrs. The top-heavy IMF scenario was recently challenged by Löckmann et al. (2010) who argued that this would predict an overabundance of stellar remnants resulting in a mass-to-light ratio larger than observed.
The predicted density profile of a relaxed stellar system in the vicinity of a SMBH is a cusp with a radial density profile of $n \sim r^{-\gamma}$, $\gamma \approx 7/4$ (Bahcall-Wolf cusp). Strictly speaking, this is only true for a single stellar mass cusp. In multiple mass configurations, γ can range from 1/2 to 11/4. Recent observations have shown that the projected radial distribution of the giant population is actually flat at small radii from Sgr A* (Do et al., 2009; Buchholz et al., 2009; Bartko et al., 2010b). There may even be a central hole in the 3D distribution of late type stars (Buchholz et al., 2009; Schödel et al., 2009). In either case, the visible distribution seems quite inconsistent with a Bahcall-Wolf cusp. It is possible that a hidden Bahcall-Wolf cusp is present consisting of stellar remnants or unresolved main-sequence stars. However, this would require the stellar luminosity function to change in the few innermost arcseconds. The bright stars need to be removed by mechanisms acting preferentially close to the SMBH. Collisional stripping of stellar envelopes (Genzel et al., 1996; Alexander, 1999) is such a mechanism that keeps stars from reaching their peak luminosity. Tidal stripping close to the SMBH can deplete the giants in a similar way (Davies et al., 2006). Another explanation might be a top-heavy or truncated IMF (Nayakshin & Sunyaev, 2005) that produces preferentially massive stars as observed in the young disks. Massive stars quickly become stellar remnants compared to evolved low mass stars that dominate the KLF. Merritt (2009) argues that the absence of a Bahcall-Wolf cusp can be naturally explained if the stellar population is not relaxed. They find that the relaxation time scale in the innermost parsec is greater than $5 - 10$ Gyrs. The most important question to discriminate between depletion processes and a relaxation time effect is therefore, whether the system is old enough to be relaxed.

The chapter is organized as follows; In section 6.2 we present the data and in section 6.3 the spectral classification and calibration of spectral indices. In section 6.4 we construct the H-R diagram that is then fit with model populations in section 6.5. The star formation history, IMF and mass composition of the nuclear cluster is presented in section 6.6. The results are discussed and compared with other works in section 6.7. We conclude in section 7.2.

6.2 Observations and data processing

This work relies on spectroscopic and imaging data obtained at the VLT in Cerro Paranal Chile between 2003 and 2010. The observations were carried out under the program-ids 075.B-0547, 076.B-0259, 077.B-0503, 179.B-0261 and 183.B-0100.

6.2.1 Imaging and photometry

The photometric data were obtained with the adaptive optics camera NACO (Rousset et al., 2003; Hartung et al., 2003). The photometric reference images were taken on the 29th of April 2006 and on the 31st of March 2010. We used the H- and K'-band filter together with a pixel scale of 27 mas/pixel. To each image we applied sky-subtraction, bad-pixel and flat-field correction (Trippe et al., 2008). All images of good quality obtained during the same night were then combined to a mosaic with a FoV of $40 \times 40''$.

Diffuse background

In terms of mass, the resolved stellar population represents only the tip of the iceberg. The bulk of the stellar mass is unresolved. Therefore the diffuse background emission of the GC contains valuable information on the cluster composition and its formation. Naturally it is very challenging to estimate the unresolved background in a crowded stellar field. A significant fraction of the background light originates from the uncorrected seeing halos of bright stars. Furthermore, anisoplanatism complicates precise photometry across the Field of View (FoV) when using AO. By using multiple point spread function (PSF) photometry on NACO images Schödel (2010) tried to overcome these limitations. The resulting photometry for resolved stars was published in Schödel et al. (2010) and a map containing the unresolved background flux was published in Schödel (2010). We used H-band data from both publications to derive the fraction of light contained in the diffuse background. The H-band has the advantage that it is least affected by the surrounding nebular emission.
Since no completeness map was published by Schödel (2010), we used a superb H-band mosaic with Strehl > 20% from the 31st of March 2010. We applied StarFinder (Diolaiti et al., 2000) and converted our detections in magnitudes by referencing them to Table A2 of Schödel et al. (2010). To derive the completeness, we applied a common technique of creating and re-detecting artificial stars of various brightness. As a limiting magnitude, separating diffuse background from resolved sources, we used $m_{H,\mathrm{cut}} = 19.45 \pm 0.12$. The magnitude was chosen such that the total uncorrected flux of all detected stars is equal to the completeness corrected flux of stars brighter than the magnitude cut. Using an extinction of $A_H = 4.65 \pm 0.12$ (Fritz et al., 2011) and a GC distance of $R_0 = 8.3 \pm 0.35\,\mathrm{kpc}$ (Ghez et al., 2008; Gillessen et al., 2009) we obtained an absolute separating magnitude of $M_{H,\mathrm{cut}} = 0.27 \pm 0.34$. The error estimate accounts for the absolute photometric uncertainty, the cut-off, extinction and distance uncertainties. We then subtracted the difference between the stellar flux (up to the limiting magnitude) in our H-band image and the stellar flux in the Schödel et al. (2010) list from the diffuse background flux. Furthermore, we subtracted the known early-type stars since they dominate the light in the inner $10''$.
We find that the diffuse background ($m_H > 19.45 \pm 0.12$) contains $H_{\mathrm{diff}}/H = 27 \pm 9\%$ of the total (diffuse + resolved) H-band flux. The $1\,\sigma$ error contains the variation across the field (6%) and the uncertainty due to the cutoff between diffuse and resolved light $M_{H,\mathrm{cut}}$ (2%). Taking into account the completeness, we added another 3% systematic error due to undetected early-type stars.

Mass-to-light ratio

To derive the total H-band luminosity of the inner 1.2 pc, we used the resolved and unresolved stellar H-band flux stated in Schödel et al. (2010); Schödel (2010). To account for the spatially varying extinction of the GC, we used their published extinction map. Unfortunately the extinction map is only available for K-band. Therefore we scaled the map to an average H-band extinction of $A_H = 4.65$ (Fritz et al., 2011). Correcting for extinction and taking the distance into account, we obtained a luminosity of $H = 4.51 \pm 0.54 \times 10^6\, L_{H,\odot}$ enclosed within a projected radius of $r_{2D} < 1.2\,\mathrm{pc}$. From this we subtracted the contribution of known early-type stars ($0.64 \times 10^6\, L_{H,\odot}$). While the young stars are known to be close in 3D to the center, only $50 \pm 5\%$ of the old stars at a projected distance of $r_{2D} < 1.2\,\mathrm{pc}$ are also contained within a 3D distance of 1.2 pc (assuming the radial density profile of Schödel et al.2007). Applying both corrections we find a total luminosity of $H(R < 1.2\,\mathrm{pc}) = 1.94 \pm 0.33 \times 10^6\, L_{\odot,H}$. Of this value $0.52 \pm 0.2 \times 10^6\, L_{\odot,H}$ can be attributed to the diffuse background. The dynamical mass enclosed (excluding the SMBH) is $M(R < 1.2\,\mathrm{pc}) = 1.4 \pm 0.7 \times 10^6\, M_\odot$ (Genzel et al., 2010). Thus we derive a total mass-to-light ratio of $M/H = 0.7 \pm 0.4\, M_\odot/L_{\odot,H}$ and a diffuse mass-to-light ratio of $M/H_{\mathrm{diff}} = 2.6 \pm 1.7\, M_\odot/L_{\odot,H}$.
By assuming an average intrinsic colour of $m_{H-K} = 0.2$ we can convert the total H-band luminosity into a K-band luminosity of $K(R < 1.2\,\mathrm{pc}) = 3.0 \pm 0.44 \times 10^6\, L_{\odot,K}$. The corresponding mass-to-light ratio is $M/K = 0.5 \pm 0.3\, M_\odot/L_{\odot,K}$. The mass-to-diffuse-light ratio is $M/K_{\mathrm{diff}} = 1.9 \pm 1.2\, M_\odot/L_{\odot,K}$. The bolometric mass-to-light ratio is $M/L_{\mathrm{bol}} = 0.7 \pm 0.4\, M_\odot/L_{\odot,\mathrm{bol}}$.

6.2.2 Spectroscopy

Our spectroscopic data were obtained with the adaptive optics assisted integral field spectrograph SINFONI (Eisenhauer et al., 2003; Bonnet et al., 2004). We used all high quality SINFONI data sets available to us, and taken between 2003 and 2010. In total we used 32 fields with pixel scales between 25 and 100 mas. The data output of SINFONI consists of cubes with two spatial axes and one spectral axis. Depending on the plate scale, an individual cube covers $0.8'' \times 0.8''$ or $3.2'' \times 3.2''$; the spectral resolution varies between 2000 and 4000 depending on the chosen bandpass and the field of view. Roughly 70% of the stars used in this work were observed at a resolution of $R \sim 2000$. We used the data reduction SPRED (Schreiber et al., 2004; Abuter et al., 2006), including bad-pixel correction, flat-fielding and sky subtraction. The wavelength scale was calibrated with emission line gas lamps and fine-tuned on the atmospheric OH lines. Finally we removed the atmospheric absorption features by dividing the spectra through a telluric spectrum obtained in the respective night.

Deep spectroscopy of the GC

Very good seeing conditions and long integration times on two SINFONI fields allowed us to perform the deepest census of the GC population so far. The two fields cover roughly 18 square arcseconds and are $\sim 50\%$ complete down to $m_K < 18$. The location of the fields can be seen in Fig. 6.1. Both fields were placed in regions with low extinction and without bright stars in the vicinity. One of the fields (East), at a distance of $7.4''$, probes the disk region. The second field (North) is located at the outer rim of the disks at $13.5''$. The richness of faint stars can be seen in Fig. 6.1. The identification of a $m_K < 17$ star as late-type requires only two hours of integration on source. The prominent CO bandheads are easy to identify and the multiplicity of the lines helps to rule out misidentifications in noisy spectra. However, the identification of an early-type star is much more challenging. The early-type stars are identified by the hydrogen Brγ line. Unfortunately the line is less prominent than the CO bandheads. The identification is further hindered by the surrounding nebular Brγ emission. This emission is patchy and varies significantly in intensity and velocity on scales of $1''$. Depending on the location of the star, this can lead to a wrong background subtraction during the data analysis mocking a stellar line. Because the stellar absorption line in A-stars is a broad Lorentzian, it is clearly different from the narrow Gaussian emission line of the gaseous background. Thus in case of sufficient SNR an identification is possible. To achieve a sufficient signal-to-noise ratio (SNR) an integration time of about five hours on source is required to identify an early-type star as such with $m_K < 18$.

6.2.3 Source selection

The selection of stars used in the H-R diagram fitting is based on a master list of $\sim$ 6000 stars at projected radii between $0.1'' < r < 25''$ (or 4×10^{-3} to 1 pc), for which Trippe et al. (2008) derived proper motions as well as K-band photometry. The list consists of well isolated stars identified on several images without overlapping neighbors (separation > 130 mas). For our final analysis we retained only those entries in the master list that also had an unambiguous identification in a corresponding SINFONI cube. In total we collected ~ 1300 spectra. After removing duplicates (due to overlapping fields), roughly 1000 spectra remained. Out of this sample we used only stars with a SNR > 10 and a CO index EW(CO) > 3.5 (i.e. no early-type stars). The SNR was measured in the continuum bands stated in Table 6.1. This left us with about 800 giants for which we were able to determine individual temperatures and velocities. In order to have a homogeneous and deep sample, we used in the H-R diagram fit only stars contained in fields with a completeness $> 50\%$ at $m_K = 15$ (see next section). The remaining sample consisted of 450 stars with magnitudes between $0.5 < M_K < -8$. The contribution of fore- and background stars is negligible in the GC. The contamination due to stars which are not members of the cluster is of the order 1% (Buchholz et al., 2009).

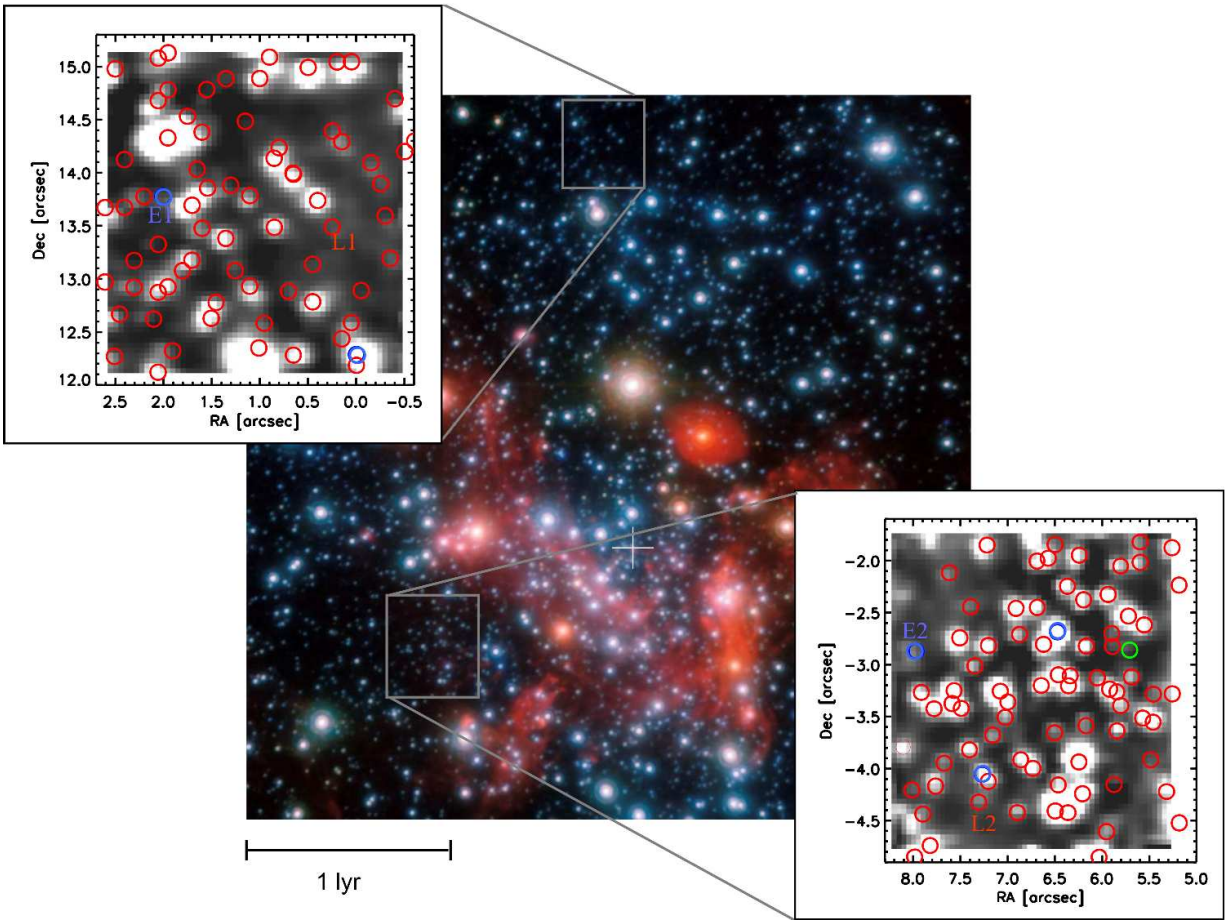

Figure 6.1 Three-color image of the innermost 1 pc of the Milky Way (K-band: blue; L-band: red). The white cross indicates the position of Sgr A*. The U-shaped nebular emission visible in the L-band, the so called Mini-Spiral, is powered by the ionizing radiation of the young O/WR stars in the vicinity. The position of the two deep spectroscopic fields is indicated. All photometrically detected stars not confused with neighboring stars are indicated by open circles. The color coding resembles the stellar type. Cold giants with confirmed CO bandheads are indicated in red. Hot main sequence stars identified by Brγ absorption are indicated in blue. Green stars are not identified.

Table 6.1 Equivalent width measurement intervals

Feature	Wavelengths (μm)
^{12}CO(2, 0) band	2.2910-2.3020
^{12}CO(2, 0) continuum I	2.2300-2.2370
^{12}CO(2, 0) continuum II	2.2420-2.2580
^{12}CO(2, 0) continuum III	2.2680-2.2790
^{12}CO(2, 0) continuum IV	2.2840-2.2910

6.2.4 Detection probability

The spectroscopic fields used in this work differ in spatial resolution, covered area and integration time. The main limitation for spectroscopy in the GC is stellar crowding. This is why we probed most of the inner 1 pc with the small scale (100, 25 mas) AO-assisted modes of SINFONI. For these observations, we used typically one hour of integration time on source. Two additional cubes (100 mas) are exceptionally deep with integration times of 4.5 and 7.8 hours on source. The spectroscopic completeness of these cubes is $> 50\%$ at $m_K < 18$. The results of the deep observations are discussed in Sec. 6.3.1. The spectroscopic completeness was determined by comparing the total number of stars contained in the master list, with the number of stars for which we could extract spectra. The photometric completeness of the images was determined as described in Sec. 6.2.1. All observed fields and the combined completeness (for $m_K = 15$) are shown in Fig. 6.2. Fields with a high completeness of up to 80% are found at several arcsecond distance from Sgr A*. Further in, the completeness degrades due to stellar crowding. Only the inner one arcsecond is sampled with the smallest pixel scale (25 mas) and reaches a completeness of about 50%.

6.3 Spectral classification

The K-band provides two prominent spectral features allowing a spectral classification. Early-type stars (T > 5000 K) can be identified by the presence of a Brγ absorption line. Late-type stars (T < 5000 K) on the other hand show weak or no Brγ absorption but strong absorption line blends known as CO bandheads. The bandheads appear at the spectral type $\sim$ G4 and increase in strength up to M7. The strength also increases with luminosity class from dwarfs to giants and to supergiants. Yet, for this work only giants are of interest. Main sequence stars with spectral type G4 and cooler are fainter ($m_K > 20$) than the detection limit. Supergiants of the same spectral type on the other hand are extremely bright ($m_K < 9$) and easy to identify (Blum et al., 2003).

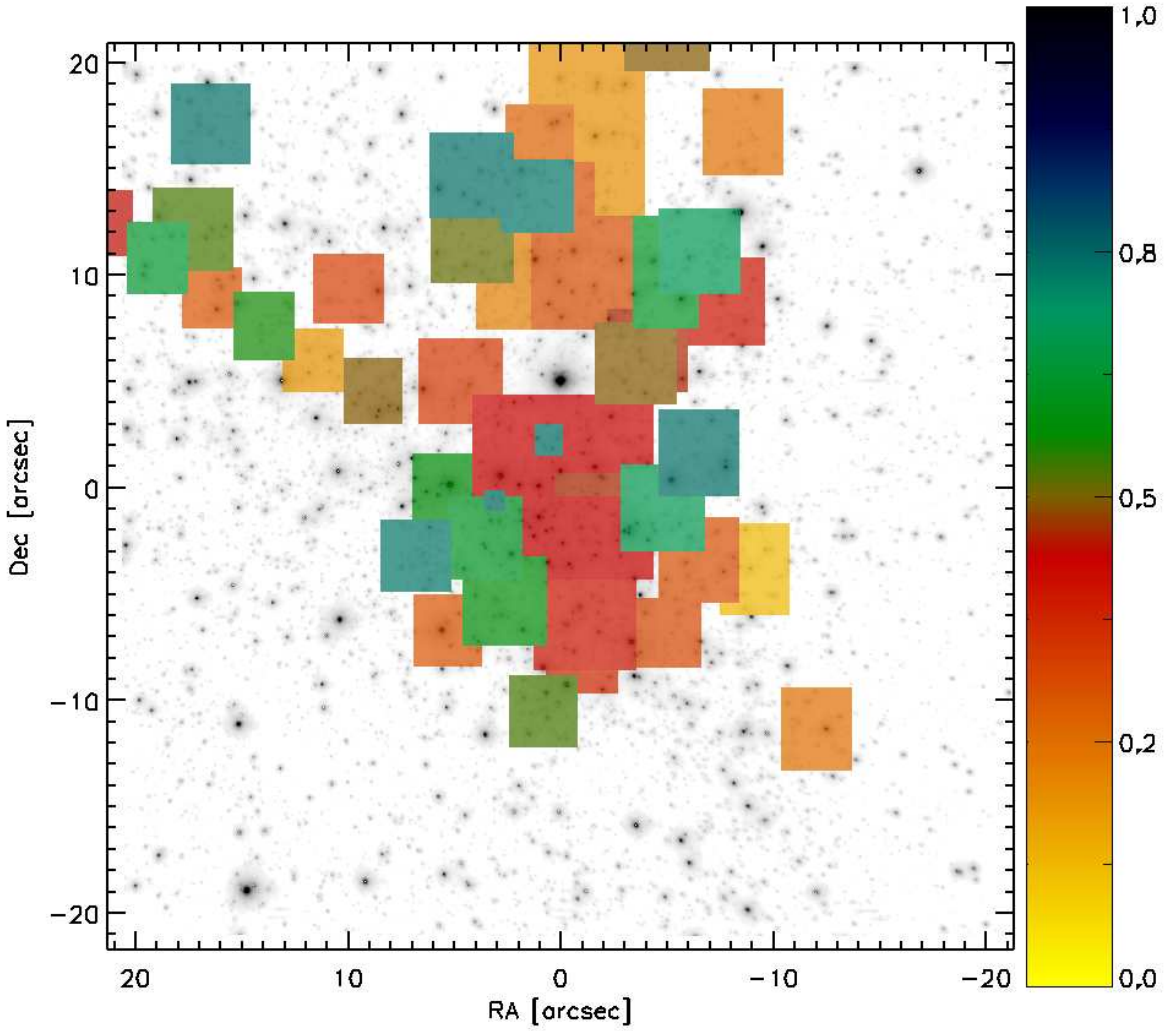

Figure 6.2 The AO assisted SINFONI fields overlaid on a GC image. The color of the fields indicates the combined spectroscopic and photometric completeness for a $m_K = 15$ star. The completeness is mainly driven by the exposure time of the individual fields and the observing conditions of the respective night.

6.3.1 Deep census of the GC population

The two deep SINFONI fields allowed a deep census of the GC population with 50% completeness down to $m_K < 18$.

A-star detection

Fig. 6.1 shows the deep fields. Red and blue circles mark stars identified as late-type or early-type. One star was not confirmed as early-type (green circle), but showed no CO bandheads and is therefore deemed to be an early-type candidate. Within the 18 square arcseconds of the two fields, we thus detected five early-type stars and one candidate. Their spectral type was determined by comparison with template spectra of Wallace & Hinkle (1997) and the absolute K-band magnitude M_K taken from Allen & Cox (2000). Three of them were brighter than $m_K < 17$ and were identified as dwarfs with spectral types between B2 and B8. The two faintest early type stars identified were B9/A0 dwarfs with $m_K = 17.2$ and $m_K = 17.6$. These stars are the faintest main-sequence stars reported so far in the Galactic Center. Stars of that spectral type have main-sequence lifetimes between 360-730 Myrs and masses between $2.2 - 2.8\,M_\odot$ (Allen & Cox, 2000). The spectra of the two A-stars are shown in Fig. 6.3. For comparison, two spectra of late-type giants of equal K-band luminosity are shown. The candidate is of similar luminosity falls in the same main-sequence category.

K-band luminosity function

The deep census of the GC allowed us to construct a KLF with $12 < m_K < 18$ (Fig. 6.4). The best fitting slope of the luminosity distribution $\mathrm{d}\log N/\mathrm{d}m_K = \beta$ is found to be $\beta = 0.33 \pm 0.03$. This is consistent with the results of Buchholz et al. (2009), who determined the slope of stars with a limiting magnitude of $m_K < 15.5$. As already discussed by Alexander & Sternberg (1999), Genzel et al. (2003) and Buchholz et al. (2009), the slope is typical for an old, bulge-like population. This is in good agreement with our H-R diagram fitting (Sec. 6.5.1) showing that most of the star formation occurred more than 5 Gyrs ago. However, the KLF alone is not sufficient to constrain the star formation history for an old population. The KLF alone cannot constrain the actual formation history and the IMF since the KLF slope is very insensitive to both parameters (Löckmann et al., 2010). For example, the admixture of young and bright giants is hardly detectable in the KLF due to their low number. Yet, they can be easily identified in the H-R diagram.

Origin: Disk members?

One of the observed fields is centered on the disk region, while the second field probes the outer rim of the disks. Thus the early-type stars in the two observed fields are potential disk members. To test for membership, we used the same method as described in Bartko et al. (2010b). The 3D velocity and the positions of all five stars are given in Table 6.2. The last column indicates a likely disk membership. We find that the two A-stars are clearly

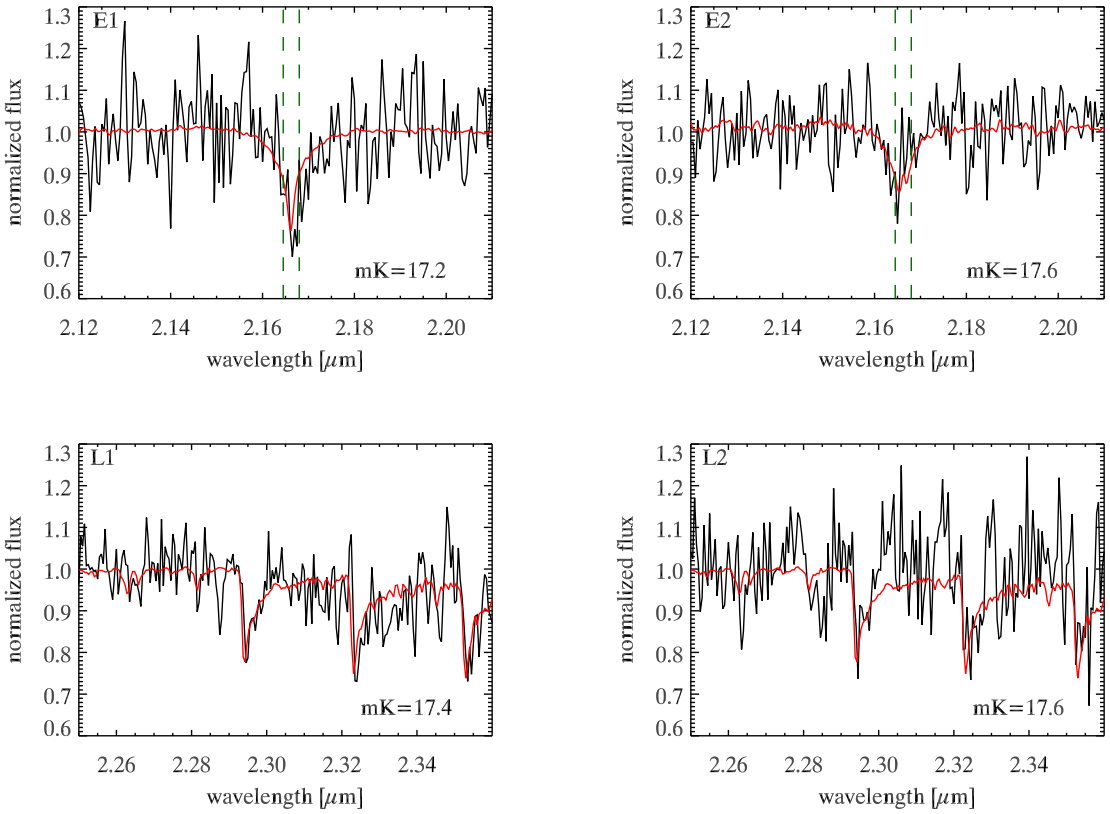

Figure 6.3 Spectra of the faint A0/B9V main-sequence stars in the Galactic Center (upper panels). The red line shows B9/A0 V template spectra of the solar neighborhood (Wallace & Hinkle, 1997). The dashed bars indicate the width of the nebular emission in the vicinity of the stars. The name in the upper left corner relates the spectrum to the star in Fig. 6.1. For comparison, two late-type spectra of similar brightness ares shown in the lower panels. The corresponding late-type templates are indicated in red.

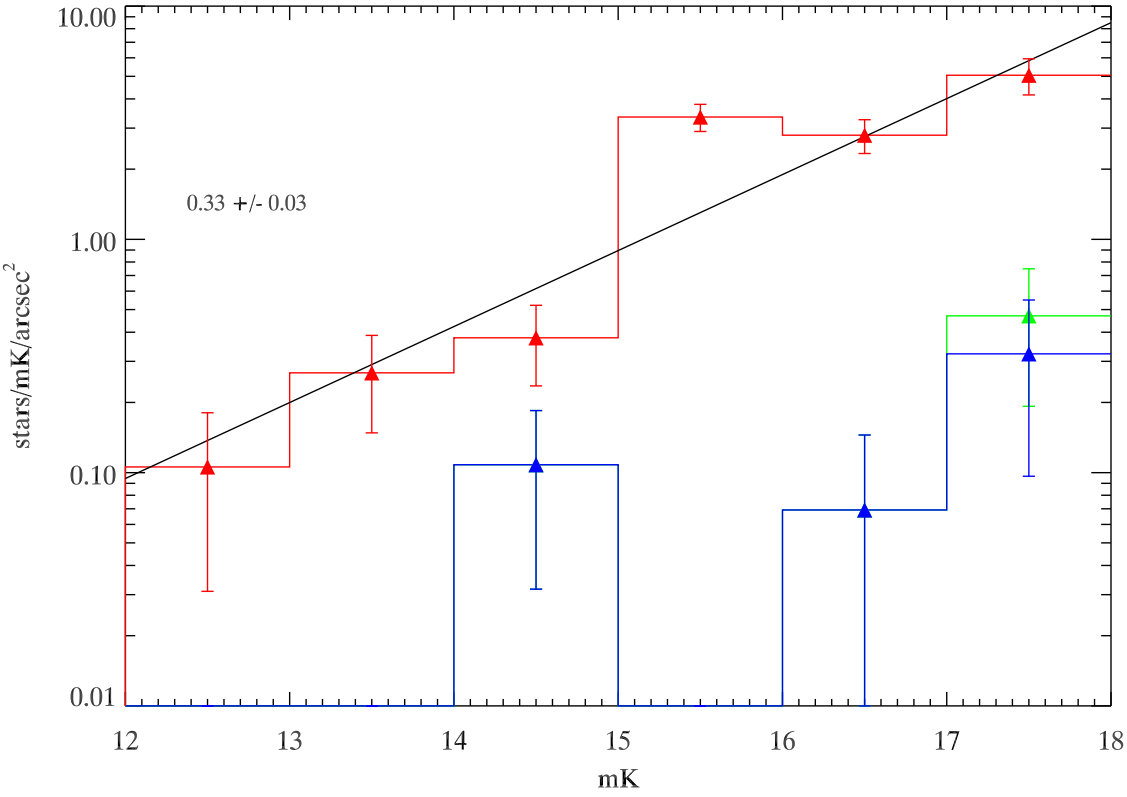

Figure 6.4 Completeness corrected KLF of the confirmed early- (blue) and late-type (red) stars found within the two deep spectroscopic fields. The green KLF shows the early type stars including the unidentified star. The solid line indicates the best-fit powerlaw to the late-type KLF.

Table 6.2 Early type stars contained in the deep spectroscopic fields.

Field	mK	RA[a][″]	Dec[a][″]	v_x [mas/yr]	v_y [mas/yr]	v_z [km/s]	Disk member[b]
North	14.1	0.0	12.3	2.44 ± 0.10	0.55 ± 0.24	-100 ± 40	CCWS
North	17.2	2.0	13.8	0.62 ± 0.27	0.96 ± 0.4	116 ± 55	no
East	14.2	6.5	-2.7	-2.73 ± 0.14	-3.73 ± 0.26	-60 ± 7	no
East	16.4	7.3	-4.1	2.89 ± 0.23	-1.25 ± 0.16	-163 ± 44	no
East	17.7	8.0	-2.7	2.19 ± 0.39	-0.12 ± 0.24	-41 ± 52	no

[a]Distance in arcseconds relative to Sgr A*.

[b]Potential members of the clockwise disk (CWS) or the counter-clockwise disk (CCWS) as defined by Bartko et al. (2009).

not disk members. Among the brighter B-stars, only one is consistent with the counter-clockwise disk (CCWS). This supports the results of Bartko et al. (2010b) who find a disk IMF skewed towards massive stars. Their disk KLF predicts roughly the same number of stars with $m_K = 14$ as with $m_K = 17$. A Chabrier/Kroupa IMF on the other hand predicts five times more $m_K = 17$ stars. Although the statistical significance of only five early-type stars is limited, it is intriguing that we find one $m_K = 14$ disk member (consistent with the average B-star density) but no fainter disk members. The faint B/A-stars exhibit an isotropic orientation (Bartko et al., 2010b) and are most likely the remains of older star bursts.

6.3.2 Supergiant IRS7

Two red supergiants are known to reside within 1 pc of Sgr A*
(Blum et al., 2003; Paumard et al., 2006). Those supergiants are significantly younger than the rest of the old stellar population. The supergiant IRS 7 is the youngest of this particular luminosity class. Carr et al. (2000) find an initial mass of $20\,M_\odot$ and stellar age of ~ 7 Myrs and attribute it to the recent starburst. This is supported by its kinematics (Bartko; priv. comm.) placing IRS 7 on the clockwise disk system. We simulated a 6 Myr star burst as found by Paumard et al. (2006) and Bartko et al. (2010b) with the IAC-STAR code (see following sections). The predicted ratio of red supergiants ($T_{\rm eff} < 5000$ K; $m_K < 9$) to blue supergiants ($T_{\rm eff} > 6000$ K; $9 < m_K < 14$) is between 0.4-0.5% (independent of the assumed IMF). This is in good agreement with the observed ratio of 118 blue supergiants with $m_K < 14$ (Bartko et al., 2010b) to one supergiant, i.e. a ratio of 0.9%. The second supergiant has an age of a few ten Myrs (Blum et al., 2003) and is thus older than the disks.

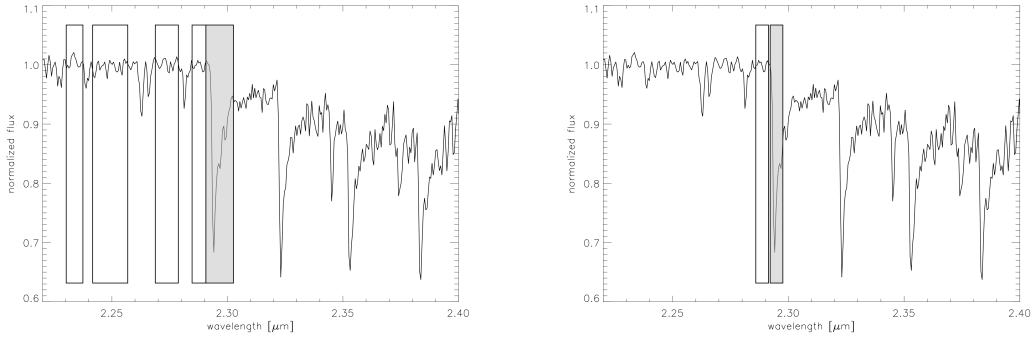

Figure 6.5 Left: Index definition of Frogel et al. (2001). The gray area indicates the line region and the white area indicates the continuum regions used for the fit. Right: Index definition of Kleinmann & Hall (1986). An adaptation of that index was used in Blum et al. (2003) and Maness et al. (2007).

6.3.3 CO index definition

The ^{12}CO$(2,0)$ bandhead has been widely used as a temperature indicator. This has brought up numerous definitions of CO indices. A detailed comparison of regularly used index definitions was recently performed by Mármol-Queraltó et al. (2008). The analysis showed that some index definitions are systematically more affected by spectral resolution, velocity error, curvature of the spectrum and SNR than other definitions. In particular, the index definition of Kleinman & Hall (1986) proved to be very sensitive to those effects. The index measures the continuum and the line flux in two narrow bands in close proximity.A similar index was used in previous studies of the Galactic Center population by Maness et al. (2007) and Blum et al. (2003). However the authors used a wider bandpass than Kleinmann & Hall (1986) (0.015 μm instead of 0.0052 μm). In the following the index is referred to as BL03. Systematic errors in the measurement of the CO strength lead to systematic errors in the temperature estimation. Since the temperature is a tracer of the stellar age, this might lead to a bias in the determination of the star formation history. Indeed, the paucity of cool stars in the GC is the chief constraint which led Maness et al. (2007) to conclude a top-heavy IMF may have persisted throughout the star formation history of the Galactic Center. To estimate the impact of systematics in light of this recent work, we tested the index BL03 against various effects and compared its performance with the alternate index proposed by Frogel et al. (2001, FR01). It uses several narrow bandpasses to estimate the CO continuum with a linear fit (see Tab. 6.1). The line and continuum regions for both index definitions can be seen in Fig. 6.5.

Index computation

Before computing the indices, each stellar spectrum was shifted to rest-wavelength. We then divided the spectrum by a second-order polynomial fit to remove the curvature of the spectrum. For the continuum fit, we excluded regions with significant absorption lines; the polynomial fit is necessary to account for the the large ($A_K \sim 3$) and spatially variable extinction in the GC. We then computed the BL03 index according to the recipe of Blum et al. (2003). The FR01 index was computed in a similar way, with the bandpasses as described in Frogel et al. (2001). The continuum level $w_{\rm C}(\lambda)$ is estimated with a linear fit to the intervals stated in Table 6.1. The equivalent width is measured according to:

$$\mathrm{EW(CO)} = \int_{\rm band} (\frac{w_{\rm C} - w_{\rm line}}{w_{\rm C}}) \mathrm{d}\lambda. \tag{6.1}$$

We tested both indices (BL03, FR01) with template spectra of different resolution. We also reddened the template spectra artificially to determine the impact of extinction.

Systematic error sources

Reducing the resolution from R $\sim$ 3000 to R $\sim$ 2000 decreases the BL03 CO index by a factor of $\approx$ 0.92. The artificial reddening and the corresponding change of curvature of the spectrum, causes a reduction of $\approx$ 0.94. Both effects cause the BL03 CO index to be underestimated by a factor between 0.90-0.85. The systematic underestimation of the BL03 CO strength leads to an overestimation of the stellar temperatures by ~ 200 K. The FR01 index decreased by less than a factor 0.98 due to extinction. Degrading the resolution from R $\sim$ 3000 to R $\sim$ 2000 shows no measurable impact. We estimate the combined systematic effect to be less than 0.97 ($50\,K$). The BL03 index suffers also from contamination of the Mg I line contained in the continuum bandpass of the index. The average Mg I line strength of the GC giants is similar to the calibration giants. Thus, the continuum estimation is not biased. Yet, the line shows some intrinsic scatter introducing a statistical error in the CO index computation. To minimize the statistical and systematic error sources, we therefore adopted the index definition of FR01. We have to note that the results of Blum et al. (2003) did not suffer from the resolution dependence of their CO index because the bulk of their GC spectra were of the same resolution as the comparison stars.

6.3.4 Temperature calibration

For the temperature calibration we used stellar spectra of giants with known $T_{\rm eff}$. In total we used 33 giants with spectral types G0-M7 and metallicities $-0.3 <$ [Fe/H] < 0.2. The spectra were obtained from the NOAO IR-library (Wallace & Hinkle, 1997) with R $\sim$ 3000; the IRTF-library with R $\sim$ 2000 (Rayner et al., 2009) and from Förster Schreiber (2000) with R $\sim$ 2000. The corresponding temperatures were obtained with the help of the SIMBAD database. The CO-$T_{\rm eff}$ relation for the template giants can be seen in Fig. 6.6.

The best-fit to the data in the range $3.5 < \mathrm{CO} < 24$ is (where CO is the FR01 index in units of [Å]):

$$T_{\mathrm{eff}} = 5832^{\pm 130} - 208.25^{\pm 32.84} \cdot \mathrm{CO} + 11.38^{\pm 2.48} \cdot \mathrm{CO}^2 - 0.34^{\pm 0.06} \cdot \mathrm{CO}^3. \qquad (6.2)$$

The residual scatter is 119 K. The average metallicity of the calibration stars of [Fe/H] = −0.1 is somewhat below the average metallicity in the GC of [Fe/H] = 0.14 (Cunha et al., 2007). To account for the metallicity dependence of the CO strength, we add a constant offset of 50 K to the temperatures of the GC giants (estimated with the help of Mármol-Queraltó et al. (2008); their Fig. 14).

Systematic temperature uncertainty

The systematic errors in the derivation of the temperature are the main drivers in the age uncertainty of a giant population (at a given metallicity). As discussed in the previous section, the CO index computation might be biased on a ~ 50 K level. More important however is the theoretical uncertainty. The Padua and Geneva Isochrones can differ by up to 80 K for the same star. Strictly speaking, this is not an observational uncertainty but in the fitting procedure the theoretical uncertainty must be taken into account. We included the bias by assuming a total systematic uncertainty of 100 K. To visualize the impact of temperature uncertainties, Fig. 6.7 shows the theoretical age vs. median temperature relation for red clump stars ($0 < M_{\mathrm{bol}} < 1$). Especially for old ages, the age interpretation is very sensitive to temperature changes. Small temperature biases of the order 100 K might change the derived age by several Gyrs. In the star formation history fitting, we used not only red clump stars. However red clump stars make up more than one third of all observed giants. Thus, the systematic uncertainty of the red clump population is representative for the whole giant population.

6.3.5 Red clump spectrum: evidence for old ages and near solar metallicity

The majority of the GC stars are red giants (RG). The RG phase is associated with the hydrogen-shell burning phase of a star. While the burning shell propagates outward through the stellar interior, the star expands and cools down. During this evolution, the star increases its brightness and climbs up the RG branch. Discontinuities in the stellar interior cause the brightness of the star to drop temporarily, when the burning shell passes a discontinuity. This happens several times during the ascent of the RG branch. This creates an overdensity of stars at a typical luminosity referred to as the red clump (RC).

GC red clump

The observed K-band magnitude and the spectral CO index allowed the determination of the bolometric magnitude and temperature for individual GC stars. The bolometric magnitude M_{bol} follows directly from the intrinsic, de-reddened M_K. To derive the intrinsic

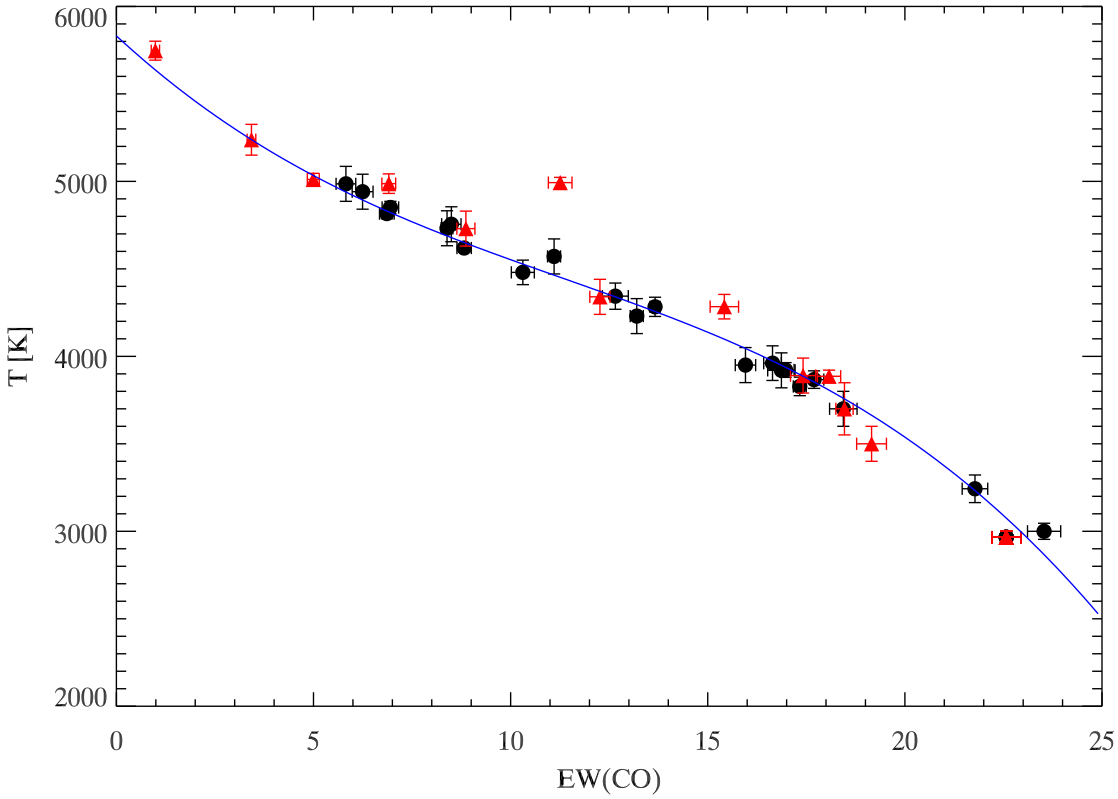

Figure 6.6 The EW(CO)-T_{eff} relation for the template giants is shown. Red triangles indicate spectra with a resolution of R $\sim$ 3000, black dots represent spectra with a resolution of R $\sim$ 2000. One 10 σ outlier can be seen. This particular star has a metallicity ([Fe/H] = -0.5) significantly lower than the other template stars ($<$ [Fe/H] $>= -0.1$). It was only included for comparison, but was not considered in the fit. The solid line shows the best fit to the data. The fit is reliable between $3 <$ EW(CO) < 24. The fit residual RMS is 119 K.

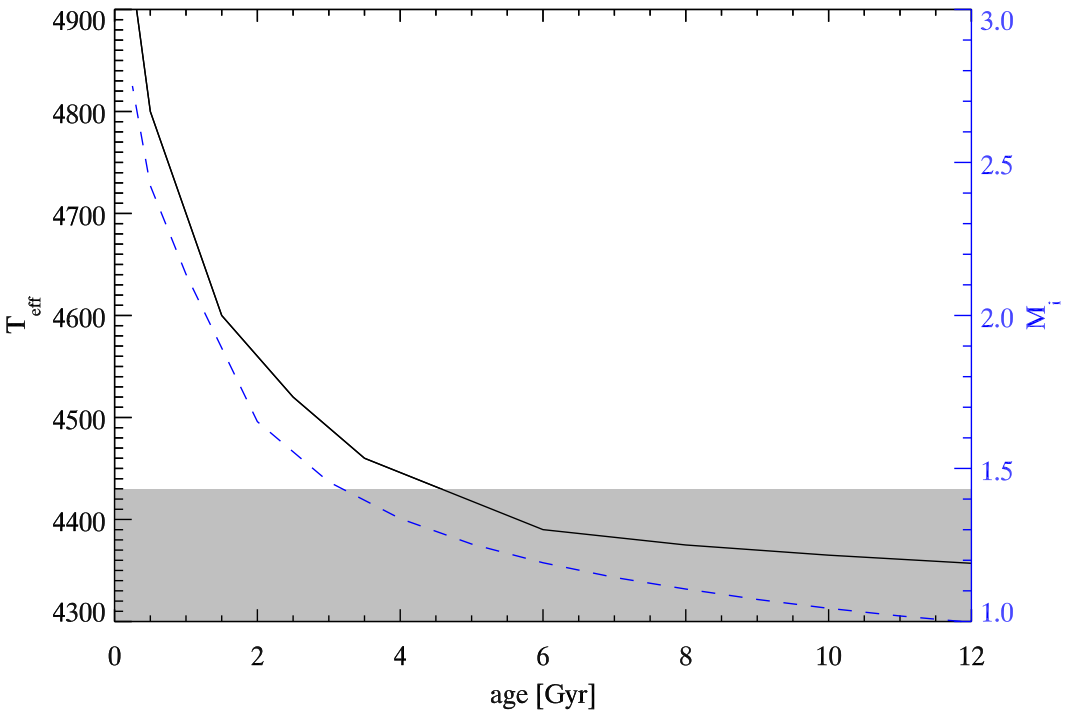

Figure 6.7 Relation between age and median temperature of the Red Clump is shown (solid line). Overplotted is the relation between age and mean initial mass of the Red Clump population (dashed line). The shaded area indicates the $T_{\rm eff}$ uncertainty. The plot illustrates the temperature sensitivity to the age of the red clump population. For ages >5 Gyrs, the age resolution decreases significantly.

M_K we used a distance modulus of 14.6 (8.3 kpc). The extinction was calculated for each star individually, following Bartko et al. (2010b). We used for each star the 20 nearest neighbors to derive the median H-K colour. By assuming an intrinsic colour of $\Delta m_{H-K} = 0.1$ (typical for K giants) we derived the reddening. By assuming a powerlaw extinction $A_\lambda \sim \lambda^{-2.21}$ (Schödel et al. 2010, Fritz et al.(2011) we computed the A_K extinction for each star. The bolometric correction (BC_K) was taken from Blum et al. (2003) [$BC_K = 2.6 - (T_{\rm eff} - 3800)/1500$]. The assumed BC_K is consistent with the bolometric correction library from Lejeune et al. (1997) used in the subsequent population synthesis models. The bolometric $1\,\sigma$ uncertainty is 0.32 magnitudes. It is caused by the photometric error, the temperature- and the extinction uncertainty. The stellar $T_{\rm eff}$ follows directly from the CO strength. The statistical $1\,\sigma$ $T_{\rm eff}$ uncertainty derived by error propagation of the measured CO index uncertainty is 200 K. The systematic $T_{\rm eff}$ uncertainty is 100 K (see Sec. 6.3.4). The

red clump of the GC giants can be found at a luminosity of $M_{\rm bol} = 0.6$ and a temperature of $T_{\rm eff} = 4310\,{\rm K}$ (see Fig. 6.10). Since the red clump is narrow, both in magnitude and temperature, i.e. all stars have very similar spectral features, it is a viable approach to construct a median spectrum of the GC red clump stars. In order to construct a high SNR spectrum, we used 234 red clump stars with bolometric magnitudes $0 < {\rm M_{bol}} < 1$ corresponding to $15.1 < m_K < 16.1$. The average SNR of individual spectra is between 10 and 15. All spectra were normalized and shifted to rest-wavelength as described in the previous section. Most of the spectra have a resolution of $R \approx 2000$. Spectra with a higher resolution were interpolated to match the latter. The equivalent integration time of the combined spectrum is of the order 300 hours. Figure 6.8 shows the resulting median spectrum of the GC giants.

Temperature estimate from high SNR spectrum

We compared the median spectrum with available library stars. The template star matching the co-added spectrum most closely is a K3 III giant with a temperature of 4330 K. The agreement of the spectra is impressive. Only the sharpest peaks are slightly smeared out due to a residual velocity error. The ^{12}CO bandheads at 2.294, 2.322, 2.352 and 2.383 μm are well represented. Even the weaker bandheads of ^{13}CO at 2.345 and 2.373 μm match the template (Fig. 6.8). The comparison with colder and warmer giants (Fig. 6.9) shows the sensitivity of the CO bandheads to the stellar temperature. The median temperature of the red clump as derived by the stacked spectrum $T_{\rm eff} = 4330\,{\rm K}$ agrees very well with the median value ($T_{\rm eff} = 4310\,{\rm K}$) of the individual low SNR spectra. The Ca I and Na I line blends are moderately sensitive to temperature as well as to the surface gravity $\log g$. The Ca I lines are in good agreement with the template. The same is true for the iron line blends at 2.22 and 2.23 μm as well as Mg I, Si I and Al I. Unfortunately almost all of the atomic lines are contaminated with weaker atomic lines and lines of CN. This excludes the possibility of a spectral synthesis fit at the given resolution. However qualitatively, it is clear that the GC spectrum is closely matched by a solar metallicity spectrum, in agreement with the work of Cunha et al. (2007).

Sodium line blend: Potential evidence for mixing processes

The strongest deviation between our average spectrum and the K3 III template is found in the Na I lines. They seem to be intrinsically stronger than in the solar neighborhood. None of the template spectra in the temperature range of the red clump can reproduce the Na I strength. An increased Na I strength was reported previously in low-resolution spectra by Blum et al. (1996). The Na I lines are actually blends of a couple of atomic lines and CN lines. The individual contribution depends on the stellar temperature. For temperatures similar to a K3 III giant, sodium is the most important line. Cooler spectra are heavily influenced by Sc and the coolest spectra are dominated by CN. For a detailed analysis of lines in K-band spectra see Wallace & Hinkle (1996). Carr et al. (2000) used high resolution spectra of IRS 7 to derive abundances. They found that the increased line

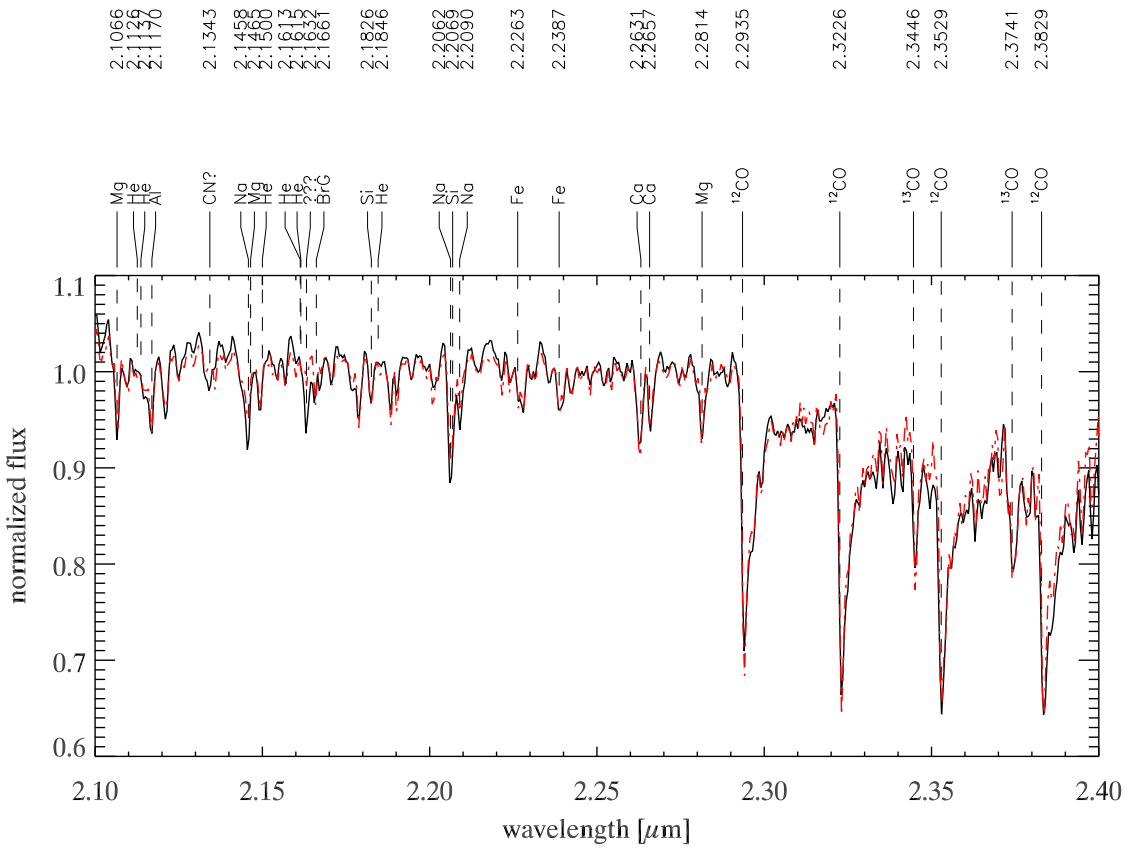

Figure 6.8 The median spectrum of 234 GC red clump giants (black). Each individual spectrum has been normalized and shifted to rest-wavelength. The median spectrum of the GC red clump is closely matched by a K3 giant of the solar neighborhood (red) with a temperature of 4330 K. The most prominent lines are indicated. Almost every line is actually a blend of atomic and molecular lines. In case of a line blend, the most important line is indicated.

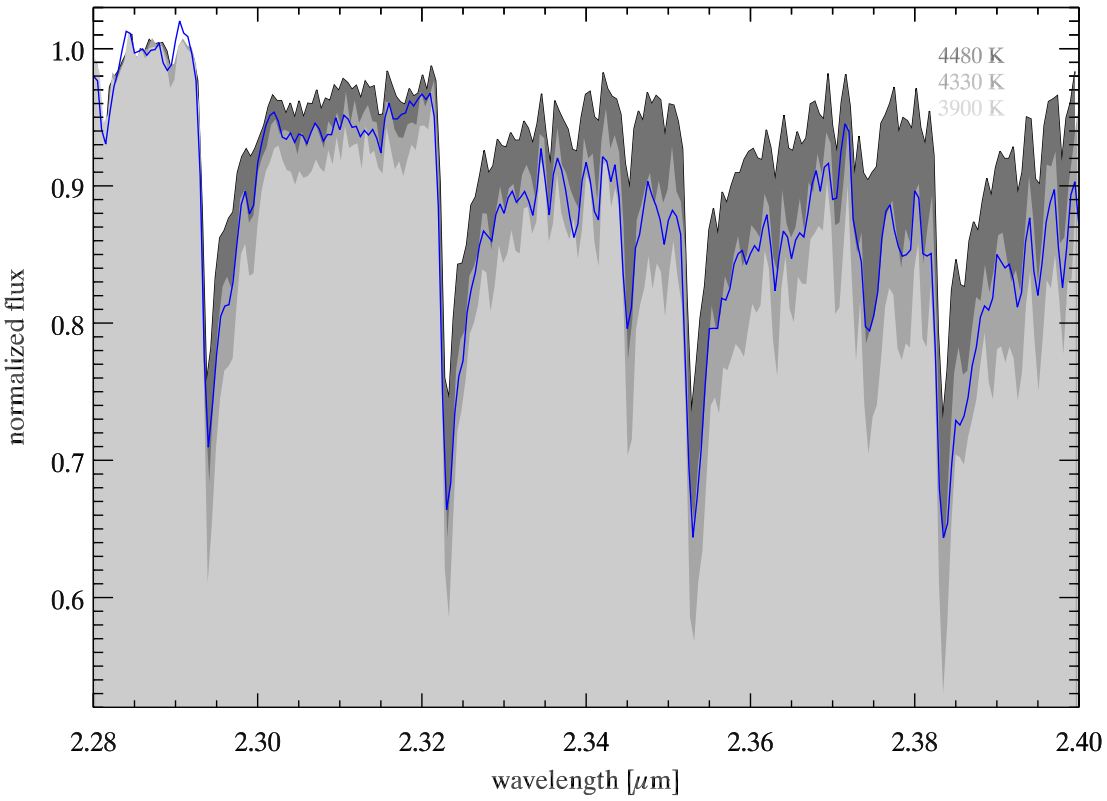

Figure 6.9 The temperature dependence of the CO bandheads is shown. The median spectrum of 234 GC red clump giants (blue) is compared with three giants of the solar neighborhood with temperatures between 4480 and 3900 K (gray shaded areas).

strength of the Na I complex is mainly caused by stronger CN lines. The CN lines reflect extreme CNO abundances in the atmosphere of IRS 7, which they claim is probably the result of increased rotational mixing.
Cunha et al. (2007) also find CN-cycled material in the atmospheres of three luminous GC giants, however not as deeply mixed as in IRS 7. Increased rotational mixing, is predicted for dense stellar clusters, where tidal spin-up can lead to significantly higher rotation speeds of main-sequence stars (Alexander, 2005). This might explain the increased CNO material in the outer atmosphere layers of the luminous GC giants. Evidence for increased rotational mixing taking place in a supergiant like IRS 7 with a mass of 20 $M_\odot$ and a lifetime of a few Myrs, are hard to transfer to the red clump giants of the GC with masses of only 1-2 $M_\odot$ and ages of Gyrs. This is especially true since IRS 7 is significantly cooler (3600 K) than the red clump.
However, Maeder & Meynet (2000) note that red giants with masses $M < 1.5\,M_\odot$ are susceptible to extra-mixing and Alexander (2005) notes that tidal spin-up is most effective in long-lived low mass stars. Thus, the strong sodium lines might indicate that the red clump stars have undergone a mixing process different from the solar neighborhood, for example due to tidal spin-up. In principle, the sodium line strength can also reflect a peculiar chemical composition of the Galactic Center. With the current knowledge we cannot rule out that possibility. However, rotational mixing provides a convincing explanation for the increased sodium strength. This might provide interesting conclusions on the stellar evolution since fast rotating stars tend to be more luminous and redder and can provide evidence for the existence of an underlying dense stellar cusp of low-mass main-sequence stars (Alexander, 2005).
Apart from the Na I lines, the average spectrum shows no peculiarities. Small deviations of the GC spectrum at 2.219 and 2.349 μm are caused by poorly subtracted nebular emission of the Mini-Spiral. The deviation at 2.317 μm on the other hand coincides with a telluric line. Overall the agreement is intriguing and validates the method of constructing a median spectrum a-posteriori.

6.4 Construction of the H-R diagram

We constructed an H-R diagram for the GC cluster using the same distance modulus and extinction as described in Sec. 6.3.5. The H-R diagram is displayed in Fig. 6.10. For comparison, we also included the data of Blum et al. (2003) probing the luminous giants and supergiants in the inner 2.5 pc. The comparison data were rescaled to the updated extinction values used in this work. Although Blum et al. (2003) and this work rely on different temperature calibrations, the overlap regions match very well. The GC population is compared to isochrones (Bertelli et al., 1994) with $Z = Z_\odot$ and $Z = 2.5\,Z_\odot$ metallicity (Fig. 6.10, left). The right panel of Fig. 6.10 shows the comparison with with a synthetic model population. The model population represents the case of continuous star formation over 12 Gyrs with a GC metallicity of $Z = 1.5 Z_\odot$ (Cunha et al., 2007).

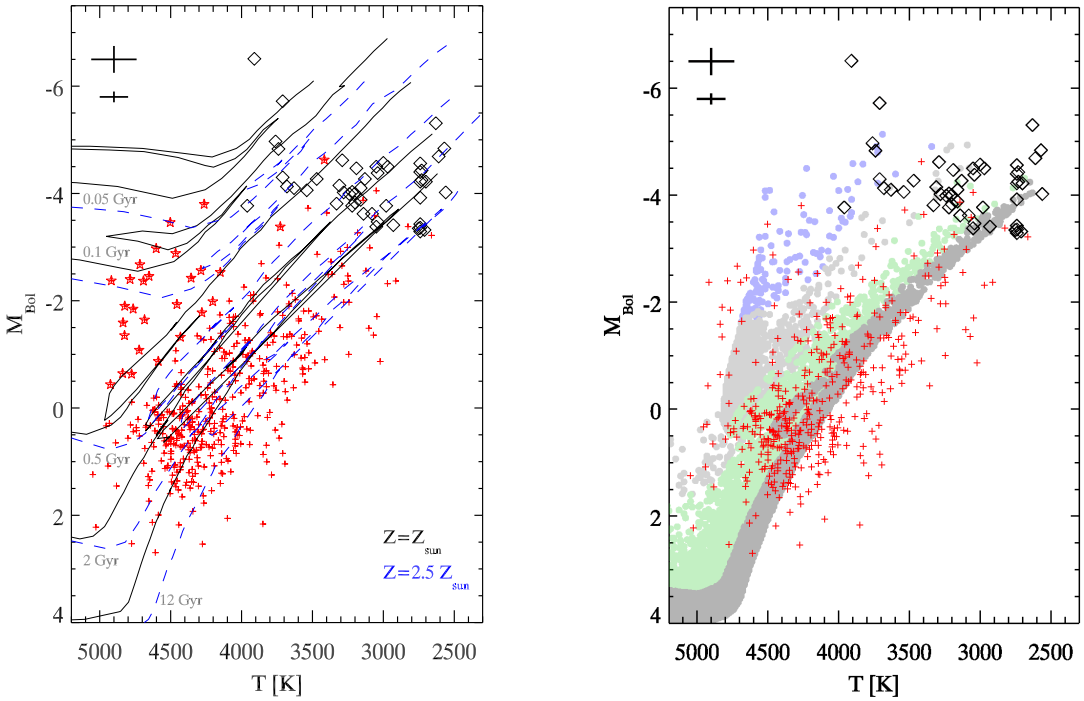

Figure 6.10 **Left:** H-R diagram of the cool Galactic Center stars; this work (red crosses). Stars younger than 0.5 Gyr are indicated by star symbols; data points from Blum et al. (2003) are indicated as black diamonds. Overplotted are isochrones for ages (from left to right) 0.05, 0.1, 0.5, 2 and 12 Gyrs with solar metallicity (black, solid) and 2.5 times solar metallicity (blue, dashed). The upper black cross shows the statistical error and the lower cross shows the systematic uncertainty. **Right:** Observed H-R diagram (red crosses) overlaid on a synthetic model population assuming 12 Gyrs of continuous star formation; the metallicity is $Z = 1.5\,Z_{\odot}$ (Cunha et al., 2007); Different age intervals of the synthetic population are indicated; $5 < t < 12$ Gyrs (dark gray); $1 < t < 5$ Gyrs (green); $0.2 < t < 1$ Gyrs (gray); $0.05 < t < 0.2$ Gyrs (blue). The synthetic population was created with the code of Aparicio & Gallart (2004). The code used the Bertelli et al. (1994) stellar evolution library and the Lejeune et al. (1997) bolometric correction library.

6.4.1 Features of the H-R diagram

The H-R diagram shows several distinct features. The most prominent feature is the RG branch consisting of old ($> 1\,\mathrm{Gyr}$) stars with masses of the order $1\,\mathrm{M}_\odot$. The GC red clump can be identified as an overdensity of stars at a luminosity of $M_{\mathrm{bol}} = 0.6$. This agrees very well with the red clump in the solar neighborhood measured by Groenewegen (2008). The mean red clump temperature derived by individual spectra agrees very well with the estimate based on the high SNR median red clump spectrum (Fig. 6.3.5). A second overdensity can be found at $M_{\mathrm{bol}} = -0.8$ and $T_{\mathrm{eff}} = 3900\,K$. This feature is sometimes referred to as the AGB bump. All afore mentioned features are tracers of an old population. The H-R diagram shows a second branch of giants at $T_{\mathrm{eff}} = 4800\,\mathrm{K}$. This warm giant population is bright ($M_{\mathrm{bol}} < 0$) and separated from the cold (old) branch in the same magnitude range. Yet, only $\sim 10\%$ of the giants between $0 < M_{\mathrm{bol}} < -4$ (corresponding to $11.5 < m_K < 15.5$) can be attributed to the young branch. Similar features are known in globular clusters with multiple stellar populations. The comparison of the GC H-R diagram with Chabrier/Kroupa populations of different ages can be seen in Fig. 6.10 (right). Several obvious features are matched. The red clump is well represented in the data. The cool branch of giants with ages greater than 1 Gyr is obvious. The temperature and luminosity of the warm branch is matched by giants younger than 0.5 Gyrs. A deficiency of stars with ages of $\sim$1 Gyr can be seen as a gap in the diagram. We don't detect a significant Horizontal Branch of old and metal poor giants as would be typical for old globular clusters. This supports the assumption of a predominantly old and metal rich population.

Outliers

The coolest temperatures we find cannot be reproduced by even the oldest solar metallicity isochrones. Those outliers might be explained by a population of metal rich stars ($Z > 2.5\,Z_\odot$). However, this does not contradict the current assumption of a near solar metallicity in the GC. The cold outliers account for less than 8% of the total population. Since metallicity studies in the GC (Ramírez et al., 2000; Cunha et al., 2007) have probed not more than ten late-type stars, a small metal rich population might have gone undetected. This can be compared to the situation in the Bulge (Baade's Window), where a high metallicity tail of stars ($Z > 2.5\,Z_\odot$) makes up about 15% of the population (Zoccali et al., 2008). Another explanation might involve stellar model uncertainties. Most of the outliers show the same luminosity as bright and cool AGB stars. Stellar models of these stars still suffer from large uncertainties. Model isochrones treat this evolutionary phase in a simplified manner and are thus rather unreliable. Furthermore, stars in these stages are known to pulsate with periods of hundreds of days. During the pulsation, an individual star can change its temperature by up to 500 K (Lançon & Mouhcine, 2002). All systematic effects considered by us, lead to an overestimation rather than an underestimation of the stellar temperature. Yet, some of the stars can be heavily dust obscured and thus appear too faint for the given temperature. In the following fitting procedure we ignored stars that were cooler than allowed by the isochrones and the temperature uncertainty. This excludes

only a small number of the old stars. Therefore we are confident that the impact on the results is negligible.

The young giant branch

Roughly 10% of the observed GC giants with magnitudes between $0 < M_{\rm bol} < -4$ appear to belong to a branch of young ($< 500\,$Myrs) giants. With masses between $2.5\,M_\odot < M < 6\,M_\odot$ those stars are descendants of main sequence B-stars. They are tracers of an intermediate age population in the Galactic Center. Their stellar age is smaller than the typical non-resonant two-body relaxation time in the Galactic Center of the order $t_{\rm nr} \gtrsim$ few Gyrs in the GC (Alexander, 2005; Merritt, 2009). However, close to the SMBH, orbits are near-Keplerian. This causes interactions between stars to build up coherently. The randomization of the angular momentum vectors happens therefore on the fast vector resonant-relaxation timescale $t_{\rm vr} <$ few ten Myrs (Hopman & Alexander, 2006).
However, the eccentricity and semi-major axis distribution is randomized on the slow scalar resonant timescale $t_{\rm sr}$ (Hopman & Alexander, 2006), comparable to $t_{\rm nr}$ for $r > 0.1\,$pc. The mean stellar mass of the young giants ($3.2\,M_\odot$) is significantly larger than the average mass of the old giants ($1\,M_\odot$). The more massive stars tend to sink to the center of a cluster due to dynamical friction exerted through the drag of lighter background objects. The mass segregation timescale in the Galactic Center is larger than in normal stellar clusters due to the presence of the SMBH and the corresponding higher velocity dispersion. The mass segregation timescale $t_s \sim t_{\rm nr}\frac{\overline{M}}{M_\star}$ scales with the relaxation time $t_{\rm nr}$ but is also a function of the individual stellar mass $M_\star$ and the mean stellar mass $\overline{M}$ (Alexander, 2005). Assuming the mean stellar mass is $\overline{M} \approx 1\,M_\odot$, the segregation time is $t_{\rm s} \approx \frac{1}{3}t_{nr} > 1\,$Gyr. This is still significantly larger than the age of the young giants. Thus the radial distribution could not have changed significantly since the stars formed (neither through relaxation, nor through mass segregation). Yet, the angular momentum vectors (i.e the orientation of the orbits) will have undergone randomization.

Kinematics and distribution

To assess the dynamical state of the young giants we computed their orbital distribution. We followed the method of Bartko et al. (2009), who used statistical arguments to infer the 3D distribution of a stellar population out of the 3D velocity and projected distance distribution. A coherent motion within a stellar system can be detected as a statistical preference for a angular momentum direction. However the orbital distribution of the young giants shows no significant excess as would be the case for a disk or a streamer. The orientation of the angular momentum vectors is consistent with being isotropic, as expected due to the fast vector resonant relaxation. The radial distribution of the young giants compared to the cool giant population is shown in Fig. 6.11.

Both populations exhibit the same radial density distribution. The density distribution of the total giant population has been described as a core or even a hole close to the SMBH (Buchholz et al., 2009; Bartko et al., 2010b; Schödel et al., 2010). In any case, the

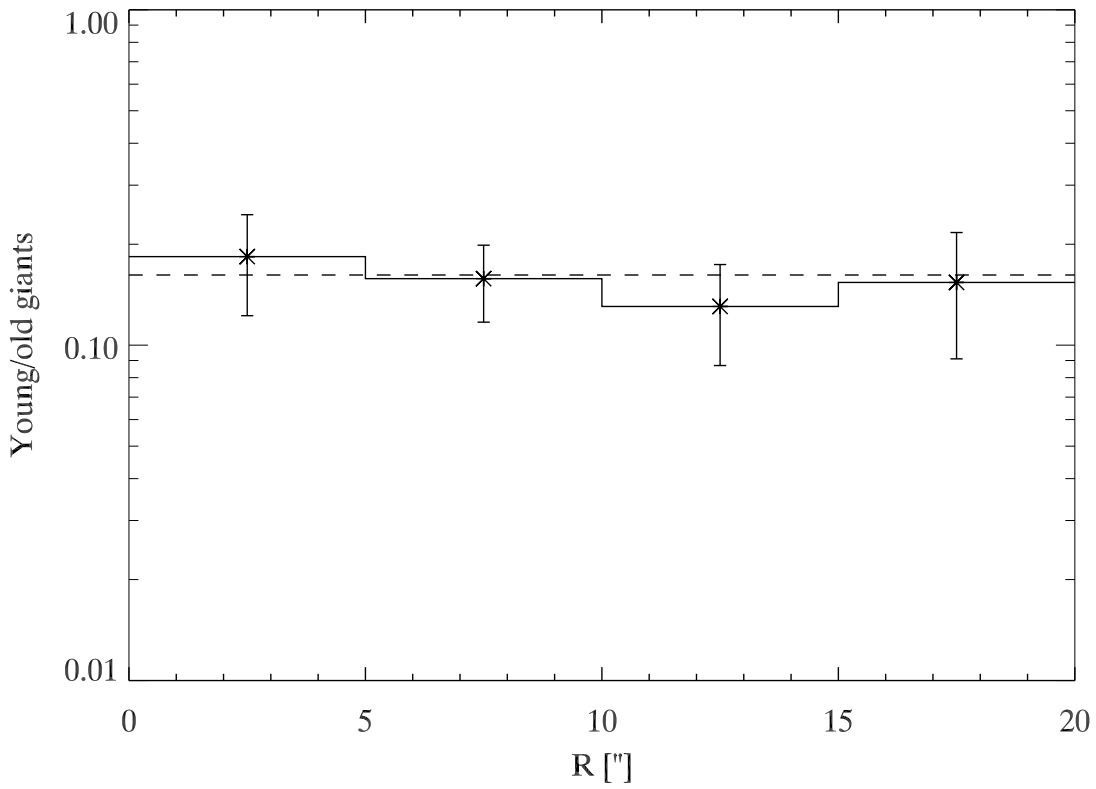

Figure 6.11 Ratio of young-to-old giants with magnitudes between $0 < M_{bol} < -4$ as function of radius. The average ratio is indicated (dashed line). The errors are the Poisson errors of the young giants in the given radial bin. The ratio is consistent with being flat, indicating that the young giants exhibit the same radial distribution as the old giants.

distribution differs significantly from a Bahcall-Wolf cusp, the predicted final state of a relaxed population. Given the age of the young giants, they must have formed rather close to the SMBH, either in-situ or transported in by in-falling clusters. Since the radial density distribution evolves only slowly on timescales of $\sim$ few Gyrs this means that the young giants still contain information on their initial distribution. The 3D velocity of the young giants compared with the cool giants in the same magnitude bin is shown in Fig. 6.12. The 3D velocity was computed, assuming a distance of 8.3 kpc to the Galactic Center. The maximum 3D velocity $v_{\rm max} = \sqrt{\frac{2GM_\bullet}{r}}$ for stars to be bound is indicated in the figure. The projected distances r yields a lower limit for the physical 3D distance R. The kinematics of the young population are consistent with the old stars. Using a Kolmogorow-Smirnov test to asses the likelyhood that the young giants 3D velocities can be drawn from the cold population returns a probability of 70%. The fact that both giant populations share the same radial distribution is surprising. The young giants ($M_{\rm ZAMS} \approx 3\,M_\odot$) are three times more massive than their old counterparts with a lifetime too short to experience relaxation and especially to change their angular momentum significantly. However, it renders a radially varying IMF unlikely. The latter is a valid claim although star formation history and IMF are highly degenerate, since one effect would need to cancel exactly the other to emulate a radially constant distribution of young-vs-old giants.

6.5 Calculation of the star formation history

To derive the star formation history, we compared the observed distribution of giants in the H-R diagram to model populations. We restrict our analysis to the $m_K < 15$ magnitude range with $> 50\%$ completeness. This left us with 450 giants for the fit. We repeated the calculation with a completeness limit of 80%. The results were similar, yet with larger uncertainties. Thus we are confident that no bias is introduced due to the completeness limit chosen. The synthetic model populations were created with the IAC-STAR code (Aparicio & Gallart, 2004). The code allows a selection of different stellar evolution and bolometric correction libraries for the computation. We chose the Bertelli et al. (1994) stellar evolution library and the Lejeune et al. (1997) bolometric correction library since these are the only libraries with evolutionary tracks of stars with masses $> 10\,M_\odot$. The code requires several input parameters such as metallicity, age and slope of the IMF. Since age and metallicity introduce some degeneracy, we adopted the mean metallicity found by Cunha et al. (2007). Thus, we set up model populations with a metallicity of $Z = 1.5\,Z_\odot$. For the calculation of the star formation history, we applied a method similar to Blum et al. (2003). We defined four age bins (50-200 Myrs, 0.2-1 Gyr, 1-5 Gyrs and 5-12 Gyrs) with constant star formation rate within each age bin. The bins were chosen such that the evolutionary tracks are distinct enough to be resolved with the given data quality. The isochrones for stars with ages $>$ few Gyrs are very similar. Therefore, the older age bins were chosen to be wider than the younger age bins. The younger age bins were selected by visual comparison of the model populations with the data. Fig. 6.10 shows the chosen age bins. To study the impact of the IMF, we created models with various IMF slopes between

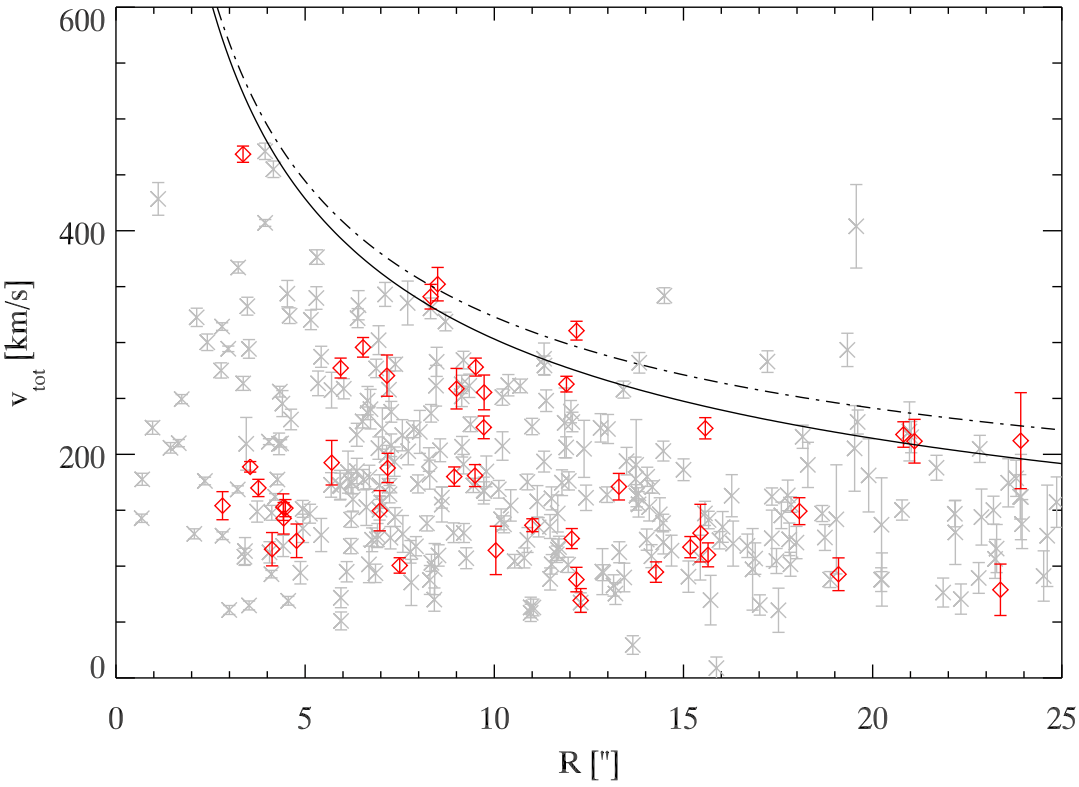

Figure 6.12 The 3D velocity of the warm giants (red) with magnitudes of $0 < M_{bol} < -4$ and the cold comparison sample (gray) is shown. The maximum allowed velocity for stars to be bound is indicated; SMBH alone (solid line); SMBH + cluster mass (dashed line).

$-2.7 \leq \alpha \leq -0.45$. Among the models, we included a Chabrier/Kroupa IMF ($\alpha = -2.3$), a top-heavy IMF ($\alpha = -0.85$) (Maness et al., 2007) and a flat IMF with a slope of $\alpha = -0.45$ as it was found recently for the young stellar disk (Bartko et al., 2010b). We note, that the star formation could have proceeded in episodic bursts. Yet, given the quality of the data, it is not possible to distinguish between a burst and a continuous formation within an age bin. Therefore the derived star formation rate is an average across the age bin.

6.5.1 Fitting procedure

We added Gaussian noise to the synthetic model populations, representing the statistical errors of $M_{\rm bol}$ and $T_{\rm eff}$. Then we removed stars from the synthetic populations according to the estimated completeness as a function of K-band magnitude. The completeness is not a function of temperature, since we used a minimum SNR criterion. We then binned the data and the model populations into an H-R diagram with a binsize of $1.5\,\sigma$ of the typical errors. The data were then fit as a linear combination of the H-R diagrams of the 4 model populations (4 age bins). For the fit we used the IDL routine TNMIN (Markwardt, 2009). As a minimization parameter we used the Poisson maximum likelyhood parameter $\chi^2_\lambda = 2\sum_i m_i - n_i + n_i\ \ln(\mathrm{n_i}/\mathrm{m_i})$, where m_i is the number of stars predicted by the model and n_i is the number of observed stars in the ith bin of the H-R diagram (Mighell, 1999; Dolphin, 2002). The contribution of each age bin determines the relative star formation rate of that bin. The best-fitting star formation rate for various IMFs is given in Table 6.3.

Uncertainty and quality of the fit

To assess the fit uncertainty we used a method generally referred to as bootstrapping. We constructed 1000 H-R diagrams by drawing random stars out of the data. Each star was allowed to be drawn any number of times. To include the systematic uncertainty of the data and the theoretical isochrones, we added a random temperature offset with a Gaussian σ of 100 K to the whole data set. The constructed H-R diagrams were fit again with the model populations. The scatter of the derived relative star formation rates represents the $1\,\sigma$ uncertainty of the relative star formation rate (see Table 6.3). Note, the star formation rate uncertainty is mainly driven by the systematic temperature uncertainty. To judge the quality of each model fit, we produced 1000 Monte Carlo data sets, each containing 450 stars drawn randomly from the respective model (not the original data). Calculating the variance in each bin resulted in a variance diagram. We defined the fit quality as $\chi^2 = \sum_i \frac{(m_i - n_i)^2}{\sigma_i^2}$, where σ_i^2 is the variance in bin i, m_i is again the number of model stars and n_i the observed number of stars in bin i. The values for χ^2, the number of degrees of freedom and the corresponding probability that the data can be drawn from the model population are represented in Table 6.3. The numbers of degrees of freedom are equal to the number of populated bins minus the number of free parameters. Fig. 6.13 illustrates the residuals for various models. Each panel shows the residual model - data weighted by the variance (Dolphin, 2002). The color coding indicates bins where the model predicts more stars than observed (bright) respectively where the model underpredicts the number

of stars (dark). The first panel of Fig. 6.13 shows the best-fit model, while the second panel shows a continuous star formation (both assume a Chabrier IMF). The continuous model predicts too few old (i.e. cold) stars compared to the observations, while it predicts too many young (i.e. warm) stars. The data is well fit by a mostly old (> 5 Gyrs) population with an admixture of recently formed stars ($<$ few 100 Myrs) as in case of the best-fit model. The discrepancy between a continuous formation scenario and a time varying star formation increases in case of IMFs favoring the formation of massive stars (right two panels).

6.6 Results

The data fit best a normal Kroupa/Chabrier IMF (49% acceptance probability, see Tab. 6.3) but either flatter or steeper IMF can be accommodated within the 2 sigma uncertainties. The distribution in the H-R diagram does not strongly constrain the IMF, in contrast to the diffuse light and dynamical mass discussed in Sections 6.6.2 and 6.6.2. This is not surprising, since the old giant branch contains stars with zero age main sequence (ZAMS) masses between $1\,M_\odot < M < 1.2\,M_\odot$. Thus the mass interval is too small to be significantly affected by changes of the IMF slope. The slope can affect the abundance of young giants, since they cover the mass range $2.5\,M_\odot < M < 6\,M_\odot$. However their abundance depends sensitively on the star formation rate of the last few hundred Myrs. Furthermore, the bright and massive end of the population suffers from low number statistics. This makes statements on the IMF slope uncertain. In general, the IMF and the star formation rate as a function of time are largely degenerate. Given the coarse sampling of the age bins, the data is not sufficient to constrain the IMF by the fitting procedure itself. The fit only allows to derive relative star formation rates for each assumed IMF. However, it is possible to constrain the IMF using the measured dynamical mass. Since each model predicts a certain mass composition of the population, it is possible to distinguish between different models. In any case, no acceptable fit was achieved for continuous star formation scenarios, irrespective of the assumed IMF.

6.6.1 Star formation rate over cosmic time

In the following we only consider the formation scenario with a Chabrier/Kroupa IMF. This is motivated by the slight preference of the fitting, the intriguing total mass prediction of the model matching the dynamical measurements and the agreement with the observed diffuse background light (see next sections). We find that the giant population of the Galactic Center is old. Fig. 6.14 shows the star formation rate as function of time (assuming a normal IMF). The formation rate more than 5 Gyrs ago was on average $3 \pm 0.6 \times 10^{-4} M_\odot/yr$. According to our fit, roughly 80% of the total mass formed more than 5 Gyrs ago. The formation period was followed by a period of reduced star formation lasting another 4-5 Gyrs. The star formation rate reached a minimum about 1 Gyr ago. During the last few hundred Myrs, the formation rate increased again. The disk of young stars are part

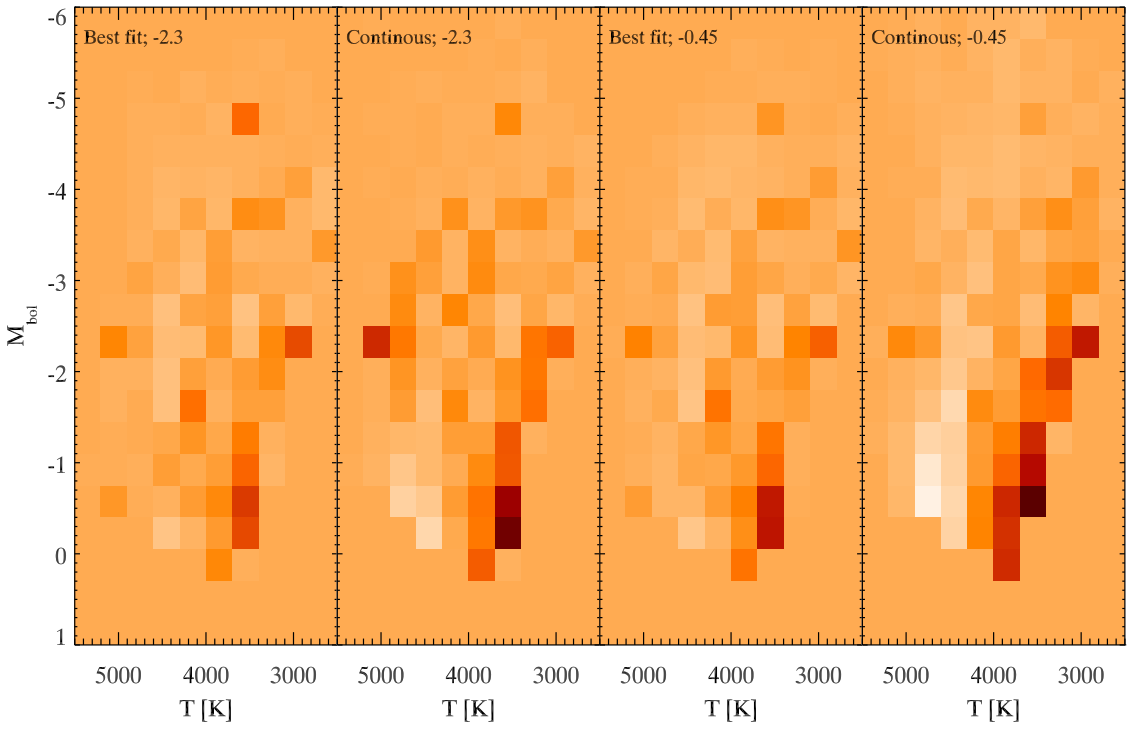

Figure 6.13 Residual diagrams of two best-fit models (with a normal Kroupa IMF, $\alpha = -2.3$ and a flat IMF, $\alpha = -0.45$) compared with models of continuous star formation and the same IMFs. Each panel shows the residual model - data H-R diagram weighted by the variance in each H-R bin. Lighter areas indicate the model overpredicting the number of stars in the corresponding bin compared to the actual data. Darker regions indicate bins where the model predicts too few stars compared to the data. It is apparent that the data is well matched by models allowing for a time varying star formation rate. The continuous star formation models predict too few old stars on the cold giant branch, while they overpredict the number of young and massive giants on the warm branch. The discrepancy is worse in case of the flat IMF. The best-fit models however reproduce both branches and show only little discrepancies.

Table 6.3 The star formation rate for each age bin and various model IMFs.

Model	Age bin [Gyr]	IMF slope [a]	χ^2/d.o.f. (prob.)[b]	Absolute SFR $[10^{-4} M_\odot yr^{-1}]$	$\sigma_{\rm SFR}$
Model 1	12 - 5	-2.7 (-1.3)	122/94 (3%)	3	0.6
	5 - 1	...	...	0.3	0.5
	1 - 0.2	...	...	1	0.5
	0.2 - 0.05	...	...	12	3
Model 2	12 - 5	-2.3 (-1.3)	105/104 (49%)	3	0.6
(Chabrier)	5 - 1	...	...	1	0.5
	1 - 0.2	...	...	0.5	0.5
	0.2 - 0.05	...	...	8	2
Model 3	12 - 5	-1.5	157/106 (0.1%)	13	3
	5 - 1	...	...	2	1
	1 - 0.2	...	...	1	0.7
	0.2 - 0.05	...	...	11	3
Model 4	12 - 5	-0.85	143/100 (0.3%)	126	27
(Top-heavy)	5 - 1	...	...	24	11
	1 - 0.2	...	...	6	3
	0.2 - 0.05	...	...	50	12
Model 5	12 - 5	-0.45	131/107 (6%)	614	124
(Flat)	5 - 1	...	...	97	43
	1 - 0.2	...	...	22	10
	0.2 - 0.05	...	...	145	34
Continuous	12 - 0.05	-2.3 (-1.3)	178/105 ($< 0.01\%$)	2	...
Continuous	12 - 0.05	-1.5	181/111 ($< 0.01\%$)	6	...
Continuous	12 - 0.05	-0.85	176/116 ($< 0.01\%$)	34	...
Continuous	12 - 0.05	-0.45	211/115 ($< 0.01\%$)	113	...

[a] The upper and lower mass cutoff is: $0.5 < M < 120$. The models 1 and 2 extend to $0.1 < M < 120$ with a flatter slope between $0.1 < M < 0.5$.

[b] Outlier corrected χ^2 and degrees of freedom. Outliers are bins off by more than $10\,\sigma$. The d.o.f. corresponds to the number of populated H-R diagram bins (ignoring significant outliers) minus the number of fit parameters. Model 1-5 have four independent fit parameters (age bins), while the continuous models have only one free scaling parameter. In brackets, the acceptance probability is stated.

of the increased formation rate. Our results are in excellent agreement with the earlier findings of Blum et al. (2003) (compare Fig 6.14). The recent period of star formation accounts for about 10% of the total formed mass. Note, the recent star formation rate seems to be higher than several Gyrs ago. However the bin widths are very different. Each bin represents an average formation rate. The actual formation several Gyrs ago can have happened on short bursts with significantly higher star formation rates. The present day cluster contains roughly 50% of the total processed gas mass in living stars and 10% in remnants. The rest has been lost via stellar winds, explosions and potentially been swallowed by the SMBH. For simplicity, we set up a simple analytic model that approximates the measured SFR as function of time (solid line in Fig. 6.14).

$$\mathrm{SFR}(t) = 6.8 \times 10^{-5}\,\mathrm{M}_\odot/\mathrm{yr} \times e^{t/5.5\,\mathrm{Gyrs}} + 4.3 \times 10^{-3}\,\mathrm{M}_\odot/\mathrm{yr} \times e^{-t/0.06\,\mathrm{Gyrs}}. \tag{6.3}$$

where t is the look-back time. The integration of the model yields the integrated mass as function of time. As Fig. 6.15 shows, about half of the cluster mass formed before a redshift of one. This suggests, that the nuclear cluster formed at a time, when the galaxies build up most of their stellar mass. In that sense, the nuclear cluster formed at the same time, or shortly after the bulge, about 10 Gyrs ago (Zoccali et al., 2008).

Implications from the faint main-sequence population

The two confirmed A-stars and the one candidate (Sec. 6.3.1) are ideal tracers for star formation during the last few hundred Myrs. Early-type stars with K-band magnitudes $17 < m_K < 18$ (assuming $A_K = 2.8$ and $R_0 = 8.3\,\mathrm{kpc}$) are main sequence B9/A0 dwarfs with average lifetimes of 500 Myrs. Late-type stars in the same magnitude range can only be giants that have already left the main sequence. These giants have ages between 1 to 12 Gyrs. Thus the number count ratio of the two populations provides a measure of the star formation efficiency during the last 500 Myrs relative to earlier star formation. This ratio is largely independent of systematic uncertainties since it avoids issues like incompleteness and spectroscopic detectability. We included the candidate star, in the early-type population. In total we found three (two confirmed) early-type stars and 30 late-type stars in this magnitude bin. We used the IAC-STAR code and found that in case of continuous star formation over 12 Gyrs with a Kroupa IMF, the predicted early-to-late ratio is close to unity. The observed ratio therefore argues for a average star formation rate during the last 500 Myrs of only about $10 \pm 6\%$ of the average formation rate 1-12 Gyrs ago. To convert the relative formation rate into an absolute rate, we used the star formation rate inferred in the previous section and calculated an average rate of $2.3 \pm 0.5 \times 10^{-4}\,M_\odot$ between 1-12 Gyrs look-back time. Using this value, we obtained an average star formation rate of $2.3 \pm 2.1 \times 10^{-5}\,M_\odot$ during the last 500 Myrs (see Fig. 6.14). Within the errors this is consistent with the one derived by the H-R fitting. The A-star ratio provides an independent measurement of the relative star formation rates. It is another indicator for the early formation of the nuclear cluster.

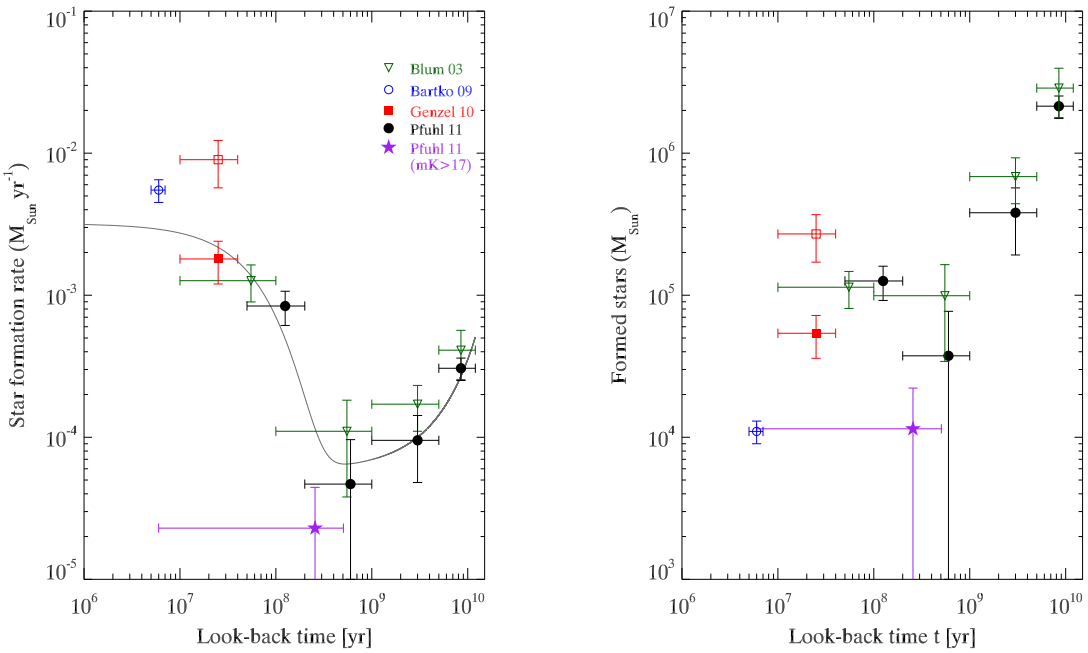

Figure 6.14 **Left:** Star formation rate of the Galactic Center as function of time. The black circles represent the best-fit to the H-R diagram with a Chabrier/Kroupa IMF. The mass error is given by the 1σ error of the fit. The age error is simply the width of the age bin. For comparison, the star formation history derived by Blum et al. (2003) scaled to a radius of 1.2 pc is indicated (green triangles). The star formation rate derived by red supergiants (Genzel et al., 2010) within 1 pc (red square, filled) and within 2.5 pc (red square) and the stellar disks (blue circle) (Bartko et al., 2009) are indicated. The star symbol (purple) indicates the recent star formation rate inferred by the early-to-late ratio of faint GC stars (Sec. 6.6.1). The solid gray line shows a simple exponential model (see text) of the star formation as function of time. **Right:** The total mass formed in each age bin is shown. Although star formation occured at a high rate during the last few hundred Myrs, the total mass contribution is $< 10\%$. The bulk of the stellar mass formed more than 5 Gyrs ago.

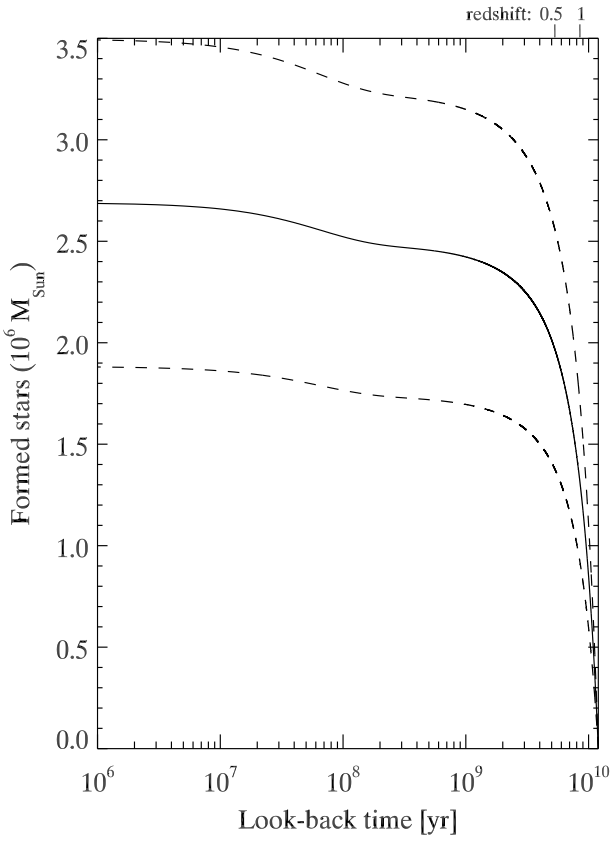

Figure 6.15 The integrated mass as function of time as obtained by Eq. 3 in Sec. 6.6.1 is shown. The dashed curves represent the $1\,\sigma$ uncertainty. Note, today's cluster mass is only about 50% of the total formed mass. The remaining mass is lost due to stellar evolution.

Comparison with previous work

Maness et al. (2007) found that the giant population of the GC is on average warm and thus young. Consequently, they favored models with a normal IMF and an increasing star formation rate or a top-heavy IMF and continuous formation. Maness et al. (2007) used a CO index that is very sensitive to systematic effects. In particular, their CO index, though widely used, was recently discovered to vary with spectral resolution (Mármol-Queraltó et al., 2008). Since no suitable library was publicly available at the time of writing, they also used template libraries with resolutions between $R \sim 3000 - 5000$ to calibrate their $R \sim 2000$ data. The sum of the effects caused an underestimation of the CO equivalent width and an according overestimation of the stellar temperatures. This led to the interpretation of a mostly young giant population. Applying the same methods as Maness et al. (2007) together with a CO index that is less susceptible to systematic effects and using the newly available library of Rayner et al. (2009) with $R \sim 2000$, allowed us to revisit the star

formation history of the Galactic Center.

6.6.2 The mass composition of the nuclear cluster

The present-day mass composition of the nuclear star cluster depends sensitively on the formation history and the IMF. The mass contribution of stellar remnants and stars as well as the total amount of consumed gas depends on the age and the IMF of a population. The consumed gas mass is larger than the sum of remnant and stellar mass because a significant mass fraction is lost due to stellar evolution. Since massive stars lose a larger fraction of their initial mass, the gas consumption increases with flatter IMFs for the same total stellar mass. The same is true for the remnant mass. Massive stars have main-sequence lifetimes that are significantly shorter than the age of the galaxy. Therefore many generations of massive stars evolve through time and finally end as remnants. Thus, IMFs that favor massive stars produce more and heavier remnants. As a consequence, the mass contribution of stars still burning hydrogen drops with flatter IMF slopes.

Constraints from the dynamical mass

Various models have been fit to the data (Sec. 6.5.1). Each model yields the star formation rate as function of time under the assumption of a certain IMF. To derive the absolute mass contribution, it is necessary to scale the models according to the actual star counts. To get a representative number for the nuclear cluster we used the stellar surface density from Schödel et al. (2007). As discussed in Sec. 6.1 the radial extent of the NSC is $\sim 5\,\mathrm{pc}$. Our data, however, probed only the inner $30''$ (1.2 pc). Therefore we restricted ourselves to that radius. By assuming $30''$ as a sharp edge, the surface density from Schödel et al. (2007, their fig. 12) yields ~ 18200 stars with $m_K < 17.75$ within a projected radius of $30''$ from Sgr A*. Between 45% to 55% of the projected stars are also contained within a 3D distance of $30''$, depending on the radial density profile derived by Schödel et al. (2007). Thus, we assumed a total of 9100 stars with $R_{3D} < 1.2\,\mathrm{pc}$ to scale the remnant-, stellar- and total gas mass for each model. Table 6.3 shows the derived star formation rate for each model IMF. Fig. 6.16 shows the mass composition for the models derived in Sec. 6.5.1. The model predictions have to be compared with the dynamical mass estimates of the nuclear cluster (see Fig. 6.16). The total mass enclosed within $30''$ is $5.7 \pm 0.9 \times 10^6\,M_\odot$. The SMBH contributes $4.3 \pm 0.5 \times 10^6\,M_\odot$ (Ghez et al., 2008; Gillessen et al., 2009), while the remaining $1.4 \pm 0.7 \times 10^6\,M_\odot$ (Genzel et al., 1996; Trippe et al., 2008; Schödel et al., 2009; Genzel et al., 2010) are contained in stars and stellar remnants. Numerical simulations of Freitag et al. (2006) have shown that during 10 Gyrs about $4 \times 10^5\,M_\odot$ stellar and $1 \times 10^5\,M_\odot$ remnant mass is removed from the cluster by the SMBH through tidal disruption and inspiral. The cluster composition is scaled to match the observed number of giants. Thus, the inferred stellar mass intrinsically accounts for stars lost to the SMBH because giants and giant progenitors are equally likely to be disrupted as unresolved main-sequence stars constituting the bulk of stellar mass. The situation for remnants, however, is different. The main remnant contribution comes from stellar BH dominating the mass density

in the inner 0.1 pc. Due to their mass ($\sim 10 M_\odot$) they are significantly affected by mass segregation and more likely to inspiral into the SMBH. Consequently, the inspiral of stellar BHs has to be taken into account in the mass budget. We simply added $10^5\,M_\odot$ with an uncertainty factor two to the observed dynamical mass to constrain the IMF. We took the value determined by Freitag et al. (2006) as being constant with IMF. This might be the weak point in the line of argument, since Freitag et al. (2006) assumed a Chabrier/Kroupa IMF in their simulations. As Fig. 6.16 shows, the cluster composition depends sensitively on the assumed IMF. For flatter IMFs, the number of stellar BH increases, however, the mean mass increases accordingly making mass segregation less efficient. Thus the actual mass transfer between the cluster and the SMBH as function of IMF can only be addressed by further simulations. Keeping the limitations in mind, the dynamical mass plus the removed mass therefore make IMFs with a slope flatter than $\alpha = -1.1$ unlikely. Even if the transferred mass is significantly higher, models flatter than $\alpha = -0.8$ violate the total enclosed mass (SMBH+cluster). Mechanisms that expel remnants or stars are very inefficient. One mechanism is the evaporation of stars from the nuclear cluster. However, for the GC the timescale is greater than a Hubble time (Alexander, 2005). Mass segregation is another mechanism for removing stars. This mechanism moves low-mass constituents outward, and high-mass constituents inward, without changing the radial density profile significantly. Miralda-Escudé & Gould (2000) suggest that inward migration of a considerable number of bulge stellar blackholes can remove low mass stars from the nuclear cluster. According to their model, the low mass stars are supposed to form a core with a radius of 1-2 pc. Observations however find a core radius of about 0.3 pc (Schödel et al., 2007). If the observed core is related to mass segregation, then the effect is smaller than predicted. Our constrains on the IMF are however not weakened by potential mass segregation. Our models use the number of observed stars as a scaling for the total processed mass (and remnants produced). Therefore if low mass stars are removed from the inner region, our scaling underestimates the remnant mass. The inferred stellar mass however is not changed, because giants and unresolved main sequence stars have very similar masses ($\sim 1\,M_\odot$). Thus the total predicted mass will grow if we take into account that low mass stars are removed due to mass segregation. This makes our statement on the IMF constrains even more significant. In general, it is very hard to remove mass in form of stars and remnants from a nuclear cluster (a SMBH binary, however is able to remove stars efficiently). The processed gas mass, unlike stars and remnants, can be expelled from the nuclear cluster due to supernovae or AGN activity in the distant past of the SMBH. Stellar winds are also able to remove gas from the cluster. While the low mass main-sequence stars and giants have wind speeds significantly lower ($v_{\rm wind} \sim$ few 10 km/s) than the escape velocity of the NSC the most massive stars ($v_{\rm wind} \sim 1000$ km/s) can efficiently remove gas from the cluster (McLaughlin et al., 2006; Martins et al., 2007). Therefore, the processed gas mass cannot constrain the IMF although flat IMFs require a factor hundred greater gas masses than Kroupa like IMFs. Summarizing the arguments we can say that IMFs flatter than $\alpha > -1.1$ violate the observed cluster mass. IMFs flatter than $\alpha > -0.8$ exceed even the total mass (SMBH+cluster).

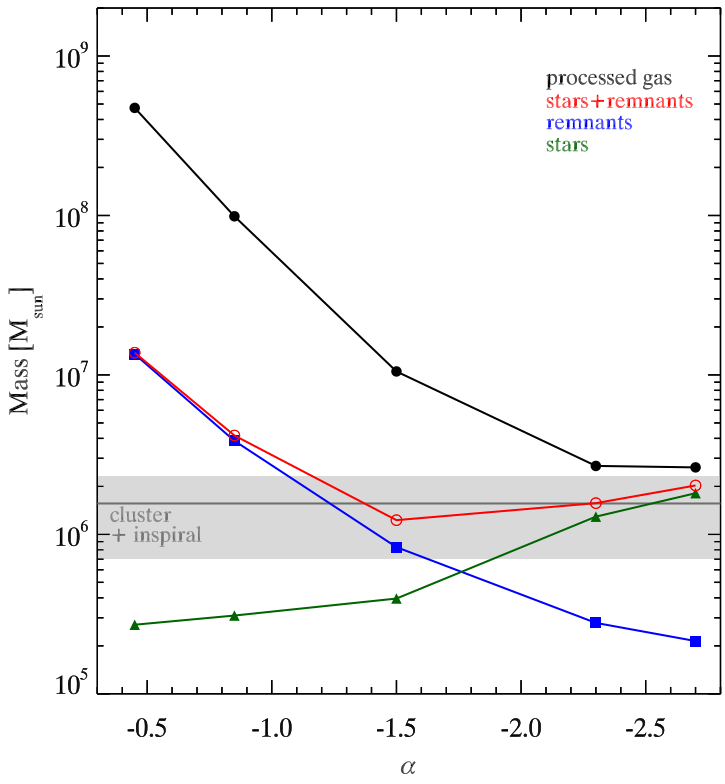

Figure 6.16 Mass composition of the inner 1.2 pc after 12 Gyrs of star formation. The composition and total mass depends sensitively on the assumed IMF. The symbols show the five fitted models (Tab. 6.3) with various IMF slopes $-2.7 \leq \alpha \leq -0.45$. Green triangles represent the stellar mass, blue squares represent the remnant mass, red open circles show the sum of remnant and stellar mass and black filled circles show the total processed gas mass. The dark gray horizontal line indicates the dynamical mass within 30″and its uncertainty (light gray area).

Constraints from the diffuse H-band background

As discussed in Sec. 6.2.1, depending on the IMF and star formation history the diffuse background light from faint unresolved stars may probe the bulk of the stellar population. We find that the diffuse background contributes $H_{\rm diff}/H = 27\pm9\%$ to the total H-band flux. Furthermore, we derived a mass-to-diffuse-light ratio of $M_{\rm dyn}/H_{\rm diff} = 2.6 \pm 1.5\, M_{\odot}/L_{H,\odot}$. In the following we used the inverse ratio $H_{\rm diff}/M_{\rm dyn}$ for convenience. We compared both quantities to our best-fit models (Sec. 6.5.1). To show how $H_{\rm diff}/H$ and $H_{\rm diff}/M$ depend on the IMF slope and overall star-formation history, we used the population synthesis code *STARS* (Sternberg, 1998) to compute these ratios for a range of IMFs and star-formation time-scales t_0 for simple histories $SFR(t) \propto e^{-t/t_0}$. We considered a Kroupa IMF, and also three power-law IMFs, $dN/dm \propto m^{-\alpha}$, with α equal to -1.5, -1.35, and -0.85. All of the IMFs range from 0.01 to 120 $M_{\odot}$. We used Geneva evolutionary tracks for solar metallicity stars, combined with empirical colors and bolometric corrections for dwarfs, giants, and supergiant stars. For low-mass stars (< 0.8 $M_{\odot}$) we computed the H-band luminosities along the lower main-sequence using the calibrations of Henry & McCarthy (1993). We considered exponentially decaying ($t_0 = 3$ Gyr), continuous ($t_0 = \infty$) and exponentially increasing ($t_0 = -3$ Gyr) star-formation rates, for an assumed cluster age $t = 13$ Gyr, and fixed dynamical mass $M_{\rm dyn} = 1.5 \times 10^6 M_{\odot}$. The results are displayed in Figure 6.17 in the $H_{\rm diff}/M$ versus $H_{\rm diff}/H$ plane. The gray areas indicate the measurement including the $1\,\sigma$ uncertainty. Figure 6.17 shows that $H_{\rm diff}/M$ and $H_{\rm diff}/H$ both decrease for flatter IMFs. This behavior is due to the relative increase in remnant mass from massive stars, and the reduction in the relative fraction of diffuse light from low mass stars. For a given IMF, $H_{\rm diff}/M$ decreases but $H_{\rm diff}/H$ increases, as the history is altered from increasing, to steady, to declining star-formation, because the total luminosity for fixed mass is reduced for this sequence of histories, while the fraction of light produced by the accumulating long-lived low-mass stars is increased. In Figure 6.17 we also indicate the positions of the best-fit models discussed in Sec. 6.5.1 and listed in Table 6.3. Figure 6.17 shows that the observed $H_{\rm diff}/M$ and $H_{\rm diff}/H$ ratios require steep (canonical) IMFs and continuous or mildly decaying star-formation. In particular, flat IMFs with $\alpha > -1.5$ are inconsistent with the observations

Our measurements of the diffuse H-band background can be compared to the findings of Löckmann et al. (2010), who used the diffuse K-band background together with the dynamical mass to derive $M/K_{\rm diff} = 1.4^{+1.4}_{-0.7}\, M_{\odot}/L_{\odot,K}$, which was then compared with model predictions. Their mass-to-diffuse-light ratio is somewhat lower than our value ($M/K_{\rm diff} = 1.9 \pm 1.2\, M_{\odot}/L_{\odot,K}$), yet consistent within the errors. The difference originates from the assumed extinction value. Löckmann et al. (2010) used $A_K = 3.3$ published by Buchholz et al. (2009). However, this value is 0.5 magnitudes (factor 1.6) higher than the most recent one published by Schödel et al. (2010) and Fritz et al. (2011). Correcting for this difference removes the discrepancy between their finding and ours. Their analysis favored an IMF steeper than $\alpha = -1.3$ together with a continuous star formation rate or an increasing star formation rate. Our analysis confirms their finding of a steep IMF. Taking into account the revised extinction our finding of an early star formation is also

consistent with the findings of Löckmann et al. (2010). However, we additionally used the ratio of diffuse-light to total light to constrain the star formation history even further.

6.7 Discussion

All statements concerning the star formation history of the NSC have been made under the assumption that the traced population is representative for the whole cluster. The radial extent of the cluster is ~ 5 pc, i.e. larger than the radii probed with our SINFONI observations. However, the inner 1.2 pc contain already $6 \times 10^6\ M_\odot$ of the total $30 \times 10^6\ M_\odot$. Thus we cover about 20% of the total cluster mass and gives us confidence that our results are somewhat representative for the whole cluster.

6.7.1 Initial Mass Function in the GC

We find that the old giant population must have formed with a IMF steeper than $\alpha < -1.3$, probably with a normal Chabrier/Kroupa IMF. In any case, the IMF must have been significantly different from the IMF observed in the young stellar disks. Paumard et al. (2006) and Bartko et al. (2010b) found that the young stellar disks in the GC have formed preferentially massive stars. They favored an almost flat IMF with $dN/dm \sim m^{-0.45}$ (Bartko et al., 2010b). This indicates that the environmental conditions at the time of formation were different in the past. The nuclear cluster probably formed at a time, when the SMBH itself was younger and less massive. With the radius of influence smaller than today, the gravitational potential resembled more a normal cluster. Consequently the IMF was closer to the universal one. The nuclear cluster might also have been contaminated by in-spiraling clusters that had formed outside of the Galactic Center. Depending on their mass, clusters within several 10-100 pc can spiral into the NSC during a Hubble time (Agarwal & Milosavljević, 2011). Both effects lead to an IMF significantly steeper than the one observed in the young stellar disks today.

6.7.2 Star formation in the vicinity of the GC

The Galactic Center region shows star formation at all ages. The massive Arches and Quintuplet clusters at distances of a few ten pc were formed 2 and 4 Myrs ago (Figer et al., 2002, 1999). The stellar disk in the central cluster was formed about 6 Myrs ago (Paumard et al., 2006; Bartko et al., 2009) and at roughly 50 pc distance the Sgr B2 cloud harbors several massive star cluster in the making. Figer et al. (2004) used HST photometry of several fields within 100 pc of the center to derive the star formation history. They find a continuous star formation in their FoV. Genzel et al. (2003) and Buchholz et al. (2009) used AO-assisted photometry of the nuclear cluster and found that the KLF is well matched by a bulge-like (8-10 Gyr) population with an admixture of young main-sequence stars. Blum et al. (2003) used spectroscopic data of the most luminous giants within 2.5 pc from Sgr A*. Our work confirms their favored formation scenario. The star formation happened

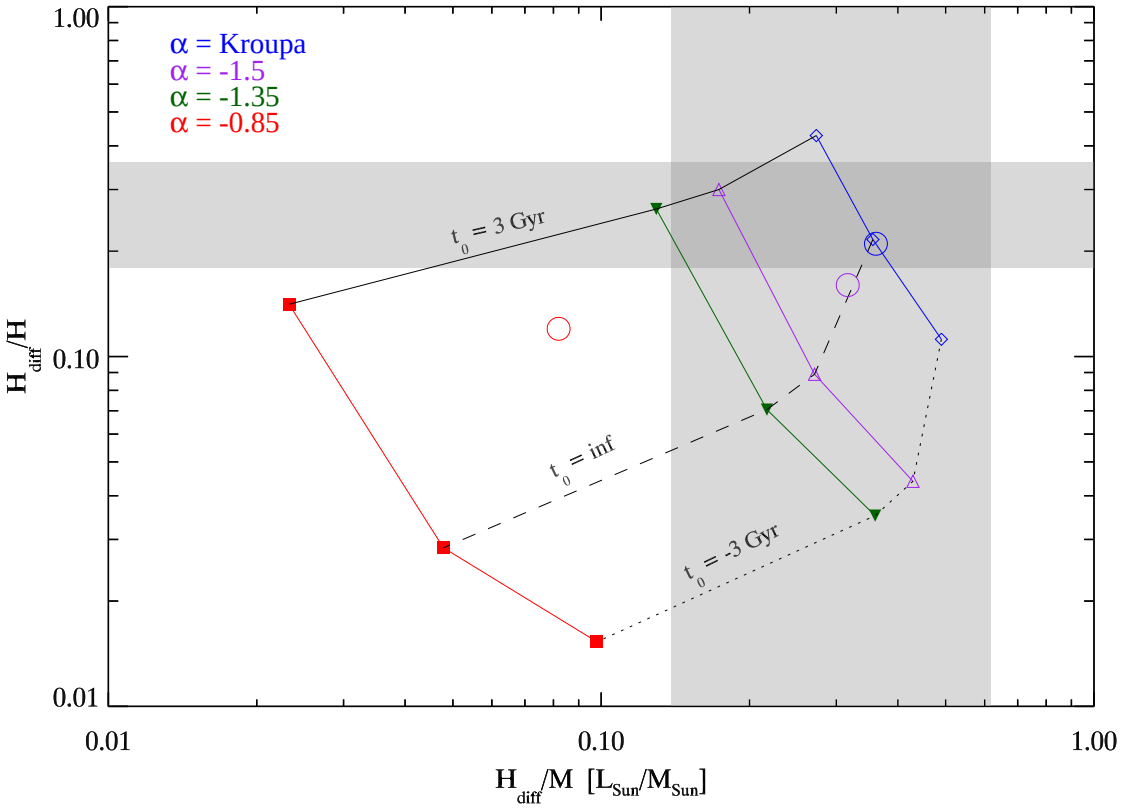

Figure 6.17 The observed ratios of diffuse background light to the total H-band luminosity $H_{\rm diff}/H$ (horizontal bar shows $1\,\sigma$ confidence interval) and the inverse mass-to-diffuse-light ratio $H_{\rm diff}/M_{\rm dyn}$ (vertical bar shows $1\,\sigma$ confidence interval) constrain the IMF and the star formation history. The colors indicate the assumed IMF. The best-fit models (Tab.6.3) are represented by open circles. For comparison, simple models with exponentially declining, constant and exponentially rising (connected by solid, dashed, dotted lines) star formation are shown. The star formation rate in this case is parametrized as $\mathrm{SFR}(t) \propto e^{-t/t_0}$, where $t_0 = \mathrm{inf}$ corresponds to continuous star formation, $t_0 = 3\,\mathrm{Gyr}$ corresponds to a burst with an exponential decline timescale of 3 Gyrs and $t_0 = -3\,\mathrm{Gyr}$ corresponds to a raising star formation rate. The assumed cluster age is $t = 13\,\mathrm{Gyr}$. Models with an increasing star formation rate fail to produce the observed amount of background light, while models with decaying star formation underpredict the $H_{\rm diff}/M_{\rm dyn}$ ratio. The mismatch gets worse for flatter IMFs. Only the best-fit or the continuous model with a normal Kroupa IMF match both constraints.

predominantly at old times. An intermediate period showed a reduced star formation, while during the last few 100 Myrs the star formation rate was increasing. This is also consistent with findings based on the stellar disks and the number of red supergiants. Roughly 75-90% of the mass contained in the central cluster formed 5-12 Gyrs ago. The formation of the cluster might coincide with the formation of the bulge around 10 ± 2.5 Gyrs ago (Zoccali et al., 2008). The α-element ratios require the bulge to have formed on a short timescale (~ 1 Gyr). Whether this is also true for the Galactic Center cannot be answered with the given uncertainty of the data. The fact that Buchholz et al. (2009) do not find a young giant population is not surprising, since those stars make up only $\sim 10\%$ of the number counts. The KLF fitting is not sensitive enough and since the young giants are rather warm and bright, they might be attributed to the admixture of young main-sequence stars. The same is true if the results are compared to Figer et al. (2004). They, however, find a continuous star formation rate within 100 pc. This does not contradict our findings is consistent with the idea of recurrent episodic star formation in the greater Galactic Center region (Serabyn & Morris, 1996). The star formation events themselves happen on spatial scales of < 1 pc (e.g. Central-, Arches-, & Quintuplet-Cluster). If one assumes that the individual star formation events happen incoherently, then one would naturally expect a continuous star formation history on scales $>> 1$ pc. Thus Figer et al. (2004) find a star formation history that is smoothed across many episodic single events.

6.7.3 Alternative explanation for the young giants

There is another, more exotic explanation for the existence of the warm giants. The warm giants could be tidally scattered old giants. Stars, which pass the central SMBH close to the tidal disruption radius $r_t \approx 90\,\mu$as experience a major tidal disturbance. This most likely leads to spin-up mixing and possibly some mass loss. Although the observational consequences are very uncertain, it is expected that these stars will appear more luminous and hotter after the tidal interaction. Despite the small size of the tidal radius r_t, the number of tidally scattered stars, which accumulate over 12 Gyrs can be as large as 10% of the total population (Alexander, 2005). This value matches the observed percentage of warm giants. One possible way to distinguish tidally scattered old giants from young giants could be a decreased $^{12}C/^{13}C$ ratio, which might be a smoking gun for increased mixing processes. Note, the different $^{12}C/^{13}C$ ratio of giants and dwarfs are commonly accepted as evidence for mixing during the giant evolution. Other processes like tidal spin-up through other stars can increase the average rotation and lead to rotational mixing. This however seems unlikely, given the narrow distribution of the warm giants in the H-R diagram. Tidal spin-up is a stochastic process and would therefore exclude a gap between the cold giant branch and the warm giant branch. Whether the distribution in the H-R diagram would be consistent with a tidal scattering close to the SMBH needs more theoretical investigation. However a single star is unlikely to undergo more than one close interaction with the SMBH (Alexander, 2005). Overall we think that most of the warm giants are actually young giants. It seems unlikely that all stars which fall in the region of young giants are only masked old giants. We would expect a larger number of outliers, which cannot be

explained with ordinary evolutionary tracks. Furthermore, recent star formation is well established in the stellar disks. However some of the presumably warm giants could be tidally scattered old giants. The investigation of these stars could provide an independent tool to study the cluster properties, since the scattering efficiency depends on the cluster mass distribution.

Chapter 7

Conclusions and future outlook

This thesis is divided into an astronomical instrumentation- and an observation part. In the course of this thesis, we have developed two subsystems of the 2nd generation VLTI instrument GRAVITY. The guiding system stabilizes the image jitter and pupil wander in the VLTI tunnel, ensuring an optimum beam quality at the GRAVITY beam combiner instrument. The fiber coupler subsystem feeds the stabilized beam from the telescopes into single-mode fibers. Both systems have been brought from a concept study to the actual implementation.
The astrophysical results reported in this thesis are based on imaging and spectroscopy data of the Galactic Center obtained at the VLT. With the data it was possible to construct a detailed Hertzsprung-Russell diagram of the Milky Way's nuclear cluster and to infer the star formation history of the stars in the immediate vicinity of the super-massive black hole.

7.1 Instrumentation results

7.1.1 Fiber coupler development and implementation

The fiber coupler concept and opto-mechanical design developed in the course of this thesis ensures an efficient single-mode coupling of the telescope beams into the beam combiner instrument. Each fiber coupler unit provides the necessary functions to rotate the field on sky, to adjust the linear polarization orientation, to fringe-track, and to adjust the field- and the pupil positions of one telescope beam. It splits the beam with a dichroic and feeds the science band $1.95 - 2.45\,\mu$m into single-mode fibers, while the acquisition band $1.5 - 1.8\,\mu$m as well as the guiding lasers at 658 nm and 1200 nm are propagated to the acquisition camera and the guiding receiver. A special roof-prism allows splitting the field on sky for dual-field interferometry or partitioning the beam for single-field interferometry. The design ensures a diffraction limited beam and an optimum throughput.
At the time of writing the first fiber coupler unit is almost completely assembled. Most of the optics and especially the critical optical components, such as the roof-prism, the

off-axis parabolic mirrors and the half-wave plate have already been delivered to MPE. The H/K dichroic is not yet available but a contract has been placed. The main results of the fiber coupler development are:

- The fiber coupler optical design is close to aberration free. It features a nominal K-band Strehl ratio of $> 99\%$ across the $2''$ FoV of the VLTI. This exquisite image quality is achieved by a combination of off-axis parabolic mirrors to avoid field aberrations and the absence of lenses to avoid chromatic aberrations.

- When the surface accuracy of the supplied mirrors and optics is taken into account, the Strehl is still $\sim 94\%$ in the K-band.

- Given the plethora of optical functions provided by the fiber coupler, the nominal transmission of 85.9% represents what can realistically be achieved. Using gold coatings for the mirrors and anti-reflective coatings for the glass surfaces throughout the design, provides the best transmission possible in the K-band.

- A corner stone of the optics is the roof-prism. Although only $1.5 \times 4\,\mathrm{mm}^2$ in size, the prism layout allows to either split the FoV in the dual-field operation of GRAVITY or to use it as a beam splitter in the single-field operation.

- The half-wave plate, necessary to adjust the linear polarization, has been designed for operation in K-band and at the instrument temperature of 240 K. The combination of two MgF_2 and SiO_2 glass plates with different thickness optimizes the phase difference between ordinary and extra-ordinary ray to $180° \pm 0.9$. This results in a minimum polarization cross-talk of $< 0.02\%$.

- The optical design based on aluminum off-axis mirrors has many advantages compared to a lens-based design, such as reduced costs, a small overall volume and the absence of chromatic aberrations. Since the off-axis mirrors and the fiber coupler structure are made of aluminum, the design is also temperature invariant and requires no re-focusing once cooled down. Poor surface accuracy and roughness prevented the widespread application of diamond-turned aluminum mirrors in optical systems until a few years ago. However, the off-axis mirrors supplied to MPE with a surface accuracy of $< \lambda/20$ RMS at 633 nm and a roughness of $R_q = 1.7\,\mathrm{nm}$ are suitable for near infrared optics.

7.1.2 Guiding system development and control-loop performance

The goal of micro-arcsecond astrometry with GRAVITY can only be achieved if the telescope beams are actively stabilized (Section 2.7). The guiding system, presented in this thesis, has been developed for this purpose. It consists of two complementary subsystems, correcting pupil wander and image jitter between the telescopes and the beam combiner instrument.
The tip/tilt guiding system uses an artificial laser beacon to correct high frequency image

jitter occurring in the VLTI tunnel. Low frequency image drifts are sensed on sky by the acquisition camera. The combination of a laser beacon and on sky guiding provides an efficient way to correct the tip/tilt power-spectrum in the tunnel and to optimize the coupling efficiency into the single-mode waveguides of the beam combiner instrument.
The pupil guiding system uses laser beacons at the telescope spiders together with a Shack-Hartmann-like sensor that allows tracking lateral and longitudinal pupil wander. The tracking concept has been verified in a dedicated measurement campaign at the VLTI. During the campaign the pupil wander has been studied extensively under various conditions. The results allowed to optimize the pupil guiding system for the requirements of the VLTI. The pupil guiding system complements the tip/tilt guiding such that the astrometric error due to combined pupil wander and tip/tilt jitter becomes negligible.
The main results of the guiding system development are:

- The high frequency tip/tilt perturbations in the VLTI tunnel can be corrected with an analogue position sensitive diode tracking on an artificial laser beacon. The beacon itself is introduced by using the scattered light of a 658 nm laser focused onto a field plane of the star separator.

- The combination of the acquisition camera sensing slow image drifts and the position sensitive diode sensing high frequency jitter allows correcting most of the tunnel atmosphere. The system reduces the typical 54 mas 2-axis RMS (UT) tip/tilt to a residual 7.5 mas RMS. The specification of < 15 mas is clearly met with the proposed design.

- The compensation of the tunnel tip/tilt significantly increases the coupling efficiency of the single-mode fibers. In the current state, i.e. without beam stabilization, on average only about 50% of the light is coupled into the fibers. The tip/tilt guiding system can increase the effective coupling to 85%. The remaining 15% are lost due to AO tilt residuals, which can not be recovered with the guiding system.

- The pupil guiding system can measure and correct VLTI lateral and longitudinal pupil wander simultaneously. Four 1200 nm laser beacons, installed at the telescope spiders, are imaged by a lenslet array on the acquisition camera. The resulting spot pattern allows to retrieve the pupil position along and perpendicular to the optical axis.

- The control-loop model shows, that the pupil guiding system can reduce lateral pupil wander from 4% to about 0.1% of the pupil diameter and the longitudinal pupil from 1 m to about 0.1 m position uncertainty in the 80 mm beam.

- The astrometric uncertainty due to the combination of pupil wander and tip/tilt jitter can be reduced from $\sim 160\,\mu$as to $1.4\,\mu$as by active beam stabilization with the guiding system.

7.1.3 Outlook

With all the fiber coupler optics except the dichroic at hand, the natural next step is to complete the assembly of the first fiber coupler. Among the key figures to be verified are the throughput and the optical quality. The optical quality will be measured with a FISBA phase-shifting interferometer and with a commercial Shack-Hartmann sensor. Once assembled, the optical functions of the roof-prism have to be tested. Here, the minimum object separation, i.e. the edge sharpness has to be measured. Furthermore, the beam splitting mode, with one beam in transmission and one beam in reflection has to be explored and the splitting ratio has to be measured. Once delivered, the dichroic transmission and reflection curve will be characterized with a spectrometer.
In parallel with the testing of the first fiber coupler, the missing parts for the three other fiber coupler units will be ordered. While the dichroic, the half-wave plate, the roof-prism and the flat mirrors already have been ordered for all four units, the off-axis parabola require a call for tender to be placed.
Regarding the guiding system, the first AT will be equipped shortly with a set of pupil beacons. Furthermore, the tip/tilt laser beacons are about to be installed on the UT and AT star separators. Several possible suppliers for the silicon dichroic have been contacted and a decision will follow in the near future.
The integration of the fiber coupler units and the guiding system receivers in the beam combiner instrument will happen between end of 2012 and early 2013.

7.2 Star formation history of Milky Way's Nuclear Star Cluster

In this work, several methods were used to constrain the star formation history of the Milky Way Nuclear Cluster. This is the only nuclear cluster in which individual stars can be resolved and reliable age estimates can be made. For this purpose, we used 450 K-band spectra of late-type giants to derive individual stellar temperatures. By using a CO index that is insensitive to systematic effects such as reddening or instrumental resolution, together with the new stellar library of Rayner et al. (2009) we improved the temperature calibration for the red giants in the Galactic Center. In combination with K-band photometry we were able to construct a detailed H-R diagram of the giant population. The comparison of the observed H-R diagram with model populations allowed us to infer the star formation history of the Galactic Center. Our results are as follows:

1. The bulk of the Nuclear Cluster is old. Roughly 80% of the stellar mass formed more than 5 Gyrs ago. It might have formed at the same time as the Galactic Bulge at a redshift of 1-2.

2. After the bulk of the cluster had formed, a period of reduced star formation followed between 1-5 Gyrs ago. The star formation reached a minimum $\sim$ 1 Gyr ago. Our

inferred star formation history confirms and substantially improves on earlier findings of Blum et al. (2003).

3. Only during the last 200-300 Myrs star formation has set in at a significant level. A population of intermediate age giants are tracers of that period. Making up only 10% of the number counts, the intermediate age population is hardly traceable with the KLF. However, they can be clearly identified in a H-R diagram due to their high temperatures. The spatial distribution and kinematics of those giants resemble the one of the old giant population.

4. We report the first detection of main-sequence B9/A0 stars with magnitudes $17 < m_K < 18$ in the GC. They are the faintest early-type stars having been found in the Galactic Center so far. With these stars we probe the mass regime between $2.2 - 2.8\,M_\odot$ and main-sequence lifetimes of 360-730 Myrs.

5. The ratio of late-type to early-type stars in the magnitude bin $17 < m_K < 18$ yields an independent estimate of the star formation rate during the last 500 Myrs. We find that the average rate during the last 500 Myrs must have been a factor 10 lower than the average rate between 1-12 Gyrs ago. This finding supports the claim of an old cluster population.

6. We find that the bulk of the stellar mass must have formed with an IMF steeper than $dN/dm \sim m^\alpha;\ \alpha < -1.5$. Otherwise, the required remnant and stellar mass would violate the observed dynamical mass and diffuse background. Thus, the bulk of the old stars formed with an IMF significantly steeper than the one observed in the young stellar disks. We suggest that this apparent discrepancy can be naturally explained if the stars formed at a time when the SMBH itself was much younger and less massive. Consequently the sphere of influence was significantly smaller. Without the extreme environment of a SMBH, the stars formed with an IMF close to the universal one. The SMBH was fed by gas including stellar mass loss (Freitag et al., 2006) and dominated the inner few pc over time. With the growing sphere of influence, the IMF became flatter and reached the value observed in the young disk

7. The deep census of the Galactic Center using integral field spectroscopy yields a late-type KLF between $12 < m_K < 18$ with a slope of $\mathrm{d}\log N/\mathrm{d}m_K = 0.33 \pm 0.03$. This confirms the previous findings of Genzel et al. (2003) and Buchholz et al. (2009). The slope is consistent with an old Bulge like KLF (Alexander, 1999).

Taking into account systematic effects leads to an improved age estimate of the Nuclear Cluster. To improve the age estimate further, however, requires a technical leap. The main difficulty is that > 5 Gyrs old isochrones are spaced by only a few 10 K. The necessary temperature accuracy can hardly be achieved by spectral analysis. The most promising way is to detect a turnoff of the main-sequence population. This requires the spectroscopic identification of stars with magnitudes of $m_K \approx 19$. For example, the confirmation of late-type giants only 1 mag fainter than the current limit can unambiguously confirm the

presence of stars with ages of > 10 Gyrs. Yet, the required telescope time, which is needed for the spectroscopic identification of those stars, is tremendous. Furthermore, these faint stars are significantly affected by stellar crowding. Thus further progress will require the resolving power of a new generation of telescopes like the E-ELT or TMT. The same is true to derive a model-free measurement of the initial mass function in the vicinity of the SMBH.

Bibliography

Abuter, R., Schreiber, J., Eisenhauer, F., Ott, T., Horrobin, M., & Gillesen, S. 2006, New A Rev., 50, 398

Agarwal, M. & Milosavljević, M. 2011, ApJ, 729, 35

Alexander, T. 1999, ApJ, 527, 835

—. 2005, Phys. Rep., 419, 65

Alexander, T. & Sternberg, A. 1999, ApJ, 520, 137

Allen, C. & Cox, A. 2000, Allen's astrophysical quantities (AIP Press)

Allen, D. A., Hyland, A. R., & Hillier, D. J. 1990, MNRAS, 244, 706

Amorim, A. & Eisenhauer, F. 2010, *GRAVITY Beam Stabilization & Control*, VLT-TRE-GRA-15885-7101, 3.0

Amorim, A., Lima, J., Pfuhl, O., Eisenhauer, F., Kellner, S., Haug, M., Thiel, M., Carvas, P., Perrin, G., Brandner, W., Straubmeier, C., & Berger, J.-P. 2010, in Society of Photo-Optical Instrumentation Engineers (SPIE) Conference Series, Vol. 7734, 773415

Aparicio, A. & Gallart, C. 2004, AJ, 128, 1465

Aristidi, E., Agabi, K., Azouit, M., Fossat, E., Vernin, J., Travouillon, T., Lawrence, J. S., Meyer, C., Storey, J. W. V., Halter, B., Roth, W. L., & Walden, V. 2005, A&A, 430, 739

Bartko, H., Gillessen, S., Rabien, S., Thiel, M., Gräter, A., Haug, M., Kellner, S., Eisenhauer, F., Lacour, S., Straubmeier, C., Berger, J.-P., Jocou, L., Chibani, W., Lüst, S., Moch, D., Pfuhl, O., Fabian, W., Araujo-Hauck, C., Perraut, K., Brandner, W., Perrin, G., & Amorim, A. 2010a, in Society of Photo-Optical Instrumentation Engineers (SPIE) Conference Series, Vol. 7734, 773421

Bartko, H., Martins, F., Fritz, T. K., Genzel, R., Levin, Y., Perets, H. B., Paumard, T., Nayakshin, S., Gerhard, O., Alexander, T., Dodds-Eden, K., Eisenhauer, F., Gillessen, S., Mascetti, L., Ott, T., Perrin, G., Pfuhl, O., Reid, M. J., Rouan, D., Sternberg, A., & Trippe, S. 2009, ApJ, 697, 1741

Bartko, H., Martins, F., Trippe, S., Fritz, T. K., Genzel, R., Ott, T., Eisenhauer, F., Gillessen, S., Paumard, T., Alexander, T., Dodds-Eden, K., Gerhard, O., Levin, Y., Mascetti, L., Nayakshin, S., Perets, H. B., Perrin, G., Pfuhl, O., Reid, M. J., Rouan, D., Zilka, M., & Sternberg, A. 2010b, ApJ, 708, 834

Bertelli, G., Bressan, A., Chiosi, C., Fagotto, F., & Nasi, E. 1994, A&AS, 106, 275

Blum, R. D., Ramírez, S. V., Sellgren, K., & Olsen, K. 2003, ApJ, 597, 323

Blum, R. D., Sellgren, K., & Depoy, D. L. 1996, AJ, 112, 1988

Bonaccini, D. 1996, *The Paranal Model Atmosphere for Adaptive Optics*, VLT-TRE-ESO-11630-1137

Bonnet, H., Abuter, R., Baker, A., Bornemann, W., Brown, A., Castillo, R., Conzelmann, R., Damster, R., Davies, R., Delabre, B., Donaldson, R., Dumas, C., Eisenhauer, F., Elswijk, E., Fedrigo, E., Finger, G., Gemperlein, H., Genzel, R., Gilbert, A., Gillet, G., Goldbrunner, A., Horrobin, M., Ter Horst, R., Huber, S., Hubin, N., Iserlohe, C., Kaufer, A., Kissler-Patig, M., Kragt, J., Kroes, G., Lehnert, M., Lieb, W., Liske, J., Lizon, J.-L., Lutz, D., Modigliani, A., Monnet, G., Nesvadba, N., Patig, J., Pragt, J., Reunanen, J., Röhrle, C., Rossi, S., Schmutzer, R., Schoenmaker, T., Schreiber, J., Stroebele, S., Szeifert, T., Tacconi, L., Tecza, M., Thatte, N., Tordo, S., van der Werf, P., & Weisz, H. 2004, The Messenger, 117, 17

Born, M. & Wolf, E. 1980, Principles of Optics Electromagnetic Theory of Propagation, Interference and Diffraction of Light, ed. Born, M. & Wolf, E.

Buchholz, R. M., Schödel, R., & Eckart, A. 2009, A&A, 499, 483

Carr, J. S., Sellgren, K., & Balachandran, S. C. 2000, ApJ, 530, 307

Chabrier, G. 2003, PASP, 115, 763

Clenet, Y. & Gendron, E. 2010, *GRAVITY Wavefront Sensor Adaptive Optics Performance*, VLT-TRE-GRA-15882-5201, 3.0

Cunha, K., Sellgren, K., Smith, V. V., Ramirez, S. V., Blum, R. D., & Terndrup, D. M. 2007, ApJ, 669, 1011

Dali Ali, W., Ziad, A., Berdja, A., Maire, J., Borgnino, J., Sarazin, M., Lombardi, G., Navarrete, J., Vazquez Ramio, H., Reyes, M., Delgado, J. M., Fuensalida, J. J., Tokovinin, A., & Bustos, E. 2010, A&A, 524, A73

Davies, R. D., Dickinson, C., Banday, A. J., Jaffe, T. R., Górski, K. M., & Davis, R. J. 2006, MNRAS, 370, 1125

Diolaiti, E., Bendinelli, O., Bonaccini, D., Close, L., Currie, D., & Parmeggiani, G. 2000, A&AS, 147, 335

Do, T., Ghez, A. M., Morris, M. R., Lu, J. R., Matthews, K., Yelda, S., & Larkin, J. 2009, ApJ, 703, 1323

Dolphin, A. E. 2002, MNRAS, 332, 91

Eisenhauer, F., Abuter, R., Bickert, K., Biancat-Marchet, F., Bonnet, H., Brynnel, J., Conzelmann, R. D., Delabre, B., Donaldson, R., Farinato, J., Fedrigo, E., Genzel, R., Hubin, N. N., Iserlohe, C., Kasper, M. E., Kissler-Patig, M., Monnet, G. J., Roehrle, C., Schreiber, J., Stroebele, S., Tecza, M., Thatte, N. A., & Weisz, H. 2003, in Society of Photo-Optical Instrumentation Engineers (SPIE) Conference Series, ed. M. Iye & A. F. M. Moorwood, Vol. 4841, 1548–1561

Eisenhauer, F., Genzel, R., Alexander, T., Abuter, R., Paumard, T., Ott, T., Gilbert, A., Gillessen, S., Horrobin, M., Trippe, S., Bonnet, H., Dumas, C., Hubin, N., Kaufer, A., Kissler-Patig, M., Monnet, G., Ströbele, S., Szeifert, T., Eckart, A., Schödel, R., & Zucker, S. 2005a, ApJ, 628, 246

Eisenhauer, F., Perrin, G., Brandner, W., Straubmeier, C., Richichi, A., Gillessen, S., Berger, J. P., Hippler, S., Eckart, A., Schöller, M., Rabien, S., Cassaing, F., Lenzen, R., Thiel, M., Clénet, Y., Ramos, J. R., Kellner, S., Fédou, P., Baumeister, H., Hofmann, R., Gendron, E., Boehm, A., Bartko, H., Haubois, X., Klein, R., Dodds-Eden, K., Houairi, K., Hormuth, F., Gräter, A., Jocou, L., Naranjo, V., Genzel, R., Kervella, P., Henning, T., Hamaus, N., Lacour, S., Neumann, U., Haug, M., Malbet, F., Laun, W., Kolmeder, J., Paumard, T., Rohloff, R.-R., Pfuhl, O., Perraut, K., Ziegleder, J., Rouan, D., & Rousset, G. 2008, in Society of Photo-Optical Instrumentation Engineers (SPIE) Conference Series, Vol. 7013, 70132A

Eisenhauer, F., Perrin, G., Rabien, S., Eckart, A., Lena, P., Genzel, R., Abuter, R., & Paumard, T. 2005b, Astronomische Nachrichten, 326, 561

Ferrarese, L., Côté, P., Dalla Bontà, E., Peng, E. W., Merritt, D., Jordán, A., Blakeslee, J. P., Haşegan, M., Mei, S., Piatek, S., Tonry, J. L., & West, M. J. 2006, ApJL, 644, L21

Figer, D. F., McLean, I. S., & Morris, M. 1999, ApJ, 514, 202

Figer, D. F., Najarro, F., Gilmore, D., Morris, M., Kim, S. S., Serabyn, E., McLean, I. S., Gilbert, A. M., Graham, J. R., Larkin, J. E., Levenson, N. A., & Teplitz, H. I. 2002, ApJ, 581, 258

Figer, D. F., Rich, R. M., Kim, S. S., Morris, M., & Serabyn, E. 2004, ApJ, 601, 319

Forrest, W. J., Shure, M. A., Pipher, J. L., & Woodward, C. E. 1987, in American Institute of Physics Conference Series, Vol. 155, The Galactic Center, ed. D. C. Backer, 153–156

Förster Schreiber, N. M. 2000, AJ, 120, 2089

Franklin, G., Powell, J., & Workman, M. 1998, Digital control of dynamic systems, Addison-Wesley world student series (Addison-Wesley)

Freitag, M., Amaro-Seoane, P., & Kalogera, V. 2006, ApJ, 649, 91

Fritz, T. K., Gillessen, S., Dodds-Eden, K., Lutz, D., Genzel, R., Raab, W., Ott, T., Pfuhl, O., Eisenhauer, F., & Yusef-Zadeh, F. 2011, ApJ, 737, 73

Frogel, J. A., Stephens, A., Ramírez, S., & DePoy, D. L. 2001, AJ, 122, 1896

Genzel, R., Eisenhauer, F., & Gillessen, S. 2010, Reviews of Modern Physics, 82, 3121

Genzel, R., Schödel, R., Ott, T., Eisenhauer, F., Hofmann, R., Lehnert, M., Eckart, A., Alexander, T., Sternberg, A., Lenzen, R., Clénet, Y., Lacombe, F., Rouan, D., Renzini, A., & Tacconi-Garman, L. E. 2003, ApJ, 594, 812

Genzel, R., Thatte, N., Krabbe, A., Kroker, H., & Tacconi-Garman, L. E. 1996, ApJ, 472, 153

Ghez, A. M., Salim, S., Weinberg, N. N., Lu, J. R., Do, T., Dunn, J. K., Matthews, K., Morris, M. R., Yelda, S., Becklin, E. E., Kremenek, T., Milosavljevic, M., & Naiman, J. 2008, ApJ, 689, 1044

Gillessen, S. 2011, *Metrology*, VLT-TRE-GRA-15880-8001, 3.0

Gillessen, S., Eisenhauer, F., Perrin, G., Brandner, W., Straubmeier, C., Perraut, K., Amorim, A., Schöller, M., Araujo-Hauck, C., Bartko, H., Baumeister, H., Berger, J.-P., Carvas, P., Cassaing, F., Chapron, F., Choquet, E., Clenet, Y., Collin, C., Eckart, A., Fedou, P., Fischer, S., Gendron, E., Genzel, R., Gitton, P., Gonte, F., Gräter, A., Haguenauer, P., Haug, M., Haubois, X., Henning, T., Hippler, S., Hofmann, R., Jocou, L., Kellner, S., Kervella, P., Klein, R., Kudryavtseva, N., Lacour, S., Lapeyrere, V., Laun, W., Lena, P., Lenzen, R., Lima, J., Moratschke, D., Moch, D., Moulin, T., Naranjo, V., Neumann, U., Nolot, A., Paumard, T., Pfuhl, O., Rabien, S., Ramos, J., Rees, J. M., Rohloff, R.-R., Rouan, D., Rousset, G., Sevin, A., Thiel, M., Wagner, K., Wiest, M., Yazici, S., & Ziegler, D. 2010, in Society of Photo-Optical Instrumentation Engineers (SPIE) Conference Series, Vol. 7734, 77340Y

Gillessen, S., Eisenhauer, F., Trippe, S., Alexander, T., Genzel, R., Martins, F., & Ott, T. 2009, ApJ, 692, 1075

Gitton, P. & Puech, F. 2009, *Interface Control Document between VLTI and its Instruments*, VLT-TRE-ESO-15000-1826, 6.0

Glindemann, A., Algomedo, J., Amestica, R., Ballester, P., Bauvir, B., Bugueño, E., Correia, S., Delgado, F., Delplancke, F., Derie, F., Duhoux, P., di Folco, E., Gennai, A., Gilli, B., Giordano, P., Gitton, P., Guisard, S., Housen, N., Huxley, A., Kervella, P., Kiekebusch, M., Koehler, B., Lévêque, S., Longinotti, A., Ménardi, S., Morel, S.,

Paresce, F., Phan Duc, T., Richichi, A., Schöller, M., Tarenghi, M., Wallander, A., Wittkowski, M., & Wilhelm, R. 2003, in ESA Special Publication, Vol. 522, GENIE - DARWIN Workshop - Hunting for Planets

Graham, A. W. & Spitler, L. R. 2009, MNRAS, 397, 2148

Groenewegen, M. A. T. 2008, A&A, 488, 935

Hamamatsu. 2012, in http://sales.hamamatsu.com/en/support/technical-notes.php

Hardy, J. W. 1998, Adaptive Optics for Astronomical Telescopes

Hartung, M., Lenzen, R., Hofmann, R., Böhm, A., Brandner, W., Finger, G., Fusco, T., Lacombe, F., Laun, W., Granier, P., Storz, C., & Wagner, K. 2003, in Society of Photo-Optical Instrumentation Engineers (SPIE) Conference Series, ed. M. Iye & A. F. M. Moorwood, Vol. 4841, 425–436

Haug, M. & Hofmann, R. 2011, *Beam Combiner Instrument Cryostat*, VLT-TRE-GRA-15880-6101, 3.0

Hippler, S., Brandner, W., Clénet, Y., Hormuth, F., Gendron, E., Henning, T., Klein, R., Lenzen, R., Meschke, D., Naranjo, V., Neumann, U., Ramos, J. R., Rohloff, R.-R., & Eisenhauer, F. 2008, in Society of Photo-Optical Instrumentation Engineers (SPIE) Conference Series, Vol. 7015, 701555

Hippler, S. & Hormuth, F. 2010, *VLTI tunnel seeing measurements*, VLT-TRE-GRA-15880-4365, 3.0

Hopman, C. & Alexander, T. 2006, ApJL, 645, L133

Jocou, L., Perraut, K., Nolot, A., Berger, J. P., Moulin, T., Labeye, P., Lacour, S., Perrin, G., Lebouquin, J. B., Bartko, H., Thiel, M., & Eisenhauer, F. 2010, in Society of Photo-Optical Instrumentation Engineers (SPIE) Conference Series, Vol. 7734, 773430

Kleinmann, S. G. & Hall, D. N. B. 1986, ApJS, 62, 501

Kroupa, P. 2001, MNRAS, 322, 231

Lacour, S. & Bonnet, H. 2011, *Astrometric Error Budget*, VLT-TRE-GRA-15882-3201, 3.0

Lacour, S., Jocou, L., & Kervella, P. 2011, *Instrument Calibration Plan*, VLT-TRE-GRA-15882-9502, 3.0

Lançon, A. & Mouhcine, M. 2002, A&A, 393, 167

Launhardt, R., Zylka, R., & Mezger, P. G. 2002, A&A, 384, 112

Lejeune, T., Cuisinier, F., & Buser, R. 1997, A&AS, 125, 229

Lima, J. & Amorim, A. 2011, *Beam Combiner Instrument Acquisition Camera*, VLT-TRE-GRA-15885-6301, 3.0

Lindegren, L. 1980, A&A, 89, 41

Löckmann, U., Baumgardt, H., & Kroupa, P. 2010, MNRAS, 402, 519

Lu, J. R., Ghez, A. M., Hornstein, S. D., Morris, M. R., Becklin, E. E., & Matthews, K. 2009, ApJ, 690, 1463

Maeder, A. & Meynet, G. 2000, ARAA, 38, 143

Maness, H., Martins, F., Trippe, S., Genzel, R., Graham, J. R., Sheehy, C., Salaris, M., Gillessen, S., Alexander, T., Paumard, T., Ott, T., Abuter, R., & Eisenhauer, F. 2007, ApJ, 669, 1024

Markwardt, C. B. 2009, in Astronomical Data Analysis Software and Systems XVIII, ed. D. A. Bohlender, D. Durand, & P. Dowler, Vol. 411, 251

Mármol-Queraltó, E., Cardiel, N., Cenarro, A. J., Vazdekis, A., Gorgas, J., Pedraz, S., Peletier, R. F., & Sánchez-Blázquez, P. 2008, A&A, 489, 885

Martins, F., Genzel, R., Hillier, D. J., Eisenhauer, F., Paumard, T., Gillessen, S., Ott, T., & Trippe, S. 2007, A&A, 468, 233

McLaughlin, D. E., King, A. R., & Nayakshin, S. 2006, ApJL, 650, L37

Merritt, D. 2009, ApJ, 694, 959

Mighell, K. J. 1999, ApJ, 518, 380

Miralda-Escudé, J. & Gould, A. 2000, ApJ, 545, 847

Nayakshin, S. & Sunyaev, R. 2005, MNRAS, 364, L23

Paumard, T., Genzel, R., Martins, F., Nayakshin, S., Beloborodov, A. M., Levin, Y., Trippe, S., Eisenhauer, F., Ott, T., Gillessen, S., Abuter, R., Cuadra, J., Alexander, T., & Sternberg, A. 2006, ApJ, 643, 1011

Perraut, K. & Jocou, L. 2011, *Beam Combiner Instrument Integrated Optics*, VLT-TRE-GRA-15884-6501, 3.0

Perrin, G., Cassaing, F., Lozi, J., & Fédou, P. 2009, *Beam Combiner Instrument Fringe Tracking*, VLT-TRE-GRA-15882-6701, 1.0

Perrin, G., Chapron, F., Fédou, P., Jocou, L., Perraut, K., & Ziegler, D. 2011a, *Beam Combiner Instrument Fiber Control Unit*, VLT-TRE-GRA-15882-6401, 3.0

Perrin, G., Fédou, P., Dembet, R., Choquet, É., & Menu, J. 2011b, *Beam Combiner Instrument Fringe Tracking*, VLT-TRE-GRA-15882-6701, 3.0

Pfuhl, O. 2011, *Characterization of the VLTI pupil stability*, VLT-TRE-GRA-15880-7102, 1.0

Pfuhl, O., Fritz, T. K., Zilka, M., Maness, H., Eisenhauer, F., Genzel, R., Gillessen, S., Ott, T., Dodds-Eden, K., & Sternberg, A. 2011, ApJ, 741, 108

Ramírez, S. V., Sellgren, K., Carr, J. S., Balachandran, S. C., Blum, R., Terndrup, D. M., & Steed, A. 2000, ApJ, 537, 205

Rayner, J. T., Cushing, M. C., & Vacca, W. D. 2009, ApJS, 185, 289

Roddier, F. 1981, Progress in optics. Volume 19. Amsterdam, North-Holland Publishing Co., 1981, p. 281-376., 19, 281

Rousset, G., Lacombe, F., Puget, P., Hubin, N. N., Gendron, E., Fusco, T., Arsenault, R., Charton, J., Feautrier, P., Gigan, P., Kern, P. Y., Lagrange, A.-M., Madec, P.-Y., Mouillet, D., Rabaud, D., Rabou, P., Stadler, E., & Zins, G. 2003, in Society of Photo-Optical Instrumentation Engineers (SPIE) Conference Series, ed. P. L. Wizinowich & D. Bonaccini, Vol. 4839, 140–149

Schödel, R. 2010, A&A, 509, A58

Schödel, R., Eckart, A., Alexander, T., Merritt, D., Genzel, R., Sternberg, A., Meyer, L., Kul, F., Moultaka, J., Ott, T., & Straubmeier, C. 2007, A&A, 469, 125

Schödel, R., Merritt, D., & Eckart, A. 2009, A&A, 502, 91

Schödel, R., Najarro, F., Muzic, K., & Eckart, A. 2010, A&A, 511, A18

Schreiber, J., Thatte, N., Eisenhauer, F., Tecza, M., Abuter, R., & Horrobin, M. 2004, in Astronomical Society of the Pacific Conference Series, Vol. 314, Astronomical Data Analysis Software and Systems (ADASS) XIII, ed. F. Ochsenbein, M. G. Allen, & D. Egret, 380

Serabyn, E. & Morris, M. 1996, Nature, 382, 602

Seth, A., Agüeros, M., Lee, D., & Basu-Zych, A. 2008, ApJ, 678, 116

Seth, A. C., Cappellari, M., Neumayer, N., Caldwell, N., Bastian, N., Olsen, K., Blum, R. D., Debattista, V. P., McDermid, R., Puzia, T., & Stephens, A. 2010, ApJ, 714, 713

Shao, M. & Colavita, M. M. 1992, A&A, 262, 353

Sternberg, A. 1998, ApJ, 506, 721

Straubmeier, C. & Fischer, S. 2011, *Beam Combiner Instrument Spectrometer*, VLT-TRE-GRA-15883-6601, 3.0

Straubmeier, C., Fischer, S., Araujo-Hauck, C., Wiest, M., Yazici, S., Eisenhauer, F., Perrin, G., Brandner, W., Perraut, K., Amorim, A., Schöller, M., & Eckart, A. 2010, in Society of Photo-Optical Instrumentation Engineers (SPIE) Conference Series, Vol. 7734, 773432

Trippe, S., Gillessen, S., Gerhard, O. E., Bartko, H., Fritz, T. K., Maness, H. L., Eisenhauer, F., Martins, F., Ott, T., Dodds-Eden, K., & Genzel, R. 2008, A&A, 492, 419

von der Lühe, O. 1995, *Fried parameter, isoplanatic angle and correlation lifetime at Cerro Paranal*, VLT-TRE-ESO-10000-0783

Wagner, R. E. & Tomlinson, W. J. 1982, Appl. Opt., 21, 2671

Wallace, L. & Hinkle, K. 1996, ApJS, 107, 312

—. 1997, ApJS, 111, 445

Wallner, O., Winzer, P. J., & Leeb, W. R. 2002, Appl. Opt., 41, 637

Zoccali, M., Hill, V., Lecureur, A., Barbuy, B., Renzini, A., Minniti, D., Gómez, A., & Ortolani, S. 2008, A&A, 486, 177

List of Acronyms and Abbreviations

AO	Adaptive Optics
AT	Auxiliary Telescope
CCWS	Counter Clock-Wise System
CWS	Clock Wise System
DL	Delay Lines
ESO	European Southern Observatory
FDDL	Fibered Differential Delay Lines
FoV	Field of View
FPR	Fibered Polarization Rotator
GC	Galactic Center
HWP	Half-Wave Plate
IMF	Initial Mass Function
LCU	Local Control Unit
mas	milli-arcsecond
NSC	Nuclear Stellar Cluster
NIR	Near-Infrared
OPD	Optical Path Difference
PSD	Position Sensitive Diode
PSF	Point Spread Function
PTV	Peak To Valley
rad	radian
RC	Red Clump
RMS	Root Mean Square
Sgr A*	Sagittarius A*, SMBH in the Galactic Center, Radio source
SMBH	Super Massive Black Hole
SNR	Signal to Noise Ratio
STS	Star Separator
TTP	Tip/Tilt/Piston
UT	Unit Telescope
VLT	Very Large Telescope
VLTI	Very Large Telescope Interferometer
WFS	Wave Front Sensor

Acknowledgements

I would like to thank Prof. Dr. Reinhard Genzel for giving me the opportunity to do a PhD in the inspiring and excellent environment of the infrared group of the Max-Planck-Institut für extraterrestrische Physik. I am also very grateful to my supervisor Dr. Frank Eisenhauer for all the support, advice and guidance throughout the years. The same applies to Dr. Stefan Gillessen who always had time for questions and discussion. Many thanks go to the whole GRAVITY team. It is always a great pleasure to work with this motivated team. Special thanks goes to Stefan Kellner and Marcus Haug, with whom I spent countless hours in the lab.
I would like to thank my fellow PhD students Dr. Katie Dodds-Eden, Tobias Fritz, Gilles Orban de Xivry and Peter Buschkamp for their help, distraction and many joyful hours.
Last but not least, I would like to thank my family for all the support and love they gave me.